Metal binding to the Polaris protein associated with ethylene sensing by plants

WILLIAM EDWARD MICHAELS

Metal binding to the Polaris protein associated with ethylene sensing by plants

William Edward Michaels, B.Sc. (Hons)

Thesis submitted for the degree of Doctor of Philosophy

Durham University

Department of Biosciences

Biomolecular interactions

May 2023

Metal binding to the Polaris protein associated with ethylene sensing by plants

William Edward Michaels

Copper ions are essential to life, but toxic if not tightly regulated. In the model organism *Arabidopsis thaliana*, the ER-localised ethylene receptor, ETR1, requires Cu(I) at an intramembrane site, dependent on the Cu(I)-transporting P-type ATPase RAN1. However, the detailed biochemical mechanisms of Cu(I)-delivery, and ethylene binding, are unknown.

The protein Polaris (PLS), a negative regulator of ethylene signalling, shares some characteristics of known Cu(I)-metallochaperones, and was proposed to be involved in correct Cu(I)-metalation of ETR1. Here, metal binding to PLS has been investigated *in-vitro*, allowing prediction of its likely metalation state *in-vivo*. PLS bound Cu(I) and Zn(II) in 2:1 protein:metal stoichiometries, with β_2 affinities of 3.79 $x10^{19}$ and 3.76 $x10^{12}$ M^{-2} respectively. Recently developed metalation calculators, based on metal-availability read-out from calibrated bacterial cells, were adapted to use these constants. The metal affinities of the *Arabidopsis* cytosolic Cu(I) chaperone Atx1, showed Cu(I) bound in a 1:1 and Zn(II) a 2:1 stoichiometry, and its metalation was modelled. This work showed, in *E. coli* BL21(DE3), by reading out CueR-dependent *copA* transcripts, Atx1 overexpression decreased Cu(I)-availability, when calibrated using *E. coli* JM109, with implications for heterologous expression of metalloproteins in bacteria. Availabilities, measured here, were used to correctly predict the metal preference of Atx1 in *E. coli*, when tested post-extraction. Using the Atx1 Cu(I)-affinity of 5.47 $x10^{-18}$ M as an estimate for the intracellular buffered Cu(I)-availability in the cytosol of *Arabidopsis*, the metalation of PLS as a function of Atx1 Cu(I)-metalation showed it was unlikely PLS extracts Cu(I) directly from the buffer, at least not as a 2:1 complex.

This thesis speculates upon the putative roles of PLS in the biochemical activities of ETR1, and considers some of the implications and challenges associated with the potential formation of metal-dependent 2:1 ligand:metal complexes (with analogy to PLS_2:Cu(I)) in biological systems, more broadly.

Table of Contents

List of tables and figures

Tables:

Figures:

Declaration

No portion of this work has been submitted in support of an application for another degree or qualification from this or any other University or institute of learning.

Statement of copyright

Acknowledgements

Firstly, I would like to acknowledge Prof. Nigel Robinson for his scientific mentorship and patience throughout my time in Durham. Nigel's vast knowledge and acuity have come to my rescue more times than I care to admit over these years, and I am deeply grateful for his support and direction. I would also like to thank Prof. Keith Lindsey for his help and encouragement, especially in providing the preliminary work that made this project possible.

From day one in the laboratory, Dr. Andrew Foster, Dr. Deenah Osman and Dr. Tessa Young have been, and continue to be, an incredible source of inspiration for me. I am massively indebted to them all for the time and effort they put into supporting me, both as scientists and friends, and I owe much of my knowledge and skills to them.

I would also like to thank Dr. Peter Chivers, Dr. Karrera Djoko and my thesis committee, Dr. Gary Sharples and Prof. Adam Benham for their listening ears, kind words, and valuable opinions whenever I needed them.

To my other Durham science friends, who have shared this journey with me: thank you for everything. Jack and Sam, we've been in it together since the very beginning, and I am so grateful for your support throughout, and I wish you both the best with your submissions soon! Sophie, it's been so much fun working together since you started, even through all the qPCR troubleshooting! Joy, thank you for keeping me company in the anaerobic chamber for hours on end, Josh for your endless enthusiasm and much needed coffee breaks and Arthur, your infectious passion for science which truly inspires me. To my flatmate Jenny – we made it! It is hard to put into words how glad I am that we met, thank you so much for everything, from cat memes to lobster pots. There are too many to mention all of you by name, but I am so very grateful for all your friendships here in Durham.

I am, of course, incredibly grateful to my parents and brothers for their unconditional help and encouragement through all my various life decisions to get to this point. And finally, for my partner Miriam, thank you for listening, caring, advising and being there for me throughout, I couldn't have done it without you.

List of abbreviations

BCA – Bicinchoninic acid

BCS – Bathocuproine disulfonate

BSA – Bovine Serum Albumin

cDNA – complementary DNA

CV – Column volume

Cys – Cysteine

DEAE – Diethylaminoethyl cellulose

DMSO – Dimethyl sulfoxide

DNA – deoxyribonucleic acid

DTNB – 5,5-dithio-bis-(2-nitrobenzoic acid)

DTT – Dithiothreitol

EDTA – Ethylenediaminetetraacetic acid

ER – Endoplasmic reticulum

GSH – Glutathione

HEPES – 4-(2-hydroxyethyl)-1-piperazineethanesulfonic acid

His – Histidine

ICP-MS – Inductively coupled plasma mass spectrometry

IPTG – Isopropyl β-D-1-thiogalactopyranoside

kb – Kilobases

kDa – Kilodalton

LB – Luria-Bertani growth medium

MBP – Maltose Binding Protein

Met – Methionine

MF-2 – Mag-fura-2

M_r – Molecular mass

NTA – Nitrilotriacetic acid

OD_{600} – Optical Density

PAGE – Polyacrylamide gel electrophoresis

PCR – Polymerase chain reaction

PLS – Polaris

RNA – Ribonucleic acid

rpm – Revolutions per minute

RT – Reverse Transcriptase

SDS – Sodium Dodecyl Sulfate

Ser – Serine

TAR – 4-(2-thiazolylazo)-resorcinol

TBE – Tris/Borate/EDTA buffer

TCEP – Tris(2-carboxyethyl)phosphine hydrochloride

TGN – Trans-golgi network

TNB – 2-nitro-5-thiobenzoic acid

TRIS – Tris(hydroxymethyl)aminomethane

UV – Ultraviolet

Chapter 1. Introduction

1.1 Metals in biology

1.1.1 The requirements for metals in the cell

It is predicted that approximately 50% of the enzymes of life require a metal to function (Waldron, Rutherford, Ford, & Robinson, 2009).

Within the evolutionary landscape, metals have been a key source of biological innovation. The diversity of unique physical and chemical properties, that metals can provide biological systems, has been exploited throughout evolutionary history, enabling exquisite control of cellular function. Examples range from structural motifs such as zinc fingers, through spectrally active molecules like pigments, to complex catalytic enzymes with redox properties (Buccella, Lim, & Morrow, 2019).

1.1.2 Hurdles for correct metalation *in-vivo*

Metals interact with ligands, where the ligands act as Lewis bases, donating electrons to the metal. Each metal binds different ligands preferentially based on the specific physical and chemical properties a set of ligands offer, for example its “hardness” or “softness” (Ayers, Mohamed, & Heidar-Zadeh, 2022). In classical inorganic chemistry, correct metalation can be defined by these exact properties, for example a rigid tetrahedral (coordination number of 4) arrangement will preferentially bind zinc over cobalt which binds in an octahedral (coordination number of 6) arrangement (Figure 1.1) (Rulíšek & Vondrášek, 1998).

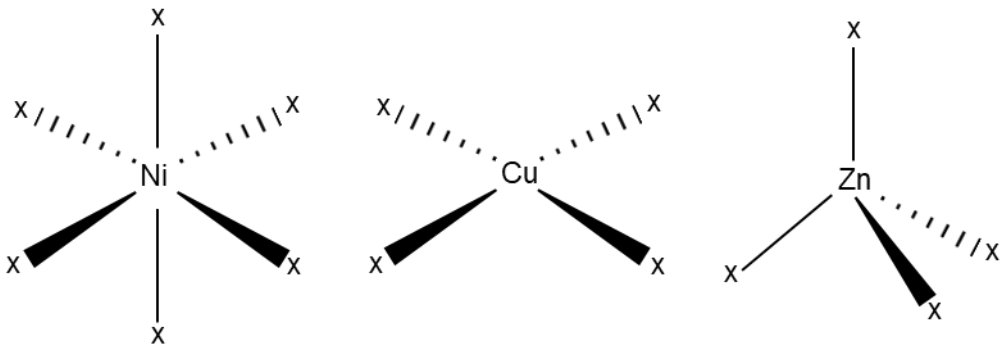

Figure 1.1, Preferential coordination geometries. Two-dimensional dash and wedge representations of the ligand coordination geometries commonly associated with Ni, Cu and Zn: octahedral, square planar and tetrahedral respectively. An “X” represents the respective ligand around the central metal ion.

In biochemistry, it has become clear that proteins cannot perfectly dictate specificity of their cognate metals by imposing a rigid co-ordination geometry, due to theirinherent flexibility, especially within nascent polypeptides. Metals such as copper can enter a folding or pre-folded protein that contains a putative cobalt site and can distort the ligands out of alignment into a favourable position for copper. In addition to distortion of existing ligands and exploitation of additional ligands, it is also possible that the incorrect metal can recruit only a sub-set of ligands from the binding site.

The difference in relative stabilities of complexes formed by divalent first-row transition metals was first described by the Irving-Williams series (Irving & Williams, 1948) where the stabilities of metalated complexes generally increased across the period. *In-vitro*, the metal binding sites in proteins tend to bind proteins ranked in this order of preference, as shown in below (Foster, Osman, & Robinson, 2014; Irving & Williams, 1948).

$$Mn(II) < Fe(II) < Co(II) < Ni(II) < Cu(II)\ (Cu(I)) > Zn(II)$$

As more reactive metals can recruit ligands from the active metal site and alter their geometry and chemistry, “mismetalated” proteins often lose functionality (Imlay, 2014). One example is the glyoxalase of *Clostridium acetobutylicum* which is activated by nickel or cobalt, forming a functionally active octahedral site. Mismetalation with tightly-binding Zn distorts the site to a functionally inactive trigonal bipyramidal geometry (Foster et al., 2014; Suttisansanee et al., 2011).

Hence, it is important that cells can somehow control metal specificity, irrespective of what the Irving Williams (IW) series predicts.

1.1.3 A special case: Copper

The emergence of copper in enzymatic processes can be traced back to the "Great Oxidation Event" 2-3 billion years ago (Kaim, Rall, & Rall, 1996), where photosynthetic production of oxygen facilitated oxidation of less soluble Cu(I) sulphides to the more soluble Cu(II) (sulphate) redox state. Copper's ability to swap between these two redox states under physiologically relevant conditions has been harnessed by cells, to shuttle potentially damaging electrons safely in the cell. For example, whilst co-ordinated within copper oxidoreductases, copper can facilitate safe electron transfer from reductants to oxidants. Before this oxidative event it is presumed that iron predominantly fulfilled this redox-based role, however the increasingly oxidative environment began to limit its use as it was oxidised to its insoluble Fe(III) state and hence was less available to the cell (Singleton & Le Brun, 2007). Iron however is still utilised for its redox chemistry in heme and FeS clusters (Connorton, Balk, & Rodríguez-Celma, 2017).

At the top of the Irving Williams series, copper can also displace the less competitive metals from their binding sites, often resulting in non-functional, mis-metalated proteins (Imlay, 2014). However, mismetalation is not the only source of copper toxicity to the cell; alongside copper's ability to donate electrons is its propensity to generate deleterious hydroxyl free radicals in the Fenton reaction, when exposed to hydrogen peroxide (Stohs & Bagchi, 1995), below.

$$H_2O_2 + Cu(I) \rightarrow OH^- + {}^{\bullet}OH + Cu(II)$$

This Cu(II) product can be further reduced to Cu(I) by plentiful thiol-containing compounds within the cell (or superoxide, a by-product of respirative metabolism), restarting the cycle to produce the damaging hydroxyl free radicals via the Fenton reaction. These free radicals cause oxidative damage to many components of the cell including proteins, DNA, and lipids and for this reason, copper must be tightly regulated to allow both the sufficient supply of copper, and to restrict its damaging toxicity. One effective method for protecting the cell from the deleterious effects of "free" copper in the cell is by maintaining the copper in its bound form through coordination with ligands. This can effectively chelate the potentially toxic Cu(I), protecting the cells from any deleterious effects. An example of this is a family of metalloproteins called metallothioneins which can form multi-nuclear clusters that bind Cu(I) via multiple cysteine residues (Thirumoorthy et al., 2007).

Proteins known as metallochaperones can also provide similar protection by binding the Cu(I), with the additional benefit of having a specificity to certain complex metal transport systems and/or directly targeting cuproproteins. The role of these metallochaperones is to deliver the potentially toxic copper directly to the location in the cell where it is required – often to metalate a cuproprotein, or to a transporter for import into another compartment or out of the cell (Robinson & Winge, 2010).

1.1.4 Cellular adaptation to the biochemistry of metals

As a result of the lack of steric selection by proteins themselves, when investigating protein metalation *in-vitro,* metalloproteins tend to bind the incorrect

metal. For example, when investigating the metal binding of the Cyanobacterial Mn(II) cupin MncA *in-vitro*, the protein preferentially binds Zn(II) over Mn(II) (Tottey et al., 2008). In order to correctly metalate MncA *in-vitro,* a 100 000-fold excess of Mn(II) relative to Zn(II) was required before the protein could be fully loaded with Mn(II). So how does the cell ensure correct metalation of proteins that can bind other metals so many orders of magnitude tighter than their cognate metals?

Within the cell, protein metalation occurs in the context of competition with a vast excess of other metal binding sites, some exchangeable and some not. The pool of alternative (exchangeable) metal binding sites is referred to as a “buffer” which provides a labile pool of various metals, accessible to the metalloproteins of the cell. It has become clear that this buffer system establishes a gradient of availabilities set inversely to the Irving-Williams series (Foster et al., 2014). The result is a balance where the affinity of a protein for its metal is complemented by the availability of the metal in the buffer i.e., metals such as Cu (with high affinities) are maintained at extremely low availabilities and metals such as Mn (with low affinities) are maintained at much higher availabilities. This effectively “levels the playing field” so as the metalation of a protein is not defined by its absolute metal affinities, but by its affinity for each metal relative to the availability of that metal within the cell. By competing affinities relative to their availabilities, as opposed to competing absolute affinities, it becomes feasible that proteins with low-affinity cognate metals, such as Mn, can avoid mis-metalation with tighter-binding metals like Cu. These availabilities have now been determined within the bacteria cell, and are used as a tool for studying protein metalation *in-vivo* across many different cell types (Osman et al., 2019).

The buffer forms the core foundations on which the availability of each metal is defined. However, throughout the life of a cell, internal requirements and external conditions fluctuate, and it becomes necessary for cells to develop mechanisms to detect and fine-tune the metal availabilities to remain within tolerable ranges. This fine-tuning is achieved through a diverse set of metal trafficking proteins which work to counteract deviations from these ranges. For example, in metal deficit, specific metal importing proteins acquire more metal in the cell, whilst in surplus, exporters and storage proteins work to remove or sequester those in excess. In humans, the importance of this regulation can be exemplified by two hereditary diseases associated with copper homeostasis malfunction for both deficiency and excess (Huffman & O'Halloran, 2001). ATP7A and ATP7B are both Cu-transporters from a large family of P_{1B}-type ATPase transporters. ATP7A exports copper to the secretory pathway for incorporation into cuproenzymes (Tümer & Møller, 2010). Non-functional mutations in ATP7A result in a multisystemic disorder of copper metabolism called Menkes disease, where the insufficient supply of copper to these enzymes can result in death in early childhood. Conversely, ATP7B functions to export excess Cu from the cell when in surplus. Defects in the function of ATP7B hence result in the hereditary Wilson's disease (Gitlin, 2003) where individuals with the disease have impaired excretion of Cu by the liver hepatocytes, resulting in toxic copper accumulation in the liver.

ATP7A is also regulated through post-translational control where it is relocated to vesicles near the plasma membrane in a copper-dependant manner (Holloway et al., 2013). This notion of post-translational sensing and regulation of metal homeostasis within in the cell (as opposed to transcriptional sensing and

regulation) is important, and has been explored throughout this work (section 1.3.3).

The correct function of these metal trafficking proteins is hence incredibly important, and as their function is often linked to their metalation, they themselves require both correct metalation and regulation which is sensitive to the metal availability within the cell. In bacteria, cells have evolved a set of “sensors”; specific DNA-binding metal-responsive transcriptional regulators, which have a range of allosteric mechanisms to regulate the transcription and hence expression of the metalloregulatory proteins. There are some known examples in eukaryotic systems, for example MTF1 which causes the metal-dependant transcription of metallothioneines (small cysteine rich proteins which scavenge surplus metals) (Günther, Lindert, & Schaffner, 2012) however examples are scarcer, and do not cover the large diversity of specific metal responses as seen in bacterial systems. There are three main categories of metal-responsive transcriptional regulators which have been characterised in bacteria: metal-dependent transcriptional -activators, -de-repressors and -co-repressors (Figure 1.2).

Again, although metal sensors maintain the metals at set levels within the cell, they themselves also need to remain correctly metalated to respond to the correct metal (Osman et al., 2017). This specificity is generally achieved through subtle changes of affinity, allostery and access (Foster et al., 2014), allowing the proteins to acquire the correct metals within the context of the intracellular buffer. Although the flexibility of a protein does not allow for imposing rigid coordination geometries, certain ligand and charge combinations can subtly modify the affinities and can be used to select for the correct metals at the level of the allosteric response requiring a specific geometry. Indeed, recently, artificial metalloprotein dimers with

covalently constrained dimer interfaces have been developed through a flexible/probabilistic protein design strategy which can selectively bind metals contrary to the Irving-Williams series (Choi & Tezcan, 2022). As non-artificial examples: on binding their cognate metals, the two winged helix turn helix sensor proteins ZntR and CueR (both metal-responsive transcriptional activators from the MerR family) cause a distortion in the DNA, facilitating RNA polymerase function and gene transcription (Hobman, 2007). ZntR and CueR share 37% identity (Brown, Stoyanov, Kidd, & Hobman, 2003), however can select for their different cognate metals despite their almost identical structure. The specificity is dictated by the affinity of the metals for the

A. Metal-dependent activators:

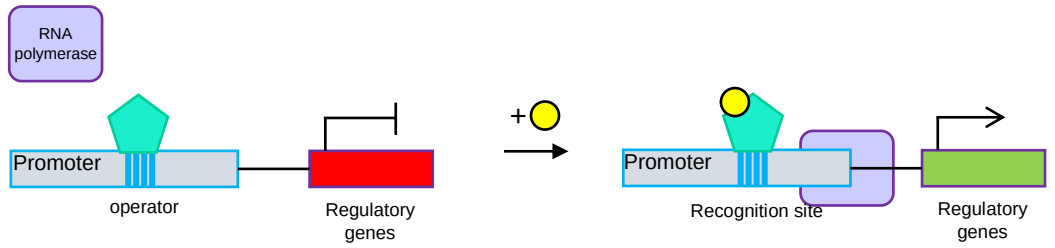

B. Metal-dependent co-repressors:

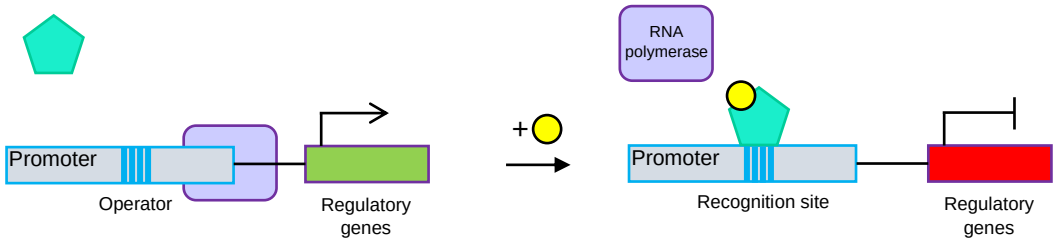

C. Metal-dependent de-repressors:

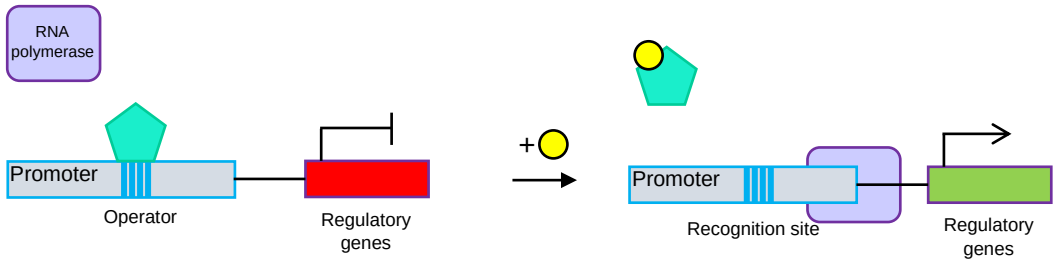

Figure 1.2, Allosteric mechanisms of transcriptional regulation by bacterial sensors. Schematic diagram showing how Metal-dependent activators, co-repressors, and de-repressors (A-C respectively) influence gene transcription. On binding their cognate metals (yellow circles), the sensors (teal pentagons) undergo allosteric changes either enhancing or inhibiting DNA binding. Changes in sensor DNA binding alter the RNA polymerase (violet box) activity, causing changes in downstream gene

binding site, where the copper site in CueR is localised adjacent to the end of a negative helix dipole and the zinc site in ZntR is not. As Zn(II) is divalent and Cu(I) is monovalent, the copper site is less favourable for zinc (Changela et al., 2003a). More importantly (and difficultly), ZntR must also be able to keep the copper out of the zinc site. The binding site in ZntR provides a coordination environment in the metal binding loop with an additional bridging phosphate or sulphate which acts as additional ligand; a site optimal for a divalent metal over a monovalent Cu(I) (Changela et al., 2003b). For CueR, the mechanism by which metal binding leads to altered DNA binding, and gene activation, also dictates the specificity due to the allostery. Upon non-cognate binding, the metal would not result in correct modification of the shape of the protein (and hence DNA) to allow RNA polymerase binding. In the case of metallochaperones, metal delivery can also be dependent on the donor-receiver protein interaction and rely on the metal access which itself is dependent on the interface between the two proteins. The large (relative to the metal) surfaces of the proteins and their potential for specific complementarity through tertiary structure and charge distribution provides a scaffold for allowing only specific proteins to exchange their metals.

1.1.5 Calculating metalation *in-vivo*: metalation calculators

Initially, the metal affinities of the sensors have been used as proxy for the availability of the cognate metal in the cell, as the dissociation constant (K_d) for each sensor approximates to the available concentration at which the sensor is in the middle of its response curve i.e., 50% metalated. Indeed, this too suggested that Zn and Cu are held much less available than metals such as Mn and Fe

(Chandrangsu, Rensing, & Helmann, 2017; Changela et al., 2003b; Foster et al., 2014; C. E. Outten & O'Halloran, 2001; Waldron et al., 2009).

However, recently it has been possible to quantitatively characterise the tolerable ranges at which the sensors respond to their cognate metals and hence provide insight into how the intracellular availabilities fluctuate. Work by Osman and co-workers (Osman et al., 2019) determined the sensitivities of a complete set of 7 metal sensors from *Salmonella enterica* and calculated the change in DNA binding for all sensors as a function of intracellular metal availability. For each of the 7 sensors, a full set of biophysical parameters were measured, including the affinities of the sensors for their metal and affinity of the Apo-sensor and metalated-sensor for their DNA promoter sites (Figure 1.3). Using these three affinities, the number of sensor molecules per cell (in the presence and absence of metal) and the number of promoter targets per cell, it became possible to measure the fractional occupancy (θ_D) of each sensor as a function of metal concentration, and hence the "tuning" of each sensor.

Using this relationship between intracellular metal availability and DNA occupancy in *Salmonella* as a scaffold for metal sensing in the cell, it has now become possible to calibrate the response of each metal sensor by measuring the maximum and minimum change in each sensor's response (by following metal-responsive transcriptional changes using qPCR) under a range of metal-supplemented growth conditions. By calibrating the response of the sensors in one organism, it then becomes possible to measure the change in DNA binding of a sensor *in-vivo* and calculate the metal availability against this calibration curve (Young et al., 2021).

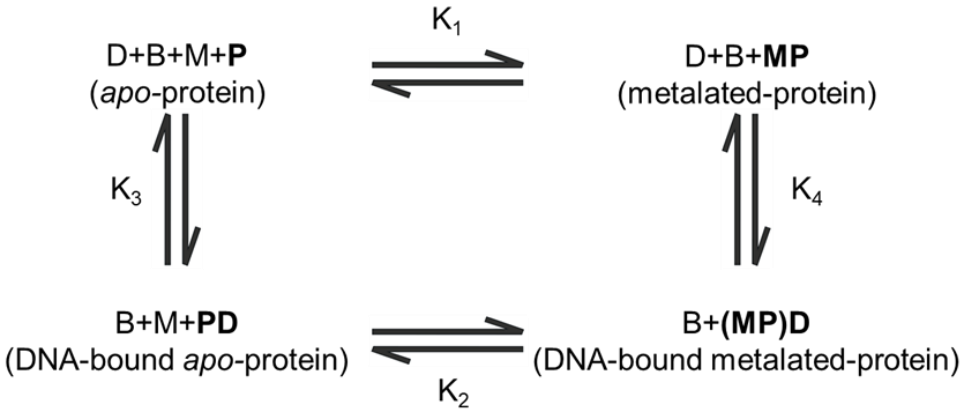

Figure 1.3, Allosteric scheme for sensor activity. Equations linking the apo-protein (P), metalated-protein (MP), apo-protein bound DNA (PD), DNA (D), buffer (B) and metalated-protein bound DNA ((MP)D). $K_{1\text{-}4}$ represent the thermodynamic equilibrium constants coupling the different states.

Such calibrations have been carried out in both *Salmonella* and *E. coli. JM109(DE3)* (Foster et al., 2022; Young et al., 2021) and have produced estimates for conditional availabilities for many relevant metals under standard laboratory growth conditions. Additionally, a full set of “idealised” availabilities within the bacterial cytosol have been produced which represent the metal availabilities at which all sensors are at the midpoint of their responses. These availabilities prompted the development of “metalation calculators” by co-workers in Prof. Robinson’s laboratory (Figure 1.4) (Foster et al., 2022; Martini, 2019; Young et al., 2021). Metalation calculators encode equations which allow the user to calculate the inter-metal competition for a single protein when the protein’s metal affinities and the metal availabilities in the cells are known. By using these calculators, it is now possible to predict the *in-vivo* metal preferences and occupancy for any protein in a living bacterial cell under the same conditions, so long as the metal affinities are known.

E. coli strain JM109 (DE3) cultured in LB (aerobic)

(Default Settings for Metal Availability)

	Metal Affinity (M)	ΔG (kJ mol^{-1})	Metal Availability (M)	Available ΔG (kJ mol^{-1})	Occupancy
Mg	1000	17.1	0.0027	-14.7	0.00%
Mn	1000	17.1	6.8e-6	-29.5	0.00%
Fe	1000	17.1	1.9e-6	-32.7	0.00%
Co	1000	17.1	6.5e-11	-58.1	0.00%
Ni	1000	17.1	1.3e-13	-73.5	0.00%
Cu	1000	17.1	4.5e-20	-110.4	0.00%
Zn	1000	17.1	1.7e-12	-67.2	0.00%
Total Metalation					**0.00%**

The calculator is based on Nature Communications 12 1195- (2021). Supported by grant **BB/V006002/1** from the Biotechnology and Biological Sciences Research Council. Background considerations and underlying assumptions

Reset | Download Results

Figure 1.4, Metalation calculators. Screenshot from metalation calculator website (https://mib-nibb.webspace.durham.ac.uk/metalation-calculators/) showing a calculator populated with metal availabilities from calibrated JM109 (DE3) cells when cultured in LB under aerobic conditions. Users populate the “Metal Affinity” column with metal affinities for the protein of interest and the “Occupancy” column is calculated as a proportion of total protein.

1.1 Metal regulation *in-plantae*

Metals are just as essential to life in plants as they are to the “organisms” discussed above. In contrast to bacteria however, it is not as well understood how biochemically, plant cells regulate the availabilities of specific metals to achieve correct metalation of theirproteins.

A large proportion of research to date has focussed on heavy metal remediation and how plants can respond to toxic increases in heavy metals such as mercury (Hg), lead (Pb) and cadmium (Cd) (Asati, Pichhode, & Nikhil, 2016). This heavy-metal stress (HMS) has been characterised by a wide array of plant responses which result in increased tolerance to heavy metal exposure (Wu, Saleem, He, & He, 2021). Despite the wide array of HMS defence mechanisms, many of these responses do not discriminate between heavy metals, and do not offer answers to how plants can specifically regulate the availability of individual essential metals within the plant cells, for example, copper.

Although some transcription factors, such as the WRKY family, have been identified that respond to HMS (Sheng et al., 2019), limited (and only very recent) examples of specific metal-dependent DNA-binding transcriptional regulators have been identified (Lilay et al., 2021). The recent discovery of the two Zn-sensors bZIP19 and bZIP23 from *Arabidopsis thaliana* represent the first specific metal-sensing proteins identified in plants upstream of a transcriptional regulatory network (Lilay et al., 2021). This lack of rigorously characterised metal-dependent DNA-binding transcriptional regulators has meant that calculators analogous to those developed in *Salmonella* cannot be simply transposed to a plant system as was the case for *E. coli*.

1.1.1 Ethylene sensing requires Cu(I)

One system that requires Cu in the plant cell is the ethylene response pathway. Despite the essentiality of copper to the functioning of the signal transduction, the mechanism of safe copper delivery to the various proteins is relatively poorly understood. This project aims to explore the mechanism by which copper is made available to the components of the ethylene signalling pathway within the plant cells.

The gaseous plant hormone ethylene (IUPAC name ethene, chemical formula C_2H_4) is one of the 5 ‘classical plant hormones’ and is involved in a variety of plant responses including fruit ripening, seed development, flowering, leaf senescence, abscission and responses to abiotic and biotic stresses (Ecker, 1995; Kendrick & Chang, 2008). Ethylene is biosynthesized by the plant, where it can diffuse across membranes throughout the plant (and indeed neighbouring plants) where it regulates a variety of processes.

The “triple response” was one of the first identified phenotypes in response to ethylene, where dark-grown eudicot seedlings have reduced root and hypocotyl growth, hypocotyl thickening and an exaggerated apical hook (Neljubov, 1901). Since its discovery, this easily identifiable phenotype has been used through a variety of genetic screens and assays to explore many different components of the ethylene signalling pathway (Binder, 2020; Guzmán & Ecker, 1990). Studies have revealed a response pathway made up of the ethylene receptors, protein kinases and transcription/response factors.

In *Arabidopsis*, there are 5 ethylene receptors belonging to 2 subfamilies: ETR1 (ethylene response 1) and ERS1 (ethylene response sensor 1) (Subfamily I) and ETR2, ERS2 and EIN4 (ethylene-insensitive 4) (subfamily II). All five bear sequence homology to cyanobacterial two component histidine kinase receptors (Gamble, Coonfield, & Schaller, 1998) where subfamily I have three transmembrane domains and subfamily II have four. All receptors localise to the ER (Y. F. Chen, Randlett, Findell, & Schallert, 2002) and contain a Cu(I) ion at residues Cys65 and His69, acting as an essential cofactor in strong-affinity ethylene binding (Rodriguez et al., 1999) (Figure 1.5). Notably, while two component sensors of the histidine kinase type are common in bacteria, they are exceptionally rare in eukaryotes with ETR1 being an exemplar.

In the absence of the ethylene, the ethylene receptors repress the ethylene responses (Rodríguez et al., 1999) by the activation of CTR1, a mitogen-activated protein kinase kinase kinase (MAPKKK) which negatively regulates ethylene responses (Kieber, Rothenberg, Roman, Feldmann, & Ecker, 1993). Conversely, in the presence of ethylene, the receptor binds ethylene, does not activate the CTR1 MAPKKK and the ethylene responses are derepressed, resulting in transcription of the ethylene responsive genes (Figure 1.6).

The transport of copper (Cu(I)) to the ER in *Arabidopsis* is dependent on the P-type ATPase RAN1 (responsive-to-agonist1). Mutations in RAN1, results in abnormal ethylene responses (Hirayama et al., 1999; Woeste, 2000). It has been shown that RAN1 plays an essential role in the biogenesis of the functional ETR1 receptor (Binder, Rodríguez, & Bleecker, 2010) . In the case of ETR1, it was shown that the N-terminal 128 amino acids are required to bind copper and facilitate ethylene binding (Rodriguez et al., 1999). The mechanism and regulation

of delivery of Cu(I) to ETR1 via Ran1 however, remains unknown. Indeed, the mechanism of Cu(I) transfer from P1-type ATPases (analogous to RAN1) to cuproproteins within the ER or TGN has not been described in any eukaryote, even though a large proportion of eukaryotic cupro-proteins are metalated via this route.

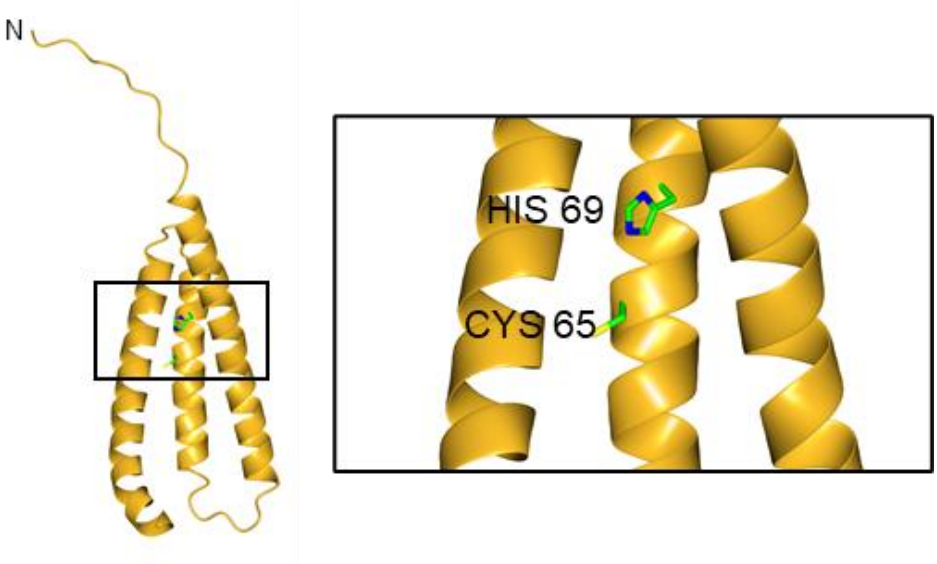

Figure 1.5, Intramembrane Cu(I) binding site of *Arabidopsis thaliana* ETR1. Predicted AlphaFold structure of the trans-membrane domain of ETR1 (Residues 1-113). Residues His 69 and Cys 65 identified as conserved Cu(I) ligands annotated (Rodriguez, 1999). Notably, the Cu(I) site appears almost central to the membrane.

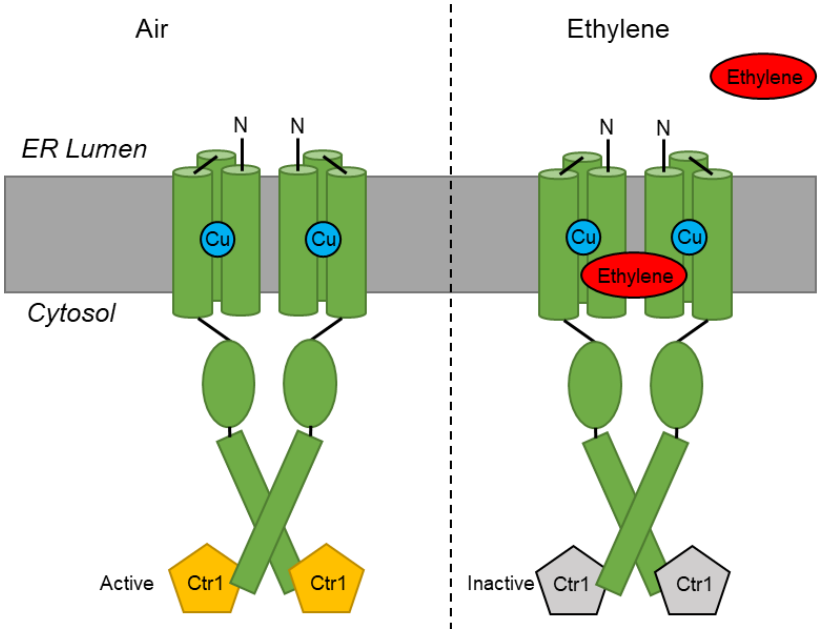

Figure 1.6, Ethylene response pathway. In the absence of ethylene, ethylene receptors (green) activate CTR1 (pentagon) which negatively regulates the downstream transcriptional changes associated with ethylene. In the presence of Ethylene, the activation of CTR1 is removed, facilitating transcriptional changes associated with ethylene.

1.2.2 Polaris: a Cu(I) metallochaperone?

Promoter trapping experiments designed to investigate polar organisation in *Arabidopsis thaliana* embryos and seedlings first identified a small protein Polaris (PLS) expressed in embryonic and seedling root tips (Topping & Lindsey, 1997). PLS has since been shown, through genetic screening of *Arabidopsis*, to be required for correct responses to cytokinins and auxins, root-cell expansion and vascular patterning in the leaf (Casson et al., 2002).

These auxin responses were later shown to be regulated by PLS via effects on ethylene signalling (Chilley et al., 2006), where the mutant, *pls*, enhanced ethylene signalling (seen in a triple response phenotype). Both the defective auxin response and enhanced ethylene response can be suppressed by genetic and pharmacological inhibition of ethylene signalling. This work suggests that the PLS protein negatively regulates the ethylene responses, which in turn influence downstream effects including auxin homeostatic changes.

1.2.3 Structure and function of Polaris

The PLS gene encodes a 36 amino acid polypeptide with predicted mass of 4.6 kD. Homologues have been identified in several different plant species, however only *Arabidopsis* subspecies contain the full-length polypeptide (Figure 1.9). Alphafold structural prediction (Figure 1.7) (Jumper et al., 2021) shows at the C-terminus a region predicted to be able to form an alpha helix, and a relatively unstructured N-terminus. Highlighted residues (MET 1, CYS 6, CYS 17 and HIS 36) are those generally considered as potential ligands for copper binding.

A.

```
A.thaliana          MKPRLCFNFRRRSISPCYISISYLLVAKLFKLFKIH    36
C.sativa            MKPRLCFNSRRRSISPCYISIS--------------    22
R.sativus           MEPRLCFTFRXRSISPCYINLLFISMSFKI------    30
E.salsugineum       MKPRLCFNFRRRSISPCYLSNILLSSRL--------    28
A.lyrata            MKPRLCFNFRRRSISPCYISISYLL-AKMFKFIKIH    35
```

B.

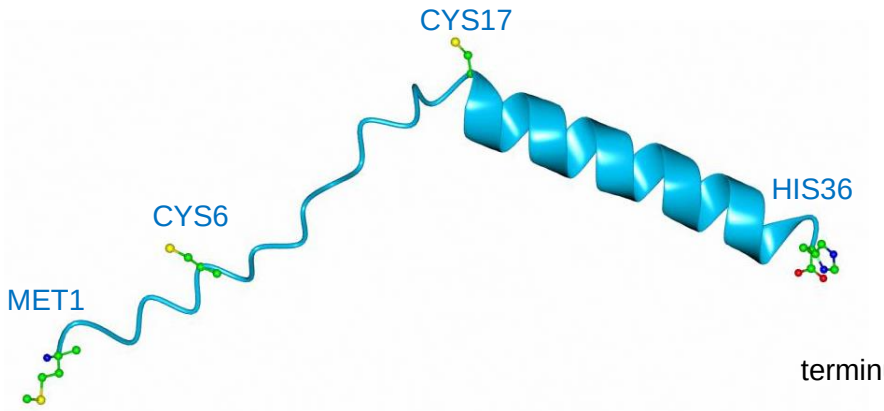

Figure 1.7, Polaris structure. A, Multiple sequence alignment for all identified homologues of PLS. B, AlphaFold structural prediction for protein Polaris from *Arabidopsis thaliana*. (Jumper et al., 2021) PBD identifier: Q8LLV8.

On examination of the PLS peptide, the two cysteines at position 6 and 17 resemble di-cysteine motifs that commonly co-ordinate Cu(I), for example in the human copper chaperone for superoxide dismutase (hCCS) (Stasser, Eisses, Barry, Kaplan, & Blackburn, 2005). The role of methionine in copper binding is generally weak and only considered supportive in addition to histidine and cysteine residues, it also tends to be a ligand for Cu(II) in more oxidising environments than the cytosol, such as the ER (Rubino, Chenkin, Keller, Riggs-Gelasco, & Franz, 2011). In some proteins such as the eukaryotic Ctr1 copper transporting proteins however, methionine residues do play a role in Cu(I) binding, although as part of methionine-rich sites or “Met motifs” (Shenberger, Marciano, Gottlieb, & Ruthstein, 2018), which are absent in the PLS protein. Hence, it is unlikely this N-terminal MET 1 is predicted to contribute significantly to the coordination of Cu(I) within the PLS protein. Histidine is also known to coordinate Cu(II) within cuproproteins via its imidazole nitrogen moiety, however due its occlusion from the putative di-cysteine motif by the predicted α-helix, it is not expected to provide a significant contribution to copper binding of PLS.

1.3 Atx1

Originally named Anti-oxidant 1, due to its role in detoxification of reactive oxygen species, the protein Atx1 was first identified in a *Saccharomyces cerevisiae* mutant deficient in superoxide dismutase (SOD) where it was shown to compensate for the lack of SOD only in copper replete cells (Lin & Culotta, 1995).

ATX1 encodes a soluble copper chaperone which has been shown in yeast to bind and deliver copper through a metal-mediated protein-protein interaction to the P_{1B}-type ATPase transporter Ccc2 (analogous to RAN1), localised on a post-Golgi vesicle (Arnesano et al., 2001; Banci et al., 2006). This Cu(I)-mediated interaction was shown by solution structure NMR and is represented in Figure 1.8. Ccc2 imports Cu into the vesicle where it is then incorporated into a multicopper oxidase called Fet3, essential in iron uptake (Pufahl et al., 1997).

Functional Atx1 homologues have been identified in a wide range of organisms including Atx1 in *Arabidopsis thaliana* (Puig et al., 2007) where it fully complemented the yeast *atx1*Δ mutants grown on iron-deficient media.

1.3.1 Structure and function of *Arabidopsis thaliana* Atx1

The *Arabidopsis thaliana* Atx1 encodes a 76 amino acid protein, of predicted mass 8159 Da, that shares the conserved sequence homology and predicted overall structure found other Atx1 homologues (Figure 1.8). The predicted structure consists of two α-helices and an antiparallel four-stranded β-sheet which make up the conserved βαββαβ where the 4 β-sheets form one side of the molecule and

the two α-helices the other (Figure 1.8). This βαββαβ structure is also known as a “ferredoxin-like fold”.

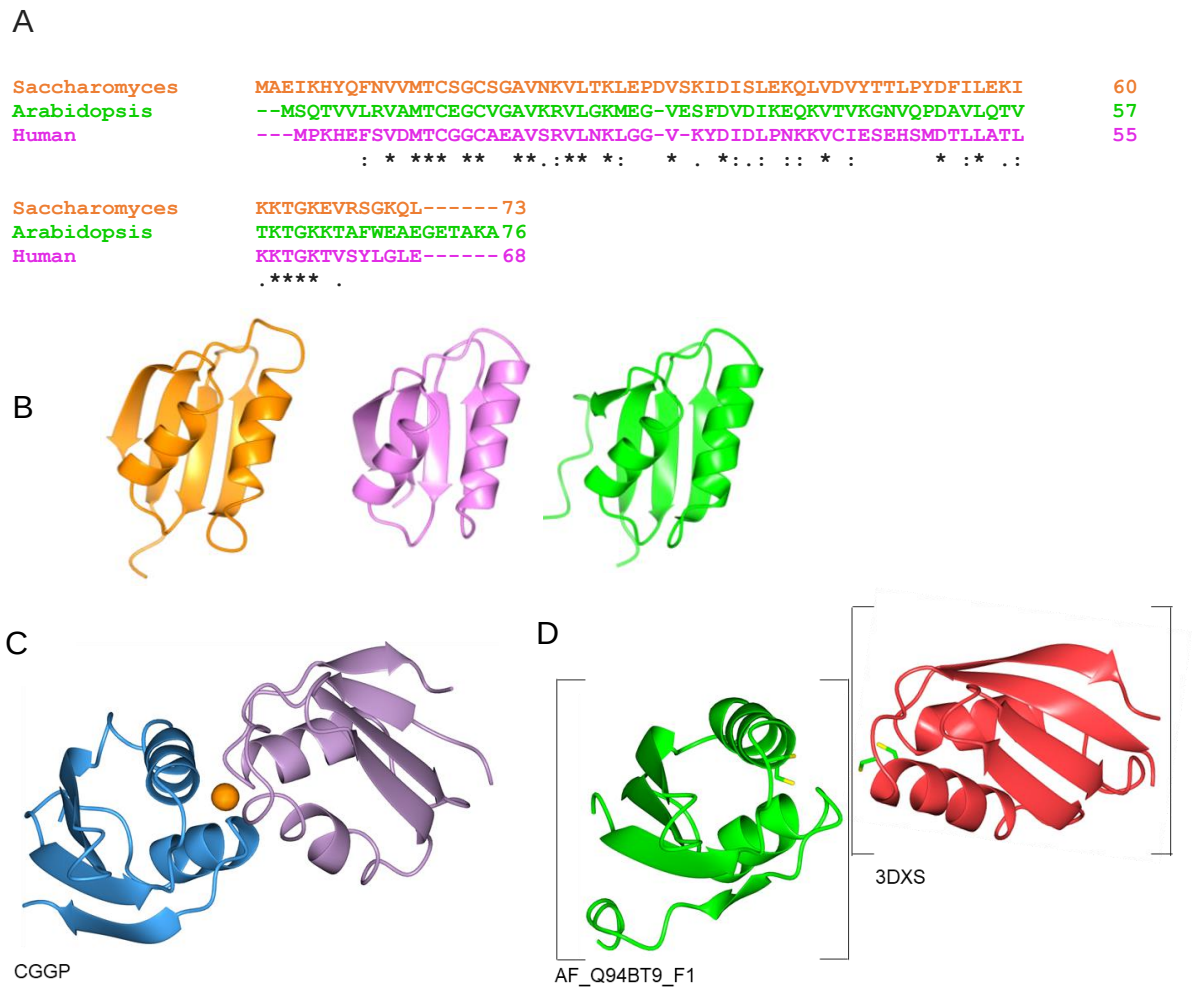

Figure 1.8, Comparison of Atx1 proteins. A, Amino acid sequence alignment of 3 homologous Atx1 proteins. B, Ribbon diagrams representing the crystal structures of Atx1 from Saccharomyces cerevisiae (orange), Human Atox1 (violet) and predicted AlphafFold structure of Atx1 from *Arabidopsis thaliana* (green). Images produced using ccpm4 software and UniProt identifiers 1CC7, 1FEE and AF-Q94BT9-F1 respectively. Alignments carried out using Clustal Omega web-tool. C, Ribbon diagram showing single solution structure of yeast Atx1 (blue) in a Cu(I)-mediated complex with the yeast Cu(I) importer Ccc2 metal binding domain (violet). D, Composite ribbon diagram taken from two structures showing the possible analogous Cu(I)-mediated interaction between *Arabidopsis* Atx1 (green, AlphaFold structural prediction) and the first MBD of the *Arabidopsis* P-type ATPase Ran1 (red, X-ray crystal structure). Conserved Cu(I)-coordinating cysteines 13 and 16 represented with cylinders.

1.3.2 Atox1 modulates function of P-type ATPase in humans

Analagous to the yeast Atx1/Ccc2 system, the human Atx1 analogue, Atox1, also interacts with a downstream P_{1B}-type ATPase, ATP7B, introduced earlier (also known as Wilsons disease protein, WNDP).

The N-terminal (cytosolic) tail of the P-type ATPases contains repeated sequence motifs resembling metal binding sites such as those found in the Atx1 protein family (Rice, Kovalishin, & Stokes, 2006). Pumps generally contain between 1 and 6 repeats and have been shown to bind Cu(I) (DiDonato, Narindrasorasak, Forbes, Cox, & Sarkar, 1997; Lutsenko, Petrukhin, Cooper, Gilliam, & Kaplan, 1997), and hence have been called “metal binding domains” or MBDs.

Experiments investigating Atox1 and ATP7B have clearly shown that Atox1 interacts with ATP7B via the MBDs present at the N-terminus of the transporter (Hamza, Schaefer, Klomp, & Gitlin, 1999; Larin et al., 1999). Indeed, some of the mutations identified in patients afflicted by Wilson’s disease, have been shown to interrupt the binding of ATP7B and Atox1 – implying the binding itself it essential for normal copper homeostasis (Lutsenko, Tsivkovskii, & Walker, 2003). Atox1 was shown to regulate the copper occupancy of ATP7B in a reversible manner, thereby regulating its activity (Walker et al., 2004; Walker, Tsivkovskii, & Lutsenko, 2002). This reversibility suggests an enhanced function for the metallochaperone Atox1 beyond the simplistic Cu delivery role – as the *apo*-Atox1 itself can remove Cu(I) from the transporter, thereby decreasing its activity.

More recently, mechanistic aspects of ATP7A regulation by Atox1 has been demonstrated (Yu et al., 2017). Here the authors show how Cu(I)-Atox1 can bind the first 3 (of 6) cytosolic MBDs, resulting in altered domain dynamics, and

activation of ATP hydrolysis and copper transport. Their findings suggest a regulatory mechanism whereby the metalation of Atox1 itself can regulate the activity of the P-type ATPase exporter.

1.3.3 A model for Atx1 in *A. thaliana*: a Cu-dependent, post-translational regulator?

Arabidopsis Atx1 shows very close sequence and structural homology to other Atx1 homologues (including Atox1) (Figure 1.8) and *Arabidopsis* also has an analogous p-type ATPase called RAN1 (previously HMA7) which contains two cytosolic tandem metal binding domains (Zimmermann et al., 2009).

Through yeast two-hybrid experiments, Atx1 was shown to interact *in-vivo* with the MBDs of the RAN1 transporter (Puig et al., 2007). Hence, using the analogous Atox1/WNDP system in humans, it becomes possible to construct a model for the Cu-dependent regulation of Cu(I) transport out of the cytosol in *Arabidopsis thaliana.* Here it is postulated that the metalation of Atx1 can bind the MBDs of RAN1 in a Cu(I)-dependent interaction analogous to the yeast system (Figure 1.8), and regulate the activity of the Cu(I) transporter RAN1 as a function of its metalation (Figure 1.9). This model infers a role for Atx1 as a Cu-dependent post-translational sensor of intracellular cytosolic Cu(I) in *Arabidopsis*.

Furthermore, in the same way that the metalation of the metal-responsive transcriptional activator CueR can be followed in *E. coli* as a proxy for Cu(I) availability, it follows that the metalation profile of Atx1 as a function of intracellular Cu(I) availability in *A. thaliana* might be used to read out the Cu availability in the cytosol.

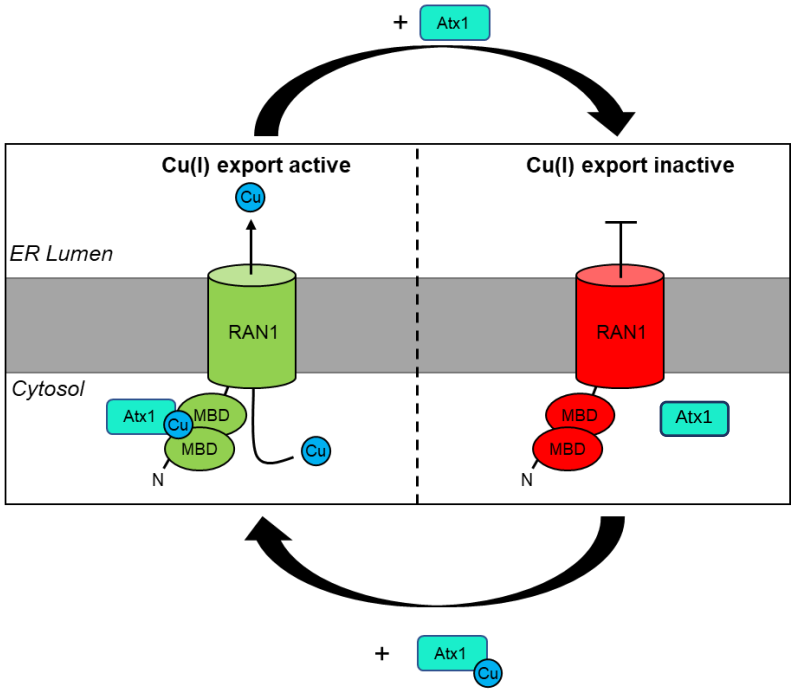

Figure 1.9, A model for the post-translational regulation of RAN1 by Atx1. Atx1 is proposed to modulate the function of the P-type ATPase RAN1 by binding the conserved metal binding domains (MBD). Cu(I)Atx1 binds and delivers Cu(I) to the MBDs, altering domain dynamics, resulting in activation of Cu(I) export into the lumen. Apo-Atx1 is able to remove Cu(I) from the MBDs on RAN1, resulting in inactivation of Cu(I) export into the lumen.

1.4 Hypotheses and aims

1.4.1 Proposed functional role of PLS as a metalloprotein involved in the delivery of Cu(I) to the ethylene receptor ETR1 via P-type ATPase RAN1.

Cu(I) is only sparingly soluble, engages in the deadly Fenton reaction producing hydroxyl radicals, and is at the top of the Irving-Williams series so is prone to mismetalate binding sites of other proteins. Hence, it is postulated that there will need to be molecules within the cell to mediate the transfer of Cu(I) from the plasma membrane importer, across the cytoplasm, to the ER Cu(I) importer RAN1, and secondly within the ER to supply target proteins, within the context of the intracellular buffer. For this project, we focus on the ER resident ethylene receptor ETR1 that contains an essential Cu(I) cofactor, delivered via a RAN1-dependent pathway in *Arabidopsis thaliana*.

A simplistic model would suggest that ETR1 is metalated from the luminal side of the ER membrane, post Cu(I) transport by RAN1. It is hypothesized that PLS acts to solubilise and stabilise the Cu(I) imported by RAN1 into the ER lumen thereby providing a source of available Cu(I) in the compartment for the metalation of cuproproteins such as ETR1.

During the course of this study, preliminary research arose that suggested PLS might be cytosolically localised, potentially in complex with RAN1 and/or ETR1. As the Cu(I) site in ETR1 is localised at the centre of the membrane, Cu(I) delivery could also be imagined from the cytosolic side of the ER membrane. We have therefore here explored the credibility of PLS acquiring Cu(I) in the cytosol.

These two alternative models can be visualised in Figure 1.10

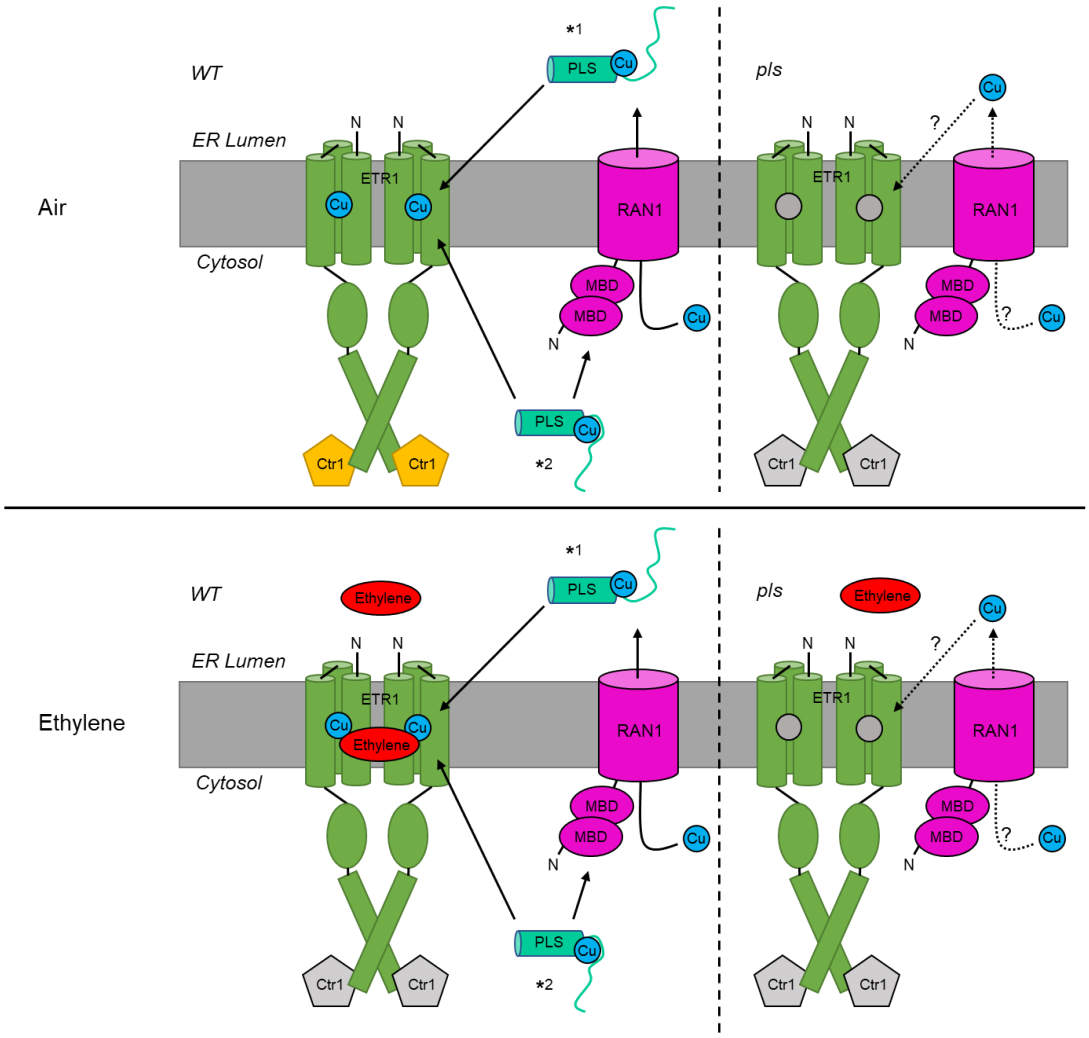

Figure 1.10, A hypothetical model for PLS in the *Arabdiopsis thaliana* ethylene response model. Models showing a hypothetical role for PLS in the ER lumen (*1) or the cytosol (*2) under air or ethylene conditions. *1, luminally, RAN1 imports Cu(I), PLS binds Cu(I), both solubilizing and stabilising the reduced form, where it is available for the correct metalation of ETR1. *2, cytosolically, PLS binds Cu(I) and facilitates correct metalation of ETR1, potentially in complex with RAN1 and/or ETR1. In the absence of functional PLS protein (*pls,* right), it is predicted that ETR1 is incorrectly metalated. ETR1 cannot activate CTR1 in the presence or absence of ethylene, and the downstream ethylene-associated transcriptional changes are derepressed, resulting in a constitutive response phenotype observed.

1.4.2 Aims

This project aims to explore the mechanism by which copper is made available to the components of the ethylene signalling pathway within plant cells.

By characterising the metalation of the two *Arabidopsis thaliana* proteins Atx1 and PLS, *in-vitro*, the predicted metalation of PLS in the plant cell might be modelled. Using the metalation of Atx1, proposed to act as a post-translational Cu(I)-dependent efflux regulator, as a read-out for the Cu(I) availability in the cytosol, it becomes possible to explore the feasibility of PLS metalation *in-vivo*.

Chapter 2. Materials and methods

2.1 Bacterial Strains

2.1.1 Growth conditions

All *E. coli* cultures in this work were cultured in lysogeny broth (LB) medium (Sambrook & Russel, 2001). Unless stated otherwise, all *E. coli* liquid cultures were grown at 37^{o}C in an orbital shaker set to 180rpm. Plated cultures, unless stated otherwise, were incubated inverted at 37 ^{o}C overnight (>16 h). All media was autoclaved prior to use and work carried out under aseptic conditions around a propane Bunsen burner. Kanamycin (50 mg ml^{-1}), carbenicillin (100 mg ml^{-1}) and chloramphenicol (34 mg ml^{-1}) stocks were prepared to 1000x working concentrations. Antibiotic stocks were made up by weight in nanopure water (kanamycin and carbenicillin) or ethanol (chloramphenicol), sterilised by filtration through 0.2 µm nylon filter (Sartorius) and stored at -20 ^{o}C.

2.1.2 Strains

All gene-cloning work for this project was carried out using the *E. coli* DH5α cloning strain. Overexpression of recombinant proteins was carried out using *E. coli* strains BL21(DE3), NEB(Express), BL21(DE3) pLysS, BL21(DE3)RIL (Table 2.1).

Table 2.1, Bacterial strain genotypes used during this work.

Strain	Genotype
DH5α	F^- φ80lacZΔM15 Δ(lacZYA-argF)U169 recA1 endA1 hsdR17 (r_K^-, m_K^+) phoA supE44 λ^-thi-1 gyrA96 relA1
BL21(DE3)	F^-ompT $hsdS_B$ (r_B^-, m_B^-) gal dcm (DE3)
NEB(express)	fhuA2 [lon] ompT gal sulA11 R(mcr-73::miniTn10--Tet^S)2 [dcm] R(zgb-210::Tn10--Tet^S) endA1 Δ(mcrC-mrr)114::IS10
BL21(DE3)pLysS	F^-ompT $hsdS_B$ (r_B^-, m_B^-) gal dcm (DE3) pLysS(Cam^R)
BL21(DE3)RIL	F^-ompT hsdS(r_B^-, m_B^-) dcm^+ Tet^r gal λ(DE3) endA Hte [argU ileY leuW Cam^r]
XL1-Blue (Agilent)	recA1 endA1 gyrA96 thi-1 hsdR17 supE44 relA1 lac [F´ proAB $lacI^q$ ZΔM15 Tn10 (Tet^r)]

2.1.4 Preparation of competent cells

Competent cells were prepared using a modified $CaCl_2$/$MgCl_2$ method (Sambrook & Russel, 2001). All solutions were sterilised in advance using an autoclave and kept on ice during the procedure

50 µL aliquots of competent cells were grown in 0.5 mL LB, 37 ^oC, 180rpm for 1 hour. Cells were streaked on petri dishes containing 20 mL sterile LB/agar and incubated overnight 37 ^oC (~16h). A single colony was picked, introduced to 10 mL LB and incubated overnight at 37 ^oC 180 rpm (16h). 100 mL LB was then inoculated with 2 mL of overnight culture and incubated with shaking to an optical density (OD_{600}) = ~0.5. Cells are pelleted in a Beckman Coulter Allegra X22R 2500rpm, 10 min, 4 ^oC and supernatant discarded. Pellet was resuspended in 25 mL of ice cold 100 mM $MgCl_2$ and incubated on ice for 5 min. Cells were pelleted again (2500 rpm, 10 min, 4 ^oC), supernatant discarded and resuspended in 5 mL ice cold $CaCl_2$ followed by a further 45mL ice cold $CaCl_2$. Cells were incubated for 1 h on ice, then pelleted (2500 rpm, 10 min, 4 ^oC), supernatant discarded and pellet resuspended in 2mL ice cold 85 mM $CaCl_2$ in 15% (vol/vol) glycerol. Cell aliquots of 50 µL were prepared into pre-sterilised 1.5 mL tubes (on ice), flash frozen in liquid nitrogen and stored at -80 ^oC.

2.1.5 Preparation of glycerol stocks

Following transformation of the correct cell type and plasmid, a single colony was used to innoculate 20 mL sterile LB and cultured overnight. Culture was gently mixed in a 1:1 ratio with sterile 50 % (vol/vol) glycerol by gentle inversion in a

rubber-gasketed 2 mL screw top tube. Stocks were flash frozen by immersion in liquid nitrogen and stored at -80 ^{o}C.

Subsequent freeze/thaw cycle are avoided by use of a heatblock pre-cooled to -80 ^{o}C. To recover bacteria – using a flame-sterilised nichrome wire loop, Bacteria are scraped from the surface of the glycerol stock and streaked onto LB agar plates with the appropriate antibiotic then grown overnight at 37 ^{o}C.

2.1.6 Transformation of competent cells

50 µL aliquots of competent cells were thawed on ice, 1 µL DNA added and mixed then left on ice for 30 minutes. Cells were placed in a 42 ^{o}C heatblock for 1 minute followed by 2 minutes on ice. 500 µL LB was added to the cells and incubated at 37 ^{o}C, 180 rpm, for 1 hour. The culture was pelleted by centrifugation for 5 minutes 35 000 rpm (PrismR Labnet), 400 µL supernatant discarded and pellet resuspended in remaining supernatant. 50 µL of resuspended material was plated out on petri dishes containing LB/agar with appropriate antibiotic for selection.

2.2 DNA manipulation

2.2.1 DNA isolation

Miniprep DNA isolation: *E. coli* cell cultures containing the relevant plasmid were grown overnight in LB. 1 mL of overnight culture was required for high copy number cloning plasmids such as pEX-A128 and 5 mL for lower copy number plasmids such as pET29a. The resulting “minipreps” contain 50 µL DNA at a concentration greater than 30 ng μL^{-1} which is typically sufficient for transformation

of competent cells. Plasmid DNA was isolated by alkaline-SDS lysis using a GenElute Plasmid Miniprep Kit (Sigma-Aldrich) according to the manufacturer instructions. Analysis of DNA purity and yield was carried out using a NanoDrop 1000 spectrophotometer (Thermo Scientific) and by agarose gel electrophoresis when required. DNA Sanger sequencing was carried out routinely (Applied Biosystems 3730 - University of Durham Biosciences department facility).

2.2.2 Agarose gel electrophoresis

Agarose gel electrophoresis was used to analyse and separate vector and insert mixtures following PCR or restriction digests. An agarose concentration was selected based on the size of DNA fragment to be analysed and was dissolved, and run, in a Tris/Borate/EDTA (TBE) buffer system (Sambrook & Russel, 2001). Agarose gels were poured and run in accordance with manufacturer guidelines (Bio-Rad), typically 100 V, visualised by the addition of 0.5 µg ml^{-1} of ethidium bromide solution to the gel prior to polymerisation.

Gels were imaged using a GelDoc gel imaging system (Bio-Rad) and, if required, bands were excised atop a UV-transilluminator using a sterile scalpel. Gel excisions were purified using a GenElute gel extraction kit (Sigma-Aldrich) according to the manufacturer instructions.

2.2.3 Restriction digest

Restriction digests were designed using two enzymes that left incompatible “sticky ends” so as to remove risk of re-circularisation during ligation. Preferentially,

enzymes were selected with compatible buffer systems to be used in a double digest. Double digests were treated with calf intestinal alkaline phosphatase simultaneously, to reduce risk of recircularization of any singly digested plasmid during ligation. Enzymes (New England Biolabs) were used in a “timesaver protocol” in “Cutsmart buffer”, which allowed total digestion of 1 µg plasmid DNA in 15 minutes at 37 ^{o}C. Reactions were stopped by heat inactivation of restriction enzymes by incubation at 65 ^{o}C for 20 minutes or by agarose gel electrophoresis.

Restriction products were analysed by agarose gel electrophoresis (see section 2.2.2), to confirm full digestion before ligation, to separate the enzymes from the DNA and to separate insert from cut vector before purification.

Inserts were either designed and manufactured synthetically (Sigma-Aldrich) as two complementary strands and annealed before insertion, or restricted from a plasmid using matching restriction enzymes to the vector. Inserts were treated with T4 polynucleotide kinase (New England Biolabs) to provide a 5’- phosphate for ligation.

In cases where sequential single digests were required, as opposed to double digests, the single cut plasmids were purified by a silica membrane based QIAquick PCR Purification Kit (Qiagen).

2.2.4 Annealing oligonucleotides

In order to anneal two complementary oligonucleotide sequences to form an insert, the matching oligonucleotides were mixed in a 50 µL reaction volume at a final concentration of 10 µM each. Reaction buffer used was 10 mM HEPES pH

7.0, 150 mM NaCl (Chelex treated). Samples were transferred to 500 µL thin-walled microfuge tubes and into a thermal cycler (TECHNE Prime) for annealing. Annealing cycle quickly ramped to 95 ^{o}C, cooled over three hours and repeated a further 2 cycles. Reaction mixture was analysed by agarose gel electrophoresis to confirm the formation of a single product, distinct from the two oligonucleotides.

2.2.5 Vector/insert ligation

Purified phosphorylated insert and dephosphorylated, double-cut, vector were incubated in the ligation reaction at a range of insert:vector ratios. 50 ng vector was used in all reactions and the concentration of insert varied to create three different ratios (2:1, 1:1 and 1:3). One reaction was included with no insert to control for recircularised single- or no-cut vector. On ice, reactions were made up to 20 µL with 1x reaction buffer before 1 µL T4 DNA ligase (New England Biolabs) was added. Reactions were mixed gently and incubated at 16 ^{o}C overnight. Reactions were heat inactivated at 65 ^{o}C for 20 minutes before chilling on ice. 5 µL of each reaction was used to transform a separate 50 µL aliquot of competent DH5α cells.

2.2.6 Colony PCR

To check for correct insertion into the vector, colony PCR was carried out. Polymerase chain reactions (PCR) were prepared, on ice, to a final volume of 50 µL containing dNTPs (dATP, dTTP, dGTP and dCTP each to a final concentration

of 400 µM), forward and reverse PCR primers each to a final concentration of 0.4 µM, 2.5 mM $MgCl_2$, GoTaq (Promega) PCR buffer (diluted from a 10x stock).

Individually picked sample colonies are touched to 15 µL nanopure water, boiled at 95 ^{o}C for 5 minutes and pelleted by centrifugation 10 min, 13,500 rpm (PrismR Labnet). 2 µL supernatant was added to each PCR reaction tube before addition of 0.5 µL GoTaq G2 Flexi DNA Polymerase (2.5 units) (Promega).

PCR reactions were performed using appropriate combination of melting, annealing and extension temperatures, using a PCR thermocycler (TECHNE Prime)

Forward and reverse primers were designed to span the insert: positive selection can be achieved based on an increase in PCR product size corresponding to the length of insert.

Correct insertion was also assayed by purification of positive transformant plasmid (via miniprep) followed by DNA Sanger sequencing (Applied Biosystems 3730 - University of Durham Biosciences department facility).

2.2.7 MBP-PLS fusion protein pMal-c5X

To produce a plasmid to encode a fusion protein of Maltose Binding Protein (MBP) to the *A. thaliana* protein, Polaris (PLS), two complementary oligonucleotide primers encoding PLS were designed to be annealed (see section 2.2.4) and inserted into the pMal-c5X plasmid (New England Biolabs). The primers were designed with one blunt and one overhanging end to be compatible with a vector (pMal) double-cut by XmnI and SalI respectively. Both primers' sequence were

optimised for heterologous expression in *E. coli* to alleviate usage of rare codons in *E. coli* (Figure 2.1).

Forward primer:

5’ATGAAACCACGCTTGTGCTTTAACTTTCGTCGTCGCTCCATTAGTCCGTGTTACATCTC
GATTAGCTATCTGTTAGTGGCGAAACTGTTCAAACTGTTCAAGATCCATTAAG 3’

Reverse primer:

5’TCGACTTAATGGATCTTGAACAGTTTGAACAGTTTCGCCACTAACAGATAGCTAATCGA
GATGTAACACGGACTAATGGAGCGACGACGAAAGTTAAAGCACAAGCGTGGTTTCAT 3’

Figure 2.1, Optimised PLS nucleic acid sequence nucleic acids making up the “sticky end” text in red.

The pMal-c5X plasmid encodes the MalE gene derived from the Hinf I fragment of the *E. coli* malB region which differs from the wild-type MBP by the addition of a methionine at the amino terminus, mutations to increase the affinity of MBP to amylose, deletion of the last 4 residues and addition of residues encoded by a spacer and protease site upstream of PLS (Figure 2.2).

After treating the annealed insert with T4 polynucleotide Kinase (PNK) (New England Biolabs) to phosphorylate 5'- ends, the insert was ligated into double-cut pMal-c5X plasmid. Positive transformants were identified by miniprep followed by Sanger sequencing (Applied Biosystems 3730 - University of Durham Biosciences department facility) using two primers designed to be complementary to ~100 DNA base pairs upstream and downstream of insertion site (Figure 2.3) (see Supplementary Figure 8.3 for sequencing alignments).

MKIEEGKLVIWINGDKGYNGLAEVGKKFEKDTGIKVTVEHPDKLEEKFPQVAATGDGPDII
FWAHDRFGGYAQSGLLAEITPDKAFQDKLYPFTWDAVRYNGKLIAYPIAVEALSLIYNKDL
LPNPPKTWEEIPALDKELKAKGKSALMFNLQEPYFTWPLIAADGGYAFKYENGKYDIKDVG
VDNAGAKAGLTFLVDLIKNKHMNADTDYSIAEAAFNKGETAMTINGPWAWSNIDTSKVNYG
VTVLPTFKGQPSKPFVGVLSAGINAASPNKELAKEFLENYLLTDEGLEAVNKDKPLGAVAL
KSYEEELVKDPRIAATMENAQKGEIMPNIPQMSAFWYAVRTAVINAASGRQTVDEALKDAQ
TNSSSNNNNNNNNNNLGIEGRMKPRLCFNFRRRSISPCYISISYLLVAKLFKLFKIH

Figure 2.2, Final expression product from engineered pMal plasmid. Amino acid coding sequence for MBP-PLS fusion protein. MBP sequence shown in black, spacer, including Factor Xa protease cleavage site (underlined), in red and PLS wildtype sequence shown in green.

Forward primer: 5′AGATGTCCGCTTTCTGGTATGCC 3′ (23bp)

132bp Upstream of insert. T_m 69.1 °C

Reverse primer: 5′TTGCTTCGCAACGTTCAAATCCG 3′ (23bp)

158bp Downstream of insert. T_m 73.4 °C

Figure 2.3, Primer design for confirmatory sequencing of the pMal-PLS insertion. Including location (relative to insert) and melting temperature (T_m).

2.2.8 Site-directed mutagenesis of MBP-PLS

In-vitro site-directed mutagenesis was used to produce three Cys/Ser MBP-PLS mutants (C6S, C17S and C6S/C17S). Reagents used were purchased in a kit produced by Agilent (QuikChange II Site-Directed Mutagenesis Kit). Two pairs of mutagenic oligonucleotide primers were designed to introduce the two Cys/Ser mutations sequentially. Primers were designed to be between 25 and 45 bases in length with a melting temperature >78 ^{o}C, mutation central to the primer and a minimum CG content of 40% (Figure 2.4).

PCR reactions were prepared, on ice, to a final volume of 50 µL containing dNTPs (1 µL proprietary mix(Agilent)) 125 ng each of forward and reverse PCR primers, 5 µL 10x reaction buffer (Agilent) and 5, 25 and 50 ng pMal-c5X(PLS) dsDNA template (from miniprepped DNA). 1 µL PfuUltra HF DNA polymerase (2.5 U μL^{-1}) was added and samples cycled in a thermocycler as per parameters in manufacturer's manual (Agilent) dependant on length of plasmid and type of mutation. A control reaction was included with supplied pWhitescript 4.5-kb control plasmid which contains a stop codon (TAA) at amino acid 9 of a *E. coli LacZ*. The control reaction incuded control primers that restore function to the β-galactosidase gene by reverting the T residue of an artificial stop codon to a C residue to produce a glutamine codon (CAA) found in the wildtype. The control reaction was transformed into XL1-Blue competent cells and grown on LB-ampicillin agar plates containing IPTG and X-gal, where positive transformants and mutants can be selected for the β-galactosidase (β-gal^{+}) phenotype of blue colour colonies. Following temperature cycling, reactions are placed on ice, treated with 1 µL *DpnI* at 30 ^{o}C for 1 h to digest parental methylated DNA. 1uL of

each DpnI reaction was used to transform 50 µL aliquots of competent cells which were plated out on LB/Agar plates with appropriate antibiotic. Positive transformant mutants were selected by either colony PCR (Supplementary Figure 8.1) or miniprep followed by Sanger sequencing.

Cys6 → Ser (TGC→TCC):

Forward primer: GG**ATG**AAA**CCA**CGC**TTG**TCC**TTT**AAC**TTT**CGT**CGT**CG

Length: 37, CG : 49%, mismatch : 2.7 % T_m = 80.5 ºC

Reverse primer: CG**ACG**ACG**AAA**GTT**AAA**GGA**CAA**GCG**TGG**TTT**CAT**CC
Length 37, CG : 49%, mismatch : 2.7 % T_m = 80.5 ºC

Cys17 → Ser (TGT→TCT):

Forward primer: **CGT**CGC**TCC**ATT**AGT**CCG**TCT**TAC**ATC**TCG**ATT**AGC

Length: 36, CG : 49 %, mismatch : 2.7 % T_m = 80.0 ºC

Reverse primer: **GCT**AAT**CGA**GAT**GTA**AGA**CGG**ACT**AAT**GGA**GCG**ACG

Length: 36, CG : 49 %, mismatch : 2.7 % T_m = 80.0 ºC

Figure 2.4, mutagenic primer design. Forward and reverse mutagenic primers designed to introduce C6 and C17 Cysteine-Serine mutations. Highlighted regions represent the mutated codon, red highlighted base is the altered base.

2.3 Protein manipulation

2.3.1 Expression and purification of MBP-PLS and mutants

The pMAL(MBP-PLS) expression plasmid was transformed into NEB express competent cells, a single colony picked and used to create 10 mL overnight cultures (section 2.1.6). Six 2.5 L conical flasks with 1 L LB culture each (pre-heated, 50 µg/mL Carbenicillin, 2 g/L Glucose) were inoculated with 10 mL overnight culture, incubated 37^{o}C, 180 rpm until OD_{600} ~0.4 was reached (mid-log phase). Cultures were induced with 200 µM IPTG for 2h, harvested by centrifugation in a Beckman Coulter Avanti J-20 centrifuge 4000 rpm, 20 min, 10^{o}C. Pellets were then resuspended in 20 mL 20 mM Tris-HCl pH 7.4, 200 mM NaCl, 1 mM EDTA (amylose column buffer) and frozen at -20 ^{o}C. Pellets were thawed in cold H_2O, 25 µL 1 M DTT (final concentration 1 mM) and 250 µL Halt protease inhibitor cocktail (ThermoFisher Scientific) were added. Cells were sonicated (Bandelin sonoplus) on ice, using a large probe, ~50% power, 30 s on, 30 s off repeated 8x, and returned to ice. MBP-PLS was further purified by ammonium sulfate precipitation. Cell debris was removed by centrifugation from sonicated material at 18 000 rpm, 4^{o}C, 30 min in a Beckman Coulter Avanti J-20 centrifuge (JLA 25.5 rotor) and supernatant retained. 2.85 g solid $(NH_4)_2SO_4$ was added to supernatant (20% saturation), and incubated for 1 h with gentle stirring. Any precipitated protein was then removed by repeated centrifugation and supernatant retained. A further 6.90 g solid $(NH_4)_2SO_4$ was added to the supernatant, incubated for 1h with gentle stirring (60% saturation). Insoluble protein at this stage was separated by repeated centrifugation and pellet retained.

Pellet was then resolubilised in 25 mL buffer without $(NH_4)_2SO_4$, (20 mM Tris-HCl pH 7.4, 200 mM NaCl, 1 mM EDTA, 1 mM TCEP).

Soluble protein was then loaded in a pre-equilibrated 5 mL MBP-Trap (GE Healthcare), prepared according to the manufacturers instruction, and washed w/ 25 mL CHELEX-treated 20 mM TRIS-HCl pH 7.4, 200 mM NaCl, 250 µM TCEP. Protein is eluted with the same buffer with an additional 10 mM maltose. Pure eluted fractions were analysed by SDS-PAGE and pooled together then concentrated on a centricon column (Corning, Spin-X UF), with a 30 kDa molecular weight nylon filter, from ~3 mL to 1 mL. Concentrated protein is then buffer exchanged into 20 mM HEPES pH 7.0, 50 mM NaCl, CHELEX-treated degassed buffer via a PD-10 into an anaerobic environment as described in section 2.4.2.

2.3.2 Expression and purification of Atx1

The wildtype *atx1* gene from *Arabidopsis thaliana* was initially optimised for expression in an *E. coli* host system using the online tool codon-optimiser (novoprolabs) (Supplementary Figure 8.2), In addition to the Atx1 coding sequence, the T7 promoter/terminator and lac operator were added (flanking the gene) to allow expression directly from the cloning vector the gene was to be supplied in. Additionally, restrictions sites NdeI and EcoRI were included to allow sub-cloning into the pET29aif expression was not optimal as added redundancy (this was indeed the case).

Atx1 was double digested from pEX182 (supplied by Eurofins) using the two enzymes NdeI and HindIII-HF (New England Biolabs) in a double digest as

described in section 2.2.3, ligated into pET29a, transformed into DH5α cells, purified by miniprep and sequenced by Sanger sequencing (Applied Biosystems 3730 - University of Durham Biosciences department facility) to confirm correct insertion (Supplementary Figure 8.11)

This plasmid was transformed into BL21(DE3) cells and selected for on LB/agar plates containing 50 µg/mL kanamycin. A single colony was then used to inoculate a 15 mL overnight starter culture. 2 mL of the starter culture was used to inoculate 1 L LB culture in a 2 L conical flask (non-baffled) containing 50 µg/mL kanamycin, cultured at 37 ^{o}C, shaking at 180 rpm, until an OD_{600} ~0.4 was reached. Then cultures were induced with 1 mM final concentration of IPTG and grown for a further 4 h period before harvesting using JLA 8.1000 rotor in a Beckman Coulter Avanti J-20 centrifuge (4500 rpm, 25 min, 10 ^{o}C). Supernatant was decanted, and pellets scooped using a spatula into round bottomed 50 mL falcon tubes before being frozen at -20 ^{o}C.

Pellets were defrosted at room temperature for 10 minutes, resuspended in 4 mL 20 mM HEPES (pH 7.0), 10 mM EDTA, 100 mM NaCl and 10 mM DTT (added fresh). Resuspended material (~ 5 mL) was then split into 800 µL aliquots in 1.5 mL microfuge tubes and sonicated (Bandelin sonoplus) using a small probe, 45-50% power, 30 s, and returned to ice. Cell debris was separated by centrifugation at 13 500 rpm, 25 minutes (Labnet, PrismR) and supernatant collected and pooled. Supernatant was syringe filtered using a 0.2 µm nylon filter and separated by size exclusion chromatography (GE healthcare, HiLoad 26.600 Superdex 75 pg) using the same buffer without EDTA and treated with CHELEX. Fractions were incubated overnight as a 10 mM DTT incubation step to ensure both full reduction of the protein thiols and metal-free pure protein.

Fractions where Atx1 was predicted to elute (~200-225 mL) were analysed by SDS-PAGE for Atx1 purity and purest fractions were pooled.

Atx1 at this stage purified with a peak in the UV spectrum at 260 nm, consistent with possible co-purification of nucleotide contaminants. Pooled fractions were run through 1 mL DEAE column (GE Healthcare) equilibrated in size exclusion running buffer and run as per manufacturers instruction. The flow-through from the column was retained and confirmed the 260 nm peak had been removed. 260 nm material can then be eluted from the column by elution in buffer also containing 1 M NaCl.

Nucleotide-free Atx1 was then concentrated from ~30 mL to 0.5 mL using a centricon (Corning, Spin-X UF) with a 5 kDa molecular weight cut-off nylon membrane, pre equilibrated in the same buffer. Pure concentrated Atx1 was buffer exchanged into the anaerobic chamber using a PD-10 desalting column.

2.3.3 Quantification of proteins (bradford/A_{280})

Protein concentrations were estimated by various independent approaches: solution absorbance at 280 nm using theoretical extinction coefficients, Thiol content analysed by Ellman's reagent and Bradford assay. In the case of pure, reduced, apo-protein, Ellman's assay was used. Concentration estimates by A_{280} solution absorbance varied, especially in the case of Atx1 which has a low predicted extinction coefficient. This has been observed previously (Xiao et al., 2011) where it was predicted to be the result of the contribution of other minor adventitious components. For this reason, quantification using Ellman's or Bradford assay were employed routinely.

Theoretical extinction coefficient for MBP-PLS and Atx1, generated using the ProtParam tool on ExPASy website (http://web.expacy.org/protparam), of 69 330 M^{-1} cm^{-1} and 5500 M^{-1} cm^{-1} respectively (Supplementary Figures 8.4 and 8.5 respectively)

Mutants lacking any thiol groups and metalated protein, were quantified using a proprietary “Coomassie Plus Assay Kit” (Thermo scientific). Bradford assays were calibrated using Bovine Serum Albumin as a standard, purchased as standard stock quantification ampules. Corrections were made to account for the relative difference in ratio of basic residues to total residues in the protein under quantification relative to the BSA standard as in supplementary Figures (Foster, Patterson, Pernil, Hess, & Robinson, 2012)

Atx1 is predicted to be 0.91 times as reactive as BSA per unit mass. MBP-PLS is predicted to be 0.78 times as reactive as BSA per unit mass.

2.3.4 SDS-PAGE analysis

Cell protein content and protein purity was routinely analysed by SDS-PAGE (Sambrook & Russel, 2001). For analysis of PLS and Atx1, pre-poured 4-20% mini-PROTEAN TGX gels were purchased (BioRad) in order to achieve higher resolution at the lower molecular weights. Ladder used was either “Precision plus protein dual standards” (BioRad), for looking at high molecular weight proteins or “Precision plus protein dual xtra standards” (BioRad), when analysing PLS or Atx1.

Gels were typically run at 100-140V until the dye front reached 3/4 of total length of the gel.

All gels were stained overnight in Instant Blue Coomassie stain (Expedeon) then rinsed the following day in water, followed by imaging using a GelDoc imaging system on a white background.

2.4 Working under anaerobic conditions

2.4.1 Production of anaerobic buffers

To remove dissolved O_2 from buffers and nanopure H_2O, to be used under anaerobic conditions, N_2 was bubbled vigorously through the buffer for a minimum for 2 h in 50 mL Falcon tubes whilst under an N_2 environment. Buffers are then passed through into the anaerobic chamber (Belle Technology) and stored for later use.

2.4.2 Transfer of Proteins into anaerobic environment

Protein stocks are transferred into an anaerobic environment via 8.3 mL disposable PD-10 desalting columns (Cytiva). 500 µL pure protein sample is passed into the anaerobic chamber via a purging port in 1.5 mL microfuge tube. Prior to protein loading, the PD-10 column is washed with 2 column volumes (CV) nanopure H_2O, 500 µL 1 mM EDTA, 2CV Nanopure H_2O and equilibrated in 2 CV anaerobic, chelex-treated buffer. Protein samples are loaded and 1 mL fractions eluted with the same buffer (under gravity), pure protein typically elutes in the 4^{th} mL.

This method allows buffer exchange and removal of reductant used during purification (DTT or TCEP) into an anaerobic environment where the protein can be quantified as apo- and fully reduced.

2.4.3 UV-visible spectroscopy (Lambda 35) air-tight cuvettes

Spectra were recorded under anaerobic conditions via air-tight, spectrosil far UV quartz cuvettes (Hellma and Starna). All data unless specified otherwise were recorded using a λ35 UV-visible (Perkin Elmer) spectrophotometer. Proteins were diluted in buffer stated in the text, any metal additions made, mixed by aspiration, and tightly lidded before being removed from the anaerobic chamber and analysed.

Whenever single readings were taken, timedrive data was also run until no further change in absorbance was observed, to ensure any reaction in the cuvette has reached equilibrium.

2.4.4 Analysis of total reduced thiol content

Anaerobically purified proteins were analysed for total reduced thiol content by Ellman's assay using 5,5'-dithio-*bis*-(2-nitrobenzoic acid) (DTNB) which reacts with thiols in a 1:1 ratio to form dianion 2-nitro-5-thiobenzoate (TNB). TNB has intense absorption at 412 nm (TNB ε_{412} = 14 150 M^{-1} cm^{-1})(Eyer et al., 2003) which can be quantified . DTNB was dissolved in 100 mM sodium phosphate, pH 8.0, 1 mM EDTA to a concentration of 4 mg mL^{-1}. GSH stock was prepared anaerobically in nanopure water to a final concentration of approximately 100 mM. GSH stock was serially diluted to 1 mM in nanopure water and quantified by the addition of DTNB stock to a final concentration of 2 mg mL^{-1} – GSH concentration was calculated

using the Beer-Lambert law using the reported extinction coefficient of TNB ε_{412} = 14 150 M^{-1} cm^{-1} (Eyer et al., 2003).

Assays were performed in a 96-well plate (Thermo) using reduced glutathione (GSH) to produce a standard curve of known reduced thiol concentration. GSH stock was serially diluted, producing a range of concentrations typically from 2.5 – 500 µM. Protein samples were prepared by 4-fold dilution to a final volume of 200 µL and 20 µL DTNB stock added to each sample or GSH standard. On addition of DTNB, reactions were left for 10 minutes to develop before absorbance measured at 412 nm.

2.5 Metal analysis

2.5.1 Preparation of metal standards

Standard metal solutions were used as standards for ICP-MS were purchased (Thermofischer scientific). Solutions came at standard concentrations, generally 1000 or 10 000 ppm. Stocks of each metal were diluted in repeated 10x dilution series in 2.5% HNO_3 (suprapure) and combined to make a final set of stocks from 100 ppm to 10 ppb for the metals Cu, Zn, Ni, Co, Fe, Mn, and Mg.

2.5.2 ICP-MS analysis

Purified protein was routinely analysed for metal content by ICP-MS. Typically, protein was diluted to a final concentration of 2 μM in 2.5% HNO_4 and analysed against a set of standards from 0-500 ppb mixed metal stocks. Protein was ensured >90% metal-free before experimentation, however typically, protein was >95% metal-free.

2.5.3 Working Metal-free

To remove contaminating metals from glassware, all glassware to be used in metal-sensitive experiments was washed by overnight immersion in 4% HNO_4.

All buffers to be used during the purification of Apo-protein or in metal-titration studies, were prepared as usual, then treated with CHELEX 100 chelating ion exchange resin (Sigma Aldrich) through a gravity-fed column. Chelex-treatment

was carried out as per the manufacturer's instructions and buffers which were pH corrected before treatment and double-checked post-treatment to ensure correct pH.

During any in-vitro experiments involving metals, it was ensured that only non-autoclaved pipette tips were used, previously, metal contamination has been observed as a result of the autoclaving procedure (unpublished observations from Prof. Robinson's Laboratory).

2.5.4 Preparation and quantification of metal-probe stocks

Metal-binding spectroscopically-active probes used during this study were routinely weighed out, transferred to anaerobic chamber and dissolved in degassed Nanopure water to a stock concentration. Probes were quantified by serial dilution in nanopure water followed by metal titration to saturation with cognate metal (quantified by ICP-MS) in 1 mL quartz cuvettes (Hellma). UV-visible spectroscopy was used to determine maximum absorbance at wavelengths corresponding to the metal:probe complexes formed with extinction coefficients reported in literature.

2.6 Experimental procedures

2.6.1 Anaerobic metal-competition titrations for MBP-PLS

All MBP-PLS titrations (including mutant titrations) were carried out under the same anaerobic conditions described above. Pure protein was exchanged into metal-free, degassed buffer (20 mM HEPES pH 7.0, 50 mM NaCl) via a PD-10 desalting column as described above. Titrations were carried out by sequential

addition of concentrated quantified metal stock – concentration of the stock was adjusted so that the total expected volume of additions during a titration would not dramatically affect the concentration (typically <5 % of total volume). Additions were made within the anaerobic chamber, aspirated to mix, and incubated until equilibrium was reached. Full wavelength scans from 200 – 800 nm were recorded after each addition.

2.6.2 Anaerobic metal-competition titrations for Atx1

All Atx1 titrations were carried out under the same anaerobic conditions described above however protein was exchanged into metal-free, degassed buffer (20 mM HEPES pH7.0, 100 mM NaCl) via a PD-10 desalting column as described above.

2.6.3 RT qPCR

2.6.3.i Primer design:

Primers were designed to amplify the metal responsive transcripts for *cueR* and *zntR* (CopA and ZntA respectively) and RpoD (Table 2.2). Primers were designed using 'Primer3Plus' (Bioinformativs.nl) online software, to produce amplicons of length 100-120 bp, CG content 20-80%, amplicon melting temperature (T_m) 70-95 ^oC, primer T_m ~60 ^oC, maximum T_M difference of 3 ^oC, primer CG content 40-60%, primer size 15-25 bp with a CG 3' clamp. Maximum self- and pair-complementarity was set to "4".

Table 2.2, qPCR primers. Forward and reverse primers (FP and RP respectively) used in the amplification of *copA*, *rpoD* and *zntA*.

Gene primer	Primer sequence
copA FP	GTCACAAACTATCGACCTGACCC
copA RP	GGATGTTGAGCAGGCGGATG
rpoD FP	GTGGCTTGCAGTTCCTTGAC
rpoD RP	GTTCTCCACCTACGCAACCT
zntA FP	TCAAATCCGGCAGCTACTTC
zntA RP	TCAAAAACAGCAGCAACACC

2.6.3.ii Cell growth conditions:

E. coli BL21(DE3) cells were cultured as in section 2.2.1 after being transformed with either pET29a(Atx1) or the same plasmid lacking the Atx1 gene (pET29a(Empty)). Cells were grown aerobically in a single conical flask from a 1:100 dilution of overnight culture until an OD_{600} of ~0.2 was reached. Cells were then split into 5 mL aliquots in 14 mL round-bottomed cell culture tubes (caps fitted loosely). The culture tubes also contained a fixed volume of concentrated IPTG and metal stock (50 µL) to result in a final concentration of IPTG of 0.2 mM IPTG and varied metal concentrations ($CuSO_4$/$ZnSO_4$). Incubation was continued for a further 2h when cell material was harvested.

2.6.3.iii RNA stabilisation:

An aliquot of 1 mL of each cell culture growth condition was immediately harvested and added to 2 mL RNA protect bacterial reagent (Qiagen) and mixed immediately by vortexing. Cell pellets at this stage were frozen at -80 ^oC prior to processing.

2.6.3.iv Cell lysis, RNA extraction and quantification:

Cell pellets were enzymatically lysed and digested using the RNA-Protect Bacterial RNA Extraction Mini Kit (Qiagen) as per manufacturers instructions. Resultant total cell RNA was then quantified using Nanodrop 1000 spectrophotometer at 260 nm and assessed for purity. A 260/280 nm ratio of >2 and 260/230 nm ratio of >2 were routinely examined to detect any protein or

organic compound (such as ethanol or guanidinium thiocyanate salts) carry-through from the purification protocol.

2.6.3.v DNAseI treatment:

RNA was treated with DNaseI (ThermoScientific) at 100 ng/µL. RNA, DNAseI and reaction buffer was mixed, centrifuged to collect, and incubated at 37 ^{o}C for 1 hr. DNaseI was then heat inactivated by incubation with 5 mM EDTA at 70 ^{o}C for 10 minutes.

2.6.3.vi Reverse transcription:

300 ng DNAseI-treated RNA was treated using the ImProm-II Reverse Transcriptase system (Promega) to produce cDNA for use in the qPCR reaction. Control reactions were also included in the absence of the reverse transcriptase (RT) enzyme to control for the presence of any contaminating DNA at this stage. All +RT and -RT samples were analysed by qPCR in parallel.

2.6.3.vii qPCR reaction:

Transcript abundance was then measured for the metal-responsive transcripts *copA* (regulated by *cueR*), *zntA* (regulated by *zntR*) and in the control gene *rpoD* in cells grown under different metal-supplemented conditions by qPCR. Reactions was carried out using 5 ng cDNA, 0.8 µM forward and reverse primers, and PowerUp SYBR Green Master Mix (ThermoFisher Scientific) in 20 µL reactions (in technical triplicate). Each condition was analysed by qPCR using a Rotor-Gene Q 2plex (Qiagen – Rotor-gene-Q Pure Detection software) in parallel to control

reactions without cDNA template (“water controls”) to control for amplification of each primer pair in the absence of template, and the samples where the reverse transcriptase was not added (“-RT controls”) to control for contaminating genomic DNA pre-reverse transcription.

2.6.3.viii Calculation of available intracellular metal concentration:

RT qPCR data was analysed using the $2^{-\Delta\Delta CT}$ method (Livak & Schmittgen, 2001) which analysed the relative changes in gene expression between treated and untreated samples, with *rpoD* as the reference gene. The *rpoD* gene encodes a sigma factor (also known as sigma 70) which is responsible for the transcription of many housekeeping genes in bacteria (Miura et al., 2015).

C_q values were calculated using the software package LinRegPCR (version 2021.2 December 2021) from the experimental amplification curves, after correcting for amplicon efficiency (Ramakers, Ruijter, Lekanne Deprez, & Moorman, 2003), where each primer pair and growth condition was treated labelled as an amplicon. Samples in which the ΔC_q value of the water-control or -RT-control (compared to the cDNA containing sample) were <10 (to the nearest integer) were rerun until controls met this requirement. A ΔC_q value difference of 10 represents 2^{10} fold difference in transcript abundance (1024x).

ΔC_q values were then calculated to give the expression of the gene of interest relative to the reference gene (*rpoD*) where:

$\Delta C_q = C_q$(gene of interest) – C_q(reference gene)

$\Delta\Delta C_q$ values were then calculated to give the expression relative to the lowest level of expression.

$\Delta\Delta C_q = \Delta C_q$(experimental condition) - ΔC_q(lowest expression condition)

The $\Delta\Delta C_q$ values are then converted into fold change (relative to the minimum expression) where:

Fold change = $2^{-\Delta\Delta Cq}$

To relate fold change in transcript abundance to the activation of the metal-responsive transcription activators, the fold change values were then converted to θ_{DM} values representing the occupancy of DNA with metalated protein:

$\theta_{DM} = 0.01 + 0.98 \times((\text{fold change}_{obs} - 1)/(\text{fold change}_{max} - 1))$

Where fold change_{obs} is the observed fold change in gene-of-interest expression under the condition being tested and fold change_{max} is the maximum fold change of gene-of-interest transcript abundance. In this case, the maximum and minimum fold change was taken from work in JM109 (DE3) (Foster et al., 2022). This equation defines the minimum and maximum responses for *cueR* and *zntR* as corresponding to a θ_{DM} of 0.01 and 0.99 (1% and 99%) respectively.

The intracellular available metal concentration was then calculated using Excel spreadsheet (supplementary dataset 1) and MATLAB code (supplementary note 3) from the work of Osman (Osman et al., 2019) using known metal affinity, DNA affinities and protein abundance calculated for the sensors in *Salmonella,* and number of DNA binding sites for *E. coli* sensors (experimentally derived) – 2 for CueR (*copA* and *cueO*) (F. W. Outten, Outten, Hale, & O'Halloran, 2000) and 1 for

ZntR (*zntA*) (Caryn E. Outten, Outten, & O'Halloran, 1999) (Supplementary Figures 8.6 and 8.7 respectively).

2.6.4 in-vivo Cu-exposure: tracking the metalation of Atx1

E. coli BL21(DE3) cells were transformed with either pET29a(Atx1) or (pET29a(Empty)) and selected for on Kanamycin LB/Agar plates (50 µg/mL). Single colonies were used to inoculate 10 mL overnight starter cultures. An aliquot of 2 mL of overnight starter material was used to inoculate 1 L LB, cultured to OD_{600} ~0.5, induced with 1 mM IPTG and 1 mM filter-sterilised $CuSO_4$ added. Cells were cultured for an additional 4h before harvesting using JLA 8.1000 rotor in a Beckman Coulter Avanti J-20 centrifuge (6000 g, 20 min, 4 ^oC).

Pellets were resuspended in 50 mL 20 mM HEPES pH 7.0, 150 mM NaCl, 10 mM EDTA. Pellets were then washed in buffer without EDTA present by successive centrifugation, decanting and resuspension repeated 3 times (Beckman Coulter Allegra X-22R centrifuge, 4000 rpm, 20 minutes, 10 ^oC). Pellets were frozen dry at -20 ^oC.

Pellets were thawed on ice, resuspended in 2 mL buffer (without EDTA), split into 1.5 mL microfuge tubes, sonicated, centrifuged at 13 500 rpm, 15 minutes (Labnet, PrismR) and supernatant kept.

Soluble lysate was then quantified for total protein by BSA-calibrated Bradford assay. 5 mg total protein was separated by size exclusion chromatography (GE

Healthcare, hi load 26/600 Superdex 75 pg) as per the manufacturer's guidelines. Fractions (5 mL) were analysed by ICP-MS for Cu and Zn, and by Bradford Assay.

Chapter 3. The metal-binding properties of the *Arabidopsis thaliana* protein POLARIS.

3.1 Purification of POLARIS

All unpublished data produced to-date used a purchased, synthetic POLARIS (PLS) peptide molecule. The PLS peptide was reported as relatively insoluble, and studies (including metal-binding affinity studies) to-date were carried out in the presence of dimethyl sulfoxide (DMSO) to sufficiently solubilise PLS (unpublished data, Prof. Keith Lindsey). As DMSO is an organosulfur solvent that dissolves both polar and non-polar compounds, it was useful for this reason. However, characterisation of the biochemical properties of PLS under these artificial conditions remains non-ideal, as the structure and function of the peptide could be altered. In addition to its solvent properties, DMSO also has the ability to act as a binding ligand to transition metals through either its sulphur or oxygen atoms (Diao, White, Guzei, & Stahl, 2012). For this reason, to obtain an accurate set of biochemical properties for PLS (especially during metal-affinity experiment), a purification scheme was established in the absence of DMSO. Here, the expression of PLS was pursued by codon-optimised heterologous expression in *E. coli*.

The initial purification of PLS provided sustained significant challenges. Initial attempts to express PLS were made by recombinant expression in the pET29a plasmid. Expression was initially tested using small-scale cultures grown at 37^{o}C, 180 rpm for 2h post IPTG induction. Recombinant expression was tested in three different expression strains: BL21 (DE3), BL21 PRil and BL21 PLysS. A range of IPTG induction concentrations from 0-1 mM were tested.

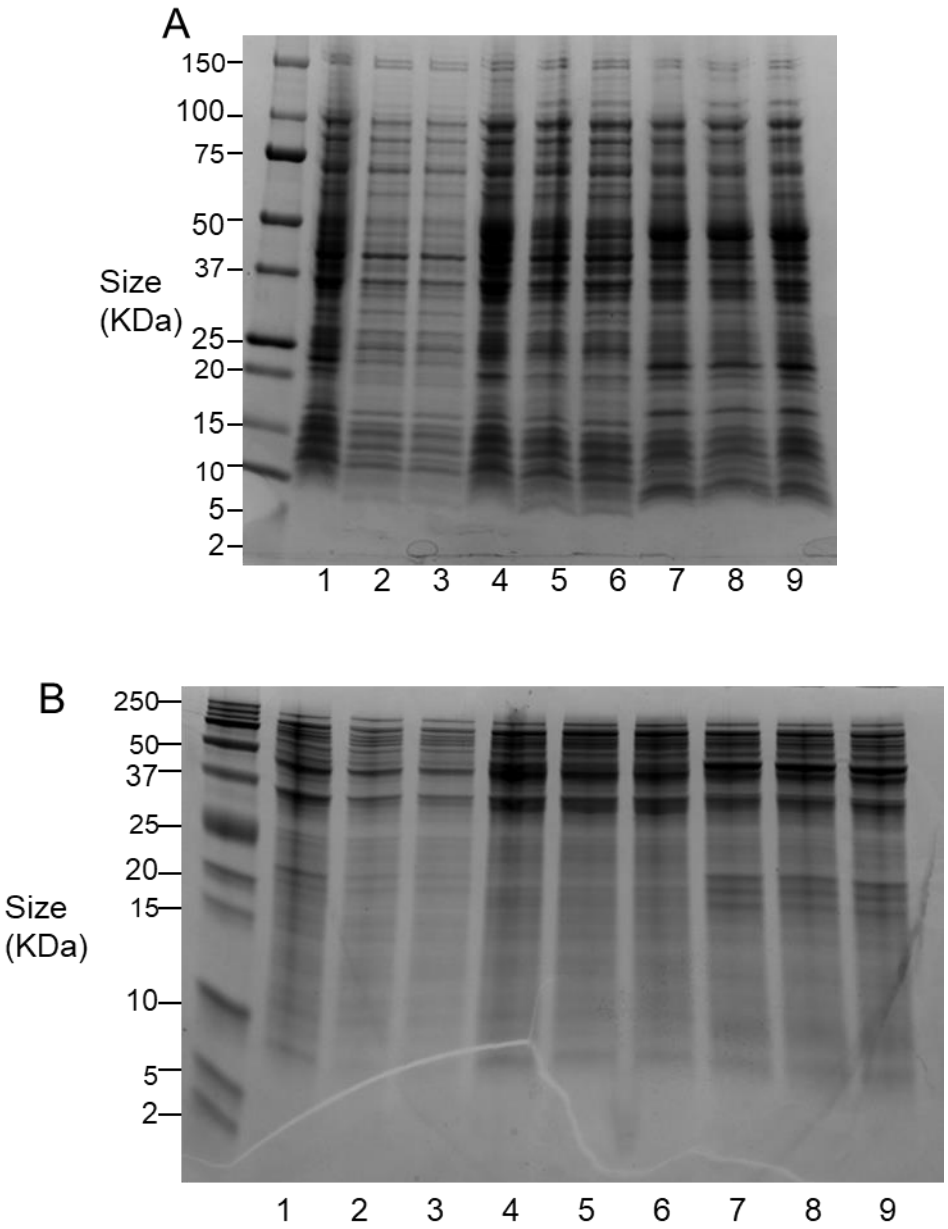

Figure 3.1, SDS-PAGE analysis of PLS expression. Maximally loaded cell lysates (15 µL) induced with 0, 0.2 and 1 mM IPTG for three strains: PRril (Lanes 1-3 respectively), BL21(DE3) (lanes 4-6 respectively) and PlysS (lanes 7-9 respectively). A, 4-20% gradient gel (BioRad), Coomassie instant blue stain. B, Tris/Tricine gel, methanol/acetic acid based stain and no dye in loading buffer.

On analysis of the cell lysates by SDS-PAGE (BioRad mini Protean - 4-20% gradient gel), no PLS protein was visualised at the expected mass of 4390 Da (Figure 3.1). Results suggested that the peptide was either not expressed in the host/vector combination or not visualised after SDS-PAGE/instantblue analysis. It was noted that no protein smaller than ~8000 Da was visualised and it was postulated PLS and other low-weight peptides could migrate out of the gel during the instant blue staining process. In order to investigate the possibility of this visualisation error, multiple techniques were employed. Samples were analysed by Tris/Tricine gel electrophoresis (Schägger & von Jagow, 1987), stained using a methanol/acetic acid based (fixing) Coomassie stain, and dye was removed from the loading buffer to remove the possibility of the dye potentially obscuring the area where PLS was expected to run (Figure 3.1). Despite extensive modifications, including increasing culture volumes and attempted observation of low molecular weight cysteine-containing proteins by Ellman's reagent, PLS could not be visualised.

Following unsuccessful expression, the pMal expression vector was selected to produce PLS as a cleavable fusion to the highly soluble maltose binding protein (MBP) to form the MBP-PLS(WT) fusion protein. The fusion would allow a larger, more visible, combined mass (46 882 Da), increasing the solubility of PLS and provide a purification method via amylose affinity purification. The PLS coding sequence (codon-optimised for expression in *E. coli*) was purchased and inserted into the pMAL expression vector as described in section 2.2.7. Cells containing the plasmid construct were screened by colony PCR (Figure 3.2) after optimisation of the reaction for $MgCl_2$ concentration, annealing temperature, and template DNA preparation (Supplementary Figure 8.1). Plasmid DNA was purified from these

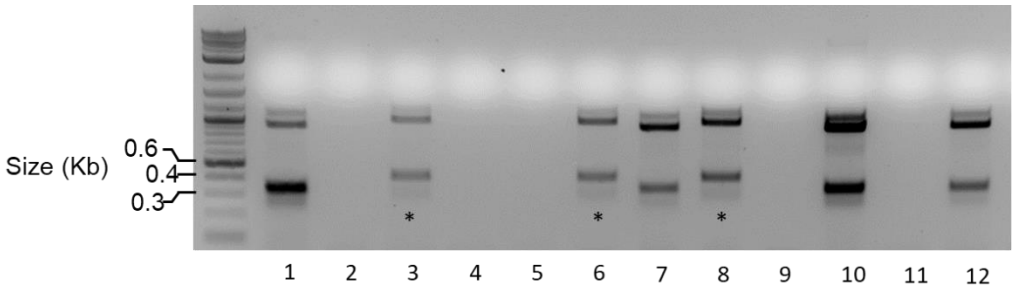

Figure 3.2, Identification of positive pMal(PLS) transformants. Agarose gel electrophoresis analysis of colony PCR reactions for 13 colonies. The "*" symbol denotes fragments where an apparent mass-shift increase was observed.

cells by miniprep and sequenced by sanger sequencing (Applied Biosystems 3730 - University of Durham Biosciences department facility) to confirm correct insertion (Supplementary Figure 8.3)

In addition to the MBP-PLS(WT), three mutants were constructed by *in-vitro* site-directed mutagenesis of the plasmid DNA. Two single mutants were created where Cysteine 6 and 17 were individually mutated to Serine residues (MBP-PLS(C6S) and MBP-PLS(C17S) respectively) and a third mutant was created where both Cysteine residues 6 and 17 were altered to Serine residues (MBP-PLS(C6S/C17S)).

MBP-PLS(WT), MBP-PLS(C6S), MBP-PLS(C17S) and MBP-PLS(C6S/C17S) were all purified using the same purification scheme as outlined section 2.3.1.

Cleavage of the MBP-PLS fusion proteins was initially attempted to produce pure PLS protein. MBP-PLS was incubated with factor Xa cleavage enzyme and cleavage monitored by SDS-PAGE (Figure 3.3). The reaction was optimised by adjustment of the buffer components, mainly [EDTA], [Ca^{2+}] and [glycerol]. PLS can clearly be observed after 24h cleavage in these small-scale pilot-experiments (Figure 3.3, B), and it was possible to achieve complete cleavage (Figure 3.3, C). Scale-up to 1L culture preparations would however prove cost prohibitive due to the concentration of factor Xa required, relative to [MBP-PLS].

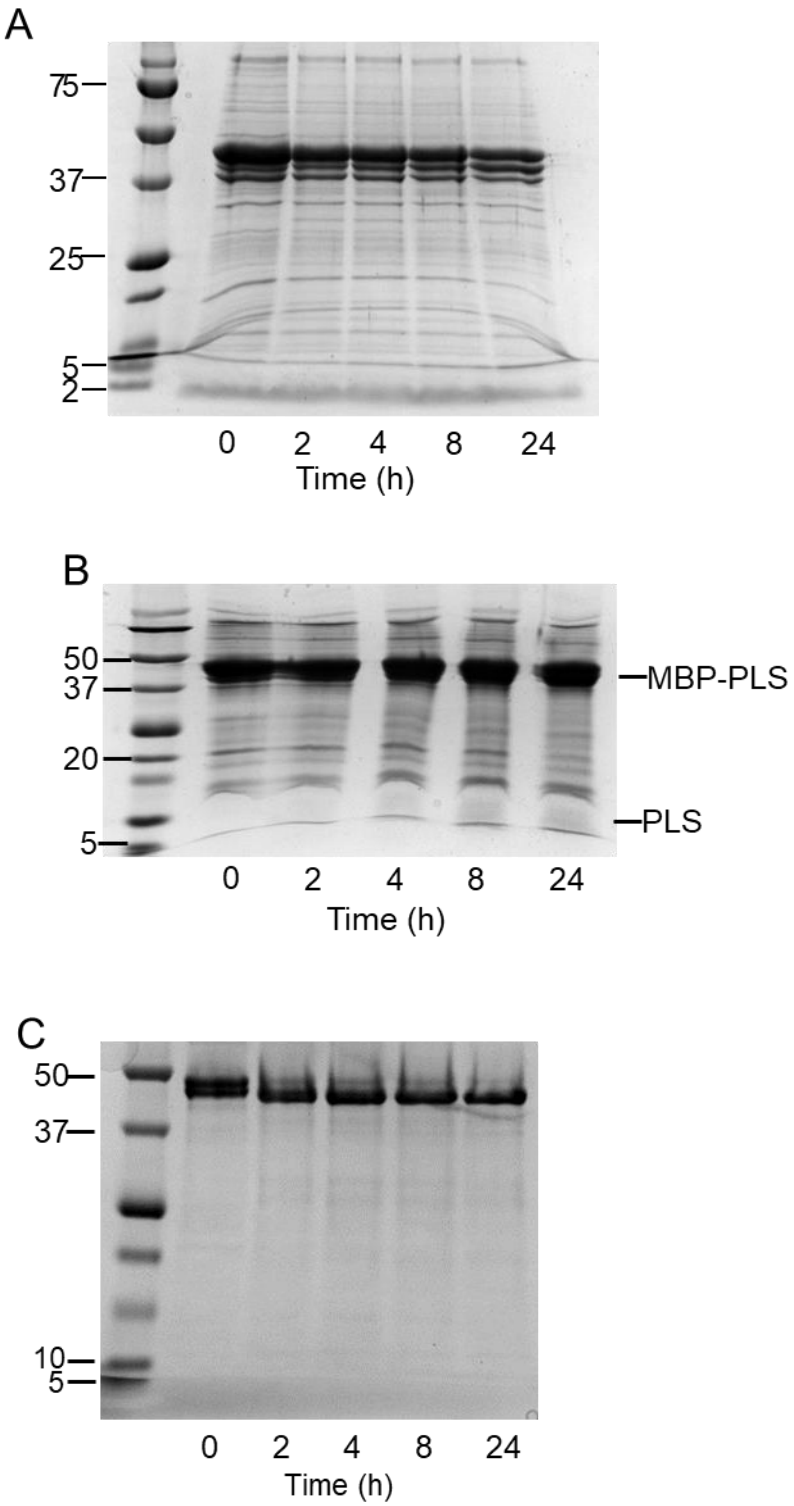

Figure 3.3, FXa cleavage. A, SDS-PAGE analysis of incomplete factor Xa cleavage of MBP-PLS(WT) for 24h at 20 ºC. B, Maximally loaded samples from "A" where the formation of scar-free PLS is apparent. C, SDS-PAGE analysis of the complete cleavage of MBP-PLS over 24h 37 ºC.

Regardless, PLS was then purified by Anion exchange chromatography using HiTrap SP (GE healthcare). pI estimations for PLS, PLS-MBP, and MBP were 10.64, 6.20 and 5.08 respectively. At pH 6.5 (reaction conditions), PLS was expected to be positively charged and could be separated from the two contaminants using an SP column by elution with increasing NaCl concentrations. A_{280} traces following the column fractions did not pick up a secondary peak as expected when a gradient elution from 50 mM – 4M NaCl was used. Again, PLS could not be visualised by Coomassie-stained SDS-PAGE, by Bradford assay, or by Ellman's assay, due to its low mass and concentration. A stepwise elution method was employed to create a concentrating step, however PLS was seen to elute at the same concentration as the major contaminants at 250 mM NaCl (Figure 3.4).

Attempts to separate the MBP-PLS and MBP contaminants from the PLS were made using a 10 kDa nylon membrane ultrafiltration device. PLS was expected to flow through the filter without a change in concentration assuming no adherance to the membrane. Results indicated that both the PLS and MBP were retained rather than passing through into the filtrate (Figure 3.5) even though the Mr of PLS was predicted to be 4.6 kDa.

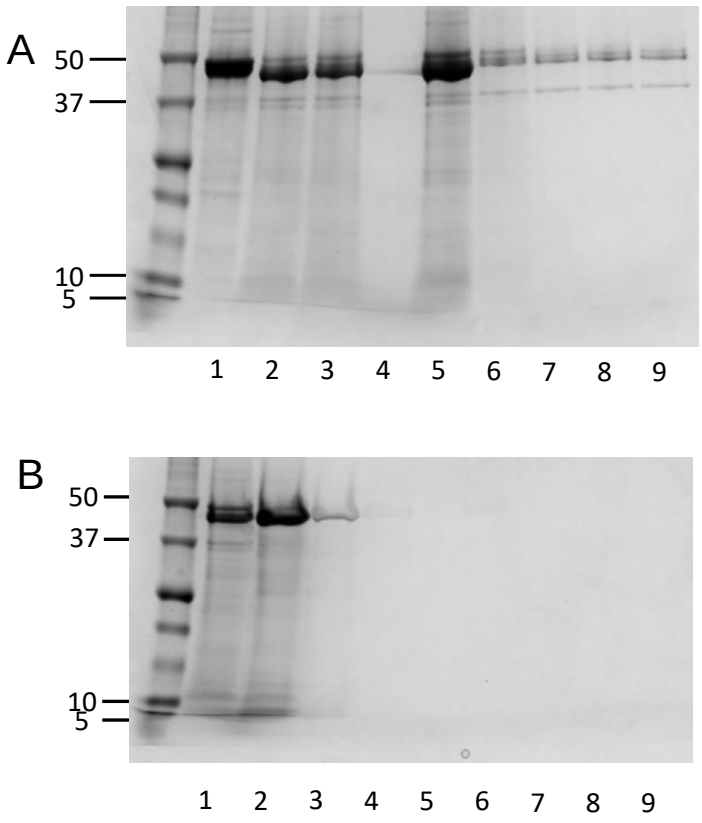

Figure 3.4, Purification of Polaris by cation exchange chromatography and centrifugal ultrafiltration. TEO-tricine gels showing eluted fractions from SP column. Gel 1: Lanes 1-3 show pre FXa cleavage, post FXa cleavage and SP-column flow-through. Lanes 5-9 show subsequent 2 mL washes at 50 mM NaCl. Gel 2: lane 1, 0.9mL elution at 250 mM NaCl followed by elution of 0.5, 0.5 and 1 mL (lanes 2-4 respectively) lanes 6-9 show elution of 0.9, 0.5, 0.5 and 1 mL respectively in buffer containing 1 M NaCl.

It was also noted that there were two proteins of low molecular weight at the approximate mass of the scar-free PLS and a hypothetical dimer. It was postulated that even under SDS-PAGE conditions and heat treatment, PLS might be able to dimerise, possibly in the presence of copper. This effect, although uncommon, has been known to occur in the Cu(I) binding protein Atx1 (*Saccharomyces cerevisiae*) (Miras et al., 2008). Here, Miras and co-workers also show the dependency on the two cysteine residues and the presence of Cu(I) for the event to occur. As PLS also has two cysteine residues, postulated to coordinate Cu(I), it is plausible that a similar effect is being observed here.

Additionally, when examining the MBP-PLS fusion by SDS-PAGE (Figure 3.3, A), three bands are observed. In continuation of the hypothesis above, it was postulated that the bands, from heaviest to lightest, could be MBP-PLS:PLS, MBP-PLS and MBP respectively.

At this stage, the decision was made to study the metal-binding properties of the intact MBP-PLS fusion protein as a proxy for PLS.

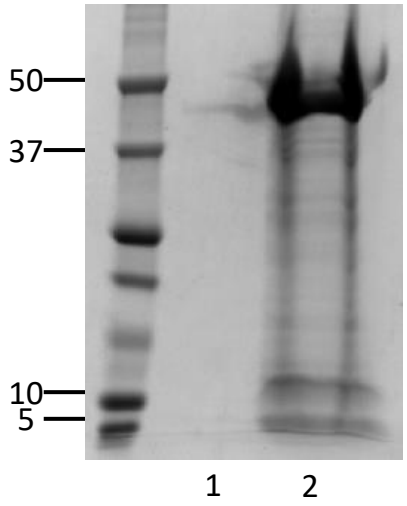

Figure 3.5, SDS-PAGE following ultrafiltration. SDS-PAGE analysis of flow through (lane 1) and retained material (lane 2) when a mixture of MBP-PLS and PLS are passed through a 10 kDa cut-off ultrafiltration device

3.2 Metal binding stoichiometries and affinities of PLS

3.2.1 Cu(I) binding properties of PLS

The Cu(I) binding stoichiometry of PLS was determined by competition between MBP-PLS(WT) and the metal-binding probe Bicinchoninic Acid (BCA). BCA is a relatively weak-binding Cu(I) probe with a Cu(I) β_2 value of 1.58 x 10^{17} M^{-2} (Xiao et al., 2011). It was predicted that by competing BCA with MBP-PLS for Cu(I), MBP-PLS would outcompete the probe for metal, stoichiometrically. As the MBP-PLS copper complex is spectrally silent with Cu(I), the BCA was used to monitor the binding events indirectly as it would outcompete all other 'adventitious' binding events. First, BCA was titrated directly with $CuSO_4$ to characterise the spectral response at 358 nm (Figure 3.6) these data were also used to quantify and corroborate the probe and metal concentration. NH_2OH was present in all Cu(I) titrations at 1 mM in order to ensure Cu(I) remained fully reduced *in-situ* (Young & Xiao, 2021a). Data was fitted using the software package Dynafit (Kuzmič, 2009) to describe formation of the 2:1 $BCA_2Cu(I)$ complex upon direct titration (Supplementary Figure 8.8) and an experimental extinction coeffiecient ε_{358} of 42 820 M^{-1} cm^{-1} was calculated. This response value is consistent with the literature value of 42 900 M^{-1} cm^{-1} (Djoko, Xiao, Huffman, & Wedd, 2007) and was used to calculate [$BCA_2Cu(I)$] hereafter.

To calculate the Cu(I) binding stoichiometry of PLS, the same titration as above, in the presence of 14 μM MBP-PLS was carried out in triplicate (Figure 3.7). Upon titration with Cu(I), the probe BCA does not respond at 358 nm until ~7 μM Cu(I) has been added. As 14 μM MBP-PLS withheld ~7 μM Cu(I) tightly from the probe,

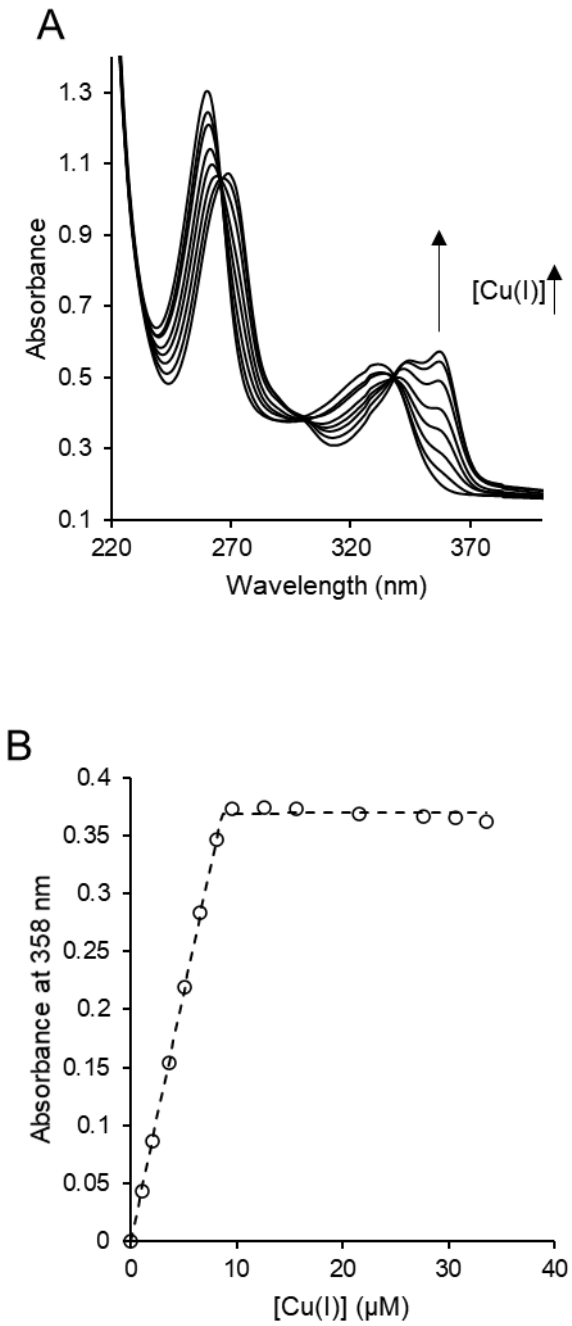

Figure 3.6, Calculating extinction coefficient $\varepsilon_{358\ nm}$ of $BCA_2Cu(I)$. A. UV-vis spectra of BCA (17.3 μM) upon titration with $CuSO_4$ to saturation (recorded anaerobically at pH 7.0) in the presence of 1 mM NH_2OH (representative sample, n=2). B. Binding isotherm of $A_{358\ nm}$ feature shown in 'A' (empty circles) and fit when modelled in Dynafit (dotted line)

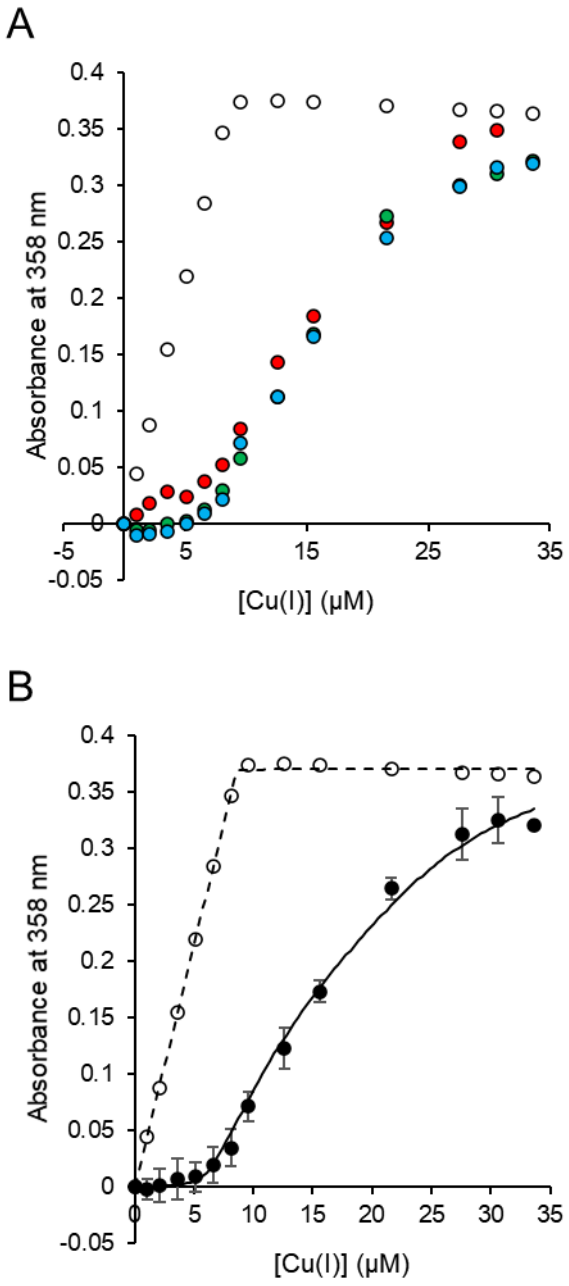

Figure 3.7, Estimation of Cu(I)-binding stoichiometry of MBP-PLS by competition with BCA. A. $A_{358\ nm}$ binding isotherm of BCA (17.3 μM) in the presence and absence of 14 μM MBP-PLS (filled and empty circles respectively) upon titration with $CuSO_4$ (recorded anaerobically at pH 7.0) in the presence of 1 mM NH_2OH (n=3, replicates 1-3 shown in red, green and blue respectively). B. Binding isotherm mean data shown in 'A', including dynafit models to describe Cu(I)-binding in the presence and absence of MBP-PLS (solid and dashed respectively) when MBP-PLS binds Cu(I) in a 2:1 stoichiometry with 2 additional weaker binding sites. Error bars represent replicate mean +/- 1 standard deviation.

the stoichiometry of Cu(I) binding is predicted to be 2:1 MBP-PLS:Cu(I). Additionally, after the protein is saturated with Cu(I), and BCA begins to bind Cu(I), the Cu(I) loading into the probe when compared to the control in the absence of MBP-PLS is non-stoichiometric, implying additional (much weaker) adventitious binding event(s). As BCA has a relatively weak Cu(I) affinity, weak-binding adventitious Cu(I) events start to compete with BCA as it reaches saturation. The binding curve was then fitted using the software package Dynafit (Kuzmič, 2009) to describe the competition between MBP-PLS binding in a 2:1 stoichiometry (with additional non-specific binding sites) and BCA binding in a 2:1 stoichiometry for Cu(I) (Supplementary Figure 8.9). This model shows a good fit to the data, in both the initial and latter parts of the titration.

It was postulated that the tight binding of Cu(I) by PLS was likely via co-ordination using the two cysteine residues C6 and C17 (Mudge, 2016, E-Thesis). To investigate the contribution of these two residues in Cu(I) binding, three mutants of MBP-PLS were created via the QuikChange method, where the codon for C6 was mutated to encode a serine (C6S), codon for C17 was mutated to encode serine (C17S) and where both codons for C6 and C17 were mutated to encode serines (C6S/C17S) (see section 2.2.8). Mutations of cysteine to serine are commonly used to test the contribution of a thiol from a cysteine on the structure or function of protein. Mutations like these have been used to investigate function in proteins with a CXXC motif (Pavlin et al., 2019) ,where the SXXS motif is unable to bind Cu(I) ions, for example in the Cu metallochaperone Cox17 (Heaton, Nittis, Srinivasan, & Winge, 2000) and metal-responsive transcriptional regulator CueR (K. Chen, Yuldasheva, Penner-Hahn, & O'Halloran, 2003).

14 μM MBP-PLS (WT), MBP-PLS (C6S), MBP-PLS (C17S) and MBP-PLS (C6S/C17S) were then individually competed with the probe BCA (10 μM) upon titration with Cu(I) (Figure 3.8). Again, MBP-PLS(WT) stoichiometrically withheld approximately 0.5 equivalents of Cu(I) from the probe, implying a Cu(I) binding stoichiometry of 2:1 protein:Cu(I). In all three mutants, the tight initial site is lost, and Cu(I) is immediately partitioned between the BCA and protein. These results show that both residues C6 and C17 are essential in the tight 2:1 Cu(I) binding site of PLS. Additionally, in all three mutants, some weaker Cu(I) binding is maintained (when compared to the control in the absence of protein). As this weaker interaction is maintained in both the WT (post-saturation) and all mutants, it is likely that the potential weaker site(s) are independent of the tight cysteine-dependent site.

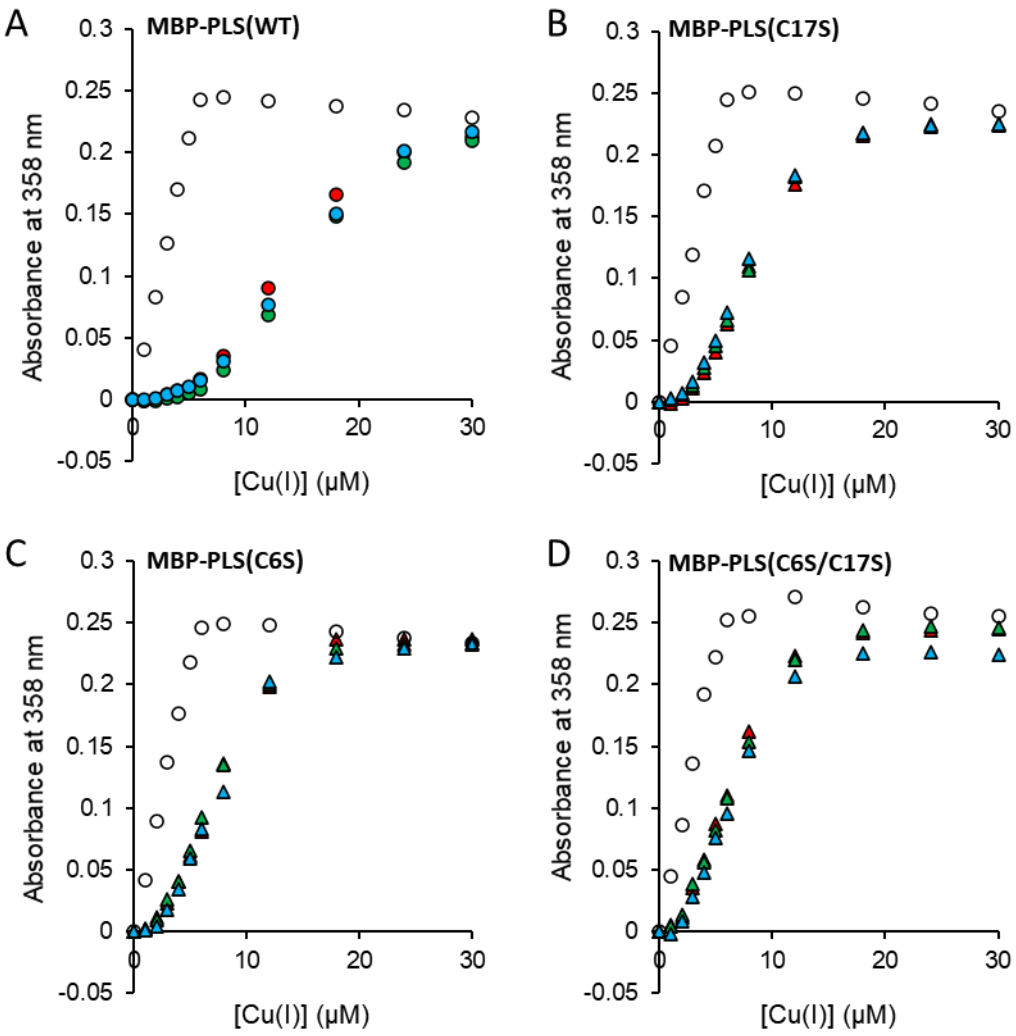

n.b. Figure continued overleaf.

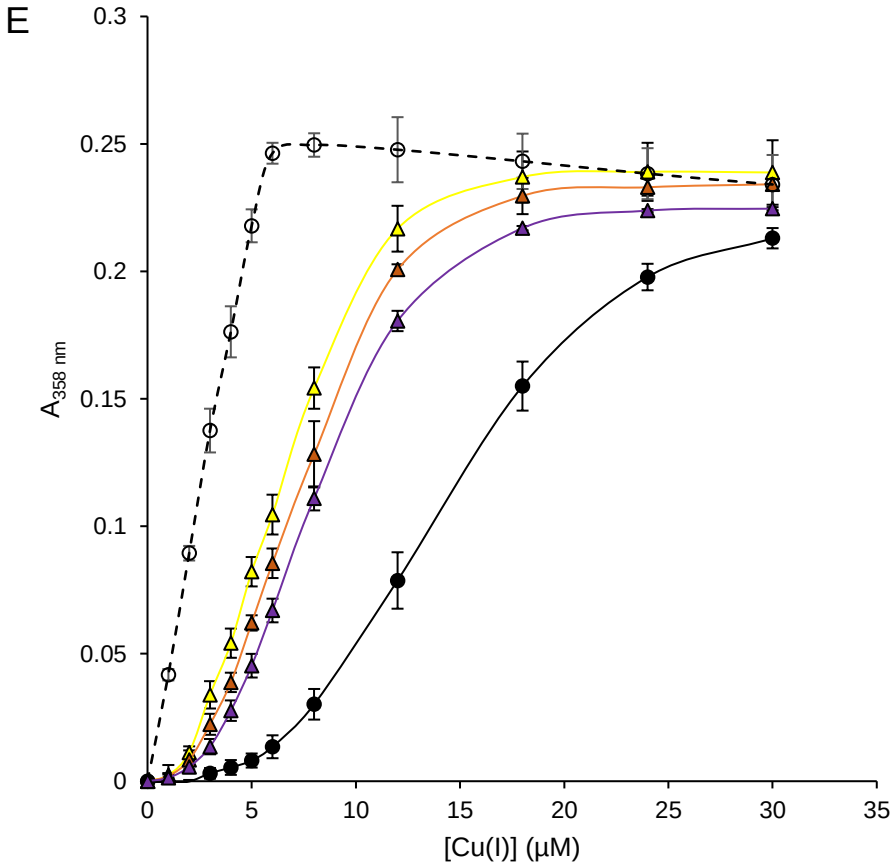

Figure 3.8, MBP-PLS requires both C6 and C17 for tight Cu(I) binding $A_{358\ nm}$ binding isotherms of BCA (10 µM) in the presence and absence (filled and empty respectively) of 14 µM MBP-PLS-(WT) (circles) and MBP-PLS mutants (B-D, triangles) upon titration with $CuSO_4$ (recorded anaerobically at pH 7.0) in the presence of 1 mM NH_2OH (n=3, replicates 1-3 shown in red, green and blue respectively). E, compilation of $A_{358\ nm}$ binding isotherms including fitted curves – MBP-PLS-C6S, -C17S and –C6S/C17S represented as orange, purple and yellow triangles respectively. Error bars represent 1 standard deviation either side of replicate mean.

To accurately characterise the affinity of the tight, cysteine-dependent 2:1 Cu(I) binding site observed in Figure 3.8, it was necessary to design a titration where there was more dissociation of Cu(I) from the protein. In order to achieve better partitioning, the tighter Cu(I) binding probe Bathocuproine Sulfonate (BCS) was employed which has a $BCS_2Cu(I)$ β_2 value of 7.94×10^{19} (Xiao et al., 2011) and extinction coefficient of $BCS_2Cu(I)$ ε_{483} = 13 300 M^{-1} cm^{-1} (Xiao, Loughlin, George, Howlett, & Wedd, 2004). 20 μM MBP-PLS(WT) and 20 μM BCS was titrated with Cu(I) and for each addition at equilibrium the response at 483 nm was monitored (Figure 3.9). Although more even partitioning was achieved between the protein and probe, the probe did not reach the expected level of saturation in the presence of MBP-PLS(WT) (the expected level of saturation would match that seen in the control titration). It is postulated that in addition to the tight cysteine-dependent Cu(I) binding site, MBP-PLS(WT) could have an additional site which results in the partial formation of a ternary complex between the probe BCS and protein, co-ordinated by Cu(I). Events such as these have been previously documented between probes that form 2:1 complexes with their metals and metalloproteins (Young, Wedd, & Xiao, 2018) and it has also been highlighted that any stable ternary complex formation can prevent accurate affinity measurements (Young & Xiao, 2021a) as any stable complex can make a significant contribution to the total speciation of the system of equations used to calculate affinities shown throughout this work. For this reason, an alternative experiment was designed using the weaker probe BCA in an excess to MBP-PLS(WT) to achieve even partitioning.

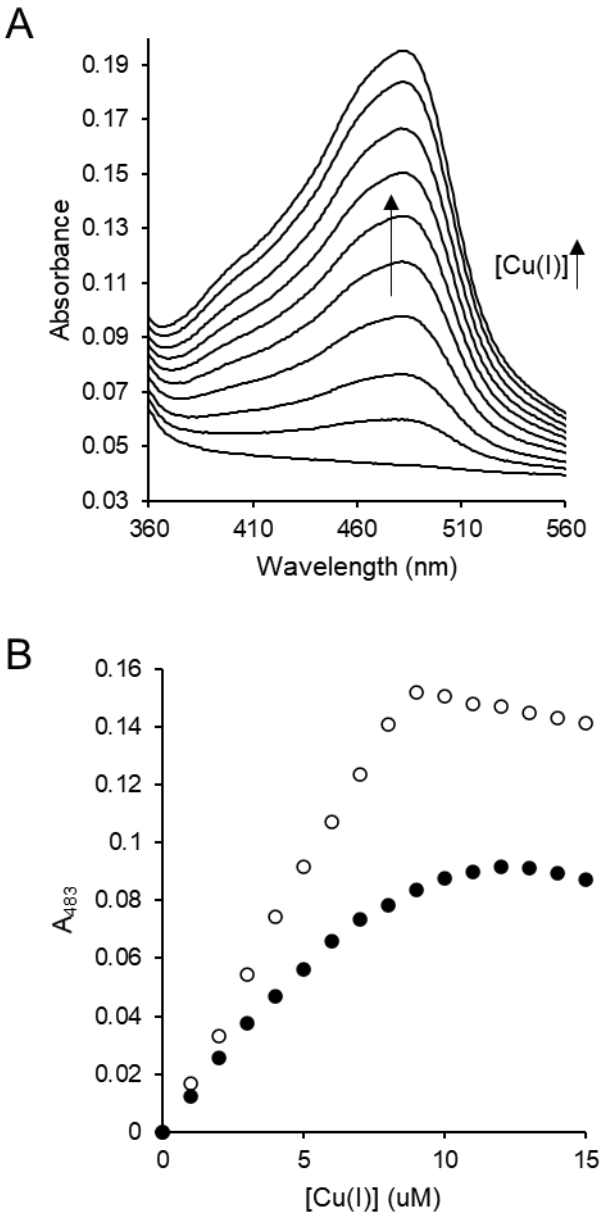

Figure 3.9, Competition between MBP-PLS and BCS for Cu(I) A. UV-vis spectra of BCS (20 µM) upon titration with $CuSO_4$ to saturation (recorded anaerobically at pH 7.0) in the presence of 1 mM NH_2OH. B. Binding isotherm of $A_{483\ nm}$ feature shown in 'A' when 20 µM BCS is titrated in the presence and absence (filled and empty circles respectively) of 20 µM MBP-PLS.

The Cu(I) affinity was estimated by competition of 10 μM MBP-PLS(WT) and 50 μM (5x excess) BCA for Cu(I) (Figure 3.11). When compared to the control titration in the absence of MBP-PLS(WT) the response of the probe upon titration with Cu(I) is diminished, reflecting the binding of Cu(I) by the tight site on MBP-PLS(WT). The Cu(I) β_2 affinity of MBP-PLS$_2$Cu(I) for can then be determined from first principles using the equation scheme outlined below,

Equation 3.1: $2\text{MBP-PLS} + \text{Cu(I)} \rightleftharpoons \text{MBP-PLS}_2\text{Cu(I)}$
where $K_{eq1} = \beta_2\ (\text{MBP-PLS}_2\text{Cu(I)})$

Equation 3.2: $\text{BCA}_2\text{Cu(I)} \rightleftharpoons 2\text{BCA} + \text{Cu(I)}$
where $K_{eq2} = 1/\beta_2(\text{BCA}_2\text{Cu(I)})$

Equation 3.3: $\text{BCA}_2\text{Cu(I)} + 2\text{MBP-PLS} \rightleftharpoons \text{MBP-PLS}_2\text{Cu(I)} + 2\text{BCA}$
where $K_{eq3} = [\text{MBP-PLS}_2\text{Cu(I)}] * [\text{BCA}]^2 / [\text{BCA}_2\text{Cu(I)}] * [\text{MBP-PLS}]^2$

Equation 3.4: $K_{eq1} = K_{eq3} / K_{eq2}$

For each titration data point, K_{eq3} can be calculated by populating equation 3.3. K_{eq1} (β_2 MBP-PLS$_2$Cu(I)) can then be calculated using K_{eq3} and K_{eq2} in equation 3.4.

Average value from triplicate data was calculated as 3.79 (±1.5) x 10^{19} M^{-2}. This value was then fitted back onto the experimental data in Figure 3.10 using Dynafit (Kuzmič, 2009) and when the additional weak affinity site was modelled, provides good fit (Supplementary Figure 8.10 shows dynafit script). Additional simulated fits of 10x tighter and weaker affinities (Figure 3.10 C) show good resolvability from the experimental dat, implying the experimental affinity measured is within the constraints of experimental design.

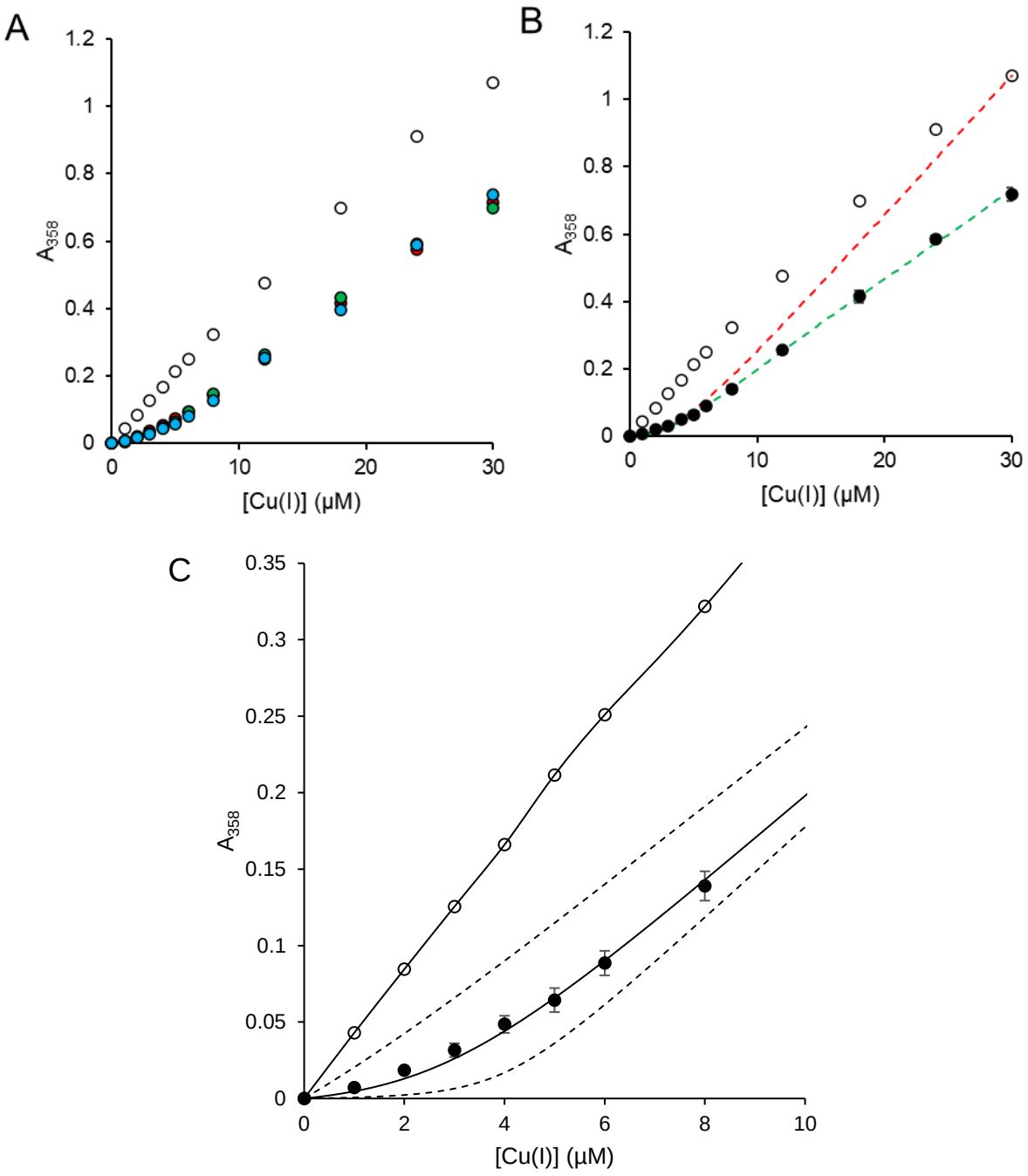

Figure 3.10, Estimation of Cu(I) β_2 affinity of MBP-PLS$_2$Cu(I) by competition with 5x excess BCA A. $A_{358\ m}$ binding isotherm of BCA (50 μM) in the presence and absence of 10 μM MBP-PLS (filled and empty circles respectively) upon titration with $CuSO_4$ (recorded anaerobically at pH 7.0) in the presence of 1 mM NH_2OH (n=3, replicates 1-3 shown in red, green and blue respectively). B. Binding isotherm mean data shown in 'A', including dynafit models to describe Cu(I)-binding of MBP-PLS when modelled as forming 2:1 complex only (red dashed line) and one additional weak binding event (green dashed line). C, expanded view of data shown in "A" including simulated fits for a 10x weaker and stronger affinity (above and below, respectively) Error bars represent replicate mean +/- 1 standard deviation.

3.2.2 Zn(II) binding properties of PLS

The Zn(II)-binding stoichiometry and affinity of MBP-PLS(WT) was determined by competition with the metal-binding probe Mag-fura-2 (MF-2).

Zn(II) binding to MF-2 can be observed by monitoring two spectral features on addition of Zn(II): increased absorption at 325 nm or decreased absorption at 366 nm. First, MF-2 was characterised by direct titration with Zn(II) – 7.7 μM MF-2 was titrated with Zn(II) up to saturation point (Figure 3.11). The linear portion of the response at 325 nm was plotted with a line of best fit. As described by the Beer-Lambert law, $A = \varepsilon c\ l$, where A is the absorbance change, ε is the extinction coefficient, c is the concentration, and l pathlength (1 cm), the gradient of the linear line of best fit = $\Delta A/c = \Delta\varepsilon$ (as c = [Zn(II)] = [MF-2], as MF-2 binds Zn(II) in a 1:1 stoichiometry). Hence, the extinction coefficient $\varepsilon_{325\ nm}$ for MF-2(Zn(II)) = 25 051 Mcm^{-1}.

In order to calculate the stoichiometry and affinity of Zn(II) binding by MBP-PLS(WT), 20 μM MBP-PLS(WT) and 7.7 μM MF-2 was titrated with Zn(II) and for each addition, when at equilibrium, the response at 325 nm was monitored (Figure 3.12). Upon Zn(II) titration, in the absence of MBP-PLS(WT), the probe responds at 325 nm stoichiometrically, until saturation of the probe at ~7.7 μM Zn(II). In the presence of MBP-PLS(WT) however, the response at 325 nm is repressed at each addition, implying MBP-PLS(WT) withheld Zn(II) from the probe. The saturation of the binding isotherm in the presence of MBP-PLS(WT) is close to 17.7 μM, implying a Zn(II) binding stoichiometry of 2:1 MBP-PLS:Zn(II).

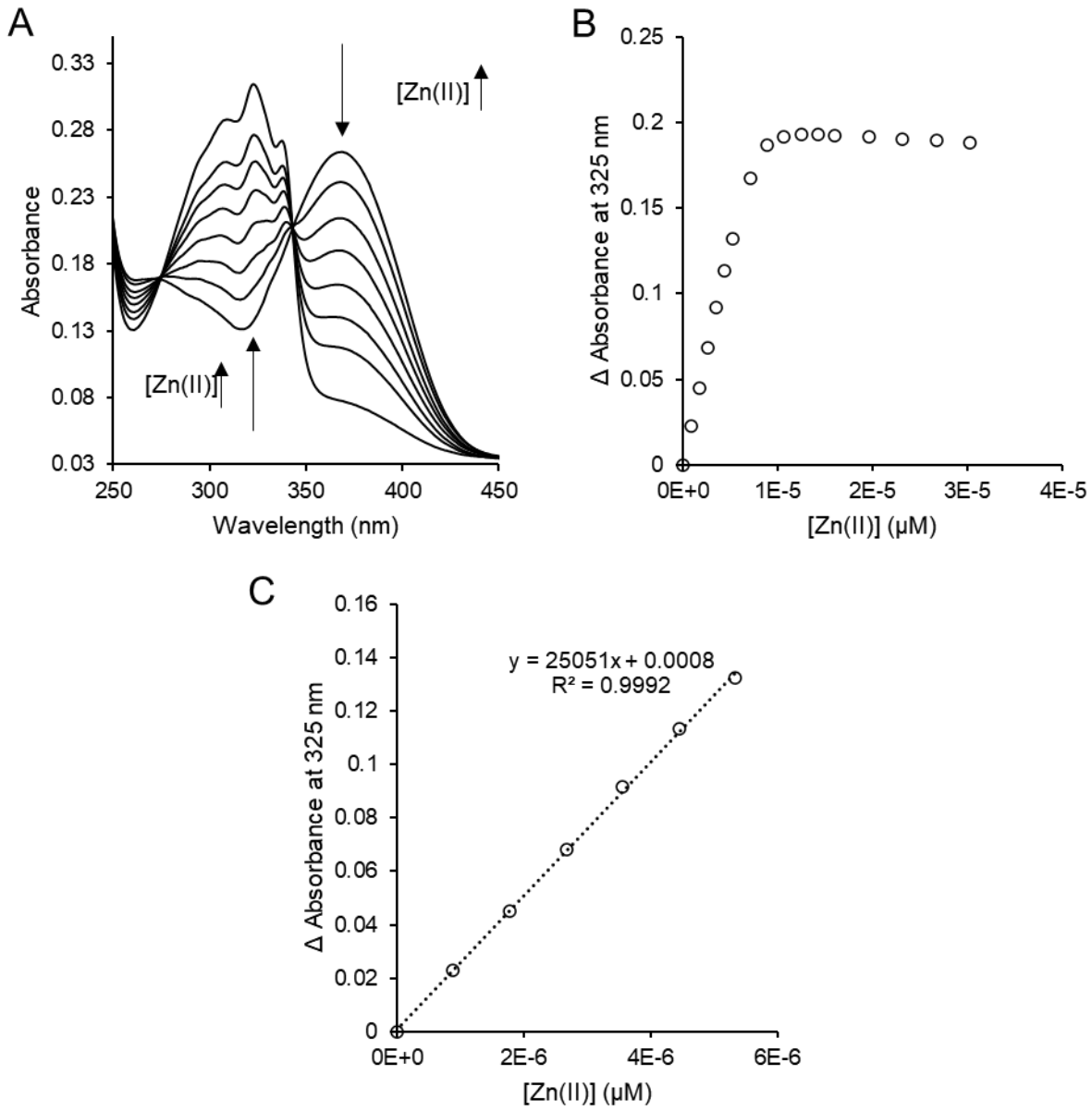

Figure 3.11, Calculating extinction coefficient ε_{325} of MF-2Zn(II). A. UV-vis spectra of MF-2 (7.7 μM) upon titration with $ZnSO_4$ to saturation (recorded anaerobically at pH 7.0). B. Binding isotherm of $A_{325\ nm}$ feature shown in 'A' (empty circles). C. Linear section of the binding isotherm shown in 'B', including line of best fit (dotted)

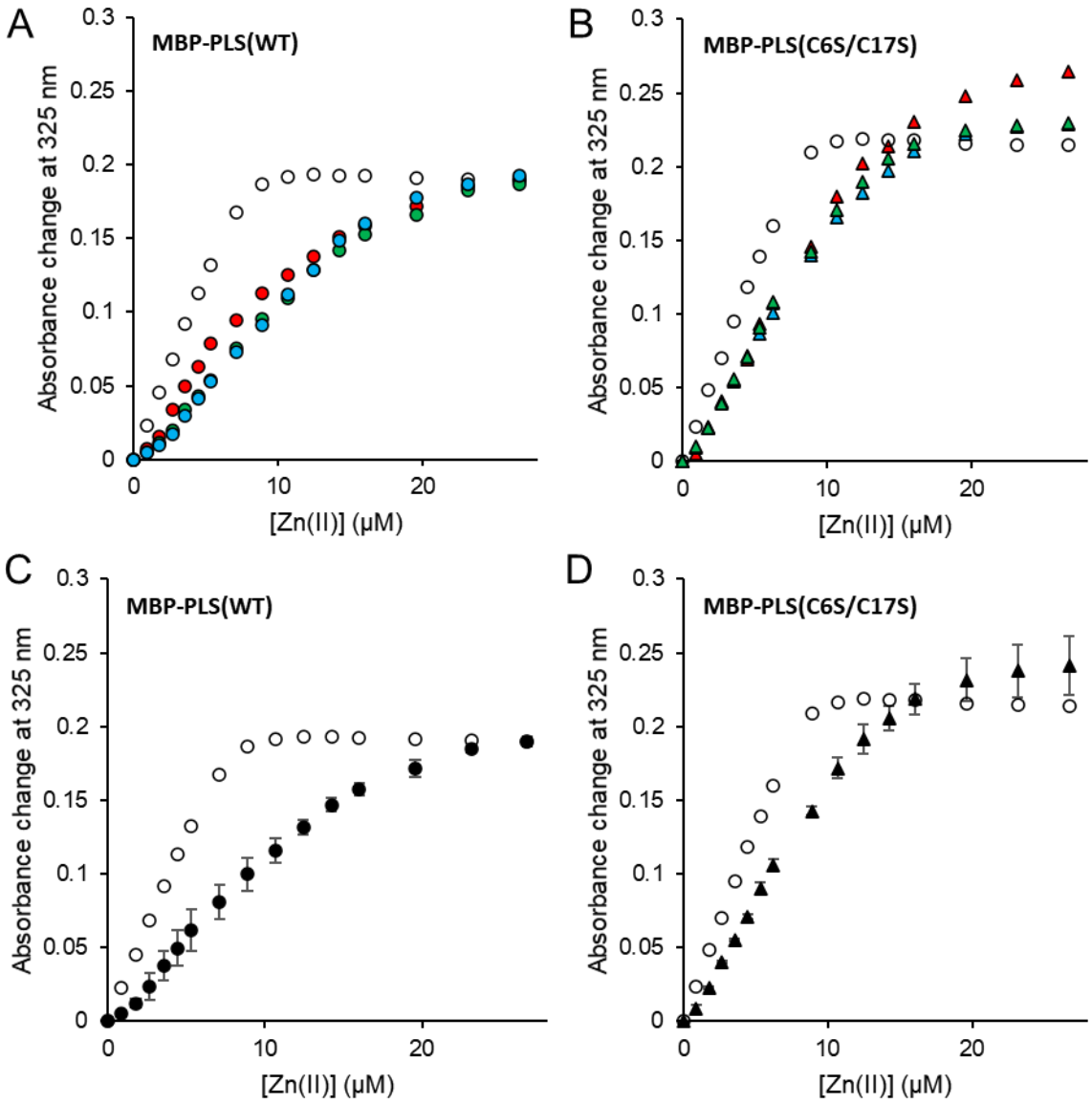

Figure 3.12, MBP-PLS Zn(II) binding titration. A, $A_{325\ nm}$ binding isotherms of MF-2 (~10 μM) in the presence and absence (filled and empty respectively) of 20 μM MBP-PLS(WT) (A, C, Circles) and MBP-PLS(C6S/C17S) (B, D, triangles) upon titration with $ZnSO_4$ (recorded anaerobically at pH 7.0, n=3, replicates 1-3 shown in red, green and blue respectively). Error bars represent 1 standard deviation either side of replicate mean.

An additional Zn(II) titration of 20 μM MBP-PLS(C6S/C17S) and ~10 μM MF-2 showed reduced competition with the probe for Zn(II) implying Zn-binding to the WT MBP-PLS is Cysteine-dependent (Figure 3.12). The MBP-PLS(C6S/C17S) retains some competition with MF-2 for Zn(II), and again this is predicted to be the result of an additional binding site, possibly on the MBP portion of the fusion.

The affinity of MBP-PLS(WT) for Zn(II) was then determined from first principles, using the data from the MBP-PLS(WT) titration, as outlined in the equation scheme below.

Equation 3.5: $2MBP\text{-}PLS + Zn(II) \rightleftharpoons MBP\text{-}PLS_2Zn(II)$

where $K_{eq1} = \beta_2\ (MBP\text{-}PLS_2Zn(II))$

Equation 3.6: $MF\text{-}2Zn(II) \rightleftharpoons MF\text{-}2 + Zn(II)$

where $K_{eq2} = K_d(MF\text{-}2Zn(II))$

Equation 3.7: $MF\text{-}2Zn(II) + 2MBP\text{-}PLS \rightleftharpoons MBP\text{-}PLS_2Zn(II) + MF\text{-}2$

where $K_{eq3} = [MBP\text{-}PLS_2Zn(II)] * [MF\text{-}2] / [MF\text{-}Zn(II)] * [MBP\text{-}PLS]^2$

Equation 3.8: $K_{eq1} = K_{eq3} / K_{eq2}$

For each titration data point, K_{eq3} can be calculated by populating equation 3.7. K_{eq1} (β_2 MBP-PLS$_2$Zn(II)) can then be calculated using K_{eq3} and K_{eq2} in equation 3.8.

On calculation of these values for the triplicate titrations, the MBP-PLS Zn(II) β_2 value was calculated as 3.76 (±1.3) x 10^{12} M^{-2}.

3.2.3 Ni(II) binding properties of PLS

To investigate the Ni(II) binding properties of PLS, and hence if PLS could feasibly bind Ni(II) within the plant cytosol, MBP-PLS(WT) was competed with MF-2 by titration with Ni(II) (Figure 3.13), where the $K_{MF\text{-}2\ Ni(II)}$ = 2.0 x 10^7 (Golynskiy, Gunderson, Hendrich, & Cohen, 2006). Upon MF-2 binding Ni(II), at equilibrium, the absorbance change at 325 nm was monitored to report on the formation of the MF-2Ni(II) complex. 20 μM MBP-PLS(WT) and 10 μM MF-2 was titrated with Ni(II) to saturation. When compared to the control curve in the absence of any protein, MBP-PLS(WT) weakly withholds Ni(II) from MF-2.

The same titration was repeated where the MBP-PLS(WT) was replaced with the MBP-PLS(C6S/C17S) to ascertain whether the weak binding of MBP-PLS(WT) for Ni(II) was dependent on the cysteine residues at position 6 or 17 (Figure 3.13). Upon titration of 20 μM MBP-PLS(C6S/C17S) and 10 μM MF-2 with Ni(II), MBP-PLS(C6S/C17S) weakly withholds Ni(II) from MF-2. When the WT and double mutant isotherms are compared, there appears to be negligible difference, implying this weak Ni(II) interaction is independent of the two cysteines residues 6 and 17.

This suggests that the Ni(II) binding of PLS is weak, does not use the cysteine residues on PLS and it is likely the observed weak binding event might be to the MBP.

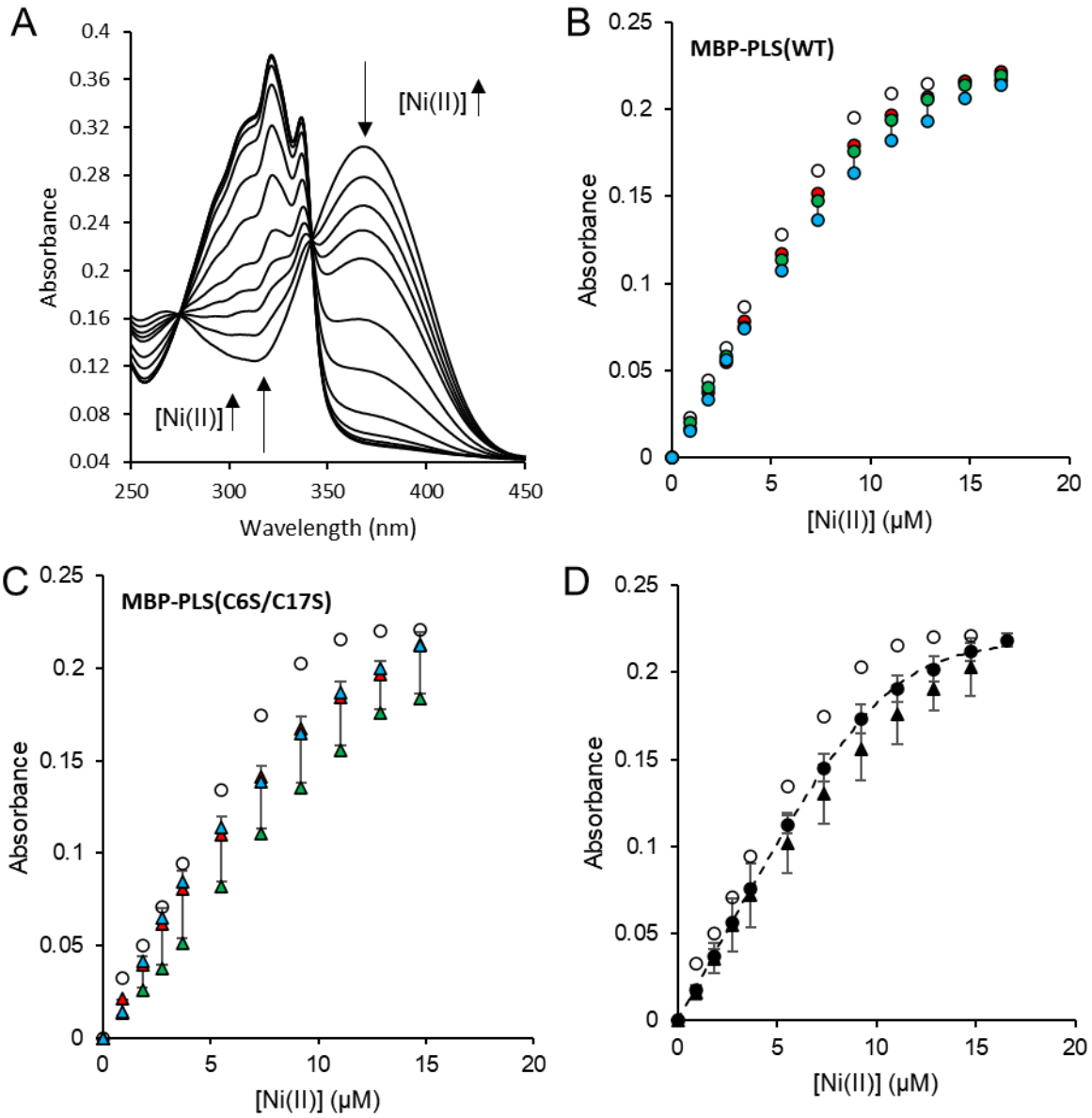

Figure 3.13, MBP-PLS Ni(II) binding titration. A, UV-vis spectra of MF-2 (10 μM) upon titration with $NiCl_2$ to saturation (recorded anaerobically at pH 7.0). B-C, A_{325} nm binding isotherms of MF-2 (10 μM) in the presence and absence (filled and empty respectively) of 20 μM MBP-PLS(WT) (B, cirlces) and MBP-PLS(C6S/C17S) (C, triangles) upon titration with Ni(II) (recorded anaerobically at pH 7.0, n=3, replicates 1-3 shown in red, green and blue respectively). D, compilation of A_{325} mean binding isotherms for MBP-PLS(WT) and MBP-PLS(C6S/C17S). Dotted line represents a Dynafit model for a theoretical fit if $PLS_2Ni(II)$ formed. All error bars represent 1 standard deviation either side of replicate mean.

3.2.4 Mn(II) binding properties of PLS

To investigate the Mn(II) binding properties of PLS, and hence if PLS could feasibly bind Mn(II) within the plant cytosol, MBP-PLS(WT) was again competed with MF-2 and titrated with Mn(II) (Figure 3.14). Upon binding Mn(II), absorbance change at 325 nm was monitored to report on the formation of the MF-2Mn(II) complex. Upon titration of 20 μM MBP-PLS(WT) and 10 μM MF-2 with Mn(II), very little dissociation of Mn(II) from the probe was observed, implying a weak interaction of the MBP-PLS(WT) with Mn(II). It should be noted that in the control curve (in the absence of protein) the binding isotherm observed was non-stoichiometric, i.e., approaching the saturation point of 10 μM MF-2 (10 μM Mn(II)), the response of the probe to Mn(II) addition is no longer linear. It is probable this is the result of the low affinity of MF-2 for Mn ($K_{d\ MF\text{-}2\ Mn(II)}$ = 9.7 x 10^{-7} (Golynskiy et al., 2006)) and possible adventitious binding of Mn(II) with components in the buffer.

The same titration was repeated where the MBP-PLS(WT) was replaced with MBP-PLS(C6S/C17S) to investigate if this weak binding event was dependent on the two cysteine residues 6 and 17 (Figure 3.14). Upon titration of 20 μM MBP-PLS(C6S/C17S) and 10 μM MF-2 with Mn(II), the protein effectively does not compete with MF-2 for Mn(II). When the binding isotherm in the absence of protein is compared to the binding isotherm in the presence of MBP-PLS(C6S/C17S), there is no difference in response. Although this initially suggests some cysteine-dependent response in the MBP-PLS(WT) titration, as it appears the WT protein withholds slightly more Mn(II) from the probe, the proportion of Mn(II) dissociation from the probe is negligible and dissociation from the probe is insufficient to establish an accurate affinity measurement. Nevertheless, as the dissociation of

Mn(II) from the probe when competed with MBP-PLS(WT) was very little, any Mn(II) binding to PLS is predicted to be very weak.

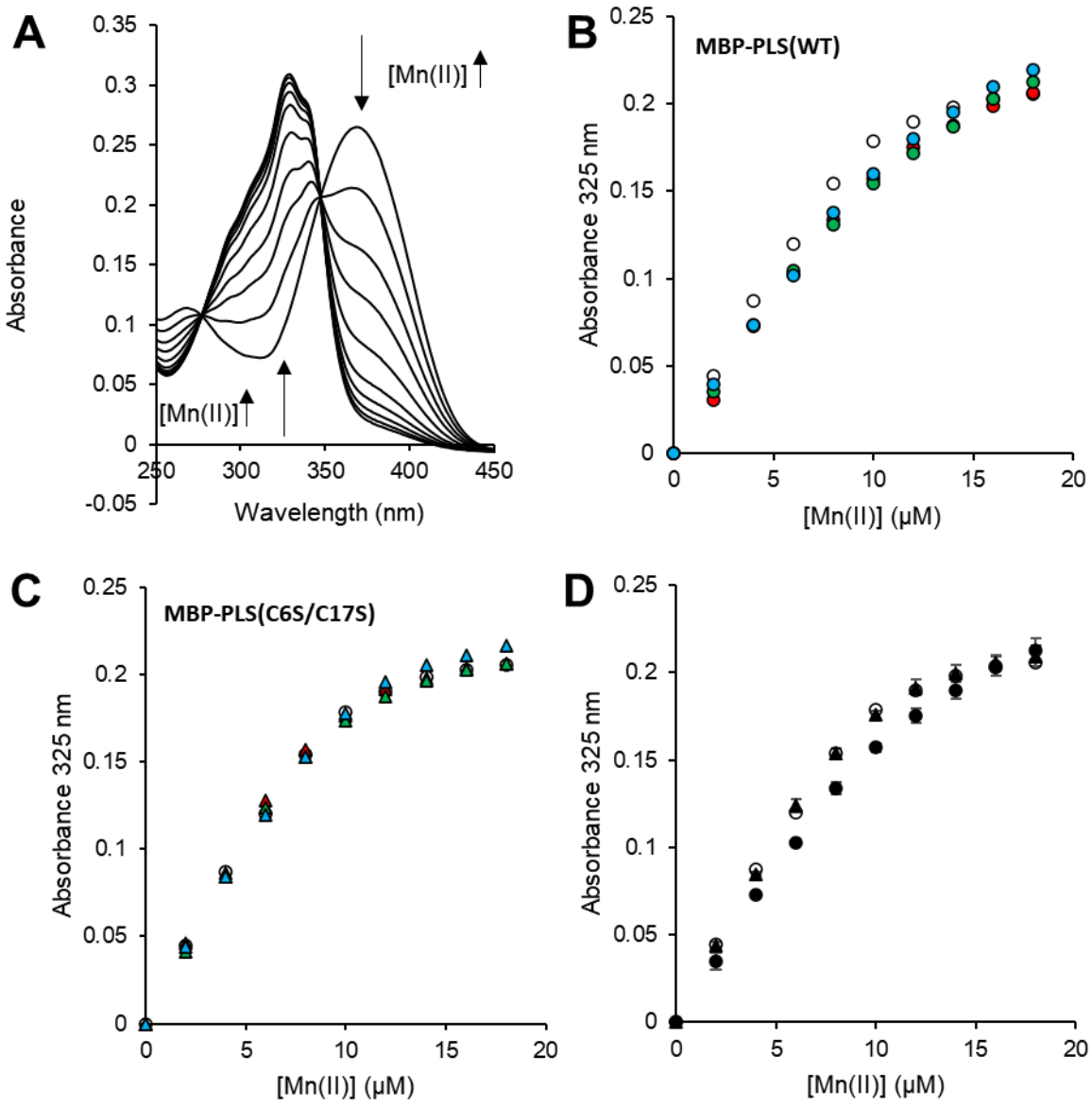

Figure 3.14, MBP-PLS Mn(II) binding titration. A, UV-vis spectra of MF-2 (10 μM) upon titration with $MnCl_2$ to saturation (recorded anaerobically at pH 7.0). B-C, $A_{325\ nm}$ binding isotherms of MF-2 (10 μM) in the presence and absence (filled and empty respectively) of 10 μM MBP-PLS(WT) (B, cirlces) and MBP-PLS(C6S/C17S) (C, triangles) upon titration with Mn(II) (recorded anaerobically at pH 7.0, n=3, replicates 1-3 shown in red, green and blue respectively). D, compilation of A_{325} mean binding isotherms for MBP-PLS(WT) and MBP-PLS(C6S/C17S). All error bars represent 1 standard deviation either side of replicate mean.

3.2.5 Fe(II) binding properties of PLS

To investigate the Fe(II) binding properties of PLS, and hence if PLS could feasibly bind Fe(II) within the plant cytosol, initially, MBP-PLS(WT) was competed with the Fe(II) binding probe 4-(2-thiazolylazo)-resorcinol (TAR) for Fe(II) (Figure 3.15). Upon titration with Fe(II), the formation of $TAR_2Fe(II)$ was spectrally observed by absorption at 720 nM where $\varepsilon_{720\ nm} = 1.956 \times 10^3\ M^{-1}\ cm^{-1}$ (Young et al., 2021). In the absence of protein, 20 μM TAR, when titrated with Fe(II), responds at 720 nm until saturation point at ~10 μM Fe(II) whereafter no further absorption increase is observed. In the presence of either 20 μM MBP-PLS(WT) or 20 μM MBP-PLS(C6S/C17S), the probe responds to Fe(II) almost identically. These results show that neither the WT or double cysteine mutant can withhold Fe(II) tightly enough from the probe TAR under these conditions.

To further investigate the possibility of Fe(II) binding, MBP-PLS(WT) and MBP-PLS(C6S/C17S) were competed with MF-2 for Fe(II) (Figure 3.16). Upon binding Fe(II), absorbance change at 325 nm was monitored to report on the formation of the MF-2Fe(II) complex. When 20 μM MBP-PLS(WT) and 10 μM MF-2 were titrated with Fe(II), MBP-PLS(WT) withholds very little Fe(II) from MF-2 when compared to the titration in the absence of protein, suggesting a comparatively weak Fe(II)-binding on the MBP-PLS(WT) protein. The titration was then repeated with the double mutant MBP-PLS(C6S/C17S), in place of the WT protein, to investigate if the metal-binding observed was dependent on the cysteine residues 6 and 17. Upon titration of the MBP-PLS(C6S/C17S) and MF-2 with Fe(II), the protein withheld very little Fe(II) from MF-2 when compared to the control titration in the absence of protein.

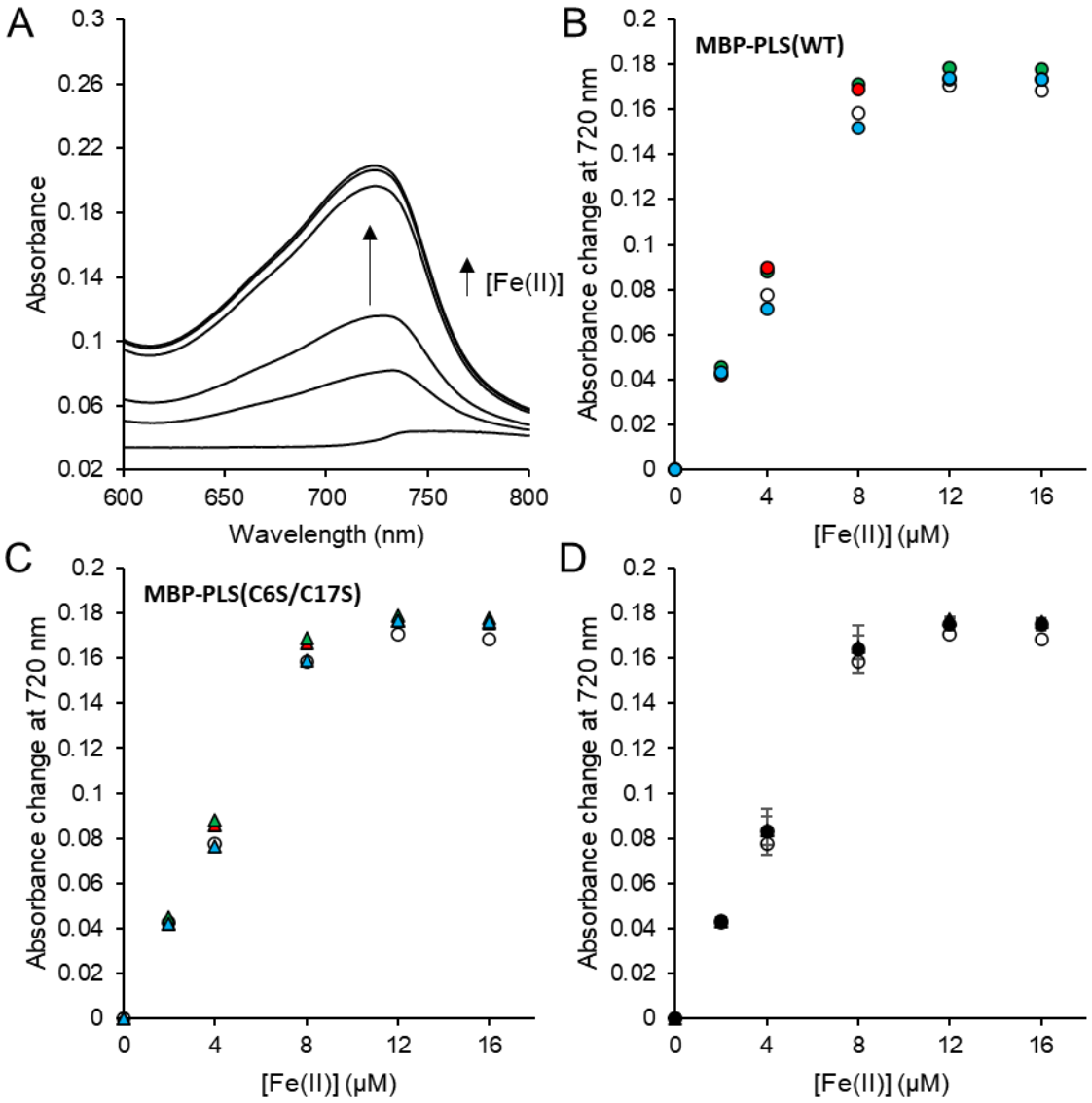

Figure 3.15, MBP-PLS Fe(II) binding titration against TAR. A, UV-vis spectra of TAR (20 μM) upon titration with $Fe(II)Cl_2$ to saturation (recorded anaerobically at pH 7.0). B-C, $A_{720\ nm}$ binding isotherms of TAR (20 μM) in the presence and absence (filled and empty respectively) of 20 μM MBP-PLS(WT) (B, cirlces) and MBP-PLS(C6S/C17S) (C, triangles) upon titration with Fe(II) (recorded anaerobically at pH 7.0, n=3, replicates 1-3 shown in red, green and blue respectively). D, compilation of $A_{720\ nm}$ mean binding isotherms for MBP-PLS(WT) and MBP-PLS(C6S/C17S). Error bars represent 1 standard deviation either side of replicate mean.

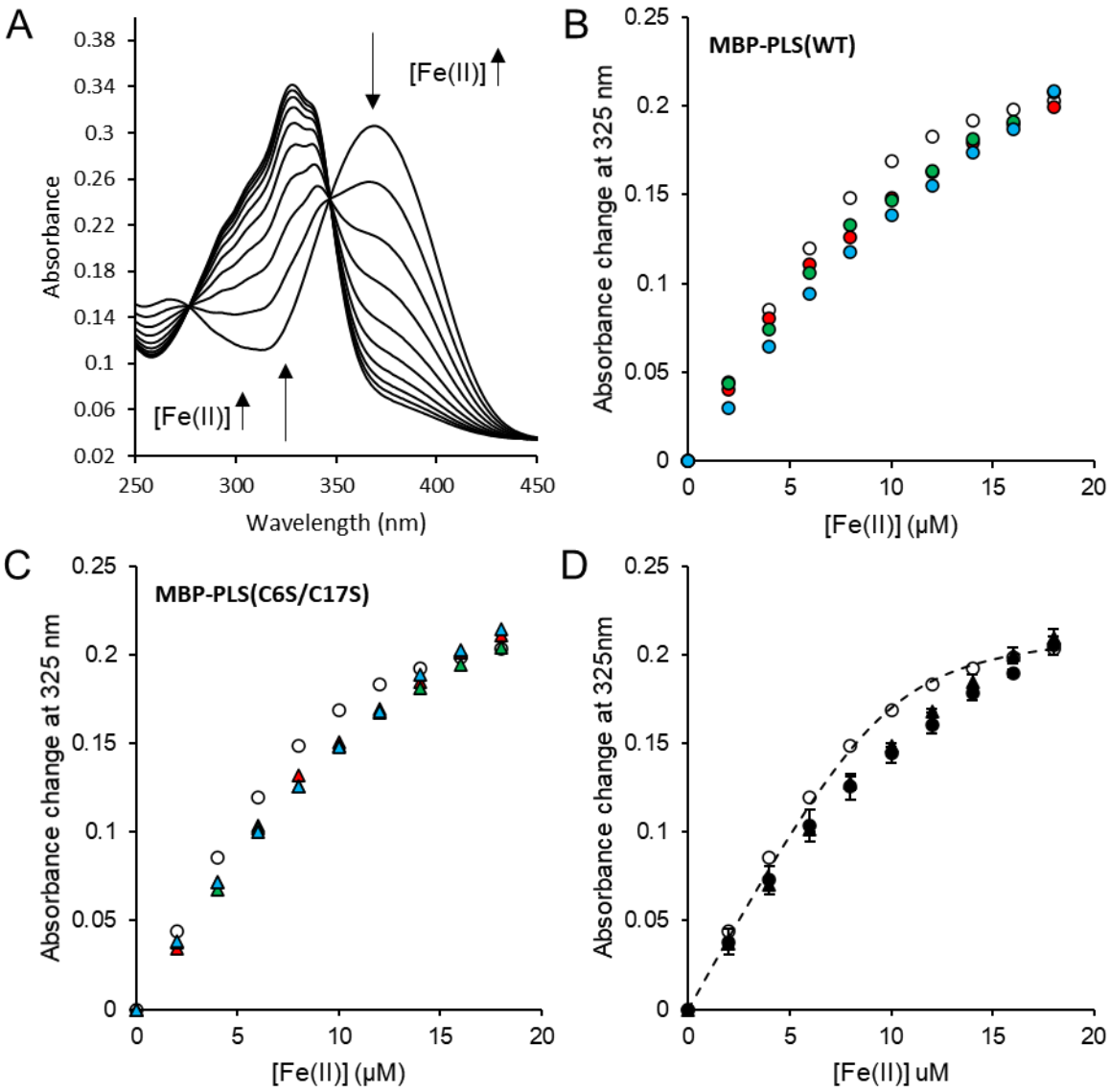

Figure 3.16, MBP-PLS Fe(II) binding titration against MF-2. A, UV-vis spectra of MF-2 (10 μM) upon titration with Fe(II) to saturation (recorded anaerobically at pH 7.0). B-C, $A_{325\ nm}$ binding isotherms of MF-2 (10 μM) in the presence and absence (filled and empty respectively) of 20 μM MBP-PLS(WT) (B, circles) and MBP-PLS(C6S/C17S) (C, triangles) upon titration with Mn(II) (recorded anaerobically at pH 7.0, n=3, replicates 1-3 shown in red, green and blue respectively). D, compilation of $A_{325\ nm}$ mean binding isotherms for MBP-PLS(WT) and MBP-PLS(C6S/C17S). All error bars represent 1 standard deviation either side of replicate mean.

When the WT and double mutant isotherms are compared, there appears to be negligible difference in metal partitioning between protein and probe, implying this weak Fe(II) interaction is independent of the two cysteines residues 6 and 17. This suggests that any binding of Fe(II) to PLS is weak, does not use the cysteine residues on PLS and it is likely the observed weak binding event might be to the MBP.

It was noted that in the absence of protein, the probe responds non-stoichiometrically (like the case of Mn(II)-binding). When fitting the experimental control data using Dynafit (Kuzmič, 2009), the apparent MF-2 Fe(II) K_d of 6.2 x 10^{-7} M appears to deviate from the literature value of 5.3 x 10^{-6} (Osman et al., 2019). This literature value however, was observed under 500 mM NaCl conditions, so it was postulated that the high concentration of Cl^- ions could be adventitiously competing with MF-2 for Fe(II). The affinity of MF-2 for Fe(II) was hence experimentally calculated under 50 mM NaCl conditions to match those conditions in the control titration and validate it's use in calculations. An experiment was designed using the probe nitrilotriacetic acid (NTA) which has a known K_d Fe(II) of 6.63 x 10^{-7} at pH 7.0 (Xiao & Wedd, 2010) to compete with MF-2 for Fe(II) and obtain an accurate affinity of MF-2 for Fe(II) under these conditions. Three titration were carried out at three different ratios of MF-2:Fe(II), chosen to be at points in the direct MF-2 titration which were still linear (i.e., when MF-2 is still in excess) and NTA was titrated in (Figure 3.17). The extraction of Fe(II) from the MF-2 Fe(II) was measured, at equilibrium, by absorbance change at 366 nm, reporting on the decrease in MF-2Fe(II) concentration and increase of NTAFe(II). The MF-2Fe(II) K_d was calculated from first principles using the data from Figure 3.17, as outlined in the equation scheme below.

Equation 3.9: MF-2Fe(II) ⇌ MF-2 + Fe(II)
Where: Keq1 = MF-2Fe(II) K_d

Equation 3.10: NTA + Fe(II) ⇌ NTAFe(II)
Where: Keq2 = K_a for NTAFe(II)

Equation 3.11: MF-2Fe(II) + NTA ⇌ NTAFe(II) + MF-2
Where: Keq3 = ([NTAFe(II)]*[MF-2])/([NTA]*[MF-2Fe(II)]))

Equation 3.12: Keq 3 = Keq1 x Keq2

For each titration data point, K_{eq3} can be calculated by populating equation 3.11. K_{eq1} (K_d MF-2Fe(II)) can then be calculated using K_{eq3} and K_{eq2} as in equation 3.12.

The average K_d MF-2Fe(II) from the three titrations was calculated as 5.34×10^{-6} M^{-1}. As this value agrees with the literature value cited earlier, it was concluded that the high concentration of Cl^- ions were not problematic and this value was used for any further calculations requiring the MF-2Fe(II) K_d.

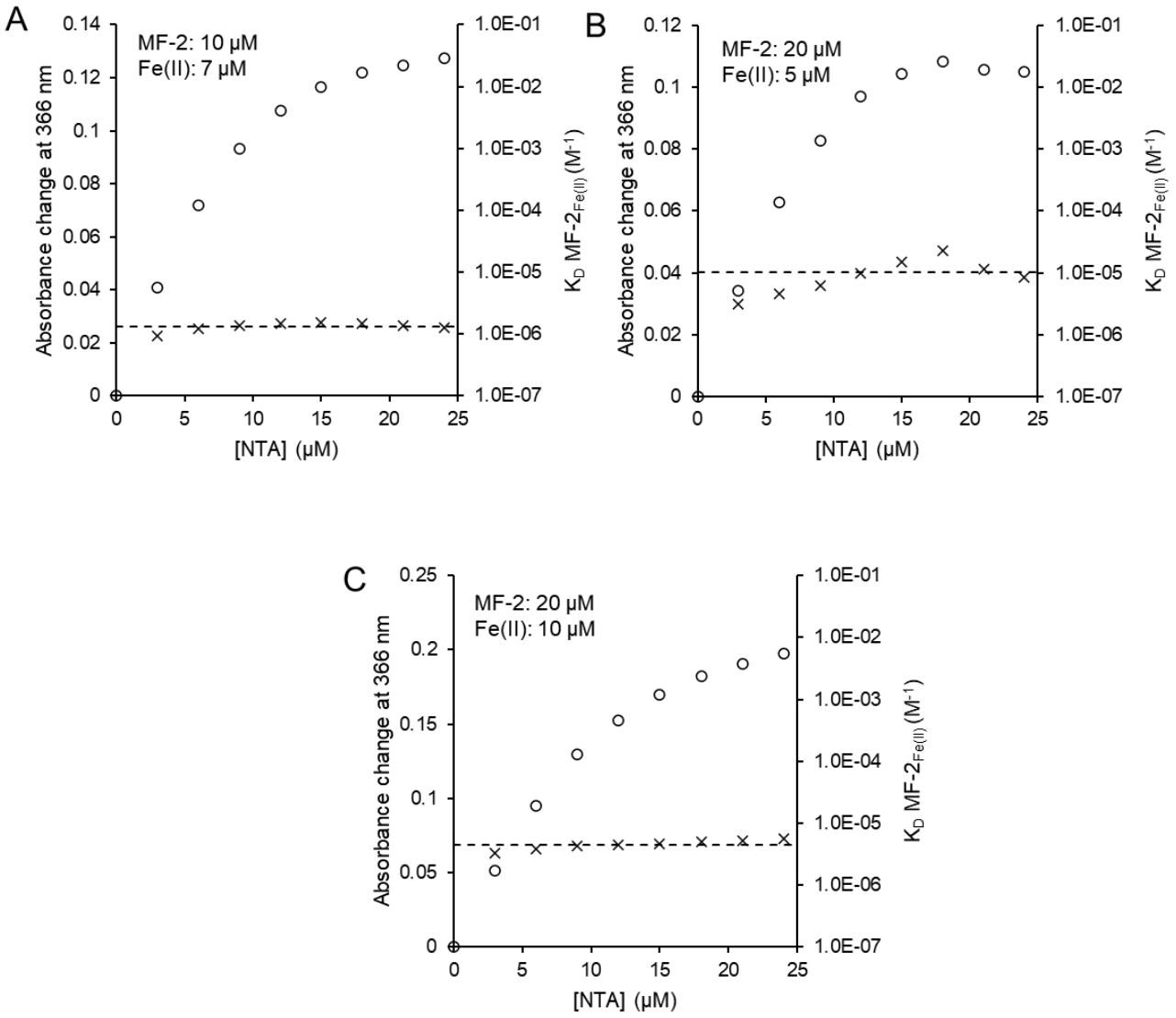

Figure 3.17 Experimental determination of K_d MF-2Fe(II) Absorbance change at 366 nm upon titration of MF-2-Fe(II) with the probe NTA (empty circles, primary *y-axis*). Experiment triplicated using three different molar ratios MF-2:Fe(II) (A-C, inset). Crosses (secondary *y-axis*) represent calculated K_d of MF-2Fe(II) for each titration datapoint, dotted lines represent average calculated K_d of MF-2Fe(II) for each titration. Average K_d for three replicates = 5.3×10^{-6} M^{-1}.

This chapter has shown that PLS binds Cu(I) in a 2:1 PLS:metal stoichiometry with a β_2 affinity of 3.79×10^{19} M^{-2} and Zn(II) in a 2:1 stoichiometry with a β_2 affinity of 3.76×10^{12} M^{-2}, both metals dependent on both cysteines C6 and C17. It was also shown that the interaction with various other metals including Ni(II), Fe(II) and Mn(II) are weak and independent of C6 and C17 residues. The affinities of PLS for Cu(I) and Zn(II) in particular have significant use when applied to novel calculators, allowing the simulation of PLS metal-occupancy given the availability of these two metals. This idea is further explored in Chapter 6.

Chapter 4. The metal binding properties of the *Arabidopsis thaliana* protein Atx1

In order to estimate the availability of Cu(I) within the cytosol of *Arabidopsis,* and hence model the metalation of PLS within this compartment, the metal binding properties of the cytosolic Cu(I)-binding metalloprotein Atx1 was measured (as set out in Section 1.3.3). By examining the estimated metalation profile of Atx1 as a function of intracellular available Cu(I), an estimate of the Cu(I) availability in the cytosol of *Arabidopsis* can be made.

4.1 Purification of *A. thaliana* Atx1

Atx1 was overexpressed in *E. coli* as a recombinant, tag-free protein and purified based on its size and charge. Crude cell lysate was fractionated by size exclusion chromatography (in metal-free buffer) and the purest Atx1-containing fractions pooled and incubated overnight in buffer containing 10 mM DTT (Figure 4.1). DTT incubation provides a reducing environment to reduce thiol moieties on the cysteine residues proposed to co-ordinate metal and had the added benefit of ensuring the protein remained *apo*-, due to the metal binding properties of the molecule (Xiao et al., 2011). The pooled sample was then separated from contaminating nucleotides by anion exchange using a DEAE column and the material was then concentrated from 30 mL to 0.5 mL using a centrifugal concentrator (Centricon) (Figure 4.1). Following buffer exchange into O_2 free buffer (no DTT), protein was routinely analysed for purity by SDS-PAGE (Figure 4.1), quantified and checked to be *apo*- by ICP-MS before experimentation as described in methods 2.5.2

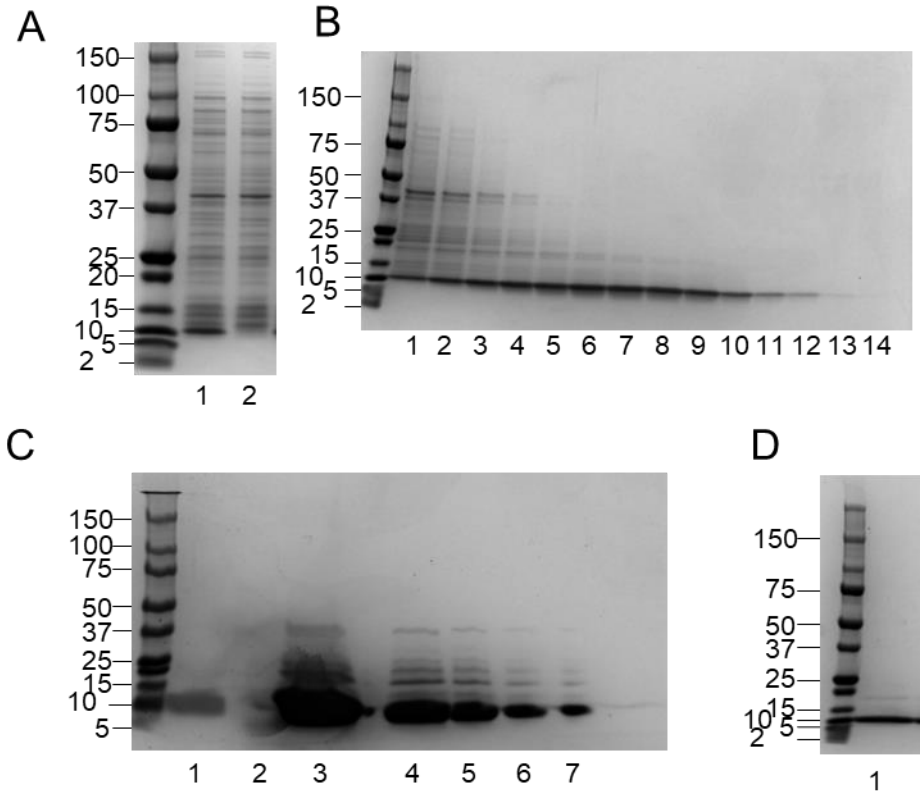

Figure 4.1, Purification of recombinant Atx1. A, SDS-PAGE analysis of soluble crude lysate from 1 L of cell overexpressing pET29a(Atx1) (lane 1) and pET29a(Empty) (lane 2). B, SDS-PAGE analysis of fractions 36-49 (lanes 1-14 respectively) collected from size exclusion chromatography when crude lysate from "A" (lane 1) was fractionated. Fractions are 5 mL, and lanes 5-9 pooled. C, SDS-PAGE analysis of the Centricon concentration step. Lane 1 shows pooled material (30 mL), lane 2 shows flow-through material from the column, lane 3 shows retained concentrated material (0.5 mL) and lanes 4-7 show a 2:1 dilution series in sample 3. D, SDS-PAGE analysis of Fraction 4 from concentrated material eluted from PD-10 desalting column into anaerobic buffer to be used in experiments.

4.2 Biochemical characterisation of Atx1

4.2.1 Determination of Cu(I) binding stoichiometry

To investigate the Cu(I) stoichiometry of Atx1, Atx1 was titrated against BCA with Cu(I) It was predicted that by competing BCA with Atx1 for Cu(I), Atx1 would outcompete the probe for metal, stoichiometrically. Upon BCA metal-binding, a spectral feature at 563 nm can be monitored, reporting on the Cu(I) metalation and formation of the $BCA_2Cu(I)$ complex.

To determine the stoichiometry of Atx1 for Cu(I), BCA was titrated with increasing amounts of Cu(I) and UV-vis difference spectra were recorded after each addition of Cu(I) came to equilibrium (Figure 4.2). The spectral response at 562 nm increased upon titration of 20 µM BCA with Cu(I), the feature saturated at ~10 µM Cu(I) as expected a probe that binds Cu(I) in a 2:1 stoichiometry. In the presence of 20 µM Atx1, the spectral response at 562 nm is absent until the addition of ~20 µM Cu(I), implying 20 µM Atx1 withholds 20 µM Cu(I) from BCA. Atx1 hence is predicted to bind Cu(I) with an affinity tight enough to outcompete the probe, in a 1:1 stoichiometry.

The titration was repeated where the BCA was substituted for the tighter Cu(I)-binding probe Bathocuproine sulfonate (BCS) (Figure 4.3). Upon BCS metal-binding, a spectral feature at 483 nm were monitored, reporting on the Cu(I) metalation and formation of the $BCS_2Cu(I)$ complex. Absorption values at 483 nm were converted into $[BCS_2Cu(I)]$ concentration values by applying the extinction coefficient ε_{483} = 13 300 M^{-1} cm^{-1}

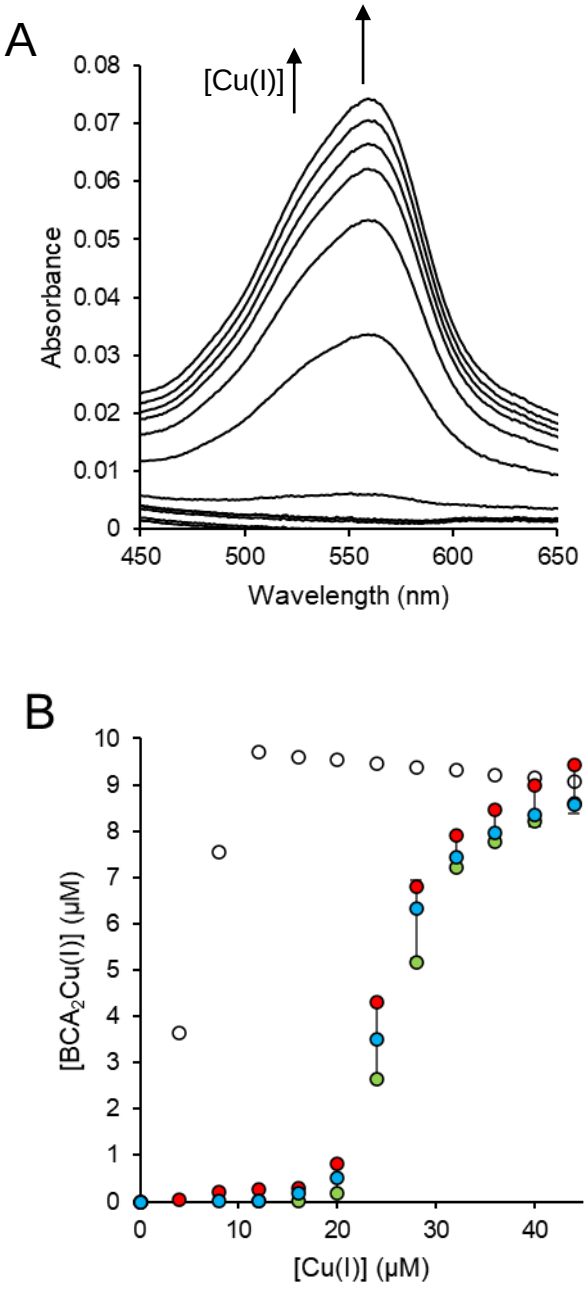

Figure 4.2, Estimation of Cu(I)-binding stoichiometry of Atx1 by competition with BCA. A. Apo-subtracted UV-vis difference spectra of Atx1 (20 μM), BCA (20 μM) upon titration with $CuSO_4$ (recorded anaerobically at pH 7.0) in the presence of 1 mM NH_2OH (replicate 1 of 3 shown as representative). B. Binding isotherm of A_{562} feature shown in 'A', error bars represent replicate mean +/- 1 standard deviation n=3 (shown). Replicates 1-3 shown in red, green and blue filled circles respectively, empty circles represent the equivalent titration in the absence of Atx1.

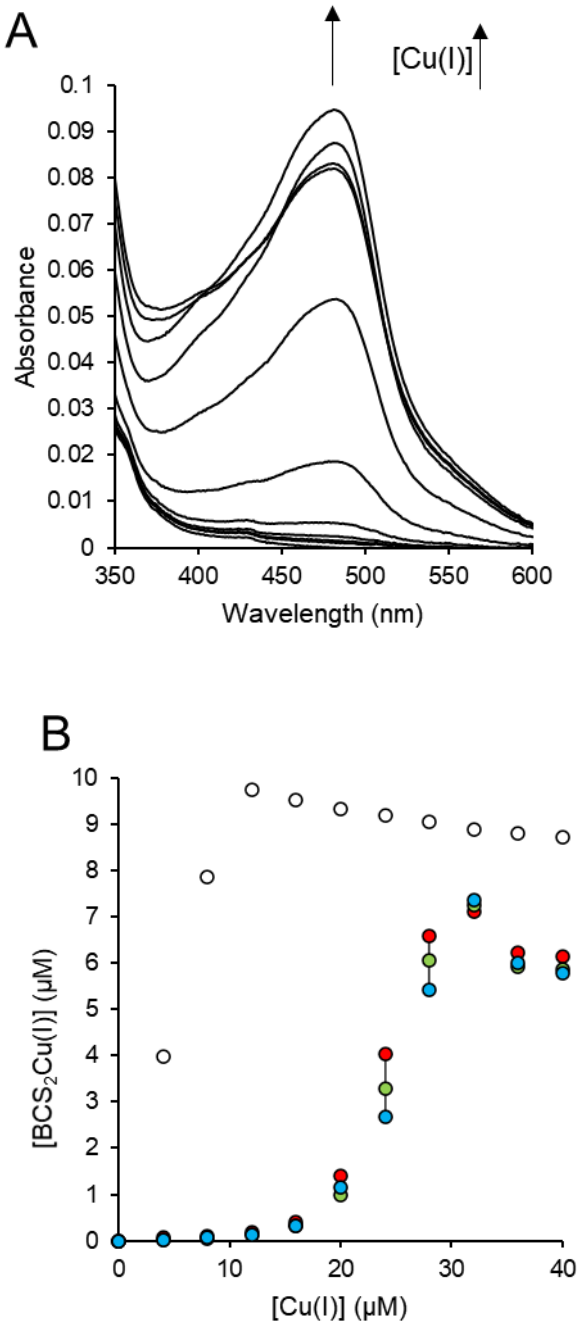

Figure 4.3, Estimation of Cu(I)-binding stoichiometry of Atx1 by competition with BCS. A. Apo-subtracted UV-vis difference spectra of Atx1 (20 μM), BCS (20 μM) upon titration with $CuSO_4$ (recorded anaerobically at pH7.0) in the presence of 1 mM NH_2OH (replicate 1 of 3 shown as representative). B. Binding isotherm of $A_{483\ nm}$ feature shown in 'A', error bars represent replicate mean +/- 1 standard deviation n=3 (shown). Replicates 1-3 shown in red, green and blue filled circles respectively, empty circles represent the equivalent titration in the absence of Atx1.

(Xiao et al., 2004) to the Beer-lambert law. The tighter binding probe BCS was substituted for BCA with the aim to partition more metal from the protein and achieve more even partitioning between protein and probe so as to allow a more accurate calculation of the Cu(I) affinity of Atx1. However, on titration of 20 µM BCS and 20 µM Atx1 for Cu(I), again, Atx1 withholds ~1 equivalent of Cu(I) from the probe, implying a Cu(I) binding stoichiometry of 1:1.

It should be noted that, in the presence of Atx1, the response of the probe did not reach the expected saturation point of 10 µM $BCS_2Cu(I)$ as in the case where Atx1 is absent. It could be that, in addition to the tight stoichiometric site, Atx1 has one extra (weak binding) site which results in the partial formation of a ternary complex between the probe and protein, coordinated by copper. Events like this have been previously documented between probes that form 2:1 complexes with their metals and metalloproteins (Young et al., 2018) and it has also been highlighted that any stable ternary complex formation can prevent accurate affinity measurements (Young & Xiao, 2021). As the ternary complex formation is expected to be a result of an additional weaker binding site however, on investigating the tighter 1:1 binding site, this additional weaker ternary site is not predicted to bind under those conditions and hence not interfere with characterisation of the tighter site.

4.2.2 Determination of Cu(I) binding affinity

To characterise the tight 1:1 Cu(I) binding site identified on Atx1, Cu(I) titrations were repeated using an excess of BCS to Atx1 (Figures 4.4, to 4.7). Increasing the [BCS]:[Atx1] allowed greater dissociation of Cu(I) from Atx1, thus allowing a more accurate calculation of the position of the equilibrium throughout the titration. An aliquot of 20 μM Atx1 was titrated against 500, 250, 150 and 50 μM BCS for Cu(I). For each titration, a Cu(I) affinity for Atx1 was calculated (Table 4.1) via equations from first principles using the equilibrium concentrations of $BCS_2Cu(I)$ and Atx1Cu(I) determined using the extinction coefficient of $BCS_2Cu(I)$ ε_{483} = 13 300 M^{-1} cm^{-1} (Xiao et al., 2004) and literature value for $BCS_2Cu(I)$ β_2 value of 7.94 x 10^{19} M^{-2} (Xiao et al., 2011), as below:

Equilibrium 1: $Atx1 + Cu(I) \rightleftharpoons Atx1Cu(I)$

where $K_{eq1} = 1/K_{d\ (Atx1Cu(I))}$ *(4.1)*

Equilibrium 2: $BCS_2Cu(I) \rightleftharpoons 2BCS + Cu(I)$

where $K_{eq2} = 1/\beta_2(BCS_2Cu(I))$ *(4.2)*

Equilibrium 3: $BCS_2Cu(I) + Atx1 \rightleftharpoons Atx1Cu(I) + 2BCS$

where $K_{eq3} = [Atx1Cu(I)] * [BCS]^2 / [BCS_2Cu(I)] * [Atx1]$ *(4.3)*

and $K_{eq1} = K_{eq3} / K_{eq2}$ *(4.4)*

For each titration data point, K_{eq3} can be calculated by populating equation 4.3. K_{eq1} can then be calculated using K_{eq3} and K_{eq2} in equation 4.4.

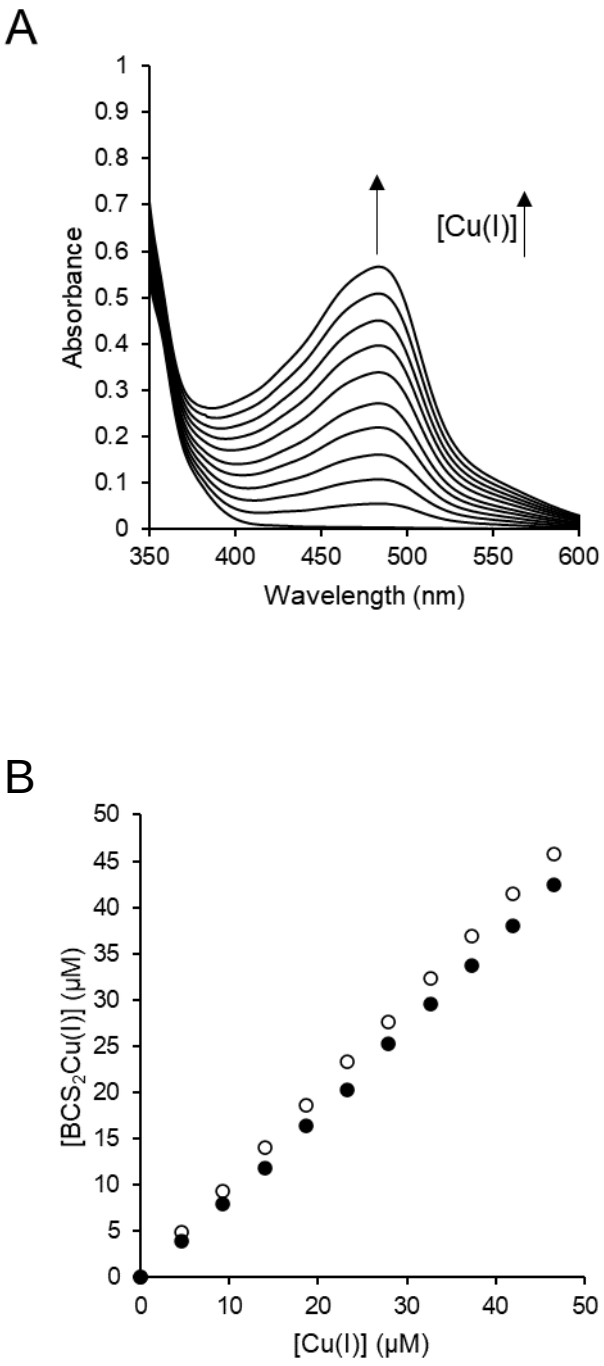

Figure 4.4, Estimation of Cu(I) Affinity of Atx1 by competition with 500 μM BCS. A. Apo-subtracted UV-vis difference spectra of Atx1 (20 μM) and BCS (500 μM) upon titration with $CuSO_4$ (recorded anaerobically at pH 7.0) in the presence of 1 mM NH_2OH (n=1). B. Binding isotherm of A_{483} feature shown in 'A' (filled circles) and binding isotherm of a control titration of 500 μM BCS in the absence of Atx1 (empty circles).

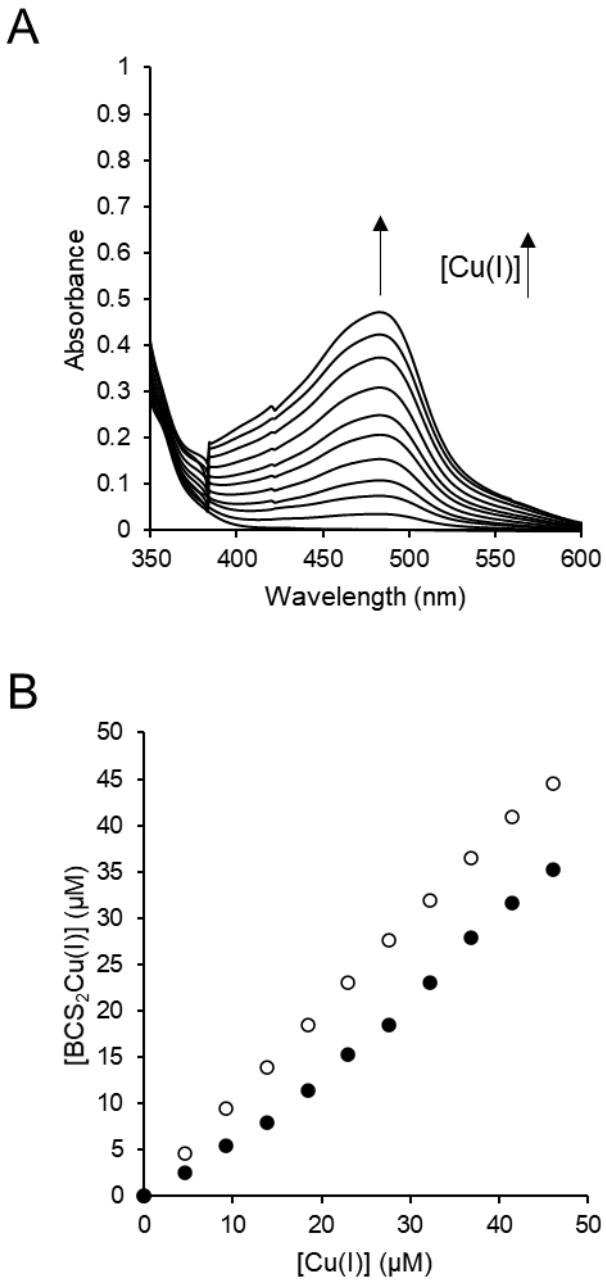

Figure 4.5, Estimation of Cu(I) Affinity of Atx1 by competition with 250 μM BCS. A. Apo-subtracted UV-vis difference spectra of Atx1 (20 μM), BCS (250 μM) upon titration with $CuSO_4$ (recorded anaerobically at pH 7.0) in the presence of 1 mM NH_2OH (n=1). B. Binding isotherm of $A_{483\ nm}$ feature shown in 'A' (filled circles) and binding isotherm of a control titration of 250 μM BCS in the absence of Atx1 (empty circles).

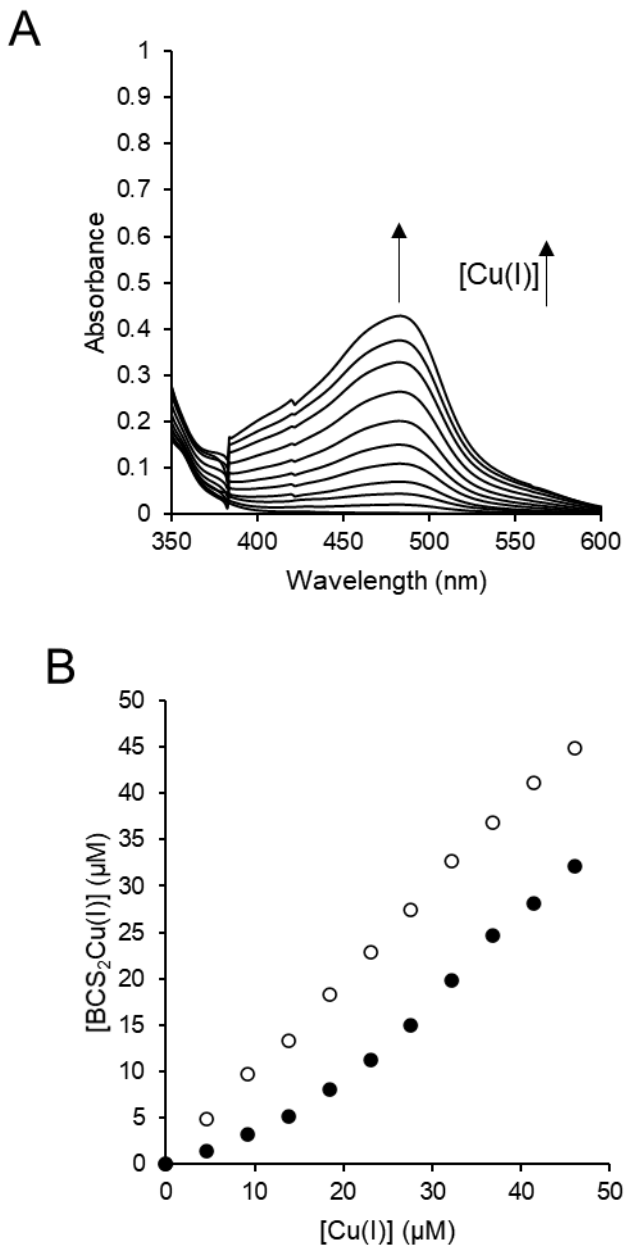

Figure 4.6, Estimation of Cu(I) Affinity of Atx1 by competition with 150 μM BCS. A. Apo-subtracted UV-vis difference spectra of Atx1 (20 μM), BCS (150 μM) upon titration with $CuSO_4$ (recorded anaerobically at pH 7.0) in the presence of 1 mM NH_4OH (n=1). B. Binding isotherm of $A_{483\ nm}$ feature shown in 'A' (filled circles) and binding isotherm of a control titration of 150 μM BCS in the absence of Atx1 (empty circles).

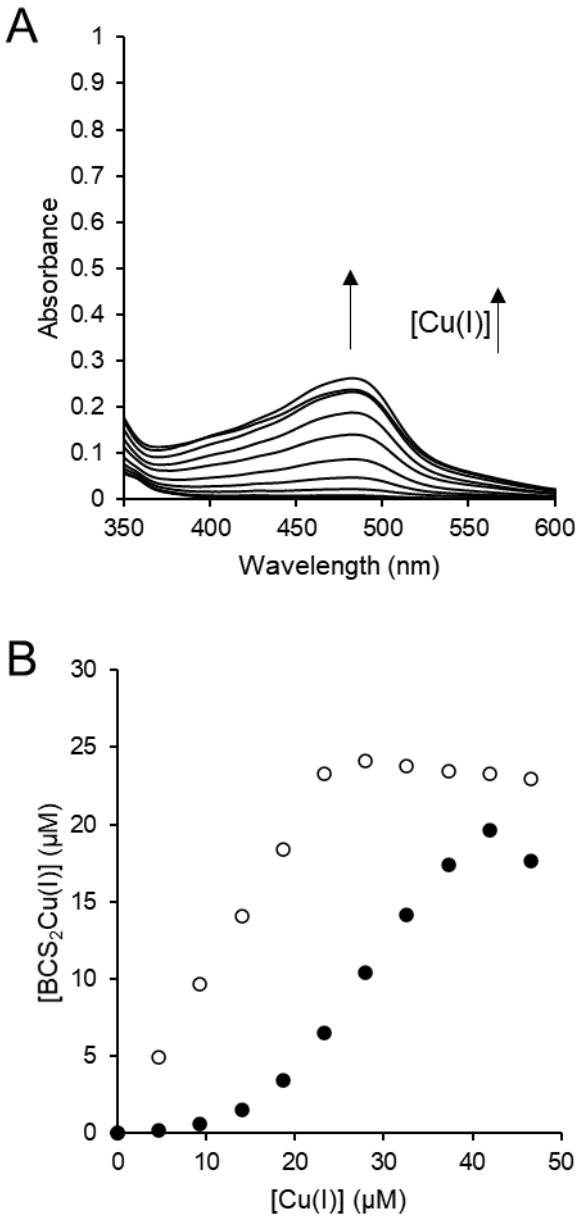

Figure 4.7, Estimation of Cu(I) Affinity of Atx1 by competition with 50 μM BCS. A. Apo-subtracted UV-vis difference spectra of Atx1 (20 μM), BCA (50 μM) upon titration with $CuSO_4$ (recorded anaerobically at pH 7.0) in the presence of 1 mM NH_2OH (n=1). B. Binding isotherm of $A_{483\ nm}$ feature shown in 'A' (filled circles) and binding isotherm of a control titration of 50 μM BCS in the absence of Atx1 (empty circles).

Table 4.1, Affinity measurements for Atx1Cu(I) interaction. Dissociation constants and average (K_d) calculated from competition titration of Atx1 with BCS for Cu(I).

[BCS] (μM)	[Atx1] (μM)	Log(K_d)	K_d (M)
500	20	-17.21	6.14×10^{-18}
250	20	-17.29	5.10×10^{-18}
150	20	-17.31	4.83×10^{-18}
50	20	-17.23	5.78×10^{-18}
		Average	$5.47 (\pm 0.6) \times 10^{-18}$

4.2.3 Determination of Zn(II) binding stoichiometry and affinity

The Zn(II) binding stoichiometry and affinity of Atx1 was determined by competition with the metal-binding probe Mag-fura-2 (MF-2). Zn(II) binding to MF-2 was observed by monitoring two spectral features on addition of Zn(II): increased absorption at 325 nm and decreased absorption at 366 nm. On titration of 20 μM Atx1 and 20 μM MF-2 with Zn(II), Zn(II) partitions between Atx1 and MF-2. From the initial titration (Figure 4.8) where equimolar concentrations of Atx1 and MF-2 were titrated, it is unclear at what concentration of Zn(II) the protein/probe solution saturates. Saturation at 40 μM Zn(II) would imply Atx1 bound Zn(II) in a 1:1 stoichiometry, however, a 30 μM Zn(II) saturation would imply Atx1 bound Zn(II) in a 2:1 stoichiometry. The binding isotherm for 325 nm and 366 nm data was simultaneously fit using the software package 'Dynafit' (Kuzmič, 2009) to obtain a Zn(II) affinity (Figure 4.9). Initial fitting using a model that describes the Atx1 binding as a 1:1 stoichiometry (supplementary Figure 8.12) provides a poor fit to the data due to the slight sigmoidal shape to the isotherm. The model was then altered to describe Atx1 Zn(II) binding as two events where the Atx1 can then form a 2:1 complex in addition to the 1:1 complex (as is the case for the cyanobacterial Atx1 Zn(II) affinity (Badarau, Baslé, Firbank, & Dennison, 2013)) (Figure 4.9). The altered model (Supplementary Figure 8.13) was a better fit to the experimental data and the K_d for these two binding events are reported in table 4.2.

The formation of an Zn(II)$Atx1_2$ species was investigated further by repeating the titration with 40 μM Atx1 so as the saturation point could be determined with better resolution (Figure 4.11). On titration of 40 μM Atx1 and 20 μM MF-2 with Zn(II), the metal partitions between both species. In the presence of Atx1, saturation at 60 μM Zn(II) would imply Atx1 binds Zn(II) in a 1:1 stoichiometry, however the binding isotherm (Figure 4.10) appears to saturate at ~40 μM Zn(II), implying a 2:1 Atx1 Zn(II) binding stoichiometry. When the isotherms are modelled (Figure 4.11), the 1:1 model now provides a poor fit to

the data. The altered model, which allows an additional 2:1 binding event, was again a better fit to the experimental data and the K_d for these two binding events, described as the dissociation constants for the equations “4.6” and “4.7” in Figure 4.9, are reported in Table 4.2.

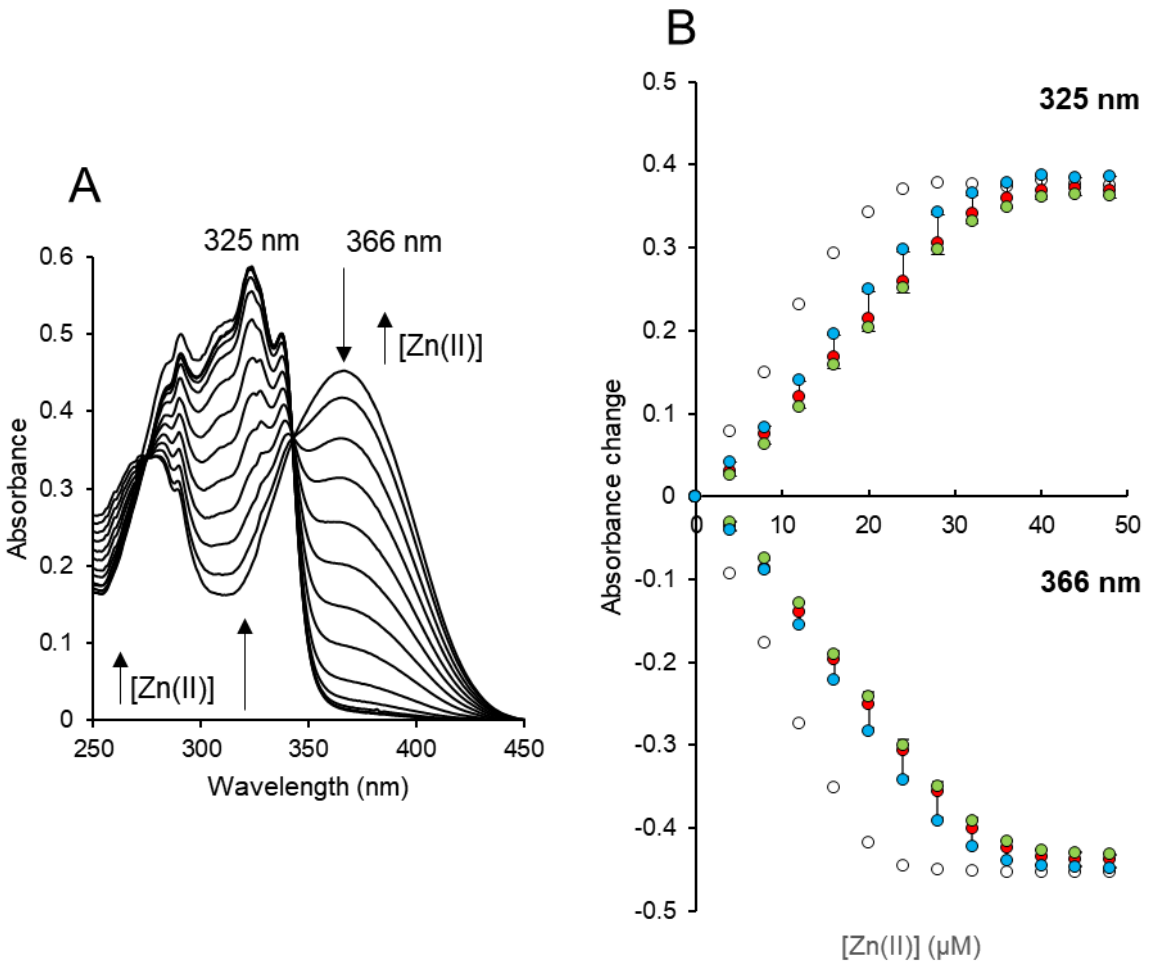

Figure 4.8, Estimation of Zn(II) Affinity of 20 μM Atx1 by competition with Mag-fura-2. A. Apo-subtracted UV-vis difference spectra of Atx1 (20 μM) and MF-2 (20 μM) upon titration with $ZnSO_4$ (recorded anaerobically at pH 7.0) (n=3, replicate 1 shown). B. Binding isotherms of $A_{325\ nm}$ and $A_{366\ nm}$ features shown in 'A' (filled circles, replicates 1-3 in red, green and blue respectively) and control titration of 20 μM MF-2 in the absence of Atx1 (empty circles).Error bars represent replicate mean value +/- 1 standard deviation.

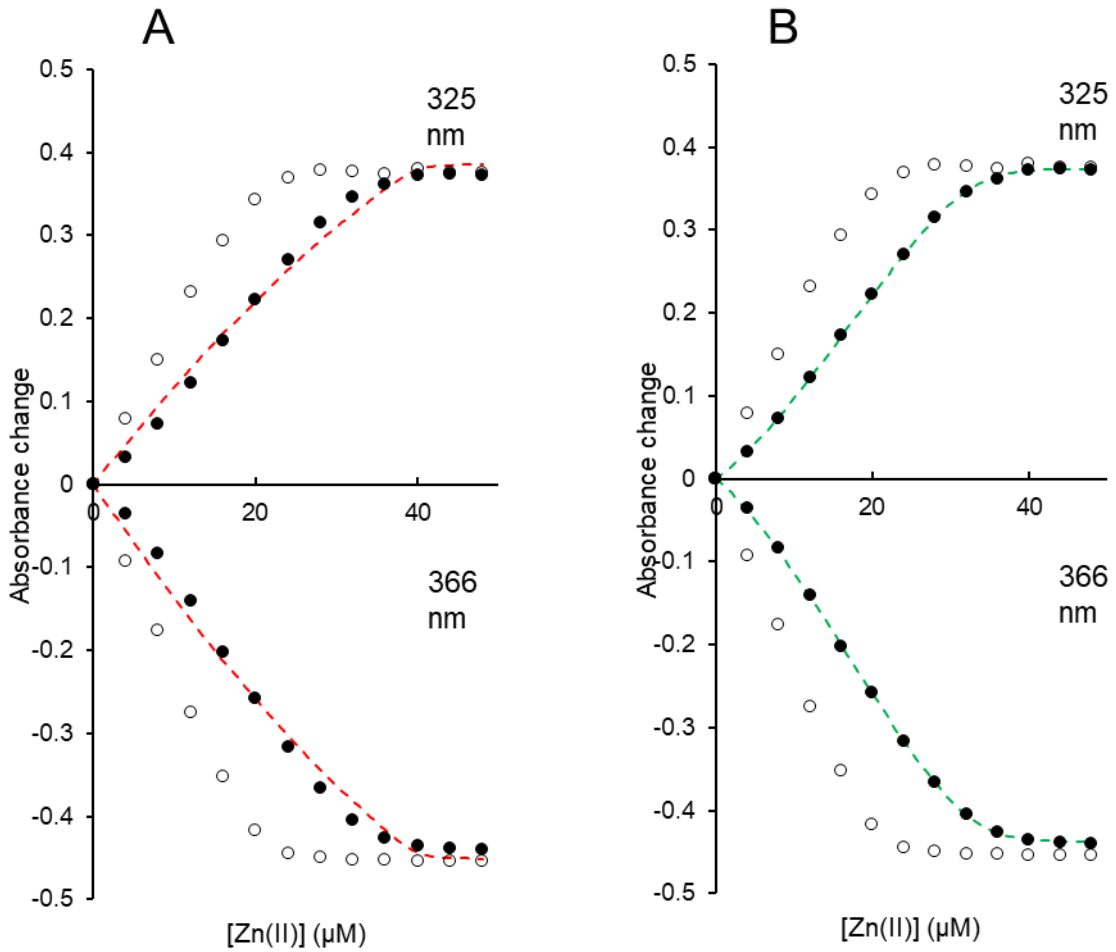

C

Equation 4.5: MF-2 + Zn(II) ⇌ MF-2Zn(II)

Equation 4.6: Atx1 + Zn(II) ⇌ Atx1Zn(II)

Equation 4.7: Atx1Zn(II) + Atx1 ⇌ $Atx1_2Zn(II)$

Figure 4.9 Modelling the Zn(II) Affinity of Atx1. A. $A_{325\ nm}$ and $A_{366\ nm}$ mean (n=3) binding isotherms (filled circles) for Atx1 (20 μM) and MF-2 (20 μM) upon titration with $ZnSO_4$ (recorded anaerobically at pH 7.0) (n=3). Control titration of 20 μM MF-2 in the absence of Atx1 included (empty circles). Dashed lines represent models, fitted to $A_{325\ nm}$ and $A_{366\ nm}$ isotherms simultaneously in Dynafit, where Atx1 binds Zn(II) in a 1:1 stoichiometry (red) and where Atx1 is also able to bind Zn(II) in a 2:1 stoichiometry (green). C, equations describing the model represented by the dashed lines in panel B.

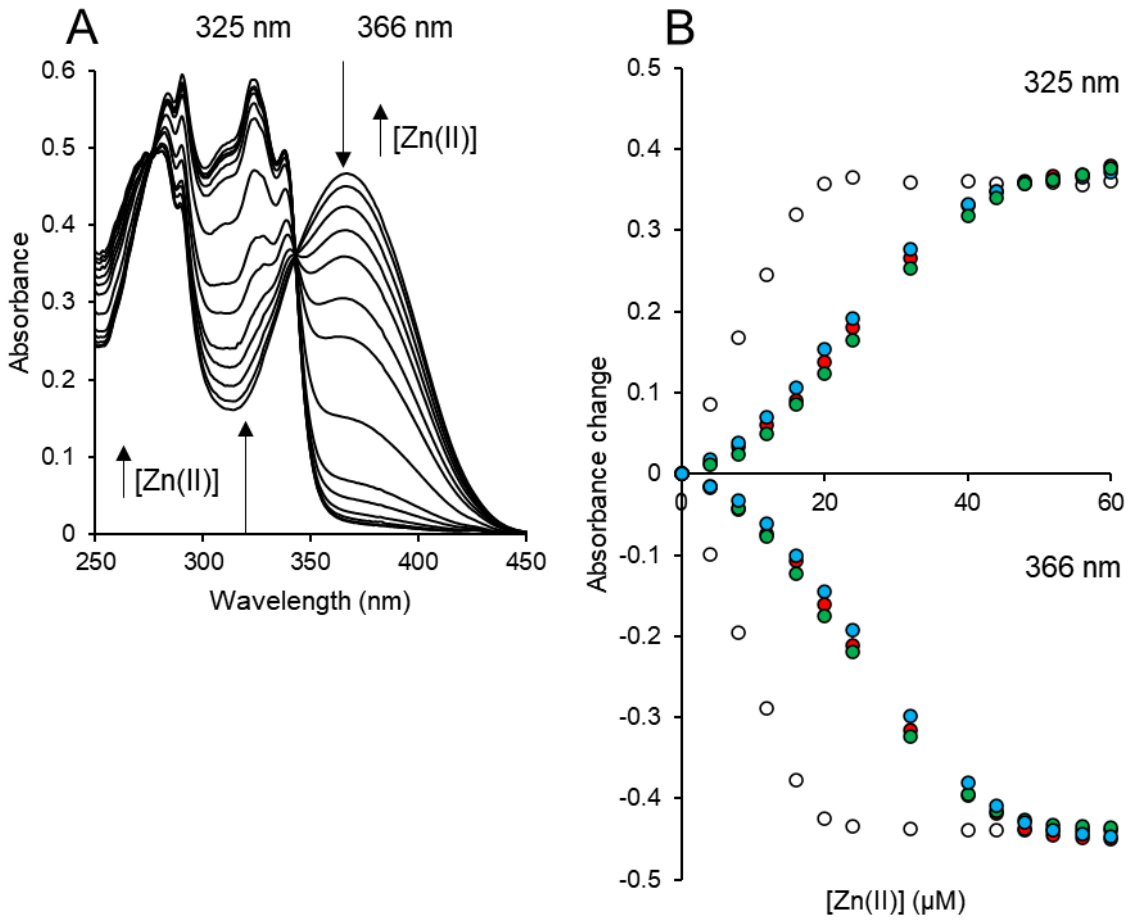

Figure 4.10, Estimation of Zn(II) Affinity of 40 μM Atx1 by competition with Mag-fura-2. A. Apo-subtracted UV-vis difference spectra of Atx1 (40 μM) and MF-2 (20 μM) upon titration with $ZnSO_4$ (recorded anaerobically at pH 7.0) (n=3, replicate 1 shown). B. Binding isotherms of $A_{325\ nm}$ and $A_{366\ nm}$ features shown in 'A' (filled circles, replicates 1-3 in red, green and blue respectively) and control titration of 20 μM MF-2 in the absence of Atx1 (empty circles). Error bars represent replicate mean value +/- 1 standard deviation.

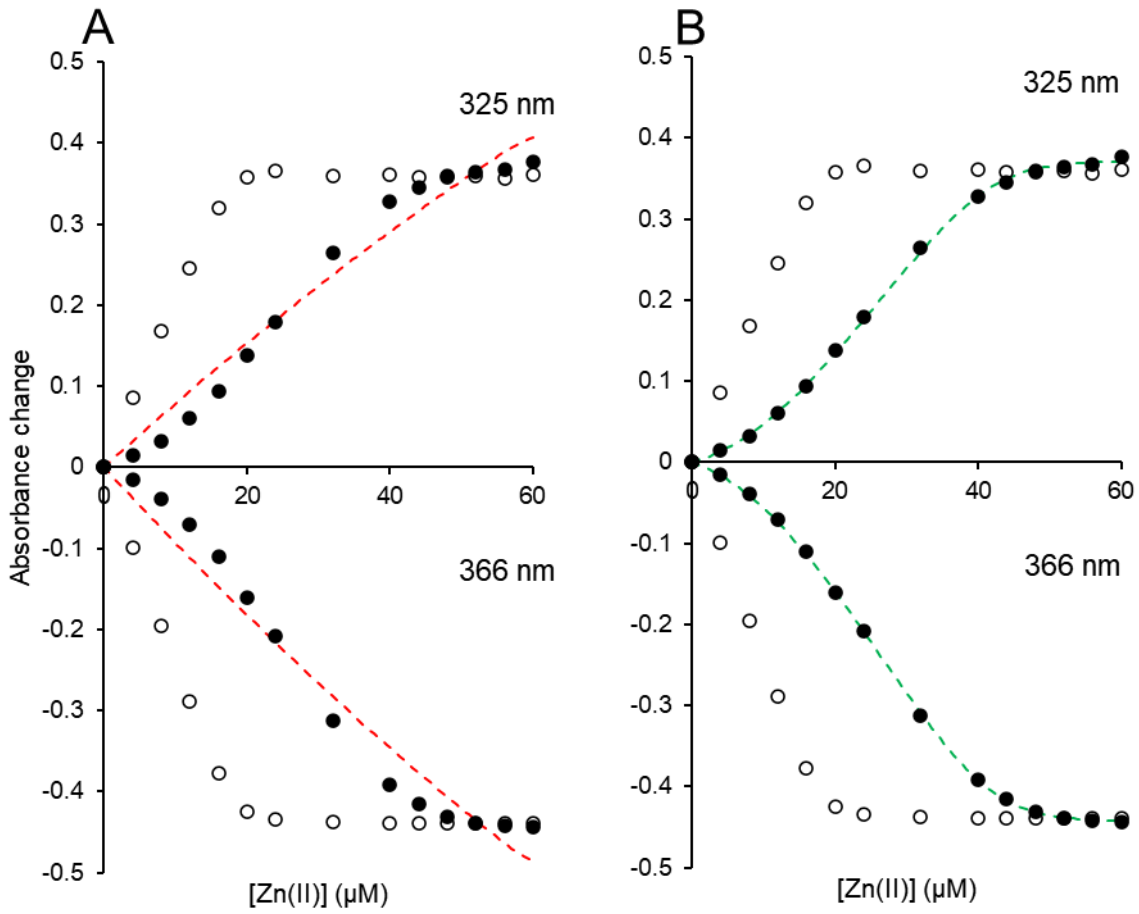

Figure 4.11, Modelling the Zn(II) Affinity of Atx1. A. $A_{325\ nm}$ and $A_{366\ nm}$ mean (n=3) binding isotherms (filled circles) for Atx1 (40 μM) and MF-2 (20 μM) upon titration with $ZnSO_4$ (recorded anaerobically at pH 7.0) (n=3). Control titration of 20 μM MF-2 in the absence of Atx1 included (empty circles). Dashed lines represent models, fitted to $A_{325\ nm}$ and $A_{366\ nm}$ isotherms simultaneously in Dynafit, where Atx1 binds Zn(II) in a 1:1 stoichiometry (red) and where Atx1 is also able to bind Zn(II) in a 2:1 stoichiometry (green).

Table 4.2, Affinity measurements for $Atx1_2Zn(II)$ interaction. Calculated dissociation constants and mean (K_d) for Atx1Zn(II) (Figure 4.9, *Equation 2*) and the dissociation of Atx1 from $Atx1_2Zn(II)$ (Figure 4.9, *Equation 3*). Mean shown for each dissociation event from two experiments carried out at 40 µM and 20 µM Atx1+/- 1 standard deviation.

	40 µM Atx1	20 µM Atx1	Average
K_{d2} *(equation 2)* (M)	8.03 $x10^{-8}$	6.20 $x10^{-8}$	7.12 (±1.3) $x10^{-8}$
K_{d3} *(equation 3)* (M)	3.75 $x10^{-6}$	4.44 $x10^{-6}$	4.09 (±0.5) $x10^{-6}$

4.3 In-vitro characterisation of Zn(II)-, Cu(I)- and *apo*-Atx1 by size exclusion chromatography.

To design an experiment to investigate the Zn(II)-metalation of Atx1, and to validate inclusion of the Zn(II)$Atx1_2$ complex in the modelling, a set of equations and methods were constructed which allow the calculation of the state of Atx1 (Zn(II)$Atx1_2$, Zn(II)Atx1 or Atx1) as a function of initial total Zn(II), and total Atx1 concentration *in-vitro*. These equations allow the prediction of [Zn(II)$Atx1_2$], [Zn(II)Atx1], $[Zn]_{free}$ and $[Atx1]_{free}$, as defined by the Zn(II)-binding model equations (Figure 4.9, C) when different concentrations of $Atx1_{total}$ and $Zn(II)_{total}$ are equilibrated *in-vitro* (Table 4.3). Equations are as follows: (where P represents Atx1)

$$P + Zn \rightleftharpoons ZnP$$

$$K_1 = [ZnP] / ([Zn][P]) \quad (4.8)$$

$$ZnP + P \rightleftharpoons ZnP_2$$

$$K_2 = [ZnP_2] / [ZnP][P] \quad (4.9)$$

$$\textit{Therefore: } [ZnP_2] / [ZnP] = K_2 [P] \quad (4.10)$$

$$Zn + 2P \rightleftharpoons [ZnP_2]$$

$$\beta_2 = [ZnP_2] / [P]^2 [Zn] = K_1 \times K_2 \quad (4.11)$$

$$[Zn]_{total} = [Zn] + [ZnP] + [ZnP_2] \quad (4.12)$$

Sub in rearranged *(1)* and *(4)*:

$$[Zn]_{total} = [Zn] + K_1[[Zn][P] + \beta_2[P]^2[Zn] \quad (4.13)$$

Hence:

$$[Zn] = [Zn]_{total} / (1 + K_1[P] + \beta_2[P]^2) \quad (4.14)$$

And:

$$[P]_{total} = [P] + K_1[Zn][P] + 2\ \beta_2[Zn][P]^2$$

So:

$$2\ \beta_2[Zn][P]^2 + [P](K_1[Zn] + 1) - [P]_{total} = 0 \quad (4.15)$$

Solve quadratic for [P]

$$[P] = \{-(K_1[Zn]+1)+Sqrt((K_1[Zn] + 1)^2 + 8\beta_2[Zn][P]_{total}) \} / 4\beta_2[Zn] \quad (4.16)$$

In order to calculate the position of the equilibrium: $Zn + 2P \rightleftharpoons [ZnP_2]$,

First calculate the approximate [Zn] using K_1, β_2, $[P]_{total}$, $[Zn]_{total}$ and [P] (estimated) using equation *(4.13).*

Then, using this approximate [Zn], recalculate [P] using equation *(4.16),* and hence a new $[ZnP_2]/[ZnP]$.

Repeat this iteration until the $[ZnP_2]/[ZnP]$ converges on a solution.

In an attempt to visualise the 2:1 Zn(II)$Atx1_2$ complex, Atx1 was loaded with Zn(II), using concentrations modelled to favour the formation of the Zn(II)$Atx1_2$ over Zn(II)Atx1. This Atx1 and Zn(II) mixture was then resolved by analytical size exclusion chromatography and the resultant fractions were analysed for [Atx1] by

Bradford reagent and UV absorbance, [metal] by ICP-MS and protein visualised by SDS-PAGE.

Initial concentrations chosen were 100 μM Atx1 and 25 μM Zn(II). This condition was chosen for several reasons: the absolute concentration of Atx1 was large enough to detect the protein by A_{280} and the [metal] by ICP-MS post-chromatography. Furthermore, the Zn(II)$Atx1_2$ complex was predicted to be 12.9x more prevalent than the Zn(II)Atx1 species and even if the sample was diluted by 50% over the course of the experiment (resulting in 50 μM Atx1 and 12.5 μM Zn(II)), the 2:1 Zn(II) species is still favoured over the 1:1 Zn(II) species by 6.6x (Table 4.3).

Table 4.3, Simulation of $ZnAtx1_2$:ZnAtx1 equilibrium. Final equilibrium positions when Apo-Atx1 is loaded with Zn(II) in the absence of competitor as defined by equations in Figure 4.13.

Inputted values		Outputted values				
[Atx1]total (μM)	[Zn] total (μM)	[Zn] free (μM)	[Atx1] free (μM)	$[ZnAtx1_2]/[ZnAtx1]$	[ZnAtx1] (μM)	$[ZnAtx1_2]$ (μM)
10	10	1.28	0.43	0.11	7.87	0.85
10	25	15.15	0.04	0.01	9.74	0.11
10	50	40.06	0.02	0.00	9.90	0.04
10	75	65.04	0.01	0.00	9.94	0.03
10	100	90.03	0.01	0.00	9.95	0.02
25	10	0.03	8.30	2.07	3.24	6.73
25	25	2.86	0.48	0.12	19.75	2.39
25	50	25.47	0.07	0.02	24.13	0.40
25	75	50.24	0.03	0.01	24.55	0.21
25	100	75.16	0.02	0.01	24.69	0.14
50	10	0.00	31.14	7.79	1.14	8.86
50	12.5	0.00	26.64	6.66	1.63	10.86
50	25	0.07	8.27	2.07	8.13	16.81
50	50	5.47	0.51	0.13	39.53	5.00
50	75	26.58	0.12	0.03	46.97	1.45
50	100	50.87	0.07	0.02	48.33	0.80
75	10	0.00	55.67	13.92	0.67	9.33
75	25	0.01	28.13	7.03	3.11	21.88
75	50	0.57	3.31	0.83	27.04	22.39
75	75	8.07	0.51	0.13	59.31	7.62
75	100	28.13	0.17	0.04	68.92	2.96
100	10	0.00	80.47	20.12	0.47	9.53
100	25	0.00	51.80	12.95	1.79	23.21
100	50	0.07	12.41	3.10	12.17	37.76
100	75	1.66	2.05	0.51	48.52	24.82
100	100	10.66	0.52	0.13	79.08	10.25

Results show that when apo-Atx1 is analysed by size exclusion chromatography, it elutes as a single peak at 14.47 mL (Figure 4.12) with a slight shoulder suggesting the possibility of some less abundant but larger molecular weight species present. However, when 100 μM Atx1 is incubated with 25 μM Zn(II), then analysed by size-exclusion chromatography, there is a Zn(II)-dependent shift in elution volume from 14.47 mL to 13.37 mL, consistent with the predicted formation of a 2:1 Zn(II)$Atx1_2$ species (Figure 4.12) in the Zn(II)-binding model. SDS-PAGE analysis confirms that the contribution of Bradford and A_{280} traces from the Zn-associated dimer and monomer peak are both from Atx1 (Figure 4.13). Additionally, the ratio of 2:1 complex to 1:1 complex appears to also be consistent with the model, with approximately half of the Atx1 in the monomeric and half in the dimeric state. These chromatogram fractions were then analysed for Cu and Zn by ICP-MS (Figure 4.13 and Figure 4.14). The Zn(II)-associated Atx1 has a Zn-peak (24.67 μM) which appears to be associated nearer to the heavier of the two protein peaks (Figure 4.15). A small Cu peak was also observed (1.86 μM), however, the peak eluted at the same volume as the lighter (monomeric) protein peak, consistent with the 1:1 Cu(I)Atx1 stoichiometry observed earlier (Figure 4.2 and Figure 4.3). The Apo-Atx1 A_{280} trace appears to have a slight “shoulder” at a larger mass which corresponds to a Zn-peak (10.17 μM) when analysed for metal by ICP-MS (Figure 4.14). As the Atx1 was confirmed >98% Zn-free post-purification by ICP-MS, it is probable that the Zn contaminated the protein during the chromatography experiment. This contaminating Zn-peak however is consistent with the prediction that the heavier peak is the Zn(II)$Atx1_2$ dimer. In both the Apo-Atx1 and Zn-associated-Atx1, the Zn peak by ICP-MS is approximately half the concentration of

the Atx1 by Bradford and A_{280}, which is consistent with a 2:1 Zn-species stoichiometry.

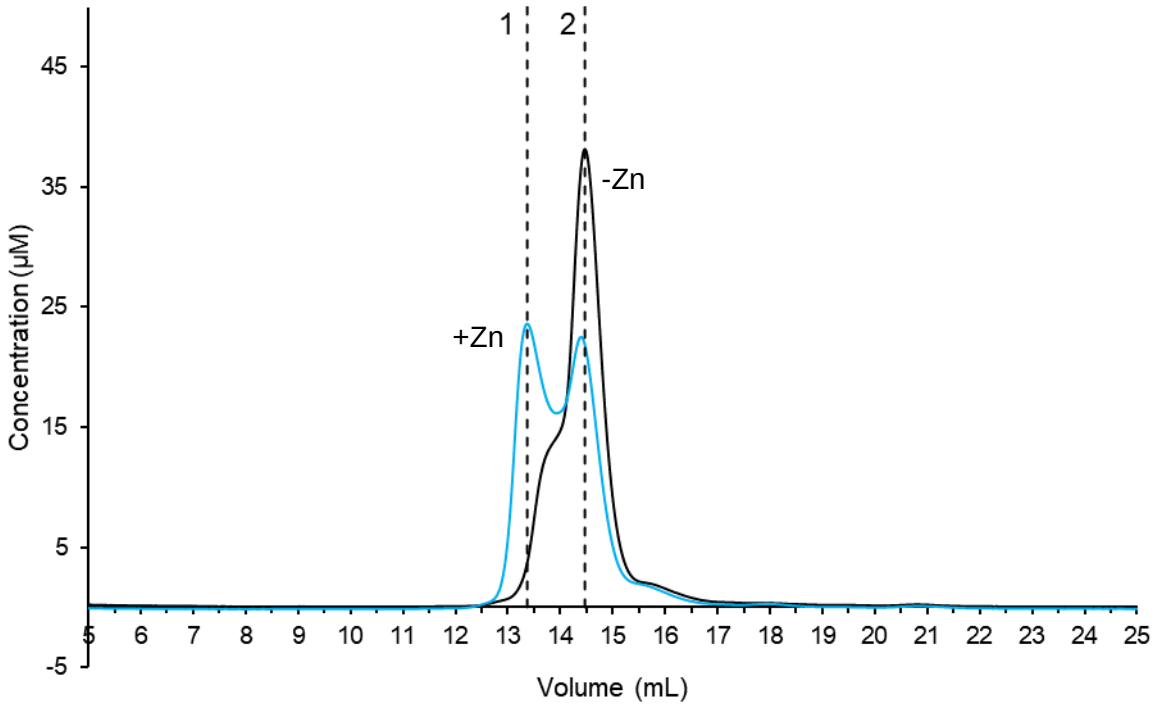

Figure 4.12, In-vitro characterisation of Apo-Atx1 and Zn-associated-Atx1 by analytical size exclusion chromatography. UV-traces following elution of 100 µM Atx1 in the presence and absence of 25 µM Zn(II) (blue and black lines respectively) [Superdex 75 10/300 GL]. Dotted lines 1 and 2 represent volumes 13.37 and 14.47 mL respectively. Data representative replicate of n=2 replicates – second replicate shown in Supplementary Figure 8.14

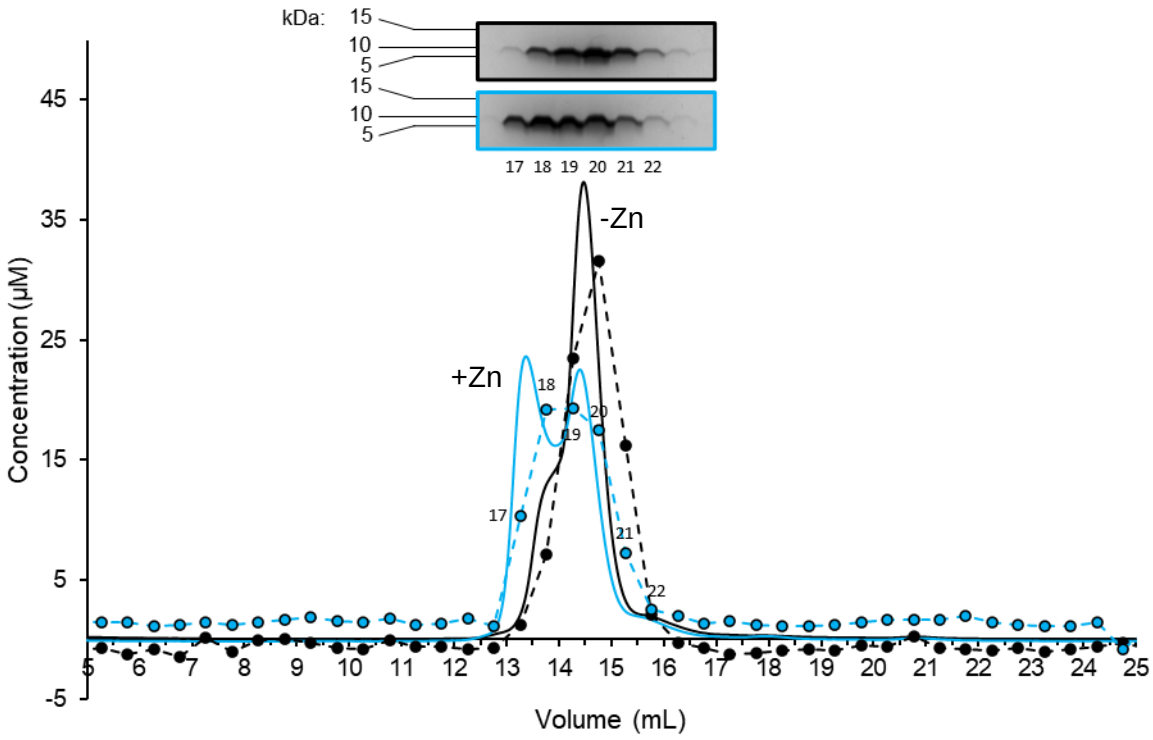

Figure 4.13, In-vitro characterisation of Apo-Atx1 and Zn-associated-Atx1 by analytical size exclusion chromatography: quantification by Bradford assay. UV-traces from figure 4.12, following elution of 100 µM Atx1 in the presence and absence of 25 µM Zn(II) (blue and black lines respectively). Quantification of fractions by Bradford assay superimposed (dotted with markers) [Superdex 75 10/300 GL]. SDS-PAGE analysis of fractions inset (colour-coded boarder with line colour). All fractional data aligned to volumetric centre of fractions (0.5 mL).

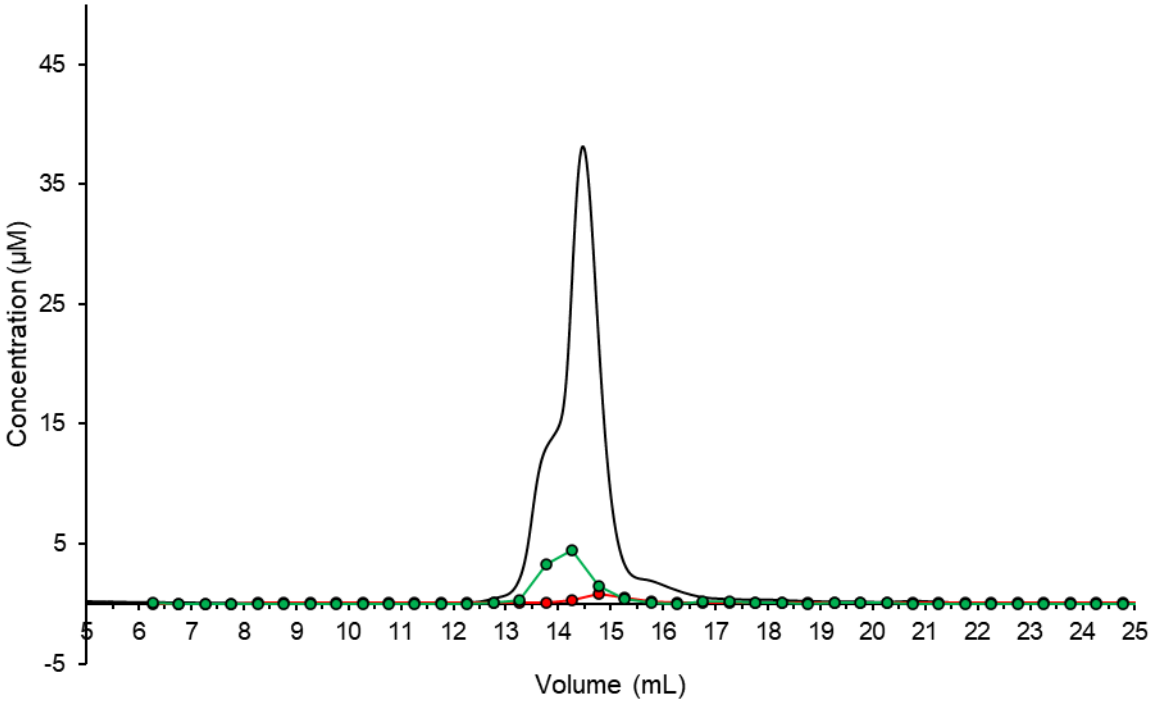

Figure 4.14, In-vitro characterisation of Apo-Atx1 by analytical size exclusion chromatography and ICP-MS. UV-trace following elution of 100uM Atx1 (black line). ICP-MS analysis of fractions for Cu and Zn shown in red and green respectively.

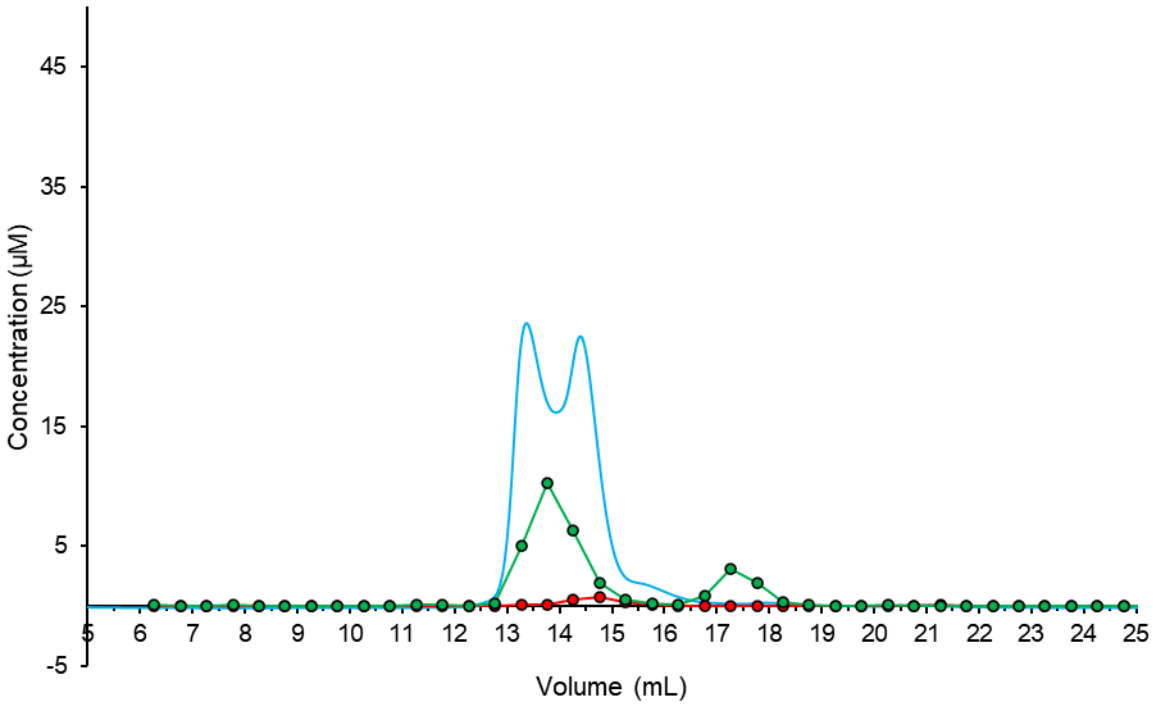

Figure 4.15, In-vitro characterisation of Zn-associated-Atx1 by analytical size exclusion chromatography and ICP-MS. UV-trace following elution of 100uM Atx1 loaded with 25 µM Zn (blue line). ICP-MS analysis of fractions for Cu and Zn shown in red and green respectively.

Apo-Atx1 was also loaded with Cu(I) to confirm the Cu(I)Atx1 species eluted as an expected monomer (Figures 4.16to 4.21). 100 μM Atx1 was loaded with either 25 or 50 μM Cu(I), separated by size exclusion chromatography and analysed in the same way as above. Both samples eluted at the same volume as the Apo-Atx1 (14.47 mL), consistent with the prediction of a monomeric Cu(I)Atx1 complex (Figure 4.16). In both cases, when analysed for [metal] by ICP-MS, Cu eluted with the monomeric protein peak (Figure 4.18 and Figure 4.19). Both samples also had slight Zn(II) contamination when analysed by ICP-MS, which also eluted with the shoulder on the A_{280} protein peak, presumed to be Zn(II)$Atx1_2$.

It is also noted that when analysed by A_{280} trace, amount of Atx1 returned is smaller than expected. When the [Atx1] is analysed by Bradford assay however, the amount of Atx1 returned is as expected (Figure 4.17). It is possible that Cu(I) binding to Atx1 affects the absorbance at 280 nm. Cu interactions with size exclusion matrices have also been observed previously (personal observation) where often not all the Cu loaded to the column can be returned without subsequent EDTA wash. Any binding of Cu with the matrix could serve as an interaction surface and may have resulted in the trapping of Atx1 on the column, although the smooth, high resolution $A_{280\ nm}$ chromatogram (Figure 4.16) would suggest otherwise, as interactions with the matrix would be expected to decrease the resolution of the technique. Further study would be required to validate any interaction such as this.

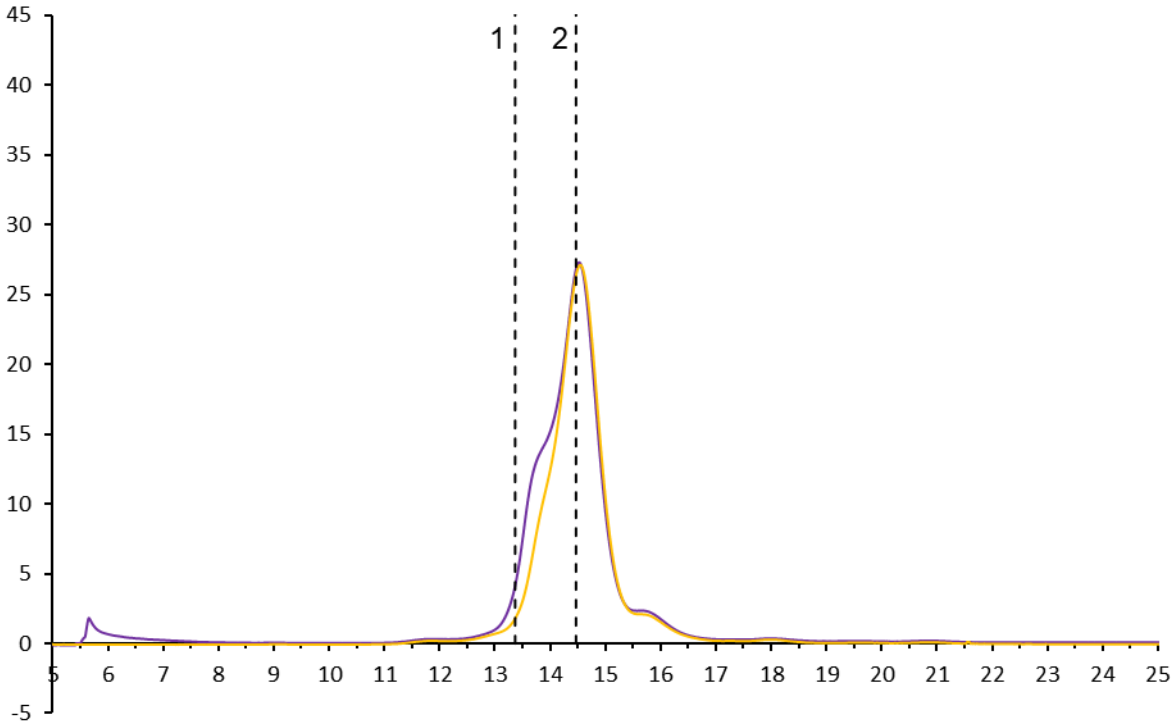

Figure 4.16, In-vitro characterisation of Cu-loaded-Atx1 by analytical size exclusion chromatography. UV-traces following elution of 100uM Atx1 in the presence of of 25 or 50 µM Cu(I) (purple and yellow lines respectively) [Superdex 75 10/300 GL]. Dotted lines 1 and 2 represent volumes 13.37 and 14.47 mL respectively.

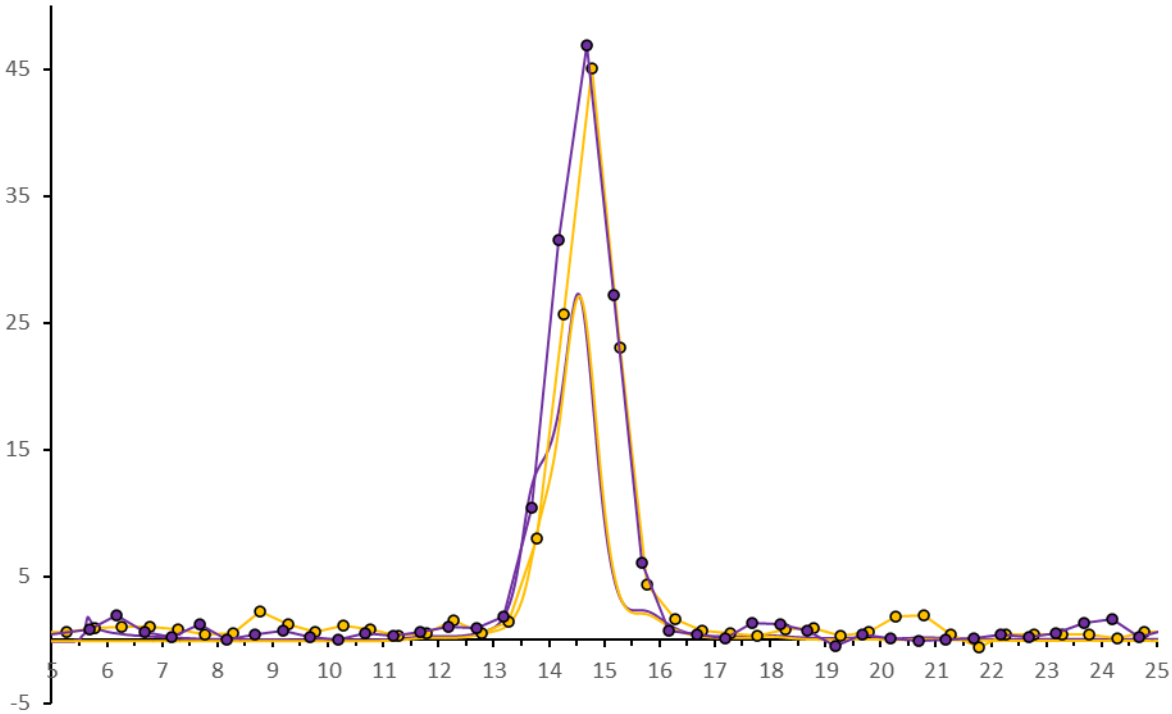

Figure 4.17, In-vitro Characterisation of Cu-loaded-Atx1 by analytical size exclusion chromatography, quantification by Bradford assay. UV-traces following elution of 100 µM Atx1 in the presence of of 25 or 50 µM Cu(I) (purple and yellow lines respectively). Quantification of fractions by Bradford assay superimposed (dotted with markers) [Superdex 75 10/300 GL].

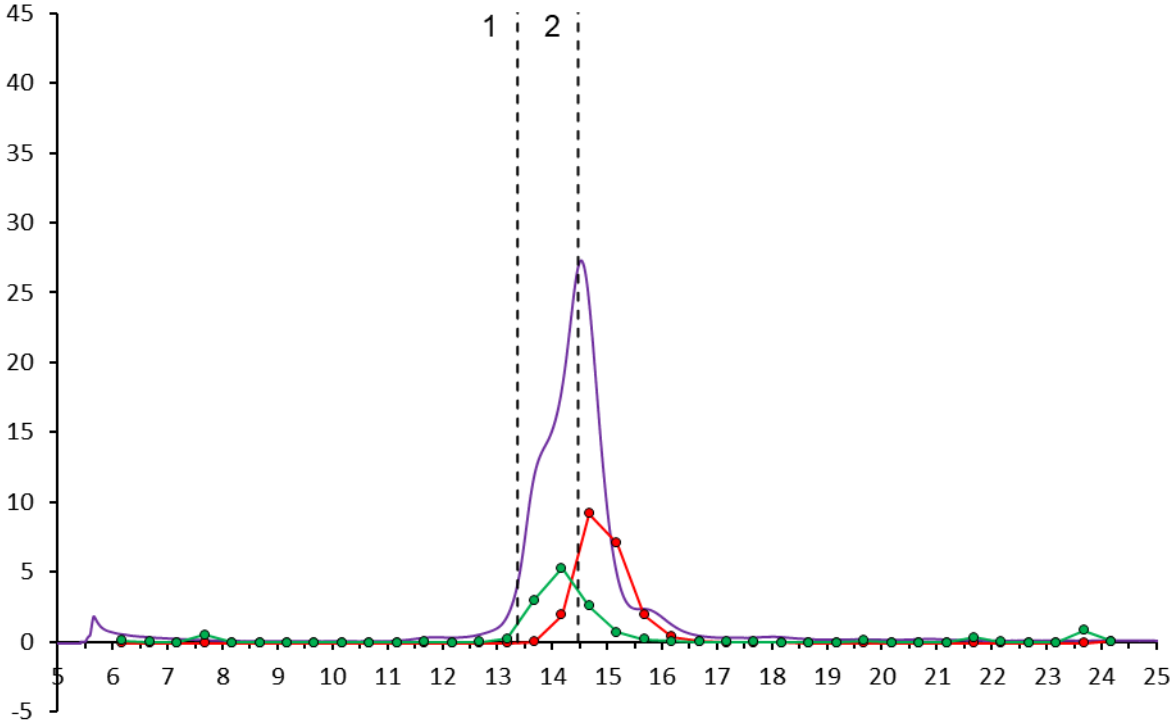

Figure 4.18, In-vitro Characterisation of Cu-loaded-Atx1 by analytical size exclusion chromatography and ICP-MS. UV-trace following elution of 100 µM Atx1 loaded with 25 µM Cu(I) (purple line). ICP-MS analysis of fractions for Cu and Zn shown in red and green respectively.

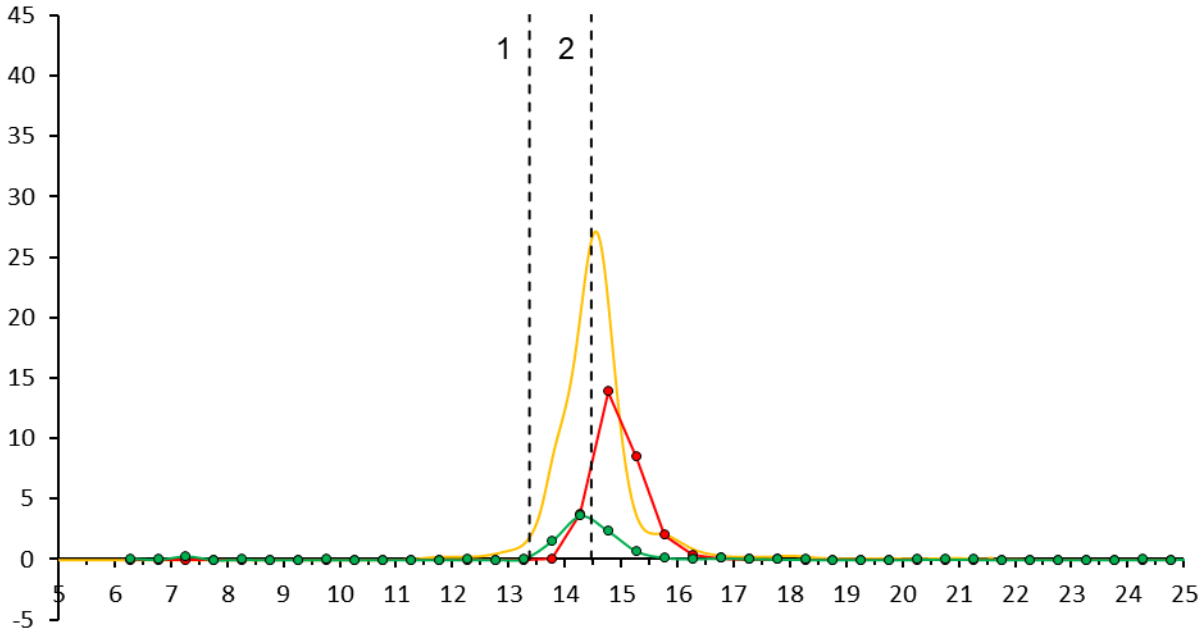

Figure 4.19, In-vitro Characterisation of Cu-loaded-Atx1 by analytical size exclusion chromatography and ICP-MS. UV-trace following elution of 100uM Atx1 loaded with 50 µM Cu(I) (yellow line). ICP-MS analysis of fractions for Cu and Zn shown in red and green respectively.

This chapter has shown that *Arabidopsis* Atx1 binds Cu(I) in a 1:1 stoichiometry with a K_d of 5.47×10^{-18} M. Further characterisation of the Atx1Cu(I) complex also confirmed the 1:1 stoichiometry by analytical size exclusion chromatography. It also showed that *Arabidopsis* Atx1 binds Zn(II) in a 2:1 stoichiometry which can be described by two binding events: *apo*-Atx1 association with one Zn(II) (with a $K_{d2}=7.12 \times 10^{-8}$ M) followed by Atx1Zn(II) association with an additional *apo*-Atx1 (with a $K_{d3}=4.09 \times 10^{-6}$ M). With these affinities and stoichiometries, it now becomes possible to model the metalation of Atx1 with both Cu(I) and Zn(II) in order to ascertain the occupancy of the protein as a function of intracellular Cu(I) and Zn(II) concentration. Calculations such as these give insight into the Cu(I) availability in the cytosol of *Arabidopsis thaliana,* where Atx1 receives Cu(I).

Chapter 5. Calculating Atx1 metalation in a living cell

5.1 In-silico model for competition of Atx1 for Cu(I) or Zn(II)

Metalation calculators to date have been developed to compete various metals for a site on a protein that bind a variety of metals. All of the current calculators use affinity data from preformed metal sites on proteins (Foster et al., 2022; Young et al., 2021). In the case of Atx1, the current calculators can be used to calculate the metalation of the Cu(I) site which is a pre-formed 1:1 stoichiometry, but cannot take into account the competition with the 2:1 Zn(II) metalation, where the assembly of the site is metal-dependent. Therefore, here, a novel set of equations have been used to describe the competition between the two different metals (Figure 5.1).

The Zn(II) binding model (Figure 4.10 and Figure 4.12) was simplified to allow only the formation of the 2:1 complex so as to make the algebra in the modelling solvable by quadratic equation as below, where P represents Atx1:

$$CuP \rightleftharpoons P + Cu$$

$$\textit{Where } K_d = [Cu][P]/[CuP] \qquad (5.1)$$

$$2P + Zn \rightleftharpoons ZnP_2$$

$$\textit{Where } \beta_2 = [ZnP_2]/[Zn][P]^2 \qquad (5.2)$$

$$CuP + Zn + P \rightleftharpoons ZnP_2 + Cu$$

$$\textit{Where } K_{eq} = [ZnP_2][Cu]/[CuP][Zn][P] \qquad (5.3)$$

Therefore:

$[ZnP_2]/[CuP] = K_d\beta_2 * [Zn]/[Cu] * [P]$ *(5.4)*

Where:

$[ZnP_2]/[CuP]$ = relative occupancy with Zn vs Cu

K_d β_2 = constants defined by measured affinities

[Zn]/[Cu] = metal availabilities derived from qPCR

[P] = amount of “free” Atx1

$[P]_{total} = [P] + [CuP] + 2[ZnP_2]$ *(5.5)*

Hence:

$[P]_{total} = [P] + [Cu][P])/K_d + 2\beta_2[Zn][P]^2$ *(5.6)*

Solve quadratic equation for [P] (“free” [Atx1])

For each set of Zn/Cu availabilities and $[P]_{total}$, first calculate the [P] (“free” Atx1) by solving the quadratic equation for [P].

Then using [P], along with the known K_d and β_2 values to calculate $[Atx1_2Zn]/[Atx1Cu]$

5.1.1 Simulating Atx1 metalation in a living cell using availabilities from *E. coli* JM109(DE3)

The Cu(I)/Zn(II) metalation of Atx1 was modelled using the calculations for a range of hypothetical concentrations of Atx1 from 1 μM – 1 M (Figure 5.1). Initially, values for the Cu(I) and Zn(II) intracellular metal availability were taken as the "midpoints" (Foster et al., 2022) of the Cu(I) and Zn(II) sensors in *E. coli* (see section 1.1.5) Under these availabilities, at concentrations of Atx1 <~10 mM, Atx1 is predicted to preferentially metalate with Cu(I) over Zn(II) (~20% occupancy). At concentrations of Atx1 > ~10 mM, Zn(II)-metalation becomes preferential over Cu(I)-metalation. The preferential metalation with Zn(II) as the [Atx1] increases was expected, because as the [Atx1] increases, the formation of the 2:1 complex is favoured over the 1:1 complex..

When the same modelling is applied using the intracellular metal availabilities measured for *E. coli* JM109(DE3) grown under LB conditions (Figure 5.1, (Foster et al., 2022)), Atx1 is not predicted to be significantly metalated with Cu at any concentration of Atx1, and at higher concentrations, again, would be increasingly metalated with Zn as the [Atx1] increases above non-physiological levels.

These Figures highlight the need to know both the metal availabilities in the cells under investigation, and the intracellular Atx1 protein concentration, in order to correctly calculate the metal-occupancies of Atx1 in the cell. This is a significant distinction, in calculating metalation of metal-dependant adducts and dimers, with biological implications considered in the discussion.

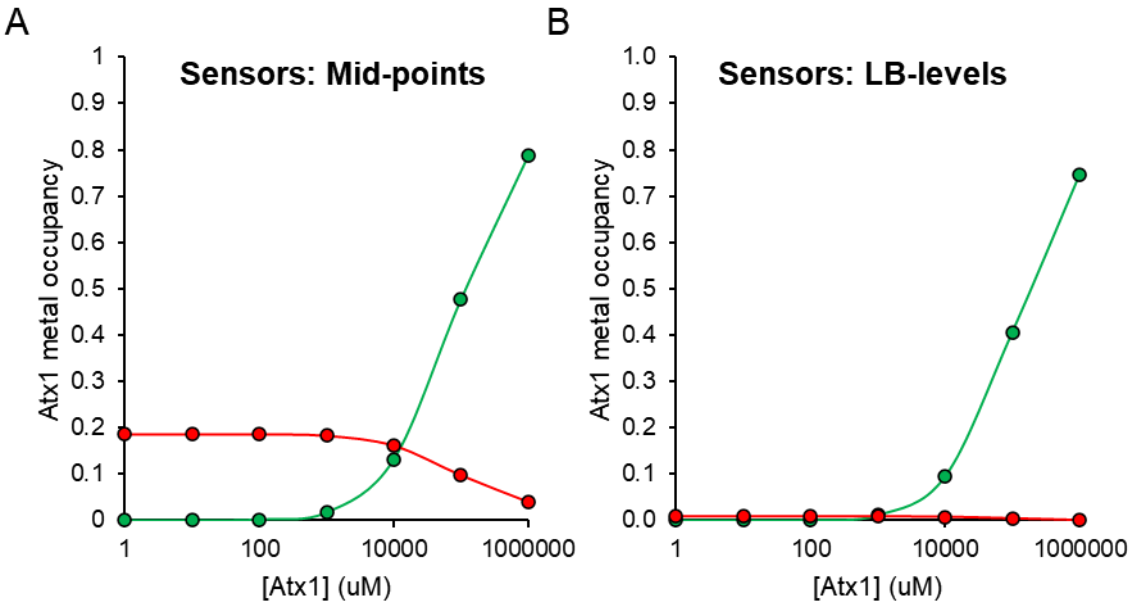

Figure 5.1, Effect of protein abundance and intracellular metal availability on Atx1 metalation predictions. Relative occupancy of Atx1 with Zn (green) and Cu (red) when Atx1 forms 1:2 and 1:1 complexes respectively and intracellular [Atx1] varied. Simulations shown using aerobic LB *E. coli* metalation calculator with free metal availabilities set to sensor response midpoints when measured in JM109(DE3) (A) and at metal availabilities measured in JM109(DE3) LB growth conditions (B)

5.1.2 Simulating Atx1 metalation as a function of the Cu(I) and Zn(II) sensor-response in *E. coli* JM109(DE3)

Metal availabilities for Cu(I) and Zn(II) were calculated for a range of θ_{DM} values from 0.01-0.99 of the metal-sensors CueR and ZntR respectively (Table 5.1) (Osman et al., 2019). These values were used in the calculations to simulate Atx1 metalation as the activation of CueR and ZntR were varied (Figure 5.2).

As the activation of CueR is increased independently of Zn(II) availability (Zn(II) is set to the aerobic LB-levels in JM109(DE3)), Atx1 is shown to increasingly acquire Cu(I). For all concentrations of Atx1 modelled, the occupancy of Atx1 varies from approximately 0-1 occupancy, demonstrating that Atx1 is predicted to be “sensitive” over the entire range of the metal sensor response in *E. coli* JM109 (DE3) and also demonstrating the “tracking” of the Cu(I) metalation of Atx1 with the Cu(I) availability in the cell (see section 1.3.3). As CueR activation is increased and the Zn(II) availability constant, no significant Zn(II) metalation is observed until Atx1 is modelled at the concentration of ~10 mM, where Atx1 can acquire Zn(II) only at low levels of CueR activation, when not out-competed by Cu(I). The driving force behind the Zn(II) metalation is the preferential metalation of the dimeric Zn(II) species over the monomeric Cu(I) species when the abundance of Atx1 increases above non-physiological levels.

As the activation of ZntR is increased independently of Cu(I) availability (Cu(I) is set to the LB-levels in JM109(DE3)), Atx1 is shown to increasingly metalate with Zn(II). However, to achieve metalation, Atx1 would have to be at extremely high concentrations in the cell, in addition to ZntR being very active. As ZntR activation is increased and the Cu(I) availability constant, no significant Cu(I) metalation is

observed at any Atx1 concentration. This is the result of the measured intracellular Cu(I) availability in JM109(DE3) cells grown in LB being very low.

These simulations highlight the need to know the concentration of Atx1 and activity of the sensors in the cell (and hence the intracellular metal availability of their cognate metals) to correctly calculate the protein metalation *in-vivo*.

Table 5.1, Zn and Cu availability as a function of θ_{DM} of the cognate sensors ZntR and CueR respectively. Values calculated using supplementary information from the work of Deenah Osman and colleagues (Osman et al., 2019).

θ_{DM} (norm.)	Zn availability (M) (ZntR)	Cu availability (M) (CueR)
0.01	3.95×10^{-14}	1.11×10^{-20}
0.05	2.05×10^{-13}	5.85×10^{-20}
0.1	4.33×10^{-13}	1.25×10^{-19}
0.25	1.29×10^{-12}	3.92×10^{-19}
0.5	3.83×10^{-12}	1.25×10^{-18}
0.75	1.14×10^{-11}	3.96×10^{-18}
0.9	3.39×10^{-11}	1.22×10^{-17}
0.95	7.15×10^{-11}	2.61×10^{-17}
0.99	3.72×10^{-10}	1.37×10^{-16}

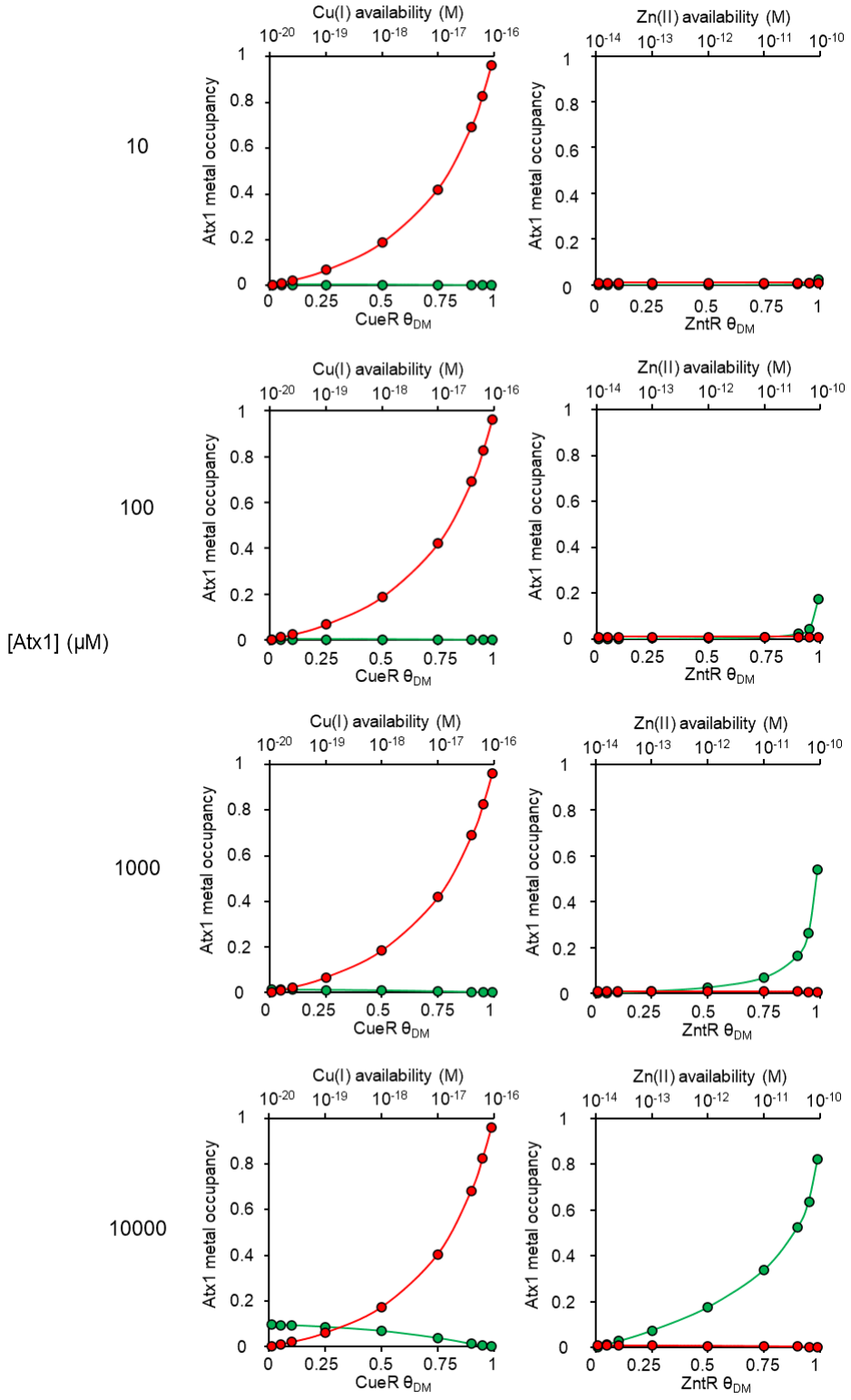

Figure 5.2, Effect of sensor activation and protein abundance on Atx1 metalation predictions. Relative occupancy of Atx1 with Zn (green) and Cu (red) when Atx1 forms 2:1 and 1:1 complexes respectively. Relative Atx1 occupancy calculated using intracellular metal concentration when sensor responses (CueR θ_{DM} or ZntR θ_{DM}) are varied from 0-1 in JM109(DE3). When sensor activation not being varied, availability is set to LB levels measured in JM109(DE3).

5.2 Effect of metal exposure on ZntR/CueR activity in *E. coli* BL21(DE3) +/-Atx1 overexpression

It is possible to measure the Cu(I) and Zn(II) metal availabilities in *E. coli* by calculating the DNA-occupancy (θ_{DM}) of the two bacterial DNA-binding metal sensors CueR and ZntR, and applying these values to the thermodynamic parameters for these two sensors, established in *Salmonella enterica* (Osman et al., 2019).

Recent work by Andrew Foster and colleagues has calibrated the metal responses in the *E. coli* cells JM109 (DE3) (Foster et al., 2022). This work has facilitated the direct measurement of the metal availability in BL21(DE3) cells by using the sensor-responses calibrated in the similar JM109(DE3) strain as a substitution for the expected responses in BL21(DE3).

Using quantitative, reverse transcriptase PCR (RT-qPCR), the abundance (relative to the minimum expression) of the metal-responsive transcripts for the proteins CopA (regulated by CueR), and ZntA (regulated by ZntR), can be measured under varying metal-supplemented growth conditions, to report on the activation (and hence DNA-occupancy) of the sensors under those conditions. These values can then be used to calculate the intracellular Zn or Cu availability inside the cells under those specific metal-supplemented growth conditions.

5.2.1 Effect of Cu exposure on CueR activation in BL21(DE3) +/- Atx1 overexpression

To identify a condition in which the θ_{DM} of CueR was high enough (i.e., the intracellular Cu availability high enough) to expect Cu metalation of Atx1 *in-vivo*, it was necessary to measure the CueR activation in the expression strain BL21(DE3), whilst overexpressing Atx1, under a range of Cu growth conditions.

BL21(DE3) were grown expressing either the pET29a(Atx1) or pET29a(Empty) plasmid (+/- Atx1 respectively) under 0 (untreated), 50, 100, 500, 1000 and 1800 μM $CuSO_4$ supplemented conditions in biological triplicate. The maximum condition was chosen as it was expected from previous work (Foster et al., 2022) that these conditions would result in less than approximately 15% growth inhibition relative to the untreated cells. Results show that in both +/-Atx1 experiments <20% inhibition was seen at the maximum Cu conditions, and the growth inhibition relative to the untreated was no different in the +Atx1 when compared to the -Atx1 strain (Figure 5.3). RNA was then extracted from each sample after 2h incubation at each growth condition, treated with DNAseI, treated with reverse transcriptase to create cDNA, and analysed by qPCR to monitor the transcription of the Cu-responsive transcript for *CopA* relative to in untreated cells. This transcript level relative to the untreated level is then used as a readout for the activation of CueR which can then be used to read out the availability of Cu(I) in the cell under each growth condition.

qPCR analysis of *CopA* expression in BL21(DE3) can be represented as fold change in *CopA* transcript relative to the minimum expression (measured in JM109(DE3) (Foster et al., 2022)) (Figure 5.4). Under all Cu growth conditions, the fold change in CopA expression is lower in the +Atx1 expression cells when

compared to the -Atx1 cells i.e., CueR is less active, and Cu(I) is at a lower availability in the cell. Beyond 500 μM Cu conditions, in cells expressing Atx1, the Fold change in CopA expression increases no further than approximately 30 fold, however in the -Atx1 strain, the expression continues to increase to approximately 80 fold when grown under 1800 μM Cu.

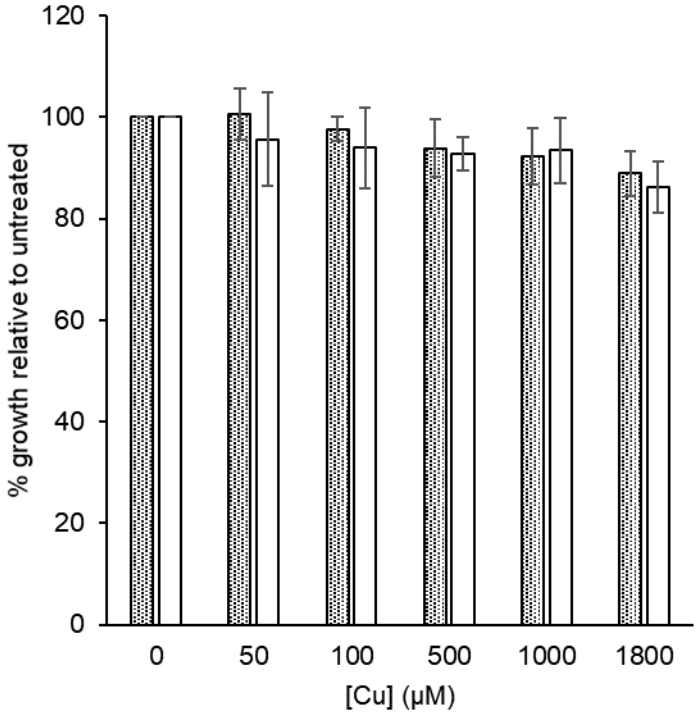

Figure 5.3, Growth of BL21(DE3) +/-Atx1 overexpression post 2h Cu-exposure. Percentage growth relative to untreated condition of BL21(DE3) +/- Atx1 expression (shaded and empty bars respectively). n=4 biological replicates, error bars represent replicate mean +/- 1 standard deviation.

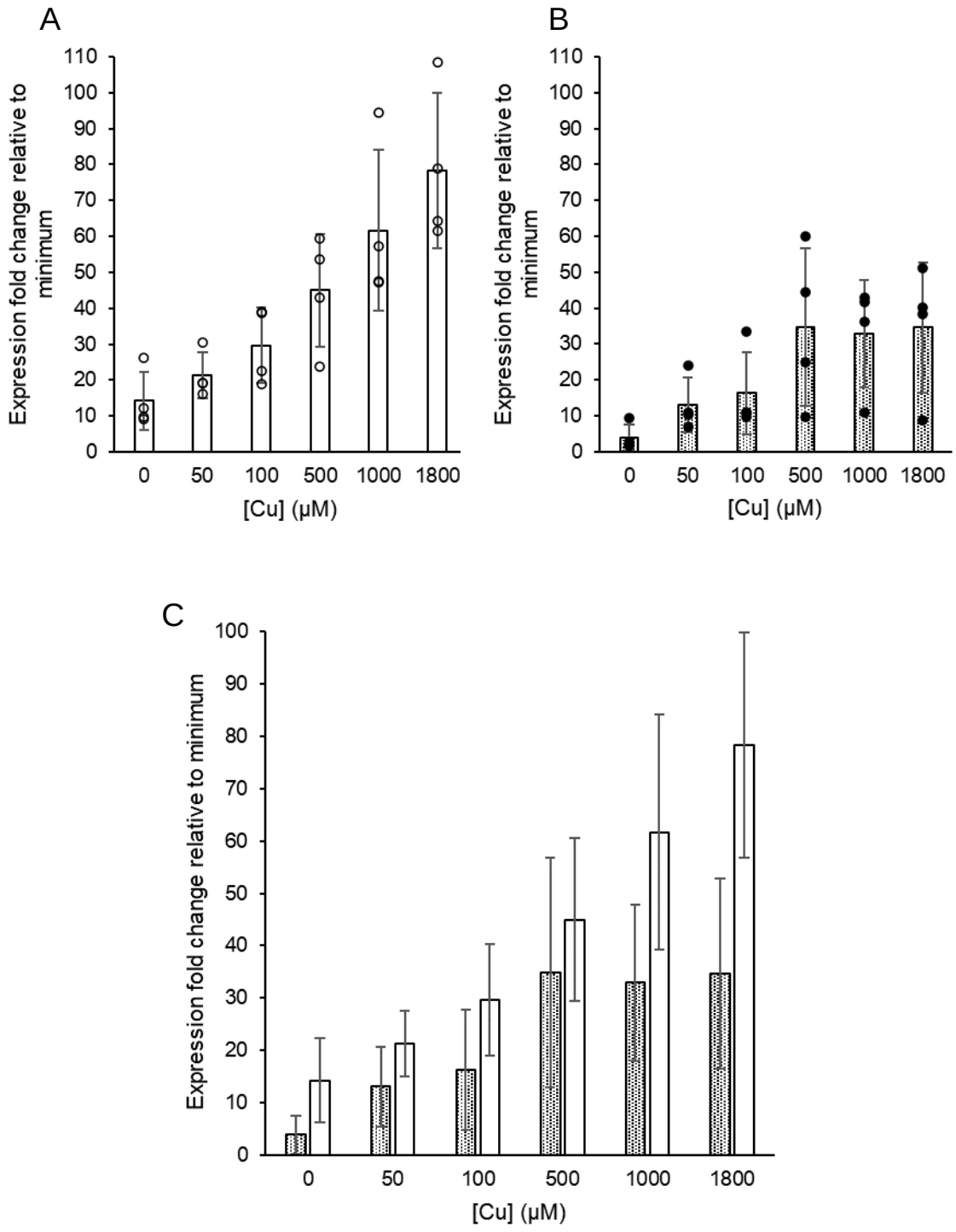

Figure 5.4, qPCR analysis of *CopA* expression in cells +/- Atx1 overexpression. Fold change in *CopA* transcript abundance relative to minimum (generated in JM109(DE3)) for BL21(DE3) +Atx1 and -Atx1 overexpression (A, shaded and B, empty bars respectively) under a range of $CuSO_4$ -supplemented growth conditions. n=4, error bars represent replicate mean +/- 1 standard deviation. C shows a data compilation for figures “A” and “B”.

These fold-change data can be converted to CueR sensor response, θ_{DM}, as a function of intracellular buffered Cu(I) concentration (Figure 5.5). Here the same observation can be seen where the -Atx1 strain is responding to copper across almost the entire calibrated range of CueR (in JM109) and the +Atx1 strain has decreased availabilities at all growth conditions.

This data is then represented on a pair of graphs (Figure 5.6) where, using the 2:1 Zn(II) vs 1:1 Cu(I) calculator (Section 5.1), the predicted concentration of Atx1 (Section 4.6.2), and the calculated Zn(II) and Cu(I) affinities of Atx1 (Section 4.2), the predicted metalation of Atx1 can be superimposed as a function of intracellular Cu(I) availability. Here, it is noted that the approximate “maximum” θ_{DM} observed in the +Atx1 strain correlates with intracellular Cu(I) availability at which Atx1 is predicted to be able to extract Cu(I) from the buffer.

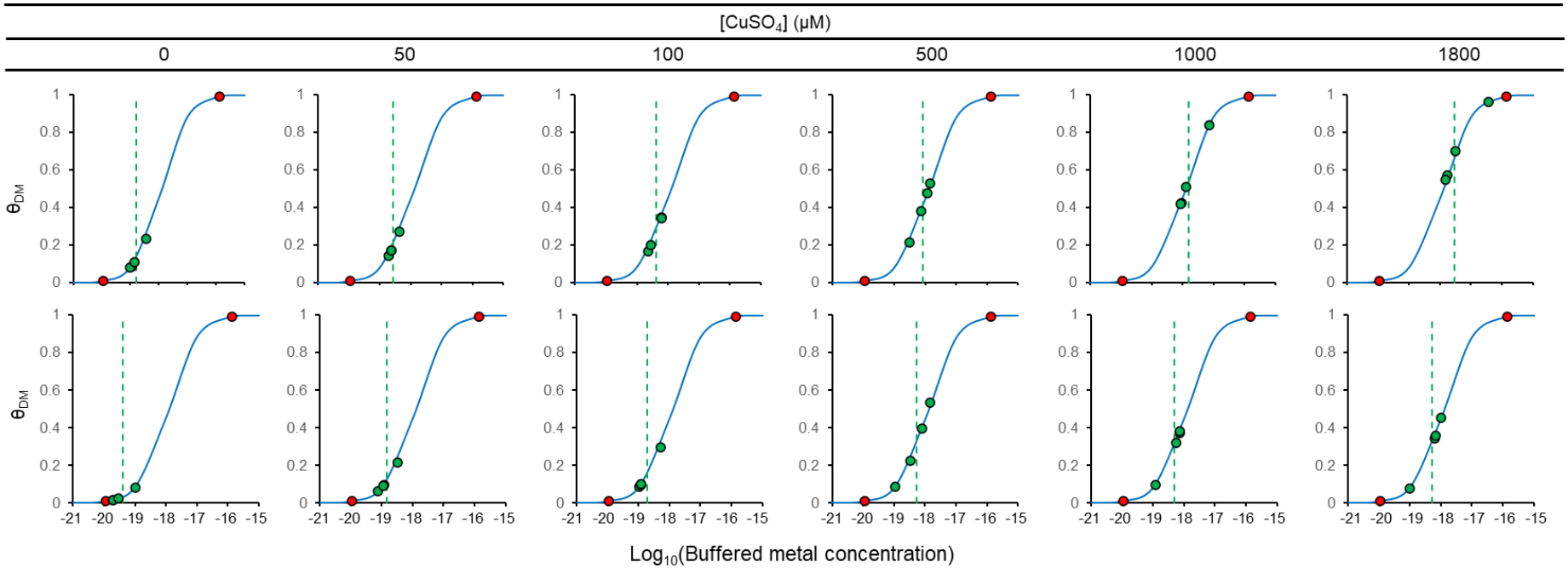

Figure 5.5, *In-vivo* Cu response in BL21(DE3) +/-Atx1 overexpression. CueR sensor response (θ_{DM}) and intracellular metal-availability in BL21(DE3) +/-Atx1 under a range of $CuSO_4$ growth conditions. n=4 biological replicates (green). The blue line represents the calibrated response of CueR in JM109(DE3) as defined by the maximum and minimum sensor response (red). Dotted green lines represent mean intracellular metal-availability of 4 replicates.

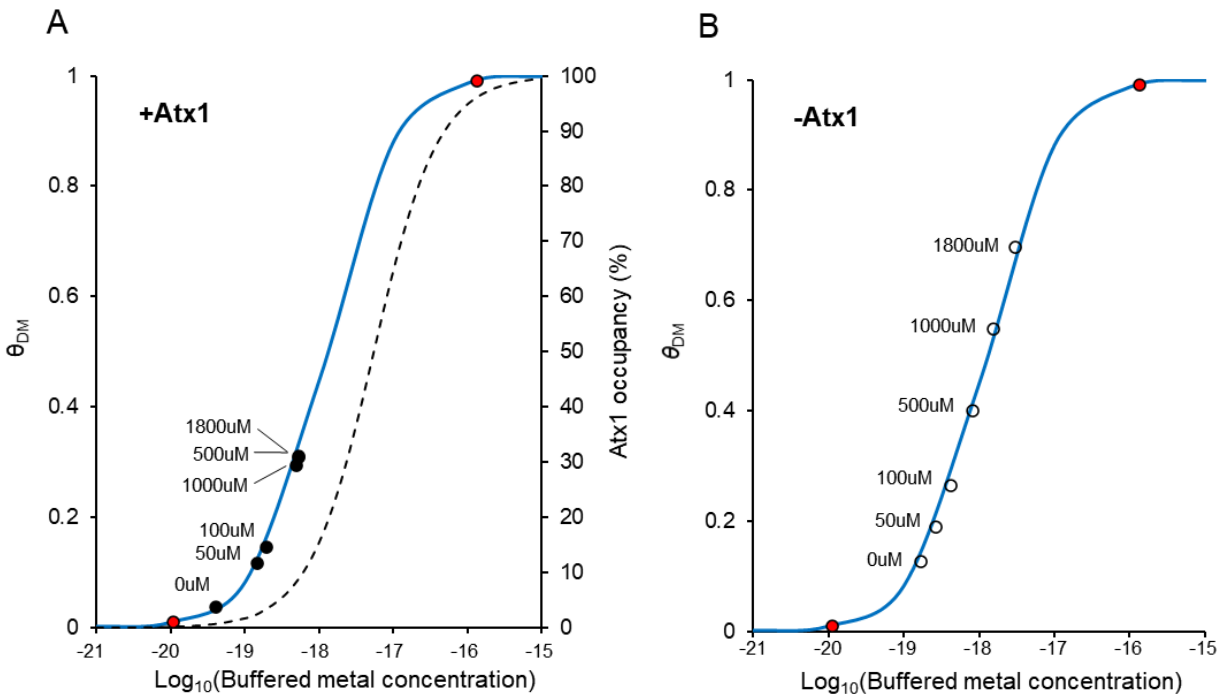

Figure 5.6, *In-vivo* Cu response in cells compared to predicted Atx1 Cu(I) metalation. CueR sensor response (θ_{DM}) and intracellular metal-availability in BL21(DE3) +Atx1 and -Atx1 overexpression (A and B respectively) under a range of $CuSO_4$ growth conditions (labelled). Mean values of n=4 biological replicates shown, +/-Atx1 represented by filled and empty circles respectively. Blue line represents the calibrated response of CueR in JM109(DE3) strain as defined by the maximum and minimum sensor response (red). Dotted line simulates the predicted Cu-metalation occupancy of Atx1, in Atx1 expressing cells (A), as a function of intracellular Cu-availability when Zn-availability set to LB-levels measured in JM109(DE3).

5.2.2 Effect of Zn exposure on ZntR activation in BL21(DE3) +/- Atx1 overexpression

To investigate the possibility of the Zn(II)$Atx1_2$ complex in BL21(DE3) overexpressing Atx1, cells were grown under high Zn conditions and the expression of the metal responsive transcripts for *zntA* were measured relative to the untreated condition. The growth condition of 0.6 mM $ZnSO_4$ was chosen as it is a high Zn-treatment which was predicted to result in minimal growth inhibition.

RNA was extracted from each sample in biological triplicate after 2 h incubation under 0.6 mM $ZnSO_4$, treated with DNAseI, reverse transcribed to create cDNA and analysed by qPCR to monitor the transcription of the Zn-responsive transcript for ZntA relative to in untreated cells.

When the raw Δ_{Cq} values are examined (Figure 5.7, see section 2.6.3 viii), it is not possible to calculate the $\Delta\Delta_{Cq}$ values from the 0.6 mM $ZnSO_4$ data, as the values lie beyond the maximum response observed in JM109. This suggests that the ZntR response in BL21(DE3) cells expressing either the pET29a(Atx1) or pET29a(Empty) is different to that observed and calibrated in JM109(DE3). To achieve accurate values for the ZntR activation and Zn availabilities under these conditions, the extremes must be experimentally re-calibrated in BL21(DE3) +/- pET29a(Atx1) and pET29a(Empty).

It is possible to carry through the calculations to predict the Zn-availability in BL21(DE3) under untreated LB conditions (Figure 5.8), and to superimpose the predicted Zn(II)$Atx1_2$ occupancy as a function of intracellular Zn availability, however, the values are not expected to be accurate and, again, recalibration of

the BL21(DE3) strain expressing the pET29a(Atx1)/pET29a(Empty) plasmids would be required to satisfy this.

A

Condition	Strain	Expression plasmid	Average Δ_{Cq} (zntA-rpoD)
0.6 mM Zn	BL21(DE3)	pET29a(Empty)	-5.7
0.6 mM Zn	BL21(DE3)	pET29a(Atx1)	-4.3
2 mM Zn (10 min)	JM109 (DE3)	none	-2.3
0.6 mM Zn	JM109 (DE3)	none	-1.9
untreated	BL21(DE3)	pET29a(Empty)	-0.6
untreated	BL21(DE3)	pET29a(Atx1)	-0.4
untreated	JM109 (DE3)	none	1.2
100 uM H_2O_2	JM109 (DE3)	none	2.7
0.5 mM EDTA	JM109 (DE3)	none	6.6
1mM EDTA	JM109 (DE3)	none	7.3

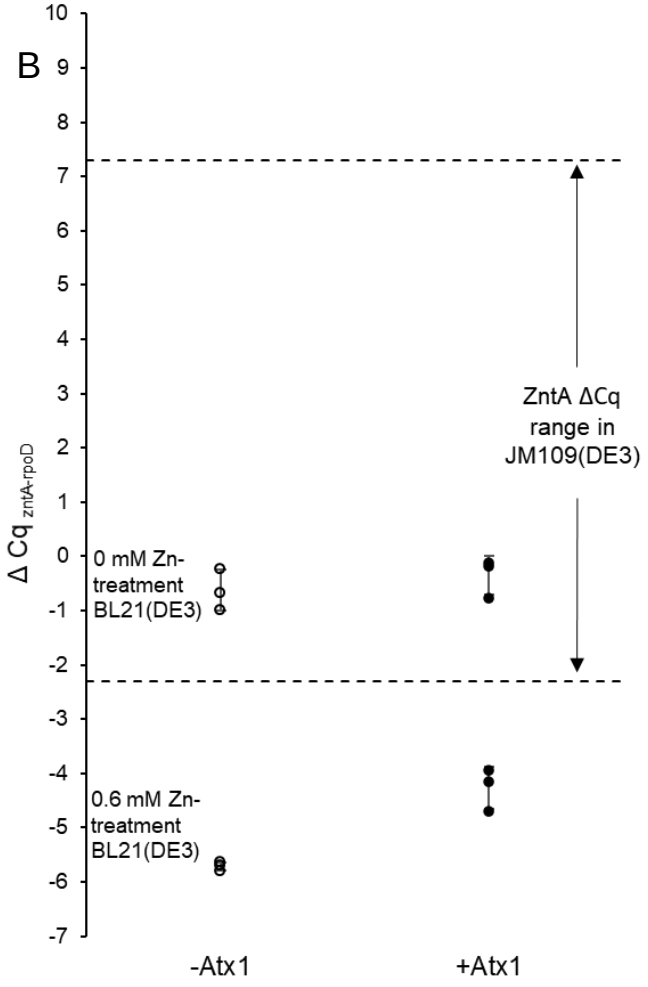

Figure 5.7, *In-vivo* Zn response in BL21(DE3) +/-Atx1 overexpression. A, Mean tabulated Δ Cq $_{zntA\text{-}rpoD}$ values for ZntR sensor response in untreated and 0.6 mM Zn-treated BL21(DE3) cells +/-Atx1 overexpression (responses in JM109(DE3) included for reference). B, ZntR sensor response represented graphically as Δ $Cq_{zntA\text{-}rpoD}$ values in untreated and 0.6 mM Zn-treated BL21(DE3) cells +/-Atx1 overexpression (filled and empty circles respectively). n=3 biological replicates. Error bars represent mean values +/- 1 std. dev.

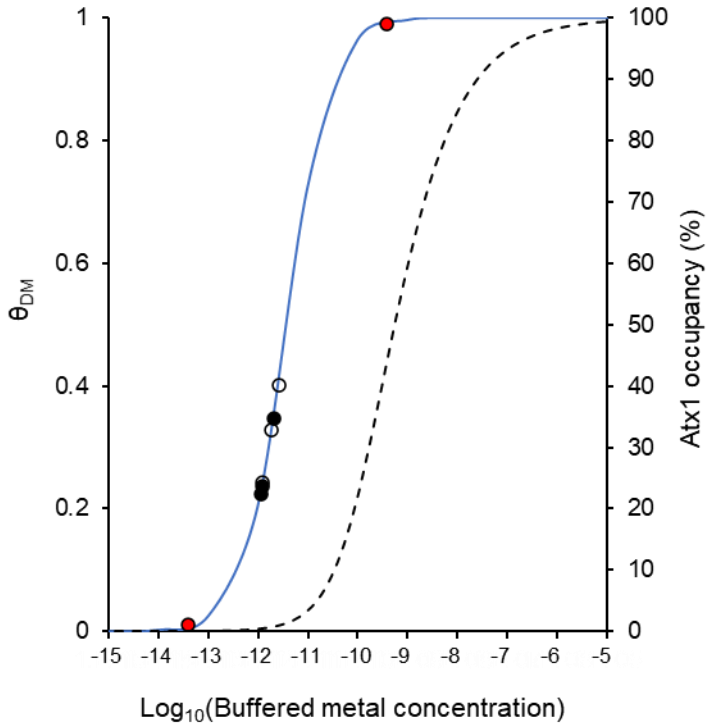

Figure 5.8, *In-vivo* Zn response in cells overexpressing Atx1 with predicted Atx1 Zn-occupancy. ZntR sensor response (θ_{DM}) and intracellular metal-availability in BL21(DE3) +/-Atx1 (filled and empty circles respectively) under untreated LB growth conditions. n=3 biological replicates are shown +/-Atx1 overexpression. The blue line represents the calibrated response of ZntR in JM109 strain as defined by the maximum and minimum sensor response (red). Dotted line simulates the predicted Zn-metalation occupancy of Atx1 as a function of intracellular Zn-availability when Cu-availability set to LB-levels measured in JM109(DE3). [Atx1] set to 536 µM as estimated in section 4.6.2

5.3 *In-vivo* demonstration of the metalation calculator

5.3.1 Following Atx1 metalation post-purification

It has previously been demonstrated that metalation of the Cyanobacterial Atx1, when expressed in *E. coli,* can be followed post-purification (Dainty, Patterson, Waldron, & Robinson, 2010). To demonstrate the calculator *in-vivo*, *E. coli* BL21(DE3) cells +/-Atx1 overexpression were grown under 1 mM $CuSO_4$ conditions, at which the intracellular Cu availability has been calculated to be 4.91 x 10^{-19} M (Figure 5.6). Cells were lysed, soluble cell lysate was resolved by size exclusion chromatography and eluent fractions analysed for copper and zinc by ICP-MS, to follow Atx1 metalation (Figure 5.9). Here, Bradford analysis of the -Atx1 soluble cell lysate fractions confirm the absence of Atx1 and Bradford/SDS-PAGE analysis of the +Atx1 soluble cell lysate fractions show Atx1 running at approximately 210 mL. ICP-MS analysis reveals both copper and zinc eluting with the Atx1. When the -Atx1-subtracted chromatogram is compared to the ICP-MS data, total zinc and copper (calculated by integrating the area under the curves) can be compared to total Atx1 and hence metal-occupancy can be read out. Here, Atx1 is calculated as ~26% metalated with Cu and ~16% metalated with Zn. It should be noted that 100% Zn-occupancy implies 100% of the Atx1 is in the $ZnAtx1_2$ complex, i.e., when [Zn] = ½ the total concentration of Atx1 (As defined in the calculator).

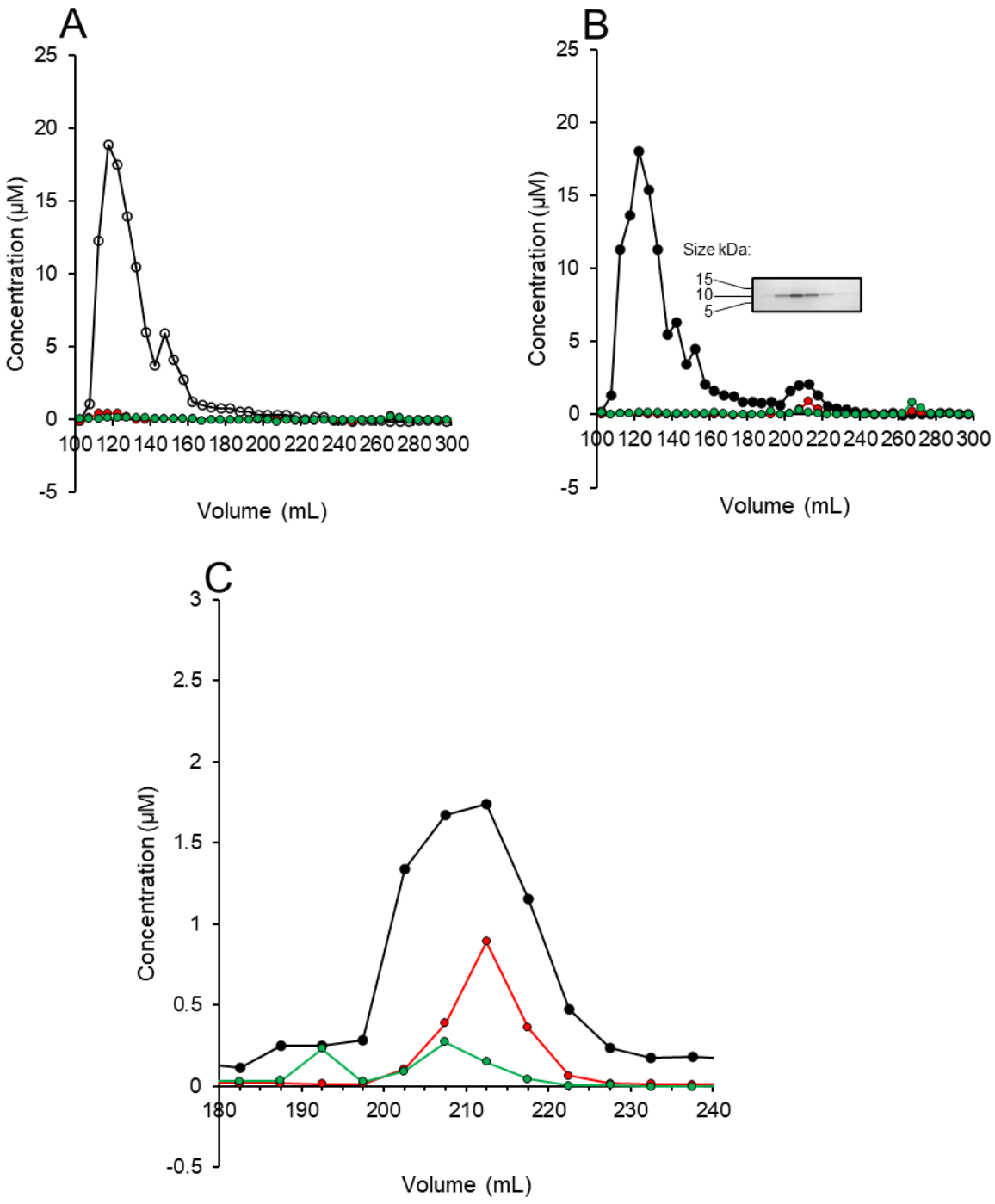

Figure 5.9, *in-vivo* metalation of Atx1 by preparative size exclusion and ICP-MS. Crude extracts of BL21(DE3) +/- Atx1 overexpression (filled and empty black circles respectively, graphs B and A respectively), cultured under 1 mM Cu, were resolved by size exclusion chromatography on S75, quantified by Bradford assay, and eluent fractions analysed for Cu (red circles) and Zn (green circles) by ICP-MS. Fractions were also resolved by SDS-PAGE (inset) stained with Coomassie instant blue. C. - Atx1-subtracted chromatogram of Atx1 elution volume in "B", including ICP-MS analysis for Cu (red circles) and Zn (green circles).

5.3.2 Estimation of the [Atx1] in the cell

From the data in Figure 5.9 C, an initial estimation for the concentration of Atx1 in BL21(DE3) pET29a(Atx1) grown under 1 mM $CuSO_4$ can be made.

The total moles of Atx1 eluted from the chromatography can be calculated as 2.95 x 10^{-8}. Assuming the cells were at mid-log phase with a cell density of ~5 x 10^8 cells/mL, the number of cells in the 500 mL culture grown is 2.5 x 10^{11}. Approximately 0.22x the total available soluble protein (from 500 mL culture) was loaded on the column; hence approximately 5.5 x 10^{10} cells' contents. The volume of each cell can be approximated as 1 x 10^{-15} L, hence the concentration of Atx1 is estimated as 536 μM.

As way of validating the approximate feasible concentration of Atx1 estimated in the overexpression strain, the following exercise was worked: If the total number of protein molecules per cell is estimated as ~4 000 000 (Milo, 2013) and it is assumed that Atx1 production in the pET system could be ~10% of total molecules per cell, the number of Atx1 molecules per cell can be estimated as 400 000. Applying Avagadro's number 6.022 x 10^{23} (Newell & Tiesinga, 2019), the moles of Atx1 can be estimated per cell as 6.64 x 10^{-19}. Given the volume of the cell is approximately 1 x 10^{-15} L, the concentration of Atx1 could be estimated as 664 μM.

5.3.3 Calculating the predicted metalation of Atx1 when grown under 1 mM $CuSO_4$ conditions.

Now the Cu availabilities have been measured in BL21(DE3) cells expressing Atx1 under a variety of $CuSO_4$ growth conditions and the approximate [Atx1] measured, the metalation of Atx1 can be predicted using the calculations developed in Section 5.1.

Under each $CuSO_4$-supplemented growth condition, using the measured Cu availability, [Atx1] estimation of 536 μM and Zn availability as measured in JM109(DE3) grown under LB conditions, the metalation of Atx1 can be predicted (Table 5.2). Under all growth conditions, very little Zn(II) is expected to be bound to Atx1 regardless of $CuSO_4$ growth conditions. In untreated conditions, Cu(I) metalation is also expected to be similarly low, however, as the $CuSO_4$ growth conditions are increased, Atx1 is expected to acquire up to >8% Cu occupancy. When the metalation predictions made here are compared to the *in-vivo* data (Table 5.3), the preferential metalation of Cu over Zn holds true, however the absolute metalation with both metals is higher *in-vivo*, especially Zn. It is worth noting however that the growth volumes used for this experiment vary from those in which the conditional metal availabilities were measured (Foster et al., 2022), where this experiment cultures were 500 mL (in unbaffled 2L conical flasks) and the conditions used in the qPCR were 5 mL (in plastic 14 mL round-bottom culture tubes). Variations such as these could possibly change the rate of aeration and hence influence the availability of metals such as Zn(II) or Cu(I) due to differing metal-requirements during aerobic respiratory metabolism (Foster et al., 2022).

Table 5.2, Atx1 metalation predictions. Predicted Zn (2:1) and Cu (1:1) occupancy when buffered Zn availability is set to levels measured in JM109 in LB, and Cu availability is varied according to measured values in BL21(DE3) overexpressing Atx1 (Figure 5.7). [Atx1] set to 536 µM as estimated in section 5.3.2.

Condition	Cu availability (+Atx1) (M)	Zn occupancy (%)	Cu occupancy (%)
0 µM Cu	4.13×10^{-20}	0.61	0.74
50 µM Cu	1.49×10^{-19}	0.59	2.65
100 µM Cu	1.95×10^{-19}	0.58	3.42
500 µM Cu	5.33×10^{-19}	0.51	8.84
1000 µM Cu	4.91×10^{-19}	0.52	8.20
1800 µM Cu	5.29×10^{-19}	0.51	8.78

Table 5.3, Test of the calculator. Predicted Zn (2:1) and Cu (1:1) occupancy when buffered Zn availability is set to levels measured in *E. coli* JM109 grown in LB, and Cu availability as measured in BL21(DE3) overexpressing Atx1 under 1000 μM Cu LB growth conditions. Observed occupancy from *in-vivo* experiment (Figure 5.10) where BL21(DE3) (+Atx1) cells were grown under 1000 μM Cu.

	Predicted occupancy (%)	Observed occupancy (%)
Cu	8.2	26.14
Zn	0.52	15.92

This chapter has explored the metalation of the *Arabidopsis thaliana* Cu(I)-binding metalloprotein Atx1 both *in-vitro* and *in-vivo.* We measured the effects of Atx1 overexpressison on the intracellular availabilities of Cu(I) and show that for all conditions tested, the Cu(I) availabilities decreased - showing significant importance to the expression of heterologous proteins in *E. coli* expression systems in future.

Using measured Cu(I) and Zn(II) affinities/stoichiometries of Atx1 (Chapter 4), intracellular Cu(I) availability level measurements from qPCR and a novel metalation calculator, we show that it is possible to effectively predict the metalation preference of Atx1 post-expression *in-vivo* after purification (with caveats discussed in Chapter 7).

By characterising the metalation of Atx1, we have gained insight into the Cu(I) availability in the same compartment that PLS is predicted to localise. This concept is further explored in Chapter 6.

Chapter 6. Calculating PLS metalation in the cytosol of *Arabdiopsis thaliana*

6.1 A calculator for the metalation of 2:1 species

In order to predict the metalation of PLS in the context of the cell, the existing metalation calculator (Young et al., 2021) was adapted to function using β_2 values in place of K_d values for affinities. This modification allows the "β calculator" to compete a protein that forms 2:1 complexes with multiple metals to predict which metal would be acquired in the context of a cell. Figure 6.1 describes the derivation of the equations describing this inter-metal competition with proteins that form 2:1 complexes with metals.

As the β_2 affinity values for Cu(I) and Zn(II) are now known for PLS (3.79×10^{19} M^{-2} and 3.76×10^{12} M^{-2} respectively, Chapter 3), the adapted "β calculator" can be used to compete the protein for the two metals and gain insight into its predicted metalation *in-vivo*. The derivation of equations used in the "β calculator" are shown below and describe the inter-metal competition of a protein (P) that forms a 2:1 complex (MP_2) with a range of metals ($M_{1\text{-}n}$).

The following equilibrium describes the formation of a 1:2 complex of metal (M) and protein (P)

$$M + 2P \leftrightharpoons MP_2$$

The equilibrium constant for the association of the reaction is

$$\beta_2 = \frac{[MP_2]}{[M][P]^2} \qquad (6.1)$$

Consider a protein which can bind n different metals (namely M_1 to M_n) each with 1:2 stoichiometry for M:P. The fractional occupancy of the protein with the metal of interest, M_i (where i=1,2,…,n.), can be defined as:

$$Fractional\ occupancy\ (\%) = 100 \text{ x } \frac{2[M_iP_2]}{[P]_{tot}} \qquad (6.2)$$

The following is the mass balance equation for the protein

$$[P]_{tot} = [P] + 2[M_1P_2] + 2[M_2P_2] + \cdots + 2[M_nP_2] \qquad (6.3)$$

Equations *(2)* and *(3)* can be combined to give

$$\frac{2[M_iP_2]}{[P]_{tot}} = \frac{2[M_iP_2]}{[P]+2[M_1P_2]+\cdots+2[M_nP_2]} \qquad (6.4)$$

Substituting *(1)* into *(4)* gives

$$\frac{2[M_iP_2]}{[P]_{tot}} = \frac{2\beta_{2i}[M_i][P]^2}{[P]+2\beta_{2(1)}[M_1][P]^2+\cdots+2\beta_{2(n)}[M_n][P]^2} \qquad (6.5)$$

Simplifying leaves the fractional occupancy in terms of metal affinities (β_2), availabile metal concentrations ([M]), and concentration of *apo*- (uncomplexed) protein ([P]).

$$\frac{2[M_iP_2]}{[P]_{tot}} = \frac{2\beta_{2i}[M_i]}{[P]^{-1}+2\beta_{2(1)}[M_1]+\cdots+2\beta_{2(n)}[M_n]} \qquad (6.6)$$

The *apo*-protein concentration is itself a function of metal affinities, total protein concentration and availabile metal concentrations. Substituting *(6.1)* into *(6.3*) and rearranging gives

$$[P]_{tot} = [P] + 2\beta_{2(1)}[M_1][P]^2 + \cdots + 2\beta_{2(n)}[M_n][P]^2$$

$$So: \left(2\beta_{2(1)}[M_1] + \cdots + 2\beta_{2(n)}[M_n]\right)[P]^2 + [P] - [P]_{tot} = 0 \qquad (6.7)$$

Can solve this equation for [P] using the quadratic formula:

$$[P] = \frac{-b \pm \sqrt{b^2-4ac}}{2a} \qquad (6.8)$$

Where: $a = 2\beta_{2(1)}[M_1] + \cdots + 2\beta_{2(n)}[M_n], b = 1\ and\ c = -[P]_{tot}$

The fractional occupancy of the protein with the metal of interest can therefore be expressed as a function of metal affinities, metal availabilities and total protein concentration (*ie* measurable parameters) by combining equations (*6.6*) and (*6.8*)

$$\frac{2[M_iP_2]}{[P]_{tot}} = \frac{2\beta_{2(i)}[M_i]}{\frac{-b\pm\sqrt{b^2-4ac}}{2a}^{-1} + 2\beta_{2(1)}[M_1] + \cdots + 2\beta_{2(n)}[M_n]} \qquad (6.9)$$

Where: $a = 2\beta_{2(1)}[M_1] + \cdots + 2\beta_{2(n)}[M_n], b = 1 \; and \; c = -[P]_{tot}$

Using equation (*6.8*), $[P]_{tot}$, known affinity values, (β_2), and buffered metal concentrations $[M_{1\text{-}n}]$, the free protein concentration, [P], can first be calculated. Then using equation (*6.6*), the fractional occupancy of each metal can be calculated (derivations made with the help of Dr Tessa Young, adapted from the existing calculator equations (Young et al., 2021)).

In addition to the available buffered metal concentration and β_2 value, the concentration of PLS must also be known to model the metalation of molecules that form 2:1 complexes, as the metalation becomes dependent on the protein concentration (see equation *(6.6),* above*)*

Figure 6.1 shows a simulation, using the β calculator, of the predicted metalation of PLS when the concentration of PLS is varied from 1 – 1 000 000 µM. The simulation was carried out using two different sets of Zn(II) and Cu(I) availabilities, measured in *E. coli* JM109(DE3) (Foster et al., 2022). First, the availabilities when the sensors were at the midpoints of their response – also called “idealised” cellular conditions and second, the availabilities measured when *E. coli* JM109(DE3) cells are grown under standard aerobic LB growth conditions. In both cases, the absolute metalation of PLS with both Zn and Cu increases as the concentration of PLS is modelled to increase.

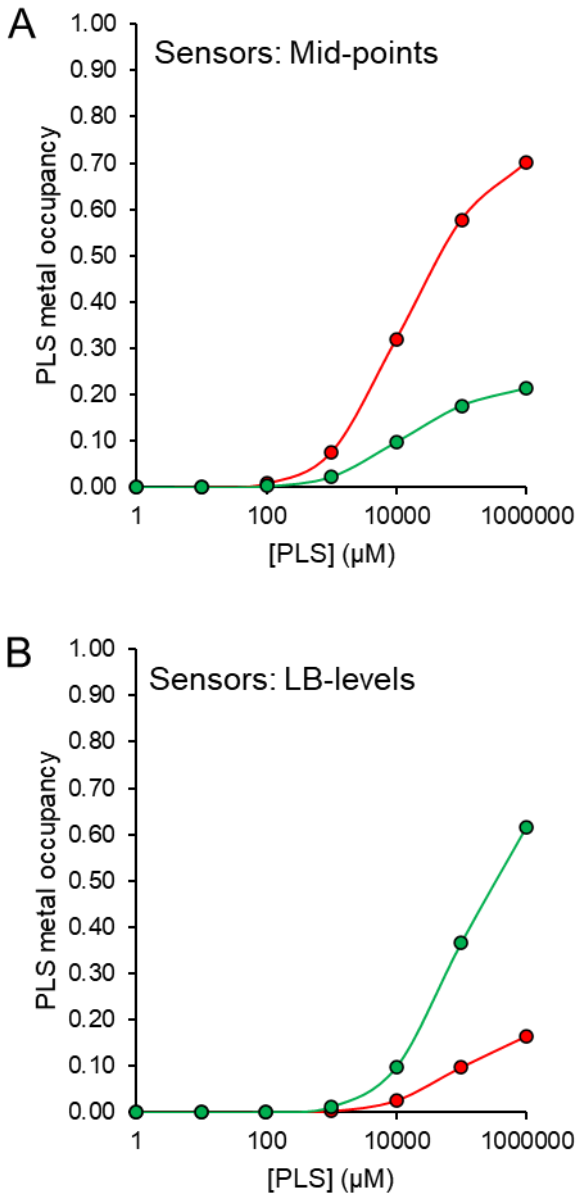

Figure 6.1, Effect of protein abundance on PLS metalation predictions. Relative occupancy of PLS with Zn (green) and Cu (red) when PLS forms 1:2 complexes with both metals, and intracellular [PLS] is varied. Simulations shown using free metal availabilities at sensor response midpoints when measured in JM109(DE3) (A) and at metal availabilities measured in JM109(DE3) LB growth conditions (B).

When the sensors are set to the midpoints, the concentration of PLS would have to be approximately 1 mM before any significant metalation is predicted, whereas when the availabilities are set at the measured LB levels, concentrations nearer 10 mM would be required before significant metalation is predicted. Interestingly, when sensors are set to the midpoints, PLS is predicted to bind Cu(I) preferentially over Zn(II). However, when the LB-measured availabilities are used, PLS is predicted to bind Zn(II) preferentially over Cu(I). This can be explained by the fact Cu(I) was measured to be much less available in cells grown in LB, when compared to the idealised cell, whereas the Zn(II) availabilities were closer to the idealised cell values. These results highlight the importance of knowing the availability of metals and the concentration of PLS where it acquires its metal, to correctly calculate its *in-vivo* metalation.

6.2 Metalation of PLS as a function of Atx1Cu(I) metalation

By using the Cu(I)-occupancy of the *A. thaliana* metallochaperone Atx1 as a proxy for the Cu(I) availability in the plant cytosol, it is possible to model the Cu(I) metalation of PLS as a function of Atx1Cu(I) metalation, and hence predict, using more physiologically relevant parameters, whether PLS is expected to acquire Cu(I) in the cytosol. Using the β calculator, the Cu(I) and Zn(II) occupancy of PLS has been modelled across the full range of Atx1Cu(I) occupancies from 1 - 99% (Figure 6.2), using the experimentally derived PLS β_2 affinities for Cu(I) and Zn(II) (see Chapter 3). The modelling was applied at a range of PLS concentrations from 1 μM – 1 mM, to investigate the effect PLS concentration has on the model and what hypothetical concentration of PLS would be required to predict significant Cu(I) metalation. In all simulations, Zn(II) availability was set to the measured values in *E. coli* JM109(DE3). At all concentrations of PLS modelled, as the occupancy of Atx1 with Cu(I) is increased, the metalation of PLS with Cu(I) increases. As the concentration of PLS modelled is increased, the metalation with both Cu(I) and Zn(II) increased – however, in order to achieve any significant Zn(II) metalation, the concentration of PLS is predicted to be unfeasibly high. When the predicted PLS metalation at the midpoint of the Atx1 “response” is examined (i.e., at the availability at which Atx1 is predicted to be 50% metalated with Cu(I)), PLS would have to be at very high concentrations in order to become metalated with Cu(I). To achieve only 25% metalation with Cu(I), the PLS concentration would be required to be approximately 1 mM. Such a high concentration requirement implies that it is unlikely PLS can directly extract Cu(I) from the buffer alone in the cytosol of *Arabidopsis* as previously imagined.

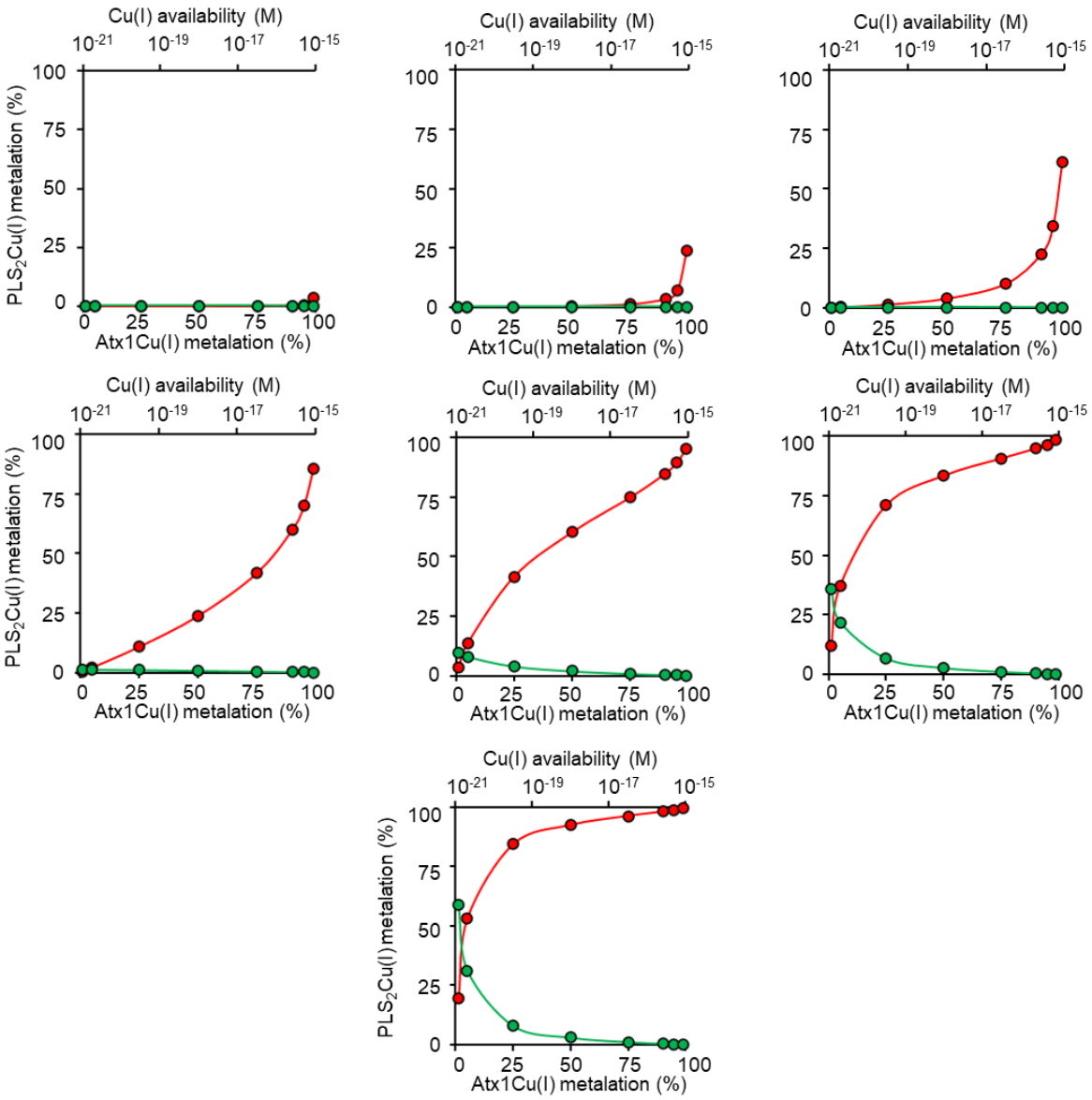

Figure 6.2, Simulating metal occupancy of PLS as a function of Atx1 Cu(I) occupancy. Percentage occupancy of PLS with Cu(I) and Zn(II) (red and green respectively) when the predicted Cu(I) occupancy of Atx1 is varied from 0.1-99.9% and [PLS] is varied from 1 µM – 1 M. Intracellular Cu(I) availability calculated when Atx1 is 1, 5, 10, 25, 50, 75, 90, 95 and 99% metalated, [Atx1] set to 536 µM (see section 4.6.2) and intracellular Zn(II) availability set to measured JM109 LB levels. All PLS-metal affinities (β_2) other than Cu(I) and Zn(II) set to 1 M^{-2}.

This chapter has shown that metalation of PLS with Cu(I) and Zn(II) can be estimated using affinities and stoichiometries as measured in chapter 3 and an approximation of the availability of Cu(I) using the metalation of the Cu(I)-binding chaperone Atx1 as a readout in the cytosol of *Arabidopsis thaliana* (from Chapters 4 and 5).

The simulations highlight the absolute necessity to understand the intracellular metal availabilities in the environment in which the protein of interest is receiving its metal. Furthermore, it seems unlikely that the role of PLS is in direct extraction of Cu(I) from the cytosol for delivery to the ethylene signalling pathway, as is explored further in chapter 7.

Chapter 7. Discussion and future work

The vital detection of ethylene by plant cells, in response to numerous exogenous stimuli and endogenous cues, is mediated by two-component sensors such as ETR1. In turn ethylene binding and detection by ETR1 is mediated by atoms of copper, potentially in direct interaction with ethylene (Figure 1.12). The metalation of ETR1 with copper is thus significant in terms of plant development and physiology but also potentially as a paradigm for the metalation of cuproproteins in endo-membranes more widely. Here, we first explored the possibility that a small protein PLS, required for normal ETR1 response, might be a cupro-protein with possible role(s) analogous to metallochaperones and redox-accessory factors in the cell. PLS is predicted to be involved in the metalation of other cuproproteins, especially those metalated with copper within internal compartments such as the ER and TGN, and of those with copper sites embedded in membranes such as the Cu_B site (albeit metalation of Cu_A could also be pertinent) of cytochrome oxidase. The results highlighted questions around the formation of metal-dependent 2:1 protein:metal complexes in biology. They also highlighted the urgent need to define metal availabilities (and metalloprotein abundances) within the compartments of eukaryotic cells in general and specifically in plants. The metal affinities of a plant metallochaperone Atx1 were determined as a first approximation of metal-availability in the plant cytosol, and again this highlighted questions around the formation of metal dependent 2:1 protein:metal complexes (with zinc in the case of Atx1). Bringing together data on the metal affinities of PLS and estimates of metal availabilities in a plant compartment, this work concluded with theoretical and experimental studies to explore and predict the likely *in-vivo*

metalation states of PLS and Atx1 and to calculate the metalation of metal-dependent 2:1 complexes in biology more generally.

7.1 *In-vitro* metal binding to PLS

To provide insight into the metalation of PLS within the context of the cell, the affinities and stoichiometries of the protein for various metals were measured *in-vitro* (Chapter 3). We showed that PLS binds Cu(I) in a 2:1 PLS:metal stoichiometry with a β_2 affinity of 3.79×10^{19} M^{-2} and Zn(II) in a 2:1 stoichiometry with a β_2 affinity of 3.76×10^{12} M^{-2}, both metals dependent on both cysteines C6 and C17.

It could be argued that the prevalence and implications of metal-mediated 2:1 complexes of small proteins and other metal-binding biomolecules, has not been adequately considered in biology. The conditions used in many analytical tools available to biochemists, for example assorted forms of native chromatography generally do not allow metal dependent dimers to remain associated – it is not common practice to buffer metals to the physiological availabilities in which the protein is functional/associated. Significantly, for metal-dependent 2:1 complexes, the concentration of the ligand also becomes especially pertinent for complex assembly, whereas this is not the case for species that form 1:1 complexes. The ability to compete these 2:1 complexes with other 2:1 complexes in a concentration-dependent manner might offer insight into these under-studied molecules, for example in shedding light on the feasibility of the delivery of a specific metal. The first iteration of a 2:1 calculator (section 6.1), allows the metalation prediction of molecules that form 2:1 complexes with metals, within the

cell, in the context of the intracellular metal availabilities. Modelling the metalation of PLS using the β-calculator has now become possible, but in comparison to the previous 1:1 calculator, requires additional information. As the formation of metal-dependent 2:1 complexes is dependent on the concentration of the protein, this value is also needed, along with the metal availability in the protein's environment.

The consideration of concentration-dependence for protein:metal:protein complexes has often not been considered and has the possibility to uncover new avenues for both spatial and temporal control of specific metal delivery within dynamic sub-cellular compartments such as the eukaryotic trans-golgi network (TGN). There is precedence for vesicular-mediated metalation, in some cases where metalation can even occur more than once, for example the eukaryotic tyrosinase acquires copper only transiently in the TGN, and is re-metalated as the vesicles develop (Setty et al., 2008). It is thought that the initial loss of metalation is driven by a decrease of pH, affecting the protonation of histidines in the binding site (Aguirre & Pilon, 2016) and as they mature, the pH increases and the tyrosinase is re-metalated. Although this appears to be a pH-dependent metalation strategy in the TGN, there may be an analogous role for (protein complex)-concentration-dependent metalation/delivery mediated by vesicular fusion or transport effecting volume and hence promoting a dilution of protein:metal complex.

In the case of PLS, the availability of metals within the various intracellular compartments of *Arabidopsis thaliana* remains unknown. Therefore, for the first time, here we set out to experimentally read-out the Cu(I) availability within a eukaryotic cell by investigating the metalation of the *Arabidopsis thaliana* cytosolic copper chaperone Atx1.

7.2 Estimating the Cu(I) availability in the cytosol using the *Arabidopsis thaliana* Cu(I) metallochaperone Atx1.

7.2.1 *In-vitro* metal binding to Atx1 from *Arabidopsis*

Experimentally derived dissociation constants for metal:protein interactions must be measured under strict conditions in order to reliably measure these metal affinity values (Young & Xiao, 2021b). For this reason, the accuracy of many historic literature estimates for these values for metalloproteins has been brought into question, for example the association constants for the human Atox1 has varied by over 10 orders of magnitude in the past from values of ~10^5 M^{-1} (Wernimont, Yatsunyk, & Rosenzweig, 2004) through ~10^{10} M^{-1} (Yatsunyk & Rosenzweig, 2007) to the recent values of 10^{17} M^{-1} (Xiao et al., 2011). With respect to the metalation of Atx1 and its related proteins, many estimates have been revisited and recalculated using strict conditions (Xiao et al., 2011). Although there are now robust estimations for the metal affinities of various Atx1 proteins across organisms such as Humans, Yeast and Cyanobacteria (Table 7.1) (Badarau et al., 2013; Xiao et al., 2011; Xiao & Wedd, 2010), there have been no affinity measurements for the *Arabidopsis thaliana* Atx1. Here, through competition studies against the standard, rigorously characterised, metal-probes BCA and BCS we show the *Arabidopsis* Atx1 binds Cu(I) in a 1:1 stoichiometry with a K_d of 5.47x10^{-18} (section 4.2.1, section 4.2.2). Further characterisation of the Atx1Cu(I) complex also confirmed the 1:1 stoichiometry by analytical size exclusion chromatography (section 4.3).

The Cu(I) K_d value obtained for the *Arabidopsis* Atx1 appears to be comparable to literature values for the cyanobacterial, human and yeast analogues, albeit very marginally weaker.

Table 7.1, Cu(I) binding affinities of related Atx1 proteins. Dissociation constants (K_d) for 4 homologous Atx1 proteins including the values generated in this work.

Atx1 source	K_d (M)	reference
Synechocystis	2.13×10^{-18}	(Badarau et al., 2013)
Human	3.98×10^{-18}	(Xiao & Wedd, 2010)
Yeast	1.99×10^{-18}	(Xiao et al., 2011)
Arabidopsis	5.47×10^{-18}	(this work, section 4.2.2)

Work by Dainty and co-workers had suggested that the cyanobacterial Atx1 might bind Zn(II) *in-vivo* (Dainty et al., 2010), hence here we explored the interaction of the *Arabidopsis* Atx1 with Zn(II) and characterised the stoichiometry and affinity of this complex. This work has shown that *Arabidopsis* Atx1 binds Zn(II) in a 2:1 stoichiometry which can be described by two binding events: *apo*-Atx1 association with one Zn(II) (with a $K_{d2}=7.12x10^{-8}$) followed by Atx1Zn(II) association with an additional *apo*-Atx1 (with a $K_{d3}=4.09x10^{-6}$), as described in section 4.2.3. These affinities were used to simulate a condition at which the 2:1 species was prevalent (table 4.3) and subsequently tested *in-vitro* by size-exclusion chromatography, confirming the validity of the 2:1 model (see Section 4.3). This binding stoichiometry (through two binding events) was also observed by Badarau and Dennison, for the cyanobacterial Atx1 (Badarau & Dennison, 2011), and the Zn(II) binding affinities generated in this work appear comparable to those measured for the cyanobacterial Atx1 (table 7.2), although again, the initial Zn(II) binding event appears slightly weaker in *Arabidopsis.* It should also be noted that the cyanobacterial Atx1 also contains an unusual third liganding histidine residue, shown to be part of the metal site and displaced on interaction with the ATPase (Banci et al., 2004). This additional residue could possibly give the cyanobacterial Atx1 a slightly tighter affinity seen here.

Table 7.2, Zn(II) binding affinities of related Atx1 proteins. Dissociation constants (K_d) for homologous Atx1 proteins from *Synechocystis* and *Arabidopsis* including affinities generated in this work. K_{d2} and K_{d3} refer to the dissociation constants 2 and 3 respectively from equations in figure 4.10.

Atx1 source	K_{d2}	K_{d3}	reference
Synechocystis	1.38×10^{-9}	6.67×10^{-6}	(Badarau & Dennison, 2011)
Arabdiopsis	7.12×10^{-8}	4.09×10^{-6}	(this work, section 4.2.3)

7.2.2 Atx1 metalation in *E. coli* expression systems

7.2.2.1 Modelling Atx1 metalation as a function of Cu-availability in E. coli

During this work, we constructed a set of equations (Section 5.1) which allow the calculation of the metalation state of Atx1 when the metal binding site of Atx1 is completed for both Zn (in a 2:1 complex) and Cu (in a 1:1 complex). The metal affinities for Cu(I) and Zn(II) for Atx1 (Section 4.2) were incorporated into this model, *in-silico*, to compete these two metals and ascertain the metalation preference of Atx1 (Figure 5.3). Here we show that when modelling the availabilities using existing setpoints and LB levels in JM109(DE3) (Figure 5.2), the activation of the Cu(I) and Zn(II) sensors (CueR and ZntR respectively) affects the metal preference of Atx1. This result was not unexpected: both sensors are metal-responsive transcriptional activators, where in metal excess (high metal availability), sensor molecules are more active, bind their cognate metal and activate genes implicated with decreasing the intracellular availability of that metal. However, the concentration of the Atx1 protein itself was also shown to affect the preferential metalation, where more abundant protein favours the formation of the 2:1 Zn(II)$Atx1_2$ complex over the 1:1 Cu(I)Atx1 complex, and less abundant protein the reverse. This phenomenon arises due to Le Chatelier's principle, where the formation of the 2:1 complex (Zn(II)) is favoured over the 1:1 complex (Cu(I)) as the concentration of protein is increased relative to metal.

When we explore the predicted Cu(I)-metalation of Atx1 (figure 5.3), the occupancy with Cu(I) appears to be tracking with Cu availability range. We observe that the predicted Cu(I) metalation of Atx1, as a function of intracellular Cu(I) availability, spans the entire physiological response range seen in *E. coli* –

where at the minimum and maximum availabilities, Atx1 is approximately 0 and 100 % metalated respectively. This observation is in support of the postulation that Atx1 may modulate the activity of the RAN1 exporter as a function of its metalation in the plant cytosol. At no intracellular copper availability (in *E. coli*) would Atx1 be predicted to be unresponsive to metal (for example is not metalated, or is saturated with Cu(I)), therefore the action of *apo*-Atx1 and Atx1Cu(I), in relation to its role in metalation and de-metalation of the MBD of Ran1 (Figure 1.11), remains plausible. Indeed, this might even suggest that the availabilities in the *Arabidopsis* cytosol might be quite close to those in the *E. coli* cytosol.

7.2.2.2 Overexpression of Atx1 affects intracellular metal availabilities in E. coli.

The activation of the copper-responsive activator CueR, when measured using *copA* transcript abundance, is lower in *E. coli* cells expressing Atx1 than cells not expressing Atx1, under all conditions tested (section 5.2.1). Additionally, when expression of *copA* is compared across the range of Cu-supplemented growth conditions, at higher concentrations of supplementation, the activation of the sensor appears to stall. Here we highlight that the intracellular availability of Cu(I), at which the *E. coli* sensor stalls, correlates with the estimated intracellular availability at which we predict Atx1 to become metalated. We postulate that as copper enters the cell, initially the availability is insufficient for the Atx1 to extract it from the buffer. As the availability increases, the proportion of metalated CueR increases and hence activates transcription associated with the production of CopA exporter. In conditions where the copper availability is elevated (those above 500 μM Cu here), the Atx1 is predicted to be able to extract Cu(I) from the

buffer – where the massively abundant Atx1 outcompetes the sensor for additional Cu(I), resulting in no further increase of θ_{DM} for the sensor and hence CopA transcription.

These observed changes in the metal availability of Cu have significant relevance to industrial biotechnology with respect to the heterologous expression of metalloproteins within *E. coli,* and the application of metalation calculators. One notable example of heterologous expression of a plant cuproprotein is the plant polyphenol oxidase (PPO), essential in production of pigments. PPOs are an economically important class of enzymes that require Cu(I) – they are classed within the type-III copper family which has a di-copper active centre. However, the mode of action of these proteins remains unknown (Kampatsikas & Rompel, 2021). There is significant interest in studying PPOs due to their role in food deterioration, especially in enzymatic browning (Taranto et al., 2017) but historically there was a lack of a recombinant expression systems to produce soluble, functional PPO in order to study the structure and function of the protein. The work of Dirks-Hofmeister et al., show that it is possible to increase the production of soluble, functional plant PPOs (tomato and dandelion) by using lower growth temperatures and, importantly, including 0.2 mM $CuCl_2$ in the growth media (Dirks-Hofmeister, Kolkenbrock, & Moerschbacher, 2013). With the ability to read out the availability of Cu in the cytosol of the expression system, it now becomes possible to subtly tweak the intracellular Cu(I) availability in recombinant expression systems by reading out the availability using qPCR with *copA*. These tweaks can be made through conditional growth changes, to match the copper availability estimation made in *Arabidopsis thaliana* in this work and ensure correct metalation of plant proteins in *E. coli* systems.

Here we have shown that by measuring the Zn-dependent transcript for *zntA* in BL21(DE3) (pET29a), it is not possible to calculate the intracellular Zn availability, as the response observed lies outside the calibrated range in *E. coli* JM109 (section 5.5.2). In order to calculate accurate estimates for the true availabilities within the BL21(DE3) cells containing the pET29a plasmid, this specific strain/vector combination would have to be recalibrated together, as was originally the case for JM109(DE3) when relating the sensor responses to those measured in *Salmonella* (Foster et al., 2022). A range of growth conditions would be chosen in BL21(DE3) pET29a, including H_2O_2, EDTA and metal-supplemented conditions to test which would produce the maximum and minimum response of ZntR (by measuring abundance of ZntA transcript). These boundary values could then be used in calculation of the $\Delta\Delta_{Cq}$ values (section 2.6.3).

BL21(DE3) and JM109(DE3) *E. coli* cells differ in their metallohomeostatic machinery. BL21(DE3), in comparison to JM109(DE3) has altered nickel and cobalt homeostasis (Pinske, Bönn, Krüger, Lindenstrauß, & Sawers, 2011). This strain has been shown to have defects in the *nik* operon, which encodes for the NikABCDE ATP-binding cassette (ABC) transporter. Amino acid mutations in NikA (a periplasmic binding protein), NikD and NikE (ATP-binding components) (Jeong et al., 2009) result in defects to nickel transport which in-turn affect hydrogenase biosynthesis in the cell (Pinske et al., 2011). The expression of the *nik* operon is also regulated by the transcriptional regulator FNR (Kang, Weber, Qiu, Kiley, & Blattner, 2005) which itself is mutated in BL21(DE3) (Pinske et al., 2011). Additionally, the Rcn system including the nickel/cobalt exporter RcnA and metal-dependent de-repressor RcnR, is completely absent from BL21(DE3) (Blaha et al., 2011; Jeong et al., 2009). Alongside the deficiencies in all the above

metallohomeostatic components, the BL21(DE3) system in this work also included the pET29a plasmid, which itself will create a Zinc requirement on the cell through expression of additional Zinc-requiring cuproproteins. For example, enzymes such as β–lactamases expressed as resistance genes, are zinc-dependent (Fabiane et al., 1998) and have their own Zn-requirements. Hence, further calibration of the whole BL21(DE3) pET29a system is required as described above.

7.2.2.3 Metal preference can be predicted correctly in Atx1 post-extraction

Calculations to predict the metalation of purified recombinant Atx1 expressed in BL21(DE3) under 1 mM Cu conditions, estimate a Cu(I) and Zn(II) metalation of 8.2 and 0.52 % respectively (section 5.3.3). Atx1 was purified under these same conditions and its metalation experimentally derived as a test for the metalation calculator (section 5.3.1). Comparison of the predicted metalation of Atx1 with the observed occupancy revealed that Atx1 does indeed preferentially bind Cu(I) in preference to Zn(II), however more metal was recorded on the protein than predicted (table 5.3), approximately 3 times more copper and 15 times more zinc. There are many factors which could result in the metalation of Atx1, and proteins in general, post-chromatography not fully reflecting the metalation of the protein *in-vivo*. This is especially the case for proteins which might bind weaker (and hence more exchangeable metals). As these metal-binding sites in the protein are inherently exchangeable (except for unique cases such as MncA which can kinetically trap metals), during chromatography, the metalation status *in-vivo* can shift during the purification protocol, resulting in analysed metalation profiles that do not match the *bona-fide in-vivo* metalation. It is possible that a contribution to

the Atx1 metalation could have been provided also by metal contamination post-purification. Zinc is a common contaminant from laboratory plasticware and growth media (Kay, 2004, and personal observations) and the buffers used in this experimental protocol were not treated with Chelex to remove these contaminating metals. Indeed, as seen in section 4.3, *apo*-Atx1 was able to pick up Zn contamination during analytical size exclusion chromatography, where even if the contamination is present at low concentrations, for example in the running buffer, the protein is exposed to a large volume where it can pick up metal during chromatography. In addition to contamination, changes in the concentration of the Atx1 during the purification process would affect the metalation of the $Atx1_2Zn(II)$ complex, as its formation is concentration dependent. As $Atx1_2Zn$ and Atx1Cu(I) elute at different volumes by size exclusion chromatography (section 4.3), during separation, the concentration of Atx1 in the two different species is likely to change and one species might be favoured over the other.

Importantly, a specific proviso of the calculators is that the protein of interest does not deplete the buffered metal pool (Foster et al., 2022). For the expression of Atx1 to decrease the intracellular Cu(I) availability within the cell here, we predict that a proportion of the protein will have to be bound to Cu(I) and acting as part of the buffer itself and depleting the buffer of Cu(I). This proportion of Atx1 that is bound to Cu(I) is not accounted for in these calculations and the resultant predictions could hence be providing an underestimate for the total metalation of Atx1 with Cu(I) *in-vivo*. A valuable future experiment would involve the addition of Apo-atx1 to cell lysate from JM109 cells, grown under a certain condition in which the Cu and Zn availability has been measured by qPCR.

7.2.3 Atx1 as a readout of the Cu(I) availability in the cell

By measuring the Cu(I) and Zn(II) affinities of Atx1 and reading out the metalation of PLS when Atx1 is predicted to be 50% metalated only gives a putative “midpoint” at which Atx1 is predicted to be in the middle of the response curve. This first estimate of the Cu(I) availability within the cytosol of *Arabidopsis thaliana* effectively only represents an “idealised” cellular cytosol. These values are indeed useful and have been used to great effect in the metalation calculators for *Salmonella,* however, as shown when comparing PLS metalation predictions using “LB” compared with “mid-point” values (Figure 6.1), predicted metalation at the sensor midpoint can dramatically vary from the correct “conditional” availabilities. As with the *Salmonella* sensors, any Cu-dependent changes in Atx1 levels would also need to be investigated and accounted for, in order to control the effects of hysteresis (Osman et al., 2019). This is the reason why the direct use of the K_d for the metalated sensor molecules does not always align directly with the midpoint of the response curve. Similarly, *Arabidopsis* also contains an additional Atx1-homologue called Arabidopsis copper chaperone (CCH) (Puig et al., 2007). CCH shares the same structure and conserved Cu(I) binding motif as Atx1 and contains a plant-specific C-terminal extension. As CCH is found in non-nucleated cells, it is the only known metallochaperone described to function intercellularly, and the C-terminal tail is thought to be involved in its translocation through plasmodesmata (Himelblau et al., 1998; Mira, Martínez-García, & Peñarrubia, 2001). The interplay between these two Atx1 proteins has yet to be shown in *Arabidopsis*, especially with respect to a role of CCH interacting with the P-type ATPase RAN1, but the action of an additional Atx1-homologue within the cytosol could also affect the availability readout.

The difficulty in using Atx1 to read out conditional cell availabilities prompts the search for alternative methods to read out these availabilities in plants. The recent emergence of other metal-responsive transcriptional regulators offers new routes for reading the availability in the cytosol of *Arabidopsis.* The two central Zn-dependent transcriptional regulators bZIP19 and bZIP23 provide a strong starting point to characterising metal availability in the cytosol, using the same methods used in characterising *Salmonella*. Interestingly the transcriptional regulator SPL7 (which is involved in regulation in response to copper in plants) seems to show metal-responsive transcriptional regulation (Aguirre & Pilon, 2016; Bernal et al., 2012). The protein has been shown to form homodimers *in-vivo* outside of the nuclei and this dimerization is thought to act as a form of post-translational control whereby the formation of the transcription factor dimer prevents the protein from entering the nucleus (Garcia-Molina, Xing, & Huijser, 2014). Despite not being shown to directly interact with copper itself, this post-translational mechanism of regulation by dimerization could provide an additional mechanism for how metal-dependent dimerization of transcriptional regulators could control metal homeostasis in nucleated organisms, and hence highlight the importance of modelling such interactions using the β-calculator developed during this work.

7.3 PLS is unlikely to extract Cu(I) directly from the cytosol of *Arabidopsis thaliana*

By using the β-calculator developed through the course of this study (section 6.1), the metalation of PLS can be predicted for various intracellular availabilities and PLS concentrations. Initial simulations using the intracellular Zn(II) and Cu(I) availabilities from both idealised *E. coli,* and LB-levels in *E. coli,* predict opposing metalation preferences (figure 6.2) highlighting the need to accurately estimate the intracellular copper availability in *Arabidopsis*. On expressing PLS metalation as a function of Atx1 metalation (and hence using Atx1Cu(I) as a readout for the copper response in *Arabidopsis*) it becomes possible to model the zinc and copper occupancy of PLS as a function of the PLS concentration (figure 6.2). We conclude that PLS is unlikely to extract Cu(I) from the cytosol in *Arabidopsis thaliana*. In order for PLS to be able to extract Cu(I) directly from the cytosolic buffer, the concentration would have to be in excess of physiologically feasible values within the cell.

7.3.1 Exploring PLS localisation

The inability of PLS to directly extract Cu(I) from the cytosol raises the question: where then is PLS localised within the cell? Could it be localised within the ER as originally envisioned at the outset of this work?

Exploring a role within the oxidising environment of the ER, it is possible that the Cu(I)-coordinating thiols would be oxidised and the MET and HIS could play a larger role in the coordination of Cu(II) instead of Cu(I). However, as the species imported into the ER by the P-type ATPase RAN1 is Cu(I), in our model, we

hypothesize that PLS would receive Cu(I) directly, stabilising and solubilising reduced Cu(I) within the ER for delivery to ETR1.

If PLS is indeed localised cytosolically, its role is predicted to not be extraction of Cu(I) from the buffer, at least not as a PLS:Cu(I) 2:1 complex. Here we postulate that PLS could have a role at the ER membrane, in coalition with ETR1 and/or RAN1. It has previously been observed that the predicted α-helix on PLS contains three repeated lysine residues spaced by 3 amino acids, resulting in an amphipathic helix that might be facilitate protein:protein interactions. Additionally, the difficulties encountered solubilising the PLS protein (fusion-free) might hint at a functional role in interaction with the membrane. Naturally, as RAN1 and ETR1 are both membrane-bound at the ER, it could be possible the action of PLS is limited to the membrane surface, where in conjunction with ETR1, RAN1 or other accessory proteins, facilitates the correct metalation of ETR1 or Cu(I) transport by RAN1.

Titrations with the probe BCS also revealed PLS' ability to form metal-mediated ternary complexes, suggesting that PLS might possibly partake in metal-dependent heterodimeric interactions. Further study is required with respect to the functional relevance of Cu(I)-mediated PLS heterodimers, especially with respect to other Cu(I) binding regulatory motifs such as the MBD on RAN1 (analogous to activity with Atx1), ETR1 and other putative copper chaperones. Characterisation of the metal affinities of multiple Cu(I)-mediated heterodimers, in conjunction with the β-calculator, could provide a powerful resource in future for elucidating the passage of Cu(I) within the cell. By extension, the relevance of a Cu(I)-dependent RAN1 MBD interaction with Atx1 in *Arabdiopsis thaliana* remains to be shown – analogous studies showing this interaction and downstream changes in domain

dynamics (as shown in the human Atox1/WNDP system) are still required, and hence the post-transcriptional regulatory function of ATX1 remains to be proven other than through analogy.

With the recent emergence of more sophisticated techniques for visualising the structure and function of membrane/bound proteins and lipids such as cryo-EM microscopy (Cheng, 2018), the role of lipids and membranes are increasingly being explored with respect to metal homeostasis. The role of lipids in metal homeostasis in plants is relatively understudied, although protein-lipid-metal interactions have been proposed to regulate aspects of metal homeostasis in plant cells (Wu, Saleem, He, & He, 2021). The plant membranes are made up of a wide array of molecules including membrane proteins and highly diverse lipids, which have been proposed to also be able to partake in membrane protein-lipid-metal interactions in regulating metal homeostasis. The metalation of some proteins has even been shown to be regulated by the type of lipids interacting with the protein (Wu et al., 2021), where the protein only binds metal in the presence of specific lipids. Thus in future, more consideration of the lipid-requirements of membrane-bound metalloproteins must be taken, when characterising the metal-binding of such proteins.

7.3.2 Paradigms from Cu(I) delivery at the mitochondrial inner membrane of yeast

Eukaryotic yeast cells largely require copper in just three compartments: the cytosol, trans-golgi network (TGN) and mitochondria (Robinson & Winge, 2010). The delivery of copper to the yeast cytochorome *c* oxidase (CcO) at the

mitochondrial inner membrane (IM) might offer paradigms for the action of PLS at the ER membrane in *Arabidopsis*. CcO, which acts as the terminal acceptor in the respiratory electron chain in most eukaryotic organisms (Ostermeier, Iwata, & Michel, 1996), contains two copper binding sites (Cu_A and Cu_B) and yeast mitochondria contain a large suite of copper metallochaperones and transporters to serve both sites (Robinson & Winge, 2010). Analogous to the Cu-binding site in ETR1, the Cu_B site of CcO is also embedded within a membrane (although here, the inner mitochondrial membrane (IM)). The metal delivery to both sites in CcO begins with the metalation of the small metallochaperone Cox17 which acquires the copper within the intramembrane space (IMS) from non-proteinaceous small molecules within the matrix. Cox17 then donates Cu(I) to the two metallochaperone pathways involved in the metalation of both copper sites: the Cu_A site via Sco1 and Cox2, or the Cu_B site via Cox11 and Cox1.

On examination of the structure of Cox17, comparisons can be drawn with PLS (Figure 7.1, Figure 1.9). During characterisation, it was clear that PLS binds Cu(I) in a 2:1 ratio, and the formation of a central Cu(I) coordinated two or four thiol groups on the two PLS molecules seems likely. This predicted dimeric structure resembles that of the structure seen in Cox17: two parallel α-helices with residues from a relatively unstructured region coordinating Cu(I) at one end (Abajian, Yatsunyk, Ramirez, & Rosenzweig, 2004).

Cox17 also contains conserved positively charged residues Lys19, Lys21 and Arg33 (Abajian et al., 2004) which have been proposed to provide a role in target recognition: where the two downstream chaperones Sco1 and Cox11 contain a negatively charged patch adjacent to their copper binding sites (Figure 7.2).

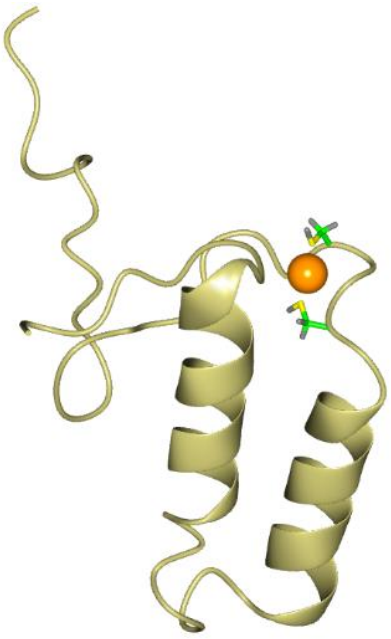

Figure 7.1, Structure of Cox17. Ribbon diagram showing NMR solution structure for the Cox17 protein bound to a copper ion (orange) Cys 23 and Cys 26 shown in coordination with the copper ion. UniProt accession: 1U96.

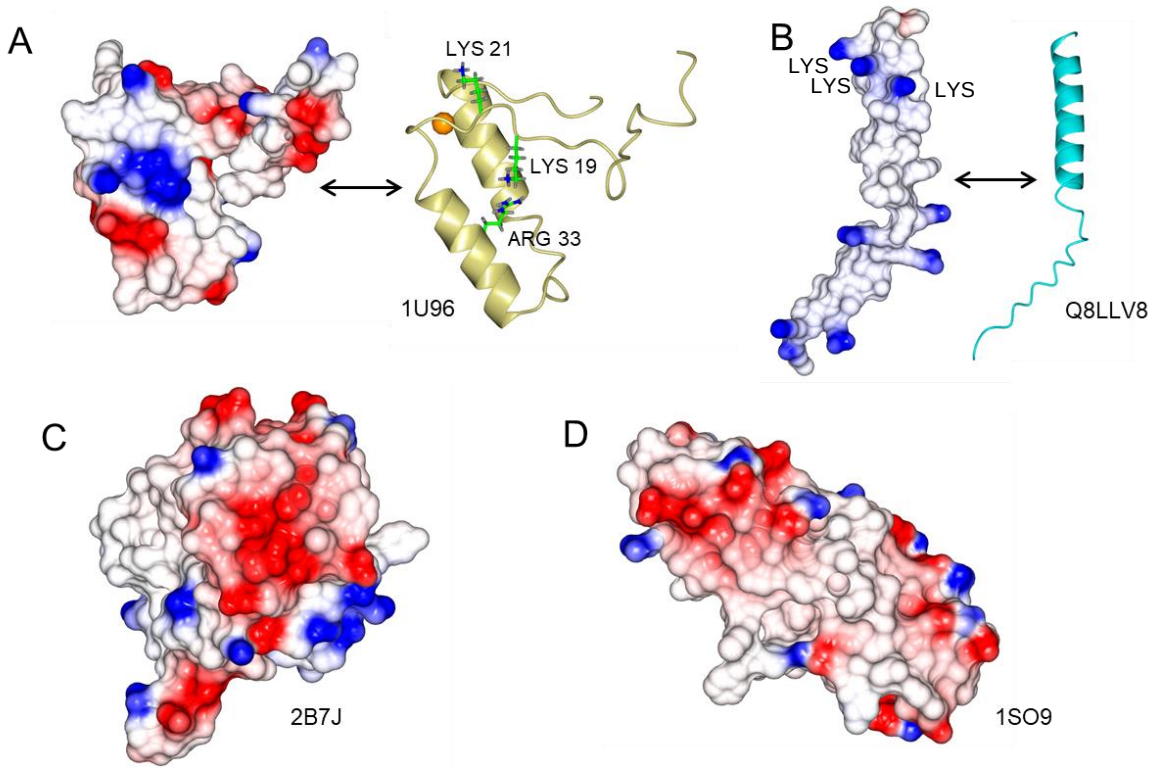

Figure 7.2, Electrostatic potential representations for Cu(I) binding proteins. Ribbon diagram showing A, Ribbon diagram and electrostatic potential surface map of yeast Cox17 solution structure bound to a copper ion, conserved positively charged amino acids labelled. B, Ribbon diagram and electrostatic potential surface map of AlphaFold predicted structure for *Arabidopsis* PLS showing three conserved lysines at the top of the α-helix. C and D show the electrostatic surface potential maps for the two yeast proteins Sco1 and Cox11 respectively, showing the red negative charge patches. UniProt accessions included. Figure generated using CCP4MG software package.

The α-helix of PLS also contains the C-terminal region repeat – KLFKLFK, creating an amphipathic helix where the lysine residues create a positively charged face due to their spacing (Figure 7.2). This predicted region has been postulated as providing the facility for PLS protein-protein interactions (Casson et al., 2002) and the precedent set by Cox17 hints towards a protein:protein interaction mechanism with respect to the action of PLS. Again, highlighting the need to explore metal-mediated heterodimeric interactions between PLS and downstream Cu-binding motifs.

As cysteine-based binding of Cu(I) is totally dependent on the deprotonated state of the ligands, electron donation becomes an important consideration, especially when the localisation of Cu(I) delivery may be more oxidising – for example within the ER lumen of *Arabidopsis*. The transfer of Cu(I) from human Cox17 to Sco1 has been shown to be coupled to electron transfer between the two proteins (Banci et al., 2008). Cox17 contains 6 cysteine residues and the Cu(I) metalated form contains two intramolecular disulphide bridges with the remaining two cysteines coordinating the Cu(I). This species was shown to donate both electrons and Cu(I) to Sco1, thereby reducing the receiver intramolecular disulfide site on Sco1 and delivering Cu(I) (Banci et al., 2008). Therefore, could there be an electron transfer role for PLS? It is possible that the predicted PLS dimer could employ 2 reduced cysteine residues to coordinate Cu (possibly in conjunction with small copper binding molecules such as GSH) and two remaining cysteines, adjacent to the Cu-binding site, remain to partake in disulfide bridge exchange as is the case for Cox17. Further study would be required to elucidate such a role as this in the $PLS_2Cu(I)$ dimer.

7.4 Mechanistic biochemical insights into ethylene sensing and signal transduction by ETR1: future hypotheses

ETR1 has homology to the bacterial two-component receptors (Chang, Kwok, Bleecker, & Meyerowitz, 1993). The mechanism which is central to the bacterial two-component receptors involves autophosphorylation of a histidine residue, followed by phosphotransfer to an aspartate residue on the receiver domain. Despite this function being retained in the ETR1 receptor, is not central to its function (Wang, Hall, O'Malley, & Bleecker, 2003).

In spite of the large volume of research in investigating the response of the ethylene receptors to ethylene binding (Binder, 2020), there remain gaps in the understanding of some specifics of signal transduction. Research has however outlined a canonical linear mechanistic pathway, regulated by ETR1, from detection to response (Figure 7.3).

The conformational changes and specific molecular rearrangements within the ETR1 trans-membrane helices, at the level of both Cu(I) and ethylene binding events, remain largely unknown. The two residues Cys 65 and His 69 have been shown to be responsible for the coordination of Cu(I) (Rodríguez et al., 1999), where their mutation to Ser and Ala respectively resulted in complete loss of Cu(I) binding. The ethylene has also been shown to bind proximally to this Cu(I) binding site (Schott-Verdugo, Müller, Classen, Gohlke, & Groth, 2019), however no research to date has shown direct interaction between the copper atom and the ethylene molecule.

Non-covalent bonds play an extremely important role in biology, for example in hydrophobic interactions, hydrogen bonding, and ionic interactions. Cation-π

interactions are another form of non-covalent interaction where a positively charged cation interacts with the negative π-face of benzene rings and other aromatic structures (Dougherty, 1996). This interaction is highly prevalent amongst the

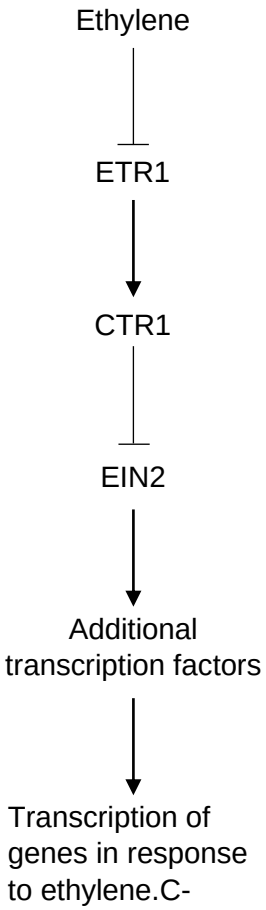

Figure 7.3, Canonical linear model for ethylene signalling via ETR1. Ethylene binds and negatively regulates the activity of ETR1. ETR1 functions to activate the protein kinase CTR1 via an unknown mechanism (Zhang, yu and Wen, 2014). CTR1 phosphorylates the membrane-tethered transcription factor EIN2, resulting in its ubiquitination and targeting for degradation (Ju *et al.*, 2012. In the absence of phosphorylation, EIN2 is cleaved and the C-terminal portion is translocated to the nucleus where it increases the transcriptional activity of several other transcription factors to promote a response to ethylene exposure. Adapted from Binder, 2020.

aromatic amino acids, especially in tryptophan where it is estimated that over a quarter of all tryptophan residues in the protein data bank experience an energetically significant cation-π interaction (Gallivan & Dougherty, 1999). Cation-π interactions have also been shown to have a functional role in the coordination of Cu(I) where within the periplasmic protein CusF, the Cu(I) is displaced from one ligand arrangement towards a conserved tryptophan (Xue et al., 2008).

In the case of the Cu(I) and ethylene binding sites in ETR1, it has been proposed that Cu(I) might directly interact with the ethylene through cation-π interaction with the delocalised electrons shared in the C=C double bond (Lacey & Binder, 2014). Therefore, here we extend a mechanistic hypothesis for the function of ETR1, based on a three state model (Figure 7.4) for the reaction cycle of ETR1 (Lacey & Binder, 2014; Wang et al., 2006), and offer 3 potential models for its regulation by PLS at the ER membrane (Figures 7.5, 7.6 and 7.7).

The model for ethylene response previously (and for simplicity in the introduction section of this work) was proposed as an “inverse-agonist” model where ETR1 is constitutively active in the absence of ethylene, and on binding ethylene, this activity is abolished. Further mutational analysis studies on ETR1 however has identified numerous mutations which allow the ethylene sensor to be held in an intermediate state (state 2), where ETR1 binds ethylene and retains its activity. This work presented a three-state model seen in Figure 7.4 which is developed further here.

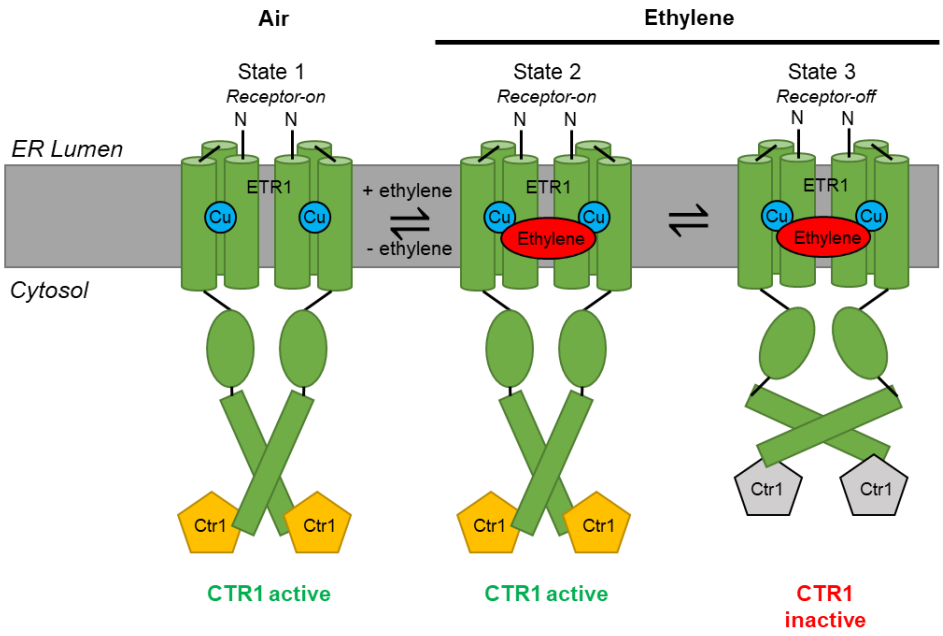

Figure 7.4, Current three-state model for ETR1 signalling. In air, ETR1 takes conformation state 1 in the "receptor on" state, ETR1 activates CTR1 (yellow pentagons) which negatively regulates the ethylene response. On binding ethylene, ETR1 takes an intermediate conformation where it remains in the "receptor on" state, activating CTR1. This state transitions to state 3 where ETR1 takes a "receptor off" conformation, CTR1 is not activated (grey pentagons) and the transcriptional changes in response to ethylene are de-repressed. Adapted from Lacey and Binder, 2014.

7.4.1 Model 1: PLS is indirectly involved in the correct metalation/delivery of Cu(I) to ETR1, either from the cytosolic or luminal face of the ER membrane.

Here we propose that there is an additional state (state 0) for ETR1 (Figure 7.5), when the ETR1 trans-membrane Cu(I) site is not correctly metalated with its Cu(I) cofactor. In this case, ETR1 cannot bind to ethylene due to a loss of cation-π interaction with Cu(I), and CTR1 cannot be activated by ETR1. The result is constitutive responses in the presence or absence of ethylene.

The binding of Cu(I) to ETR1 here is predicted to distort/recruit ligands and cause a conformational change to the “receptor-on” conformation which facilitates CTR1 activation. Ethylene binding, coordinated by cation-pi interactions with Cu(I), perturbs the Cu(I) ligands, as seen in CusF (Xue et al., 2008), resulting in a “receptor-off” conformation, and ETR1 cannot activate CTR1. In the case where no Cu(I) is bound (presumably in *pls* mutants), ligands are again not distorted into the correct conformation, ETR1 is in the “receptor off” conformation and CTR1 cannot be activated.

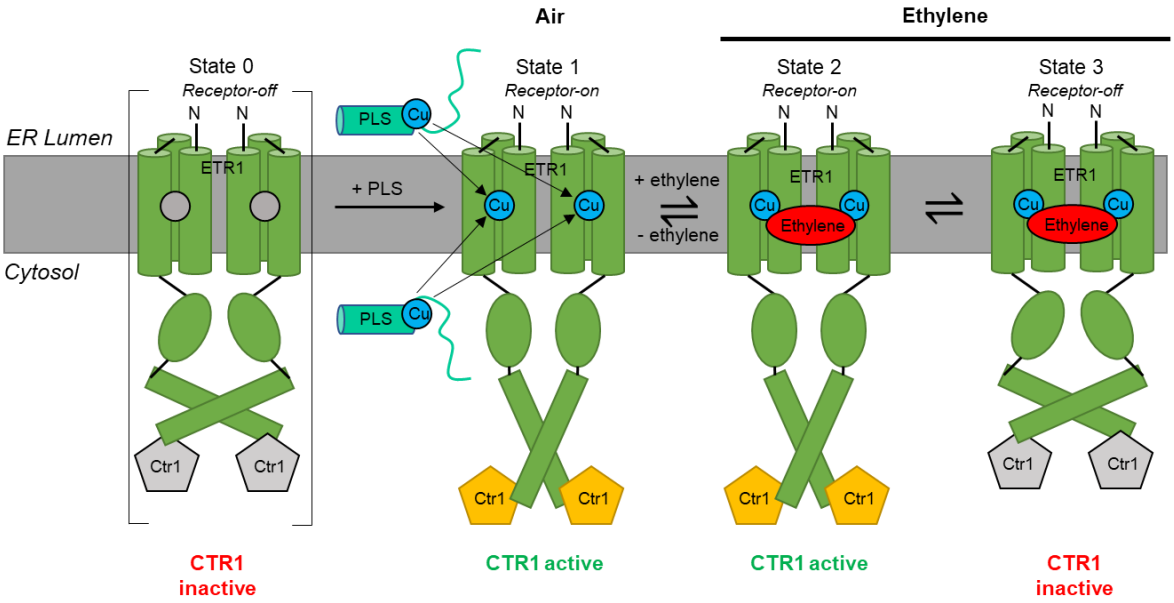

Figure 7.5, Model 1: PLS is indirectly involved in the correct metalation of ETR1 from either the cytosolic or luminal face of the ER. In the absence of correct metalation, ETR1 takes on a "state 0" conformation where ETR1 is unable to activate CTR1 (grey pentagons), resulting in the de-repression of the transcriptional changes in response to ethylene. PLS is responsible for the delivery of Cu(I) to the intra-membrane binding site in ETR1 and on delivery, the receptor enters state 1. In the absence of PLS, the prevalent state of ETR1 is predicted to be state 0 and the ethylene responses proceed constitutively.

7.4.2 Model 2: PLS facilitates the return of ETR1 from state 3 to state 2, possibly also to facilitate ethylene release from ETR1 thereby "resetting" the receptor.

The dissociation of ethylene from ETR1 has been shown to have very slow-release kinetics, with a half-life of 12 h (O'Malley et al., 2005). It is hence possible that ETR1 requires an additional mechanism for release, or for transitioning from "receptor off" state 3 back to "receptor-on" state 2.

Wang and co-workers, through identifying regions important for ETR1 signalling, identified residues at the cytosolic end of the three transmembrane-spanning helices that were required to achieve the "receptor on" state (Wang et al., 2006). It is possible that this region, at the cytosolic surface of the ER membrane, could feasibly serve as a surface for protein:protein interaction with PLS.

Therefore we propose a model where PLS, through Cu(I)-bridged heterodimeric interaction with ETR1 at the cytosolic surface of the ER membrane facilitates (via an unknown allosteric mechanism) the transition of ETR1 from "receptor off" state to "receptor on" state, thereby resetting the receptor (Figure 7.6). In the case of the *pls* mutant the receptor is jammed in state 3 ("receptor off") and CTR1 is not activated, thereby de-repessing the ethylene signalling pathway in the presence or absence of ethylene.

This mechanism also serves to a biochemical basis as to why the state 2 and state 3 in the model have different activities despite appearing identical – the difference being the association with PLS.

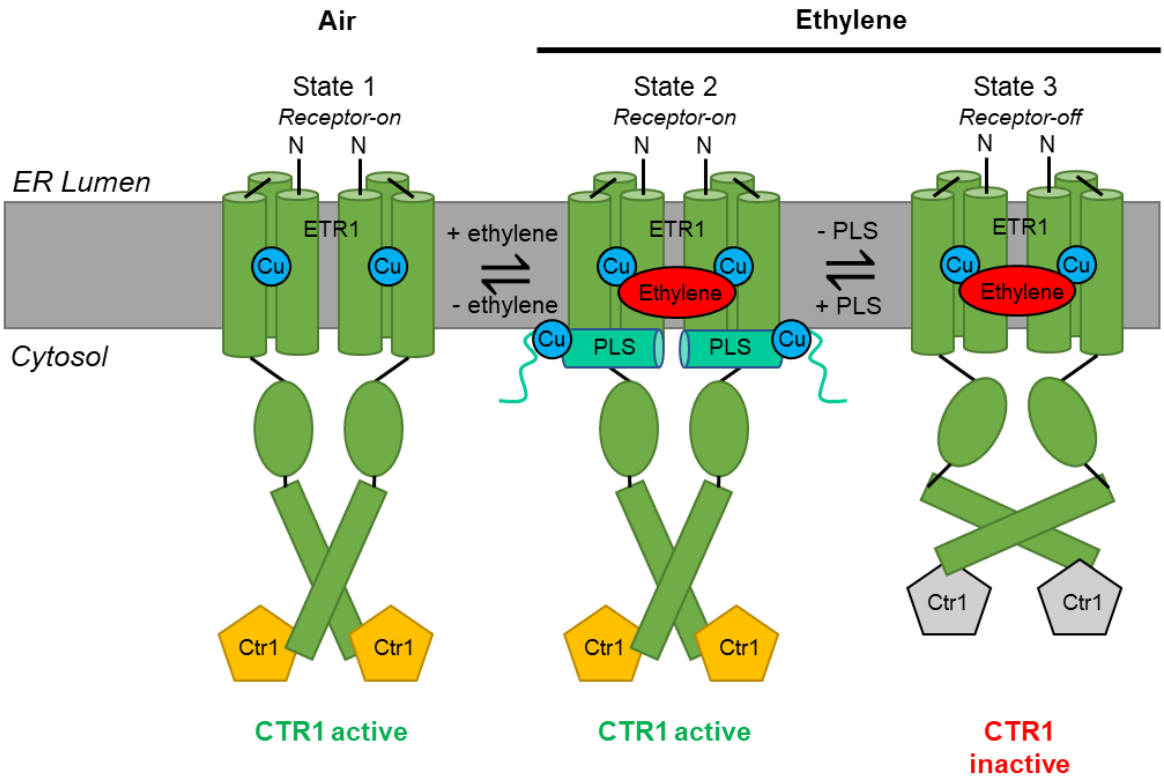

Figure 7.6, Model 2: PLS facilitates the return of state 3 to state 2. Metalated PLS binds to the cytosolic end of the trans-membrane spanning helices of ETR1 in state 3. This binding event allosterically induces a conformational change in ETR1, returning and stabilising it in the "receptor on" state 2. In the absence of PLS, in the *pls* mutant, ETR1 receptor is jammed in the "receptor off" state 3 and the ethylene responses proceed in the presence or absence of further ethylene treatment.

7.4.3 Model 3: PLS has a role in the destabilisation of the complex between CTR1 from ETR1, deprotecting it from Ethylene-mediated turnover

There remains the possibility that ETR1 does not have a circular catalytic cycle where the binding of ethylene can be reset, but where the receptor binds ethylene and is “reset” by degradation and subsequent re-synthesis.

Work by Shakeel and co-workers shows that the post-transcriptional regulation of ETR1 and CTR1 at the ER is extremely dynamic and influenced by several interacting factors. They show that ethylene can both induce the production of new sensors at the ER, but also induce the post-transcriptional turnover of receptors (Shakeel et al., 2015). They also showed that the physical association of ETR1 with CTR1 protects it from this ethylene-induced turnover.

In this model therefore we explore the possibility that the role of PLS might be to destabilise this CTR1/ETR1 interaction in state 3, thereby promoting the turnover of ethylene-bound ETR1 (Figure 7.7). Again, this structure could be a heterodimeric Cu(I)-bridged interaction between PLS and another protein resulting in allosteric change associated with destabilisation o the CTR1/ETR1 interaction.

In the *pls* mutant, CTR1 and ETR1 interaction in state 3 is stable, the receptor is not targeted for degradation/turnover and ethylene responses continue with receptors jammed in the “receptor off” conformation in state 3.

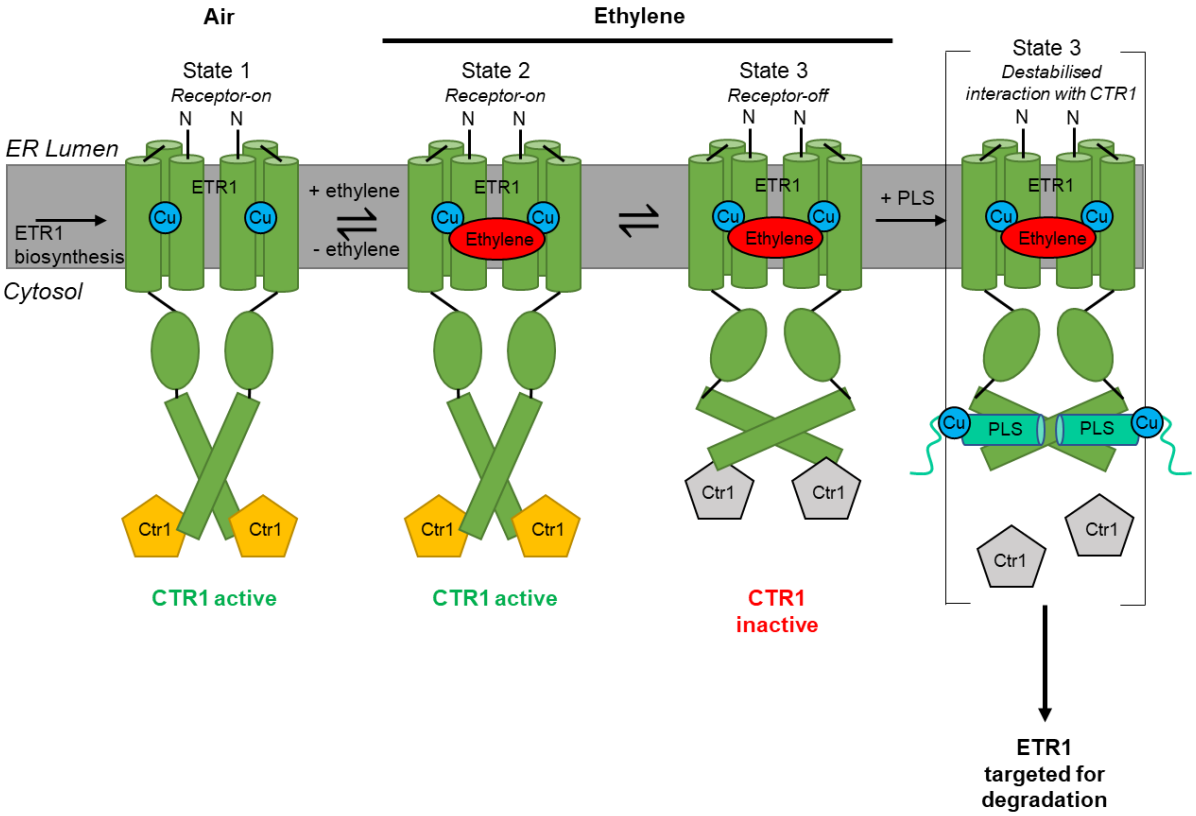

Figure 7.7, Model 3: PLS destabilises the CTR1:ETR1 complex, targeting the receptor for degradation. PLS binds to ETR1 and/or CTR1, causing allosteric changes in the conformation of one or both proteins that results in the release of CTR1 from ETR1. This destabilisation results in the recognition and targeted degradation of the ETR1 receptor thereby "resetting" the catalytic cycle. In the absence of PLS, in the *pls* mutant, ETR1:CTR1 in state 3 is stable and not targeted for degradation, the receptor is hence jammed in the "receptor off" state 3 and the ethylene responses proceed in the presence or absence of further ethylene treatment.

These three models provide three relatively speculative avenues for regulation of the function of ETR1 and the putative action of PLS. There are many studies that would be required to explore these three models in more detail. Initially, there would be merit in validating the interaction of PLS with ETR1, RAN1 and CTR1 *in-vivo* by exploring two component interactions of cloned proteins in yeast two-hybrid screening. This study would validate the prediction that PLS might interact with ETR1 (as is predicted in all three models). Various truncations of the cytosolic domain of ETR1 could elucidate the binding location for PLS, and might offer insight into the function, for example if PLS interacted with residues involved in the switching of ETR1 from “receptor on” to “receptor off” state in model 2. Alternative to yeast two-hybrid, the expression of tagged proteins, combined with high resolution microscopy could also offer routes to elucidate complexes *in-vivo* under more physiologically accurate conditions.

The putative direct interaction of Cu(I) with ethylene, via cation-π interactions, also requires further investigation – there remains the possibility that this interaction could be analysed by IR spectroscopy. Generally, homonuclear diatomic bonds (such as those in O_2, N_2, ethylene) are silent in IR spectroscopy as they have no dipole moment. However, on binding Cu(I), to the ethylene via electron donation from the Cu(I) to the π* orbital of ethylene gives rise to observable stretching frequencies at ~3000-3100 cm^{-1} (Marks, Ward, & Duncan, 2019).

7.5 Final directions

As discussed in section 7.2.3, there remains the urgent need to define metal availabilities within the various compartments of the plant cell, and those in eukaryotes in general. The recent emergence of the two bZIP family Zn-responsive transcriptional regulators show promise for exploring the cytosolic Zn(II) availability in *Arabidopsis,* although due to the scarcity of such systems analogous to those in bacteria, alternative novel approaches may be required in characterising the availabilities of the other metals.

Metal-responsive, cell-permeable, small molecule chromophores are likely to be a useful novel tool in future, used in conjunction with recent advances in high-resolution imaging techniques (Osman & Robinson, 2022). Such techniques have already been used to image copper within cells, even with selectivity for the oxidation state (Chung et al., 2019). In future, these probes offer the exciting opportunity to be calibrated in systems with known availabilities (such as *Salmonella* or *E. coli*), then applied to unknown systems, such as the various intracellular compartments of *Arabidopsis thaliana*.

8. Supplementary materials

Supplementary figure 8.1, Colony PCR optimisation for identification of positive pMal(PLS) transformants. A, Agarose gel electrophoresis for three samples, Lanes 1, 3 and 5 template DNA is from boiled cell material, 2, 4 and 6 the same colony but from purified DNA. B, Agarose gel electrophoresis of PCR reaction (pure pMal plasmid) as concentrations of $MgCl_2$ varied from 0.0 – 2.5 mM (lanes 1-6). C, Agarose gel electrophoresis of PCR reaction whilst optimising annealing temperature (varied from 60 – 70^{o}C, lanes 1-12).

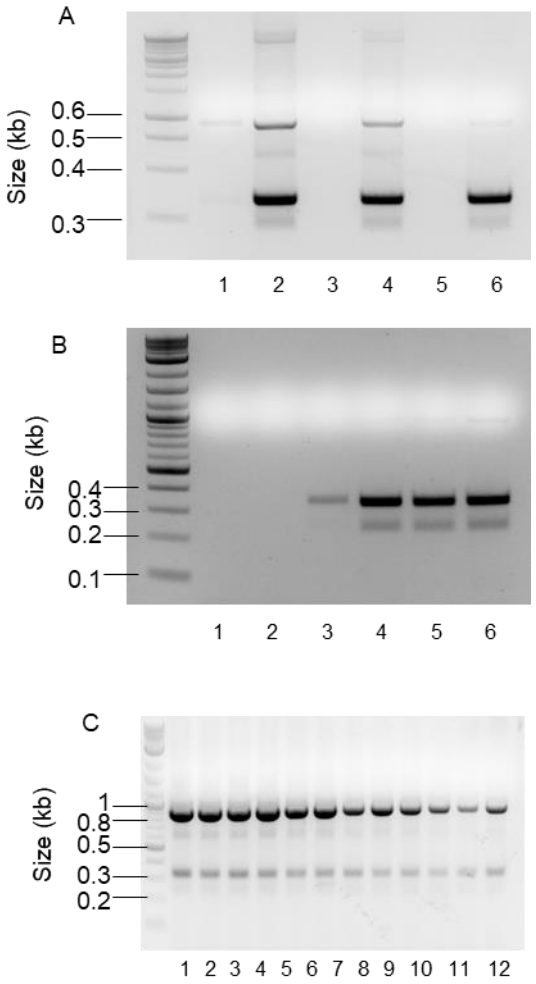

Supplementary Figure 8.2, Codon-optimisation of *Arabidopsis thaliana* gene *atx1* for heterologous expression in *E. coli*.

Wildtype gene amino acid sequence:
>sp|Q94BT9|ATOX1_ARATH Copper transport protein ATX1 OS=Arabidopsis thaliana OX=3702 GN=ATX1 PE=1 SV=2
MSQTVVLRVAMTCEGCVGAVKRVLGKMEGVESFDVDIKEQKVTVKGNVQPDAVLQTVTKT
GKKTAFWEAEGETAKAstop

Wildtype gene nucleotide sequence:
ATGTCACAGACGGTGGTGCTTAGAGTGGCTATGACATGTGAGGGATGTGTTGGAGCTGTGAAAAGAGTTCTTG
GGAAAATGGAAGGCGTGGAGTCATTTGACGTTGATATAAAGGAGCAGAAAGTGACGGTGAAAGGCAACGTGCA
GCCA
GACGCAGTTTTACAGACCGTGACGAAAACCGGAAAGAAAACGGCTTTTTGGGAAGCGGAAGGTGAAACTGCTA
AGGCTTAA

E. coli codon optimised nucleotide sequence (using novoprolabs codon-optimisation):

ATGTCTCAGACCGTTGTGCTGCGCGTTGCTATGACTTGTGAAGGTTGCGTTGGTGCAGTTAAACGTGTGCTGG
GTAAAATGGAAGGTGTTGAATCCTTCGATGTCGATATTAAGGAGCAAAAGGTCACCGTTAAAGGTAACGTTCA
GCCGGACGCGGTGCTGCAGACGGTCACCAAAACCGGTAAAAAAACCGCATTCTGGGAAGCTGAAGGCGAAACC
GCAAAGGCTTAA

Sequence supplied for insertion into pEX cloning plasmid (Eurofins:
AGATCGATCTCGATCCCGCGAAATTAATACGACTCACTATAGGGGAATTGTGAGCGGATAACAATTCCCCTCT
AGAAATAATTTTGTTTAACTTTAAGAAGGAGATATACAT**ATGTCTCAGACCGTTGTGCTGCGCGTTGCTATGA**
CTTGTGAAGGTTGCGTTGGTGCAGTTAAACGTGTGCTGGGTAAAATGGAAGGTGTTGAATCCTTCGATGTCGA
TATTAAGGAGCAAAAGGTCACCGTTAAAGGTAACGTTCAGCCGGACGCGGTGCTGCAGACGGTCACCAAAACC
GGTAAAAAAACCGCATTCTGGGAAGCTGAAGGCGAAACCGCAAAGGCTTAAGAGCTCCGTCGACAAGCTTGCG
GCCGCACTCGAGCACCACCACCACCACCACTGAGATCCGGCTGCTAACAAAGCCCGAAAGGAAGCTGAGTTGG
CTGCTGCCACCGCTGAGCAATAACTAGCATAACCCCTTGGGGCCTCTAAACGGGTCTTGAGGGGTTTTTTGA

underlined
NdeI CATATG
EcoRI – not required because the eurofins plasmid that it comes in has EcoRI just downstream of the gene.

T7 promoter/terminator

Lac operator

Supplementary Figure 8.3, Multiple sequence alignment to confirm correct PLS insertion into pMal vector system. Highlighted region represents expected coding sequence for the PLS portion of the MBP-PLS fusion.

```
Predicted     ATAACAATAACAACAACCTCGGGATCGAGGGAAGGATGAAACCACGCTTGTGCTTTAACT  233
Sequencing:   ATAACAATAACAACAACCTCGGGATCGAGGGAAGGATGAAACCACGCTTGTGCTTTAACT  155
              ************************************************************

Predicted     TTCGTCGTCGCTCCATTAGTCCGTGTTACATCTCGATTAGCTATCTGTTAGTGGCGAAAC  293
Sequencing:   TTCGTCGTCGCTCCATTAGTCCGTGTTACATCTCGATTAGCTATCTGTTAGTGGCGAAAC  215
              ************************************************************

Predicted     TGTTCAAACTGTTCAAGATCCATTAAGTCGACGGATCCGAATTCCCTGCAGGTAATTAAA  352
Sequencing:   TGTTCAAACTGTTCAAGATCCATTAAGTCGACGGATCCGAATTCCCTGCAGGTAATTAAA  275
              ************************************************************
```

Supplementary Figure 8.4, Analysis of the MBP-PLS fusion using ProtParam tool (ExPasy)

Number of amino acids: 423
Molecular weight: 46882.45
Theoretical pI: 6.20
Amino acid composition:

Ala (A)	44	10.4%
Arg (R)	10	2.4%
Asn (N)	33	7.8%
Asp (D)	24	5.7%
Cys (C)	2	0.5%
Gln (Q)	9	2.1%
Glu (E)	28	6.6%
Gly (G)	31	7.3%
His (H)	4	0.9%
Ile (I)	27	6.4%
Leu (L)	36	8.5%
Lys (K)	40	9.5%
Met (M)	8	1.9%
Phe (F)	19	4.5%
Pro (P)	23	5.4%
Ser (S)	19	4.5%
Thr (T)	19	4.5%
Trp (W)	8	1.9%
Tyr (Y)	17	4.0%
Val (V)	22	5.2%
Pyl (O)	0	0.0%
Sec (U)	0	0.0%

Total number of negatively charged residues (Asp + Glu): 52
Total number of positively charged residues (Arg + Lys): 50
Atomic composition:

Carbon	C	2125
Hydrogen	H	3295
Nitrogen	N	551
Oxygen	O	625
Sulfur	S	10

Formula: $C_{2125}H_{3295}N_{551}O_{625}S_{10}$
Total number of atoms: 6606
Extinction coefficients:
Extinction coefficients are in units of M^{-1} cm^{-1}, at 280 nm measured in water.

Ext. coefficient	69455
Abs 0.1% (=1 g/l)	1.481, assuming all pairs of Cys residues form cystines
Ext. coefficient	69330
Abs 0.1% (=1 g/l)	1.479, assuming all Cys residues are reduced

Estimated half-life:
The N-terminal of the sequence considered is M (Met).
The estimated half-life is: 30 hours (mammalian reticulocytes, in vitro).
>20 hours (yeast, in vivo).
>10 hours (Escherichia coli, in vivo).
Instability index:
The instability index (II) is computed to be 22.32
This classifies the protein as stable.

Aliphatic index: 83.57
Grand average of hydropathicity (GRAVY): -0.346

Supplementary Figure 8.5, Analysis of *Arabidopsis thaliana* Atx1 using the ProtParam tool (ExPasy)

Number of amino acids: 76
Molecular weight: 8158.47
Theoretical pI: 7.75
Amino acid composition:

Ala (A)	7	9.2%
Arg (R)	2	2.6%
Asn (N)	1	1.3%
Asp (D)	3	3.9%
Cys (C)	2	2.6%
Gln (Q)	4	5.3%
Glu (E)	7	9.2%
Gly (G)	7	9.2%
His (H)	0	0.0%
Ile (I)	1	1.3%
Leu (L)	3	3.9%
Lys (K)	9	11.8%
Met (M)	3	3.9%
Phe (F)	2	2.6%
Pro (P)	1	1.3%
Ser (S)	2	2.6%
Thr (T)	8	10.5%
Trp (W)	1	1.3%
Tyr (Y)	0	0.0%
Val (V)	13	17.1%
Pyl (O)	0	0.0%
Sec (U)	0	0.0%

Total number of negatively charged residues (Asp + Glu): 10
Total number of positively charged residues (Arg + Lys): 11
Atomic composition:

Carbon	C	354
Hydrogen	H	591
Nitrogen	N	97
Oxygen	O	112
Sulfur	S	5

Formula: $C_{354}H_{591}N_{97}O_{112}S_5$
Total number of atoms: 1159
Extinction coefficients:
Extinction coefficients are in units of M^{-1} cm^{-1}, at 280 nm measured in water.
Ext. coefficient 5625
Abs 0.1% (=1 g/l) 0.689, assuming all pairs of Cys residues form cystines
Ext. coefficient 5500
Abs 0.1% (=1 g/l) 0.674, assuming all Cys residues are reduced
Estimated half-life:
The N-terminal of the sequence considered is M (Met).
The estimated half-life is: 30 hours (mammalian reticulocytes, in vitro).
>20 hours (yeast, in vivo).
>10 hours (Escherichia coli, in vivo).
Instability index:
The instability index (II) is computed to be 24.43
This classifies the protein as stable.

Aliphatic index: 79.34
Grand average of hydropathicity (GRAVY): -0.128

Supplementary Figure 8.6, Screenshot from "Supplementary dataset 1" (Osman et al., 2019) with inputted values describing the parameters for CueR in *E. coli* BL21(DE3).

Protein:	CueR							
Cognate metal	Cu							
Dissociation constants					**Association constants**			
KMe OFF DNA	1/K1	3.30E-19	M		**a**	3.03E+18		
KMe ON DNA	1/K2	3.92E-18	M		**b**	2.55E+17		
KDNAapo	1/K3	3.20E-08	M		**c**	3.13E+07		
KDNAMe	1/K4	3.80E-07	M		**d**	2.63E+06		
KDNAMe/KDNAapo		1.19E+01	M					
Protein Abundance					**Constant values**			
P_0 (without metal)								
Protein Molecules per cell		24	multimers		**DT**	3.32E-09		
Moles per cell		3.99E-23	moles					
Cell volume		1.00E-15	liters		**Constant P0**			
[P_0]		3.99E-08	M		**A_{DM} = P0**	3.99E-08		
					(A_{DM} - DT)	3.65E-08		
P_1 (supplemented metal)								
Protein Molecules per cell		41	multimers		**Costant P1**			
Moles per cell		6.81E-23	moles		**A_{DM}= P1**	6.81E-08		
Cell volume		1.00E-15	liters		**(A_{DM} - DT)**	6.48E-08		
[P_1]		6.81E-08	M					
					Including change in protein abundance			
DNA abundance					**ΔP**	2.82E-08		
DNA targets per cell		2	targets		**$\Delta\theta_{DM}$**	1.51E-01		
Moles per cell		3.32E-24	moles					
Cell volume		1.00E-15	liters		**A_{DM}**	3.99E-08		
[DT]		3.32E-09	M		**B**	1.87E-07		
Absolute DNA Occupancy								
Basal DNA Occupancy (θ_{DM0})		1.39E-06						
Plus Metal DNA Occupancy (θ_{DM1})		1.51E-01						

Supplementary Figure 8.7, Screenshot from "Supplementary dataset 1" (Osman et al., 2019) with inputted values describing the parameters for ZntR in *E. coli* BL21(DE3).

Protein:	ZntR					
Cognate metal	Zn					
Dissociation constants					**Association constant**	
KMe OFF DNA	1/K1	3.20E-12	M		**a**	3.13E+11
KMe ON DNA	1/K2	2.27E-11	M		**b**	4.41E+10
KDNAapo	1/K3	1.10E-07	M		**c**	9.09E+06
KDNAMe	1/K4	7.80E-07	M		**d**	1.28E+06
KDNAMe/KDNAapo		7.09E+00	M			
Protein Abundance					**Constant values**	
P_0 (without metal)						
Protein Molecules per cell		34	multimers		**DT**	1.66E-09
Moles per cell		5.65E-23	moles			
Cell volume		1.00E-15	liters		**Constant P0**	
[P_0]		5.65E-08	M		**A_{DM} = P0**	5.65E-08
					(A_{DM} - DT)	5.48E-08
P_1 (supplemented metal)						
Protein Molecules per cell		29	multimers		**Costant P1**	
Moles per cell		4.82E-23	moles		**A_{DM}= P1**	4.82E-08
Cell volume		1.00E-15	liters		**(A_{DM} - DT)**	4.65E-08
[P_1]		4.82E-08	M			
DNA abundance						
DNA targets per cell		1	targets			
Moles per cell		1.66E-24	moles			
Cell volume		1.00E-15	liters			
[DT]		1.66E-09	M			
Absolute DNA Occupancy						
Basal DNA Occupancy (θ_{DM0})		1.48E-13				
Plus Metal DNA Occupancy (θ_{DM1})		5.80E-02				

Supplementary Figure 8.8, Dynafit scripts for fitting BCA control direct titration data.

```
[model]
BCA binds 1 Cu per 2 molecule

[components]
; C = Cu
; B = BCA

[task]
task = fit
data = equilibria

[mechanism]
 C + B + B  <==> CB2     :    Keq1   association

 [concentrations] ;molar
   B = 18e-6 ?

[constants] ;molar
Keq1 = 158000000000000000

[responses]
CB2 = 44444?

[data]
directory C:/Dynafit/Data
variable C

file Control2.txt

[output]

[end]
```

Supplementary Figure 8.9, Dynafit scripts for fitting competition between BCA and MBP-PLS for Cu(I).

```
[model]

MBP-PLS binds 1 Cu(I) per 2 molecules plus additional non-specific binding sites. BCA binds 1 Cu(I) per 2 molecule.

[components]

; C = Cu
; B = BCA
; P = protein

[task]
task = fit
data = equilibria

[mechanism]
    C + B + B  <==> CB2    :   Keq1   association
    C + P + P  <==> CP2    :   Keq2   association
    C + X  <==> CX    :   Keq3   association
    C + Y  <==> CY    :   Keq4   association

[concentrations] ;molar
  B = 17e-6
  P = 14e-6
  X = 10e-6 ?
  Y = 10e-6 ?

[constants] ;molar
Keq1 = 158000000000000000
Keq2 = 1e20
Keq3 = 2e12 ?
Keq4 = 8e10 ?

[equil]
  variable C
  offset = auto

set data1_1 | response CB2 = 42820
set data1_2 | response CB2 = 42820
set data1_3 | response CB2 = 42820

[output]
[set:data1_1]
X         Y
[set:data1_2]
X         Y
[set:data1_3]
X         Y
[end]
```

Supplementary Figure 8.10, Dynafit script for fitting competition between BCA and MBP-PLS for Cu(I) with additional binding site.

```
[model]

MBP-PLS binds 1 Cu(I) per 2 molecules plus one additional non-specific binding per molecule (X).
BCA binds 1 Cu per 2 molecule

[components]

; C = Cu

; B = BCA

; P = protein

[task]

task = fit

data = equilibria

[mechanism]

    C + B + B  <==> CB2    :   Keq1   association

    C + P + P  <==> CP2    :   Keq2   association

    C + X  <==> CX    :   Keq3   association

[concentrations] ;molar

  B = 50e-6

  P = 10e-6

  X = 10e-6

[constants] ;molar

Keq1 = 158000000000000000

Keq2 = 4.51e19 ?

Keq3 = 1e13

[equil]

  variable C

  offset = auto

set data1_1 | response CB2 = 42900

set data1_2 | response CB2 = 42900

set data1_3 | response CB2 = 42900

[output]

[end]
```

Supplementary Figure 8.11, Sequencing of pET29a(Atx1) to test for correct insertion of Atx1 gene. Multiple sequence alignment of sequencing result and optimised Atx1 gene sequence showing 100% identity (highlighted in blue).

```
sequencing      GGTGGNCGGANACATTCCCCTCTGAATAATTTTGTTTAACTTTAAGAAGGAGATATACAT 60
ATX1            ------------------------------------------------------------ 0

sequencing      ATGTCTCAGACCGTTGTGCTGCGCGTTGCTATGACTTGTGAAGGTTGCGTTGGTGCAGTT 120
ATX1            ATGTCTCAGACCGTTGTGCTGCGCGTTGCTATGACTTGTGAAGGTTGCGTTGGTGCAGTT 60
                ************************************************************

sequencing      AAACGTGTGCTGGGTAAAATGGAAGGTGTTGAATCCTTCGATGTCGATATTAAGGAGCAA 180
ATX1            AAACGTGTGCTGGGTAAAATGGAAGGTGTTGAATCCTTCGATGTCGATATTAAGGAGCAA 120
                ************************************************************

sequencing      AAGGTCACCGTTAAAGGTAACGTTCAGCCGGACGCGGTGCTGCAGACGGTCACCAAAACC 240
ATX1            AAGGTCACCGTTAAAGGTAACGTTCAGCCGGACGCGGTGCTGCAGACGGTCACCAAAACC 180
                ************************************************************

sequencing      GGTAAAAAAACCGCATTCTGGGAAGCTGAAGGCGAAACCGCAAAGGCTTAAGAGCTCCGT 300
ATX1            GGTAAAAAAACCGCATTCTGGGAAGCTGAAGGCGAAACCGCAAAGGCTTAA--------- 231
                ************************************************
```

Supplementary Figure 8.12, Dynafit scripts for fitting MF-2 competition data assuming 1:1 stoichiometry of binding. Fit is for both 325 nm and 366 nm data simultaneously.

```
[model]
Both molecules bind one Zinc atom

[components]
;Z   = Zinc
;M   = Mf2
;P = protein

[task]
   data = equilibria
   task = fit

[mechanism]
     M + Z <==> MZ : Keq1 dissociation
     P + Z <==> PZ : Keq2 dissociation

[constants]  ;micromolar
 Keq1  = 0.02
 Keq2  = 5e-2 ?

[concentrations] ;micromolar.
  M = 20.0
  P = 20.0

[equil]
variable Z
offset = auto
set data1_325 | response MZ = 0.019413 ?
set data1_366 | response MZ = -0.01546 ?


[set:data1_325]
X     y
X     y
X     y
X     y

[set:data1_366]
X     y
X     y
X     y
X     y


[output]
     directory J:\[filename]

[end]
```

Supplementary Figure 8.13, Dynafit scripts for fitting MF-2 competition data assuming both 1:1 and 1:2 stoichiometry of binding. Fit is for both 325 nm and 366 nm data simultaneously.

```
[model]
MF-2 binds one Zn atom, Atx1 binds Zn in either 2:1 or 1:1
stoichiometry.


[components]
;Z   = Zinc
;M   = Mf2
;P = protein

[task]
   data = equilibria
   task = fit

[mechanism]
      M + Z <==> MZ : Keq1 dissociation
      P + Z <==> PZ : Keq2 dissociation
      PZ + P <==> P2Z : Keq3 dissociation

[constants]  ;micromolar
 Keq1  = 0.02
 Keq2  = 5e-2 ?
 Keq3  = 5e-2 ?

[concentrations] ;micromolar.
  M = 20.0
  P = 20.0

[equil]
variable Z
offset = auto
set data1_325 | response MZ = 0.019413 ?
set data1_366 | response MZ = -0.01546 ?


[set:data1_325]
X     y
X     y
X     y
X     y

[set:data1_366]
X     y
X     y
X     y
X     y

[output]
      directory J:\[filename]
[end]
```

Supplementary Figure 8.14, Replicate of *"In-vitro* Characterisation of Apo-Atx1 and Zn-loaded-Atx1 by analytical size exclusion chromatography" (Fig 4.12). UV-traces following elution of 100 µM Atx1 in the presence and absence of 25 µM Zn(II) (blue and black lines respectively) [Superdex^{TM} 75 10/300 GL]. Note, consistency with Zn-dependent shift to heavier mass and Zn eluting with heavier peak, as predicted by 2:1 stoichiometry. Small amounts of Cu eluting with lighter peak, consistent with a 1:1 stoichiometry of Cu(I) binding. Green line represents [Zn] and red [Cu]

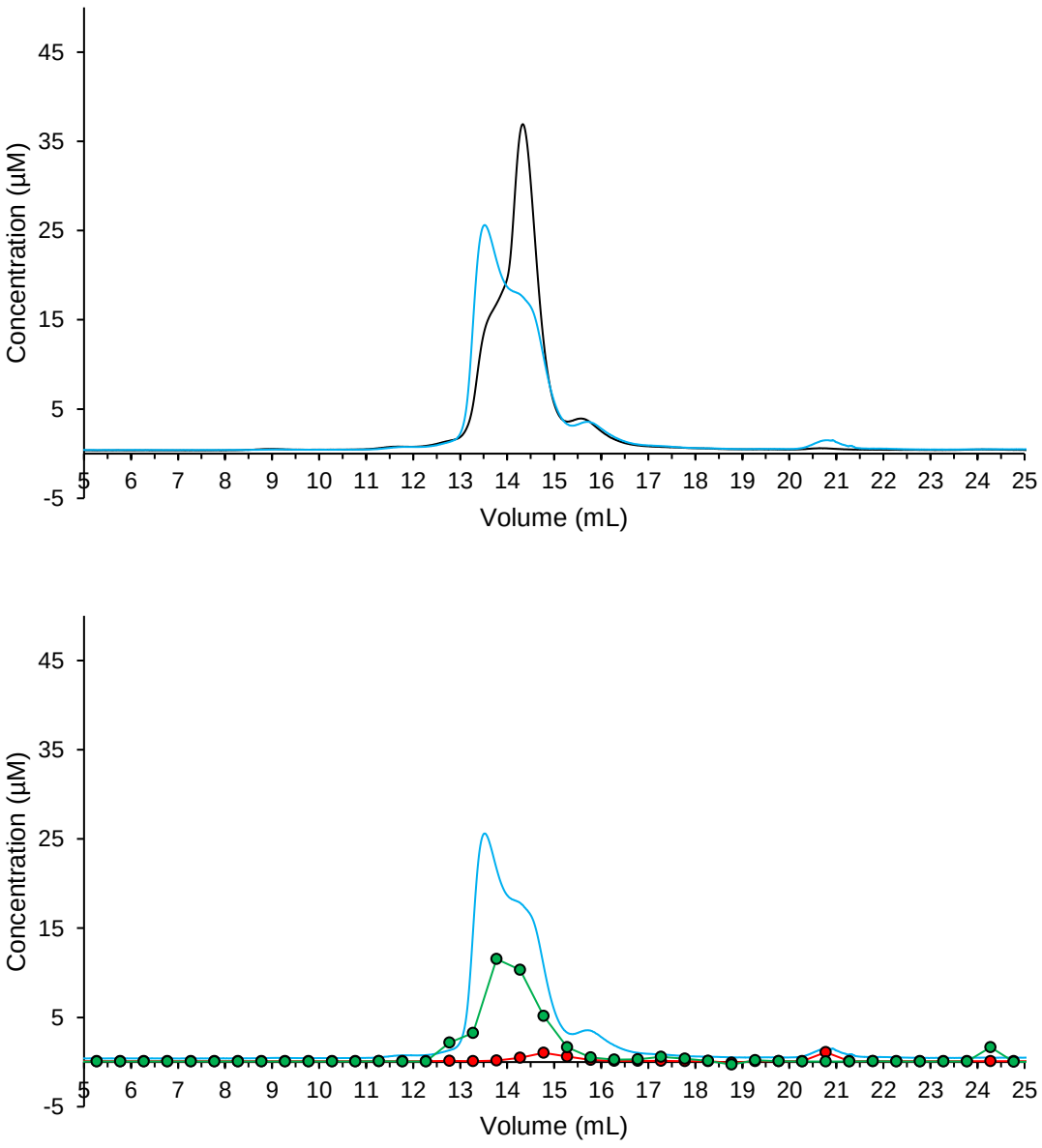

NB: figure continued overleaf.

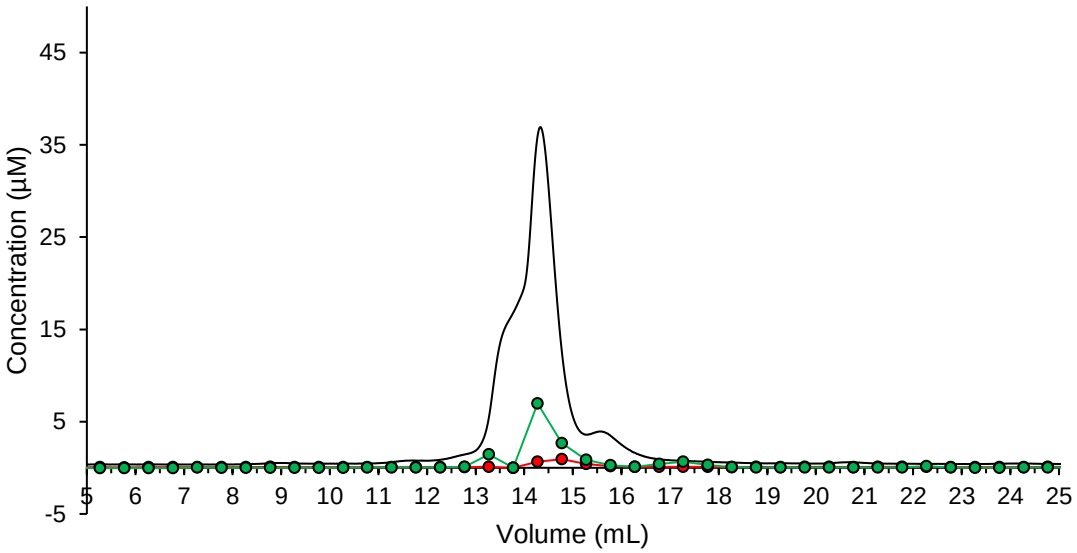
45
35
25
15
5
-5
Concentration (µM)
5 6 7 8 9 10 11 12 13 14 15 16 17 18 19 20 21 22 23 24 25
Volume (mL)

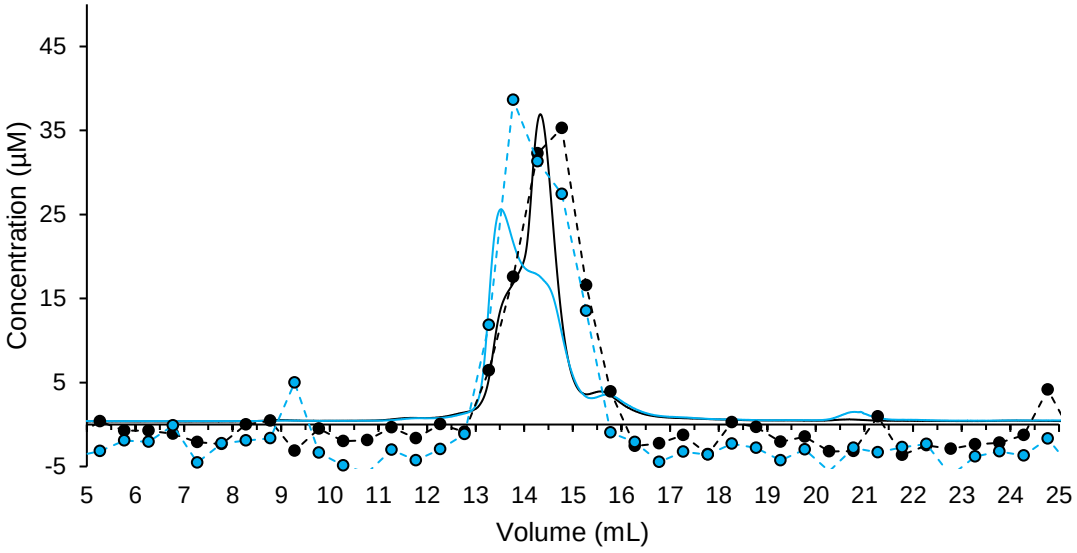
45
35
25
15
5
-5
Concentration (µM)
5 6 7 8 9 10 11 12 13 14 15 16 17 18 19 20 21 22 23 24 25
Volume (mL)

Supplementary Figure 8.15, Replicate of *"In-vitro* Characterisation of Apo-Atx1 and Zn-loaded-Atx1 by analytical size exclusion chromatography" where Zn-contamination of the Apo-sample was observed despite confirmation that the Apo-Atx1 was >95% metal-free pre-chromatography**.** It was predicted that the Zn was picked up on the size exclusion column due to insufficient wash steps between experiments. The experiment was repeated after 3, 0.5 mL 1 mM EDTA bolus washes, using the same preparation of Atx1 apo-protein (Figure 4.15) where the apo-protein returned with much less contaminating Zn – confirming the Zn-contamination was indeed on the column.

UV-traces following elution of 100uM Atx1 in the presence and absence of 25 µM Zn(II) (blue and black lines respectively) [Superdex^{TM} 75 10/300 GL]. Green line represents [Zn] and red [Cu]

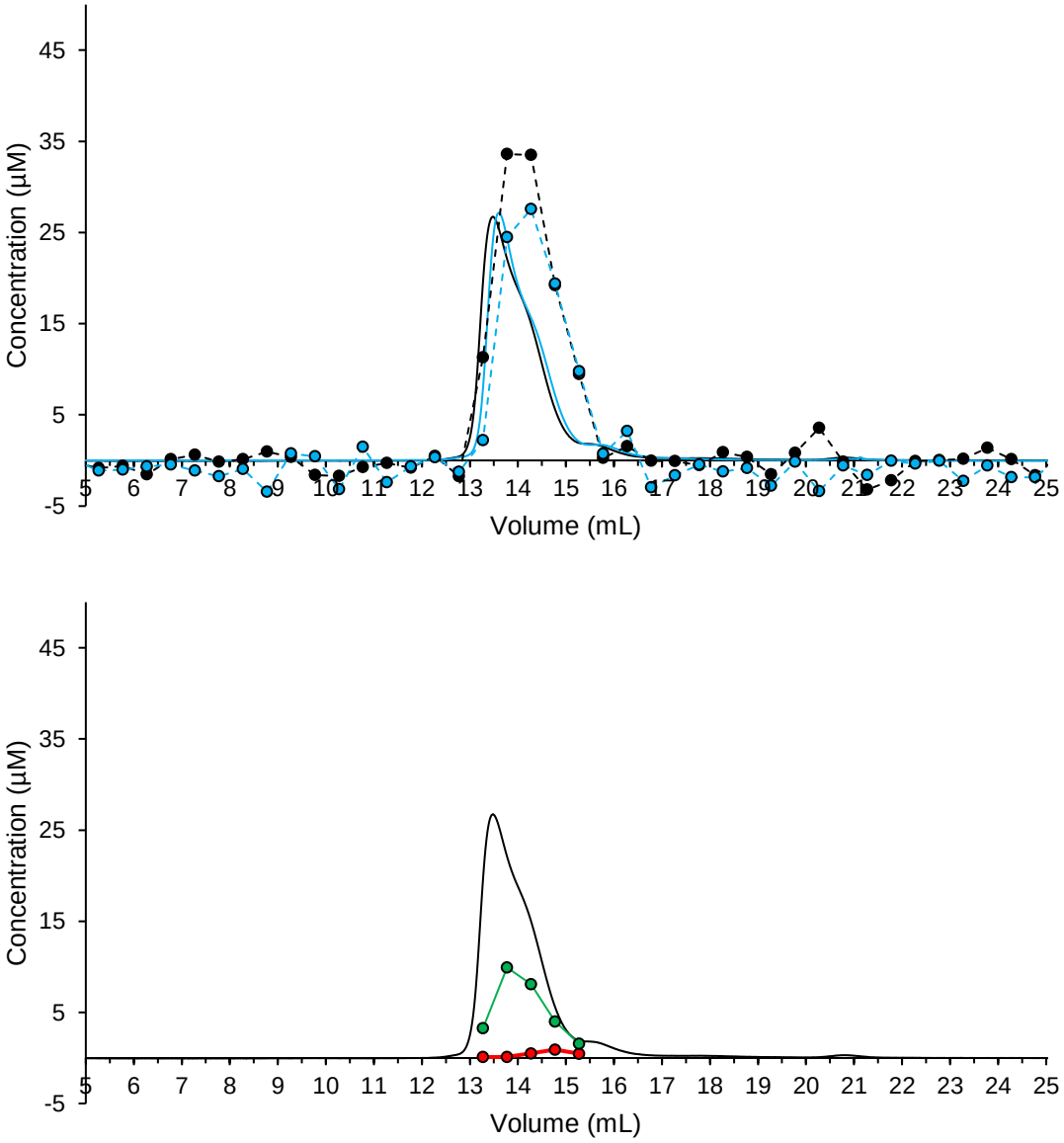

9. References

Abajian, C., Yatsunyk, L. A., Ramirez, B. E., & Rosenzweig, A. C. (2004). Yeast Cox17 solution structure and copper(I) binding. *Journal of Biological Chemistry*, 279(51), 53584–53592.

Aguirre, G., & Pilon, M. (2016). Copper Delivery to Chloroplast Proteins and its Regulation. *Frontiers in Plant Science*, 6, 1250.

Arnesano, F., Banci, L., Bertini, I., Cantini, F., Ciofi-Baffoni, S., Huffman, D. L., & O'Halloran, T. V. (2001). Characterization of the Binding Interface between the Copper Chaperone Atx1 and the First Cytosolic Domain of Ccc2 ATPase. *Journal of Biological Chemistry*, 276(44), 41365–41376.

Asati, A., Pichhode, M., & Nikhil, K. (2016). Effect of Heavy Metals on Plants: An Overview. *International Journal of Application of Innovation in Engineering & Management*, 5(3), 56–66.

Badarau, A., Baslé, A., Firbank, S. J., & Dennison, C. (2013). Crosstalk between Cu(I) and Zn(II) homeostasis in Atx1 and cognate domains. *Chemical Communications*, 49(73), 8000–8002.

Badarau, A., & Dennison, C. (2011). Thermodynamics of copper and zinc distribution in the cyanobacterium *Synechocystis* PCC 6803. *Proceedings of the National Academy of Sciences of the United States of America,* 108(32), 13007–13012.

Banci, L., Bertini, I., Cantini, F., Felli, I. C., Gonnelli, L., Hadjiliadis, N., Pierattelli, R., Rosato, A., & Voulgaris, P. (2006). The Atx1-Ccc2 complex is a metal-mediated protein-protein interaction. *Nature Chemical Biology*, 2(7), 367–368.

Banci, L., Bertini, I., Ciofi-Baffoni, S., Hadjiloi, T., Martinelli, M., & Palumaa, P. (2008). Mitochondrial copper(I) transfer from Cox17 to Sco1 is coupled to electron transfer. *Proceedings of the National Academy of Sciences of the United States of America*, 105(19), 6803.

Banci, L., Bertini, I., Ciofi-Baffoni, S., Su, X. C., Borrelly, G. P. M., & Robinson, N. J. (2004). Solution structures of a cyanobacterial metallochaperone: Insight into an atypical copper-binding motif. *Journal of Biological Chemistry*, 279(26), 27502–27510.

Bernal, M., Casero, D., Singh, V., Wilson, G. T., Grande, A., Yang, H., Dodani, S. C., Pellegrini, M., Huijser, P., Connolly, E. L., Merchant, S. S., & Krämer, U. (2012). Transcriptome sequencing identifies SPL7-regulated copper acquisition genes FRO4/FRO5 and the copper dependence of iron homeostasis in *Arabidopsis*. *Plant Cell*, 24(2), 738–761.

Binder, B. M. (2020). Ethylene signaling in plants. *Journal of Biological Chemistry*, 295(22), 7710–7725.

Binder, B. M., Rodríguez, F. I., & Bleecker, A. B. (2010). The copper transporter RAN1 is essential for biogenesis of ethylene receptors in *Arabidopsis*. *Journal of Biological Chemistry*, 285(48), 37263–37270.

Blaha, D., Arous, S., Blériot, C., Dorel, C., Mandrand-Berthelot, M. A., & Rodrigue, A. (2011). The Escherichia coli metallo-regulator RcnR represses *rcnA* and *rcnR* transcription through binding on a shared operator site: Insights into regulatory specificity towards nickel and cobalt. *Biochimie*, 93(3), 434–439.

Brown, N. L., Stoyanov, J. V., Kidd, S. P., & Hobman, J. L. (2003). The MerR family of transcriptional regulators. *FEMS Microbiology Reviews*, 27(2–3),

145–163.

Buccella, D., Lim, M. H., & Morrow, J. R. (2019). Metals in Biology: From Metallomics to Trafficking. *Inorganic Chemistry*, 58(20), 13505–13508.

Casson, S. A., Chilley, P. M., Topping, J. F., Evans, I. M., Souter, M. A., & Lindsey, K. (2002). The POLARIS gene of Arabidopsis encodes a predicted peptide required for correct root growth and leaf vascular patterning. *The Plant Cell*, 14(8), 1705–1721.

Chandrangsu, P., Rensing, C., & Helmann, J. D. (2017). Metal Homeostasis and Resistance in Bacteria. *Nature Reviews. Microbiology*, 15(6), 338.

Chang, C., Kwok, S. F., Bleecker, A. B., & Meyerowitz, E. M. (1993). Arabidopsis Ethylene-Response Gene ETR1: Similarity of Product to Two-Component Regulators. *Science*, 262(5133), 539–544.

Changela, A., Chen, K., Xue, Y., Holschen, J., Outten, C. E., O'Halloran, T. V, & Mondragón, A. (2003b). Molecular basis of metal-ion selectivity and zeptomolar sensitivity by CueR. *Science*, 301(5638), 1383–1387.

Chen, K., Yuldasheva, S., Penner-Hahn, J. E., & O'Halloran, T. V. (2003). An atypical linear Cu(I)-S2 center constitutes the high-affinity metal-sensing site in the CueR metalloregulatory protein. *Journal of the American Chemical Society*, 125(40), 12088–12089.

Chen, Y. F., Randlett, M. D., Findell, J. L., & Schallert, G. E. (2002). Localization of the ethylene receptor ETR1 to the endoplasmic reticulum of *Arabidopsis*. *The Journal of Biological Chemistry*, 277(22), 19861–19866.

Cheng, Y. (2018). Membrane protein structural biology in the era of single particle

cryo-EM. *Current Opinion in Structural Biology*, 52, 58–63.

Chilley, P. M., Casson, S. A., Tarkowski, P., Hawkins, N., Wang, K. L.-C. L. C., Hussey, P. J., Beale, M., Ecker, J. R., Sandberg, G. K., & Lindsey, K. (2006). The POLARIS Peptide of *Arabidopsis* Regulates Auxin Transport and Root Growth via Effects on Ethylene Signaling. *The plant cell online*, 18(11), 3058–3072.

Choi, T. S., & Tezcan, F. A. (2022). Design of a Flexible, Zn-Selective Protein Scaffold that Displays Anti-Irving–Williams Behavior. *Journal of the American Chemical Society*, 39(144) 18090-18100.

Chung, C. Y. S., Posimo, J. M., Lee, S., Tsang, T., Davis, J. M., Brady, D. C., & Chang, C. J. (2019). Activity-based ratiometric FRET probe reveals oncogene-driven changes in labile copper pools induced by altered glutathione metabolism. *Proceedings of the National Academy of Sciences of the United States of America*, 116(37), 18285–18294.

Connorton, J. M., Balk, J., & Rodríguez-Celma, J. (2017). Iron homeostasis in plants – a brief overview. *Metallomics*, 9(7), 813–823.

Dainty, S. J., Patterson, C. J., Waldron, K. J., & Robinson, N. J. (2010). Interaction between cyanobacterial copper chaperone Atx1 and zinc homeostasis. *Journal of Biological Inorganic Chemistry*, 15(1), 77–85.

Diao, T., White, P., Guzei, I., & Stahl, S. S. (2012). Characterization of DMSO coordination to palladium(II) in solution and insights into the aerobic oxidation catalyst, $Pd(DMSO)_2(TFA)_2$. *Inorganic Chemistry*, 51(21), 11898–11909.

DiDonato, M., Narindrasorasak, S., Forbes, J. R., Cox, D. W., & Sarkar, B. (1997).

Expression, purification, and metal binding properties of the N-terminal domain from the Wilson disease putative copper-transporting ATPase (ATP7B). *Journal of Biological Chemistry*, 272(52), 33279–33282.

Dirks-Hofmeister, M. E., Kolkenbrock, S., & Moerschbacher, B. M. (2013). Parameters That Enhance the Bacterial Expression of Active Plant Polyphenol Oxidases. *PLoS ONE*, 8(10), 77291.

Djoko, K. Y., Xiao, Z., Huffman, D. L., & Wedd, A. G. (2007). Conserved Mechanism of Copper Binding and Transfer. A Comparison of the Copper-Resistance Proteins PcoC from *Escherichia coli* and CopC from *Pseudomonas syringae*. *Inorganic chemistry,* 11(46) 4560-4568.

Dougherty, D. A. (1996). Cation-pi interactions in chemistry and biology: a new view of benzene, Phe, Tyr, and Trp. *Science*, 271(5246), 163–168.

Ecker, J. R. (1995). The ethylene signal transduction pathway in plants. *Science*, 268(5211), 667–675.

Eyer, P., Worek, F., Kiderlen, D., Sinko, G., Stuglin, A., Simeon-Rudolf, V., & Reiner, E. (2003). Molar absorption coefficients for the reduced Ellman reagent: reassessment. *Analytical Biochemistry*, 312(2), 224–227.

Fabiane, S. M., Sohi, M. K., Wan, T., Payne, D. J., Bateson, J. H., Mitchell, T., & Sutton, B. J. (1998). Crystal structure of the zinc-dependent β-lactamase from *Bacillus cereus* at 1.9 Å resolution: Binuclear active site with features of a mononuclear enzyme. *Biochemistry*, 37(36), 12404–12411.

Foster, A. W., Clough, S. E., Aki, Z., Young, T. R., Clarke, A. R., & Robinson, N. J. (2022). Metalation calculators for *E. coli* strain JM109 (DE3): aerobic,

anaerobic, and hydrogen peroxide exposed cells cultured in LB media. *Metallomics*, 14(9).

Foster, A. W., Osman, D., & Robinson, N. J. (2014). Metal preferences and metalation. *In Journal of Biological Chemistry* 289(41), 28095–28103.

Foster, A. W., Patterson, C. J., Pernil, R., Hess, C. R., & Robinson, N. J. (2012). Cytosolic Ni(II) sensor in cyanobacterium: Nickel detection follows nickel affinity across four families of metal sensors. *Journal of Biological Chemistry*, 287(15), 12142–12151.

Gallivan, J. P., & Dougherty, D. A. (1999). Cation-π interactions in structural biology. *Proceedings of the National Academy of Sciences of the United States of America*, 96(17), 9459–9464.

Garcia-Molina, A., Xing, S., & Huijser, P. (2014). Functional characterisation of *Arabidopsis* SPL7 conserved protein domains suggests novel regulatory mechanisms in the Cu deficiency response. *BMC Plant Biology,* 14(1), 1–14.

Gitlin, J. D. (2003). Wilson disease. *Gastroenterology*, 125(6), 1868–1877.

Golynskiy, M. V, Gunderson, W. A., Hendrich, M. P., & Cohen, S. M. (2006). Metal Binding Studies and EPR Spectroscopy of the Manganese Transport Regulator MntR †. *Biochemistry*, 51(45) 15395-15372.

Günther, V., Lindert, U., & Schaffner, W. (2012). The taste of heavy metals: Gene regulation by MTF-1. *Molecular Cell Research*, 1823(9), 1416–1425.

Guzmán, P., & Ecker, J. R. (1990). Exploiting the triple response of *Arabidopsis* to identify ethylene-related mutants. *The Plant Cell*, 2(6), 513–523.

Hamza, I., Schaefer, M., Klomp, L. W. J., & Gitlin, J. D. (1999). Interaction of the

copper chaperone HAH1 with the Wilson disease protein is essential for copper homeostasis. *Proceedings of the National Academy of Sciences of the United States of America*, 96(23), 13363–13368.

Heaton, D., Nittis, T., Srinivasan, C., & Winge, D. R. (2000). Mutational Analysis of the Mitochondrial Copper Metallochaperone Cox17*. *Journal of Biological Chemistry*, 275, 37582–37587.

Himelblau, E., Mira, H., Lin, S. J., Culotta, V. C., Peñarrubia, L., & Amasino, R. M. (1998). Identification of a functional homolog of the yeast copper homeostasis gene ATX1 from *Arabidopsis*. *Plant Physiology*, 117(4), 1227–1234.

Hirayama, T., Kieber, J. J., Hirayama, N., Kogan, M., Guzman, P., Nourizadeh, S., Alonso, J. M., Dailey, W. P., Dancis, A., & Ecker, J. R. (1999). RESPONSIVE-TO-ANTAGONIST1, a Menkes/Wilson disease-related copper transporter, is required for ethylene signaling in *Arabidopsis*. *Cell*, 97(3), 383–393.

Hobman, J. L. (2007). MerR family transcription activators: Similar designs, different specificities. *Molecular Microbiology* 63(5) 1275–1278.

Holloway, Z. G., Velayos-Baeza, A., Howell, G. J., Levecque, C., Ponnambalam, S., Sztul, E., & Monaco, A. P. (2013). Trafficking of the Menkes copper transporter ATP7A is regulated by clathrin-, AP-2-, AP-1-, and Rab22-dependent steps. *Molecular Biology of the Cell*, 24(11), 1735–1748.

Huffman, D. L., & O'Halloran, T. V. (2001). Function, structure, and mechanism of intracellular copper trafficking proteins. *In Annual Review of Biochemistry* 70(1), 677–701.

Imlay, J. A. (2014). The mismetallation of enzymes during oxidative stress. In

Journal of Biological *Chemistry* 289(41), 28121–28128.

Irving, H., & Williams, R. J. P. (1948). Order of Stability of Metal Complexes. *Nature*, 162(4123), 746–747.

Jeong, H., Barbe, V., Lee, C. H., Vallenet, D., Yu, D. S., Choi, S. H., Couloux, A., Lee, S. W., Yoon, S. H., Cattolico, L., Hur, C. G., Park, H. S., Ségurens, B., Kim, S. C., Oh, T. K., Lenski, R. E., Studier, F. W., Daegelen, P., & Kim, J. F. (2009). Genome Sequences of *Escherichia coli* B strains REL606 and BL21(DE3*). Journal of Molecular Biology*, 394(4), 644–652.

Jumper, J., Evans, R., Pritzel, A., Green, T., Figurnov, M., Ronneberger, O., Tunyasuvunakool, K., Bates, R., Žídek, A., Potapenko, A., Bridgland, A., Meyer, C., Kohl, S. A. A., Ballard, A. J., Cowie, A., Romera-Paredes, B., Nikolov, S., Jain, R., Adler, J., … Hassabis, D. (2021). Highly accurate protein structure prediction with AlphaFold. *Nature*, 596(7873), 583–589.

Kaim, W., Rall, J., & Rall, J. (1996). Copper A “Modern” Bioelement. *Angewandte Chemie* (International Edition in English), 35(1), 43–60.

Kampatsikas, I., & Rompel, A. (2021). Similar but Still Different: Which Amino Acid Residues Are Responsible for Varying Activities in Type-III Copper Enzymes? *Chembiochem*, 22(7), 1161.

Kang, Y., Weber, K. D., Qiu, Y., Kiley, P. J., & Blattner, F. R. (2005). Genome-Wide Expression Analysis Indicates that FNR of *Escherichia coli* K-12 Regulates a Large Number of Genes of Unknown Function. *Journal of Bacteriology*, 187(3), 1135.

Kay, A. R. (2004). Detecting and minimizing zinc contamination in physiological

solutions. *BMC Physiology*, 4(1), 1–9.

Kendrick, M. D., & Chang, C. (2008). Ethylene signaling: new levels of complexity and regulation. *In Current Opinion in Plant Biology* 11(5), 479–485.

Kuzmič, P. (2009). DynaFit—A Software Package for Enzymology. *Methods in Enzymology*, 467(C), 247–280.

Lacey, R. F., & Binder, B. M. (2014). How plants sense ethylene gas - The ethylene receptors. *Journal of Inorganic Biochemistry*, 133, 58–62.

Larin, D., Mekios, C., Das, K., Ross, B., Yang, A. S., & Gilliam, T. C. (1999). Characterization of the interaction between the Wilson and Menkes disease proteins and the cytoplasmic copper chaperone, HAH1p. *The Journal of Biological Chemistry*, 274(40), 28497–28504.

Lilay, G. H., Persson, D. P., Castro, P. H., Liao, F., Alexander, R. D., Aarts, M. G. M., & Assunção, A. G. L. (2021). *Arabidopsis* bZIP19 and bZIP23 act as zinc sensors to control plant zinc status. *Nature Plants*, 7(2), 137–143.

Lin, S. J., & Culotta, V. C. (1995). The ATX1 gene of *Saccharomyces cerevisiae* encodes a small metal homeostasis factor that protects cells against reactive oxygen toxicity. *Proceedings of the National Academy of Sciences of the United States of America*, 92(9), 3784–3788.

Livak, K. J., & Schmittgen, T. D. (2001). Analysis of Relative Gene Expression Data Using Real-Time Quantitative PCR and the 2−ΔΔCT Method. *Methods*, 25(4), 402–408.

Lutsenko, S., Petrukhin, K., Cooper, M. J., Gilliam, C. T., & Kaplan, J. H. (1997). N-terminal domains of human copper-transporting adenosine triphosphatases

(the Wilson's and Menkes Disease Proteins) bind copper selectively in vivo and in vitro with stoichiometry of one copper per metal- binding repeat. *Journal of Biological Chemistry*, 272(30), 18939–18944.

Lutsenko, S., Tsivkovskii, R., & Walker, J. M. (2003). Functional properties of the human copper-transporting ATPase ATP7B (the Wilson's disease protein) and regulation by metallochaperone Atox1. *Annals of the New York Academy of Sciences*, 986, 204–211.

Marks, J. H., Ward, T. B., & Duncan, M. A. (2019). Infrared spectroscopy of coordination and solvation in $Cu^{+}(C_2H_4)_n$ (n = 1–9) complexes. *International Journal of Mass Spectrometry*, 435, 107–113.

Martini, M. A. (2019). Thermodynamic description of bacterial metal-sensing:A cellular logic for metals. *http://etheses.dur.ac.uk*

Milo, R. (2013). What is the total number of protein molecules per cell volume? A call to rethink some published values. *Bioessay*s, 35(12), 1050.

Mira, H., Martínez-García, F., & Peñarrubia, L. (2001). Evidence for the plant-specific intercellular transport of the *Arabidopsis* copper chaperone CCH. *The Plant Journal*, 25(5), 521–528.

Miras, R., Morin, I., Jacquin, O., Cuillel, M., Guillain, F., & Mintz, E. (2008). Interplay between glutathione, Atx1 and copper. 1. Copper(I) glutathionate induced dimerization of Atx1. *Journal of Biological Inorganic Chemistry*, 13(2), 195–205.

Miura, C., Komatsu, K., Maejima, K., Nijo, T., Kitazawa, Y., Tomomitsu, T., Yusa, A., Himeno, M., Oshima, K., & Namba, S. (2015). Functional characterization

of the principal sigma factor RpoD of *phytoplasmas* via an in vitro transcription assay. *Scientific Reports*, 5(11893)

Mudge, A. (2016). The role of the POLARIS peptide in ethylene signallingand root development in Arabidopsis thaliana. Durham E-Theses. *http://etheses.dur.ac.uk*

Newell, D. B., & Tiesinga, E. (2019). *The International System of Units* (SI), 2019 Edition.

O'Malley, R. C., Rodriguez, F. I., Esch, J. J., Binder, B. M., O'Donnell, P., Klee, H. J., & Bleecker, A. B. (2005). Ethylene-binding activity, gene expression levels, and receptor system output for ethylene receptor family members from *Arabidopsis* and tomato. *Plant Journal*, 41(5), 651–659.

Osman, D., Foster, A. W., Chen, J., Svedaite, K., Steed, J. W., Lurie-Luke, E., Huggins, T. G., & Robinson, N. J. (2017). Fine control of metal concentrations is necessary for cells to discern zinc from cobalt. *Nature Communications*, 8(1), 1884.

Osman, D., Martini, M. A., Foster, A. W., Chen, J., Scott, A. J. P., Morton, R. J., Steed, J. W., Lurie-Luke, E., Huggins, T. G., Lawrence, A. D., Deery, E., Warren, M. J., Chivers, P. T., & Robinson, N. J. (2019). Bacterial sensors define intracellular free energies for correct enzyme metalation. *Nature Chemical Biology*, 15(3), 241–249.

Osman, D., & Robinson, N. J. (2022). Protein metalation in a nutshell. *FEBS Letters.*

Ostermeier, C., Iwata, S., & Michel, H. (1996). Cytochrome c oxidase. *Current*

Opinion in Structural Biology, 6(4), 460–466.

Outten, C. E., & O'Halloran, T. V. (2001). Femtomolar sensitivity of metalloregulatory proteins controlling zinc homeostasis. *Science*, 292(5526), 2488–2492.

Outten, Caryn E., Outten, F. W., & O'Halloran, T. V. (1999). DNA Distortion Mechanism for Transcriptional Activation by ZntR, a Zn(II)-responsive MerR Homologue in *Escherichia coli*. *Journal of Biological Chemistry*, 274(53), 37517–37524.

Outten, F. W., Outten, C. E., Hale, J., & O'Halloran, T. V. (2000). Transcriptional activation of an *Escherichia coli* copper efflux regulon by the chromosomal MerR homologue, CueR. The *Journal of Biological Chemistry*, 275(40), 31024–31029.

Pavlin, M., Qasem, Z., Sameach, H., Gevorkyan-Airapetov, L., Ritacco, I., Ruthstein, S., & Magistrato, A. (2019). Unraveling the Impact of Cysteine-to-Serine Mutations on the Structural and Functional Properties of Cu(I)-Binding Proteins. *International Journal of Molecular Sciences*, 20(14).

Pinske, C., Bönn, M., Krüger, S., Lindenstrauß, U., & Sawers, R. G. (2011). Metabolic Deficiences Revealed in the Biotechnologically Important Model Bacterium *Escherichia coli* BL21(DE3). *Plos One*, 6(8).

Pufahl, R. A., Singer, C. P., Peariso, K. L., Lin, S. J., Schmidt, P. J., Fahrni, C. J., Cizewski Culotta, V., Penner-Hahn, J. E., & O'Halloran, T. V. (1997). Metal ion chaperone function of the soluble Cu(I) receptor Atx1. *Science*, 278(5339), 853–856.

Puig, S., Mira, H., Dorcey, E., Sancenón, V., Andrés-Colás, N., Garcia-Molina, A., Burkhead, J. L., Gogolin, K. A., Abdel-Ghany, S. E., Thiele, D. J., Ecker, J. R., Pilon, M., & Peñarrubia, L. (2007). Higher plants possess two different types of ATX1-like copper chaperones. *Biochemical and Biophysical Research Communications*, 354(2), 385–390.

Ramakers, C., Ruijter, J. M., Lekanne Deprez, R. H., & Moorman, A. F. M. (2003). Assumption-free analysis of quantitative real-time polymerase chain reaction (PCR) data. *Neuroscience Letters,* 339(1), 62–66.

Rice, W. J., Kovalishin, A., & Stokes, D. L. (2006). Role of metal-binding domains of the copper pump from *Archaeoglobus fulgidus*. *Biochemical and Biophysical Research Communications*, 348(1), 124–131.

Robinson, N. J., & Winge, D. R. (2010). Copper Metallochaperones. *Annual Review of Biochemistry*, 79(1), 537–562.

Rodríguez, F. I., Esch, J. J., Hall, A. E., Binder, B. M., Eric Schaller, G., & Bleecker, A. B. (1999). A copper cofactor for the ethylene receptor ETR1 from *Arabidopsis*. *Science*, 283(5404), 996–998.

Rubino, J. T., Chenkin, M. P., Keller, M., Riggs-Gelasco, P., & Franz, K. J. (2011). A comparison of methionine, histidine and cysteine in copper(I)-binding peptides reveals differences relevant to copper uptake by organisms in diverse environments. *Metallomics*, 3(1), 61–73.

Rulíšek, L., & Vondrášek, J. (1998). Coordination geometries of selected transition metal ions (Co^{2+}, Ni^{2+}, Cu^{2+}, Zn^{2+}, Cd^{2+}, and Hg^{2+}) in metalloproteins. *Journal of Inorganic Biochemistry*, 71(3–4), 115–127.

Sambrook, J., & Russel, D. (2001). Molecular Cloning a laboratory manual (3rd ed.). CHSL press.

Schägger, H., & von Jagow, G. (1987). Tricine-sodium dodecyl sulfate-polyacrylamide gel electrophoresis for the separation of proteins in the range from 1 to 100 kDa. *Analytical Biochemistry*, 166(2), 368–379.

Schott-Verdugo, S., Müller, L., Classen, E., Gohlke, H., & Groth, G. (2019). Structural Model of the ETR1 Ethylene Receptor Transmembrane Sensor Domain. *Scientific Reports*, 9(1), 1–14.

Setty, S. R. G., Tenza, D., Sviderskaya, E. V., Bennett, D. C., Raposo, G., & Marks, M. S. (2008). Cell-specific ATP7A transport sustains copper-dependent tyrosinase activity in melanosomes. *Nature,* 454(7208), 1142.

Shakeel, S. N., Gao, Z., Amir, M., Chen, Y. F., Rai, M. I., Haq, N. U., & Schaller, G. E. (2015). Ethylene regulates levels of ethylene receptor/CTR1 signaling complexes in *Arabidopsis thaliana*. *Journal of Biological Chemistry*, 290(19), 12415–12424.

Shenberger, Y., Marciano, O., Gottlieb, H. E., & Ruthstein, S. (2018). Insights into the N-terminal Cu(II) and Cu(I) binding sites of the human copper transporter CTR1. *Journal of Coordination Chemistry*, 71(11–13), 1985–2002.

Sheng, Y., Yan, X., Huang, Y., Han, Y., Zhang, C., Ren, Y., Fan, T., Xiao, F., Liu, Y., & Cao, S. (2019). The WRKY transcription factor, WRKY13, activates PDR8 expression to positively regulate cadmium tolerance in *Arabidopsis*. *Plant, Cell & Environment*, 42(3), 891–903.

Singleton, C., & Le Brun, N. E. (2007). Atx1-like chaperones and their cognate P-

type ATPases: Copper-binding and transfer. *BioMetals*, 20(3–4), 275–289.

Stasser, J. P., Eisses, J. F., Barry, A. N., Kaplan, J. H., & Blackburn, N. J. (2005). Cysteine-to-serine mutants of the human copper chaperone for superoxide dismutase reveal a copper cluster at a domain III dimer interface. *Biochemistry*, 44(9), 3143–3152.

Stohs, S. J., & Bagchi, D. (1995). Oxidative mechanisms in the toxicity of metal ions. In *Free Radical Biology and Medicine* 18(2), 321-336.

Suttisansanee, U., Lau, K., Lagishetty, S., Rao, K. N., Swaminathan, S., Sauder, J. M., Burley, S. K., & Honek, J. F. (2011). Structural Variation in Bacterial Glyoxalase I Enzymes: investigation of the metalloenzyme glyoxylase I from *Clostridium acetobutylicum*. *Journal of Biological Chemistry*, 286(44), 38367–38374.

Taranto, F., Pasqualone, A., Mangini, G., Tripodi, P., Miazzi, M. M., Pavan, S., & Montemurro, C. (2017). Polyphenol Oxidases in Crops: Biochemical, Physiological and Genetic Aspects. *International Journal of Molecular Sciences*, 18(2).

Thirumoorthy, N., Manisenthil Kumar, K., Shyam Sundar, A., Panayappan, L., Chatterjee, M., Kumar, M., & Chatterjee, M. (2007). Metallothionein: An overview. *World Journal of gastroenterology.* 13(7) 993-996

Topping, J. F., & Lindsey, K. (1997). Promoter trap markers differentiate structural and positional components of polar development in *Arabidopsis*. *Plant Cell*, 9(10), 1713–1725.

Tottey, S., Waldron, K. J., Firbank, S. J., Reale, B., Bessant, C., Sato, K., Cheek,

T. R., Gray, J., Banfield, M. J., Dennison, C., & Robinson, N. J. (2008). Protein-folding location can regulate manganese-binding versus copper- or zinc-binding. *Nature*, 455(7216), 1138–1142.

Tümer, Z., & Møller, L. B. (2010). Menkes disease. *In European Journal of Human Genetics*, 18(5), 511-518.

Waldron, K. J., Rutherford, J. C., Ford, D., & Robinson, N. J. (2009). Metalloproteins and metal sensing. In *Nature*, 460(7257), 823-830.

Walker, J. M., Huster, D., Ralle, M., Morgan, C. T., Blackburn, N. J., & Lutsenko, S. (2004). The N-terminal Metal-binding Site 2 of the Wilson's Disease Protein Plays a Key Role in the Transfer of Copper from Atox1. *Journal of Biological Chemistry*, 279(15), 15376–15384.

Walker, J. M., Tsivkovskii, R., & Lutsenko, S. (2002). Metallochaperone Atox1 transfers copper to the NH_2-terminal domain of the Wilson's disease protein and regulates its catalytic activity. *Journal of Biological Chemistry*, 277(31), 27953–27959.

Wang, W., Esch, J. J., Shiu, S. H., Agula, H., Binder, B. M., Chang, C., Patterson, S. E., & Bleecker, A. B. (2006). Identification of Important Regions for Ethylene Binding and Signaling in the Transmembrane Domain of the ETR1 Ethylene Receptor of *Arabidopsis*. *The Plant Cell*, 18(12), 3429–3442.

Wang, W., Hall, A. E., O'Malley, R., & Bleecker, A. B. (2003). Canonical histidine kinase activity of the transmitter domain of the ETR1 ethylene receptor from *Arabidopsis* is not required for signal transmission. *Proceedings of the National Academy of Sciences of the United States of America*, 100(1), 352–357.

Wernimont, A. K., Yatsunyk, L. A., & Rosenzweig, A. C. (2004). Binding of Copper(I) by the Wilson Disease Protein and Its Copper Chaperone. *Journal of Biological Chemistry*, 279(13), 12269–12276.

Woeste, K. E. (2000). A Strong Loss-of-Function Mutation in RAN1 Results in Constitutive Activation of the Ethylene Response Pathway as Well as a Rosette-Lethal Phenotype. *The Plant Cell Online,* 12(3), 443–455.

Wu, D., Saleem, M., He, T., & He, G. (2021). The mechanism of metal homeostasis in plants: A new view on the synergistic regulation pathway of membrane proteins, lipids and metal ions. In *Membranes* 11(12) 984-1012.

Xiao, Z., Brose, J., Schimo, S., Ackland, S. M., La Fontaine, S., & Wedd, A. G. (2011). Unification of the copper(I) binding affinities of the metallo-chaperones Atx1, Atox1, and related proteins: Detection probes and affinity standards. *Journal of Biological Chemistry*, 286(13), 11047–11055.

Xiao, Z., Loughlin, F., George, G. N., Howlett, G. J., & Wedd, A. G. (2004). C-Terminal Domain of the Membrane Copper Transporter Ctr1 from Saccharomyces cerevisiae Binds Four Cu(I) Ions as a Cuprous-Thiolate Polynuclear Cluster: Sub-femtomolar Cu(I) Affinity of Three Proteins Involved in Copper Trafficking*. Journal of the American Chemical Society*, 126(10), 3081–3090.

Xiao, Z., & Wedd, A. G. (2010). The challenges of determining metal-protein affinities. In *Natural Product Reports*, 27(5), 768-789.

Xue, Y., Davis, A. V., Balakrishnan, G., Stasser, J. P., Staehlin, B. M., Focia, P., Spiro, T. G., Penner-Hahn, J. E., & O'Halloran, T. V. (2008). Cu(I) recognition via cation-π and methionine interactions in CusF. *Nature Chemical Biology,*

4(2), 107.

Yatsunyk, L. A., & Rosenzweig, A. C. (2007). Cu(I) binding and transfer by the N terminus of the Wilson disease protein. *Journal of Biological Chemistry*, 282(12), 8622–8631.

Young, T. R., Martini, M. A., Foster, A. W., Glasfeld, A., Osman, D., Morton, R. J., Deery, E., Warren, M. J., & Robinson, N. J. (2021). Calculating metalation in cells reveals CobW acquires CoII for vitamin B_{12} biosynthesis while related proteins prefer ZnII. *Nature Communications*, 12(1), 1–15.

Young, T. R., Wedd, A. G., & Xiao, Z. (2018). Evaluation of Cu(i) binding to the E2 domain of the amyloid precursor protein-a lesson in quantification of metal binding to proteins via ligand competition. *Metallomics*, 10(1), 108–119.

Young, T. R., & Xiao, Z. (2021a). Principles and practice of determining metal-protein affinities. *The Biochemical Journal*, 478(5), 1085–1116.

Yu, C. H., Yang, N., Bothe, J., Tonelli, M., Nokhrin, S., Dolgova, N. V., Braiterman, L., Lutsenko, S., & Dmitriev, O. Y. (2017). The metal chaperone Atox1 regulates the activity of the human copper transporter ATP7B by modulating domain dynamics. *The Journal of Biological Chemistry*, 292(44), 18169.

Zimmermann, M., Clarke, O., Gulbis, J. M., Keizer, D. W., Jarvis, R. S., Cobbett, C. S., Hinds, M. G., Xiao, Z., & Wedd, A. G. (2009). Metal binding affinities of *Arabidopsis* zinc and copper transporters: Selectivities match the relative, but not the absolute, affinities of their amino-terminal domains. *Biochemistry*, 48(49), 11640–11654.